University of Southampton

Faculty of Engineering and applied science

Institute of Sound and Vibration Research

Vibroacoustic power flow in infinite compliant pipes excited by mechanical forces and internal acoustic sources

by

Brian Ottar Olsen

Thesis submitted in fulfilment of the degree of

Doctor of Philosophy

2001

UNIVERSITY OF SOUTHAMPTON

ABSTRACT

FACULTY OF ENGINEERING AND APPLIED SCIENCE
INSTITUTE OF SOUND AND VIBRATION RESEARCH

Doctor of Philosophy

Vibroacoustic power flow in infinite compliant pipes
excited by mechanical forces and internal acoustic sources

by Brian Ottar Olsen

The present thesis is concerned with the theoretical and experimental description of vibroacoustic power flow in infinite fluid-filled pipes excited by hydroacoustic noise sources, such as flow control valves. The walls of the pipes are assumed to be compliant, so that vibrations of the shell wall induce pressure fluctuations in the fluid, and vice versa. The coupling between the pipe wall and the contained fluid is provided by the fluid loading of the pipe; the methods presented are valid for both light and heavy fluid loading.

Two distinct and complementary approaches are investigated for quantifying the vibroacoustic power flow: numerical simulations and controlled experiments.

The core of the numerical simulation approach is a vibroacoustic analogy that transforms the excitation of the fluid-filled pipe by internal turbulent flow into an equivalent vibroacoustical problem where the excitation is provided by a distribution of vibroacoustic sources applied to a pipe containing stationary fluid. When the excitation is formulated as an equivalent distribution of vibroacoustic sources (structural and acoustical), the resulting vibroacoustic power flow can be calculated via an extension of existing theory.

The necessary analytical and numerical tools for the prediction of the vibroacoustic power flow are assembled for point force excitation of the pipe wall, and for point monopole, point dipole, and point quadrupole excitation of the fluid.

The relative Mach number scaling of far-field fluid pressure radiated inside the pipe, for point monopole, point dipole, and point quadrupole, is investigated and the in-pipe results are compared to the corresponding free field results.

The proposed experimental approach involves mounting the noise source in an instrumented pipe system under controlled conditions. If one-directional wave propagation can be established (e.g. through anechoic terminations of the pipe), then the power input by the source can be inferred from modal measurements of the pipe wall response.

The modal measurements of the pipe wall response are obtained by modal decomposition of accelerometer measurements, and by direct measurements with shaped PVDF modal sensors.

Actual measurements of the vibroacoustic power flow using the proposed method are compared with numerical predictions for pipes with light and heavy fluid loading, excited both by a radial force at the pipe wall and by a transmitting hydrophone in the contained fluid.

Statement of original contribution

Both the theoretical and experimental strategies outlined in part I for quantifying valve noise are original: they were developed by the author in the course of the PhD, following suggestions from his supervisor. In particular, the theoretical approach of chapter 4 is based on an application of the acoustic analogy to the interior of a flexible-walled pipe: this has required an original exploration of the solution properties for point-dipole and point-quadrupole excitation of the contained fluid.

Part II of the thesis consists of a theoretical discussion of pipe response to structural and fluid excitation. It is assembled from various published sources including the research literature. Its originality lies in the fact that for the first time, a methodology is presented in detail for predicting the vibroacoustic power flow in pipes under such excitation.

Part III presents experiments on both light and heavy fluid loaded pipes. Some of the experimental techniques used are taken from published sources. However, the experiments include a number of original contributions; most notably the practical implementation of existing modal sensor concepts, and response measurements on a heavy fluid loaded pipe when excited by an internal transmitting hydrophone.

Contents

List of Tables

List of Symbols

A	Area
A_n	Arbitrary function
a	Radius of pipe
B_n	Arbitrary function
b	Branch number
C_n	Arbitrary function
c_f	Reference sound speed
c_f^e	Sound speed in exterior fluid
c_f^i	Sound speed in interior fluid
c_L	Thin-plate extensional wave speed, $c_L = \sqrt{E/\rho(1-\nu^2)}$
D	Extensional rigidity or membrane stiffness, $D = Eh/(1-\nu^2)$
D	Distance
E	Young's modulus
E^r	Mechanical excitation of shell wall in radial direction
E^z	Mechanical excitation of shell wall in axial direction
E^θ	Mechanical excitation of shell wall in tangential direction
e_{31}	Piezoelectric stress constant
e_{32}	Piezoelectric stress constant
F_{nb}	Modal power flow factor for given fluid-filled pipe
F^r	Mechanical force in radial direction
F^z	Mechanical force in axial direction
F^θ	Mechanical force in tangential direction
f	Arbitrary function
f	Frequency
f_l	Fluid loading (dimensional)
f_{ring}	Pipe ring frequency, $f_{\text{ring}} = c_L/2\pi a$
$\mathcal{F}$	Nondimensional fluid loading
G_f	Fluid Green function
G_s^i	Structural Green function in direction i
G_ω	Green function
H	Heaviside unit function
H_n	Hankel function of order n (commonly written $\mathrm{H}_n^{(1)}$)
h	Pipe wall thickness
I	Inverse of L-matrix
i	$\sqrt{-1}$
i	Running index

J_n	Bessel function of the first kind of order n
j	Running index
K	Bending stiffness, $K = Eh^3/12(1-\nu^2)$
k	Axial wavenumber
k_f	Acoustic wavenumber
k_e	Exterior acoustic wavenumber
k_e^r	Exterior radial wavenumber
k_i	Interior acoustic wavenumber
k_i^r	Interior radial wavenumber
L	Flügge matrix in equations of motion (nondimensional)
M	Mass
m	Circumferential mode
N	Number
n	Circumferential mode
P_{be}	Flexural (bending) power flow
P_{ex}	Extensional power flow
P_f	Fluid power flow
$P_{n,1}$	Predicted modal power flow for mode n for unit input
$P_{n,\mathrm{far}}$	Far field modal power flow for mode n
P_s	Structural power flow
P_{to}	Torsional power flow
P_κ	Power flow in given branch
p	Pressure
p_f	Reference pressure
p_e	External pressure
p_e^w	External pressure from wall vibration
p_i	Internal pressure
p_i^w	Internal pressure from wall vibration
p_i^m	Pressure from monopole
p_i^r	Pressure scattered from hard boundary
p_{ij}	Force per unit area
p^q	Pressure from quadrupole
p_ω	Frequency domain acoustic pressure
R_a	Axial amplitude ratio
R_t	Tangential amplitude ratio
r_o	Radial source position (dimensional)
r	Nondimensional radial position
r_o	Nondimensional radial position
r_{dim}	Radial position (dimensional)
S	Monopole source strength (range normalised pressure)
S	Flügge matrix in equations of motion (dimensional)
S	Surface (domain boundary)
s	Nondimensional axial position, $s = z/a$
T_{ij}	Lighthill stress tensor
t	Time
U	Displacement amplitude in axial direction

$\tilde{U}$	Modal displacement transform in axial direction
u	Axial displacement of pipe wall
$\tilde{u}$	Complex displacement amplitude of u
u^i	Displacement in direction i (w, v, u in a cylindrical coordinate system)
V	Displacement amplitude in tangential direction
$\tilde{V}$	Modal displacement transform in tangential direction
v	Tangential displacement of pipe wall
$\tilde{v}$	Complex displacement amplitude of v
W	Displacement amplitude in radial direction
$\tilde{W}$	Modal displacement transform in radial direction
w	Radial displacement of pipe wall
$\tilde{w}$	Complex displacement amplitude of w
$w_{n,1}$	Predicted modal displacement for mode n for unit input
$w_{n,\text{meas}}$	Measured modal displacement for mode n
$\mathbf{x}$	Position
$\mathbf{x}^f$	Position in the fluid
$\mathbf{x}^s$	Position in the structure (pipe wall)
$\mathbf{y}$	Source position
$\mathbf{y}^f$	Source position in the fluid
$\mathbf{y}^s$	Source position in the structure (pipe wall)
z	Axial position (dimensional)
z	Complex variable
α	Nondimensional axial wavenumber
β	Thickness ratio, $\beta^2 = h^2/12a^2$
δ	Dirac's delta function
ε_n	Constant, $\varepsilon_n = 1$ for $n = 0$, $\varepsilon_n = 2$ for $n \neq 0$
η_n	Constant, $\eta_n = 2$ for $n = 0$, $\eta_n = 1$ for $n \neq 0$
θ	Tangential position
θ_o	Tangential position of source
κ	Nondimensional wavenumber, $\kappa = ka$
ν	Poisson's ratio
ρ	Fluid density
ρ_f	Reference fluid density
ρ_e	Exterior fluid density
ρ_i	Interior fluid density
ρ_s	Material density of the structure (pipe wall)
σ	Radiation efficiency
τ	Viscous stress
ϕ_c	Cosine factor
ϕ_s	Sine factor
Ω	Nondimensional frequency, $\Omega = f/f_{\text{ring}}$
ω	Angular frequency
$\nabla_{\mathbf{y}}$	Source position gradient
∇^2	Laplacian

Acknowledgements

The present thesis is the product of an industrial PhD under the terms of the Danish Academy of Technical Sciences (the ATV). The research project has been conducted in close cooperation between the Institute of Sound and Vibration Research at the University of Southampton, and the Danish industrial enterprise Danfoss A/S, Comfort Controls Division. I would like to express my gratitude to the Danish Academy of Technical Sciences for approving and partly funding the research project.

At Danfoss A/S, I would like to thank my industrial supervisor Mr. AB Larsen for his continuous support in this project and in my career in general at Danfoss. Thanks also to the entire staff of the R&D laboratory at Danfoss A/S, Comfort Control Division, who patiently let me flood their laboratory through my experiments. I would also like to express my gratitude to my colleagues at Danfoss, who gave me support and ideas even without knowing it.

At the University of Southampton, I would especially like to thank my supervisor Prof. CL Morfey for his invaluable input to this project and for his understanding of the troubles and the learning curve of a newcomer to advanced vibroacoustics. The Institute of Sound and Vibration Research is a outstanding place to do research and I am very grateful to the entire staff and all the students. Special thanks to my review panel members Prof. PA Nelson and Dr. P Joseph, who tried (but did not quite succeed) to keep me inside the 3 year time span of a PhD.

The most heartfelt thanks of all go to them who suffered the most throughout this project: my wife Helen and my son Emil. Without their love, support, and patience I could never have accomplished anything like this!

January 2001, Brian O. Olsen

Chapter 1

Introduction

1.1 Concept of Danish Industrial PhD Fellowship Programme

The objectives of the Danish Industrial PhD Fellowship Programme are to promote technological and financial development for Danish trade and industry, and to support young employees at Danish enterprises to obtain a PhD. The Danish Academy of Technical Sciences (in Danish 'Akademiet for de Tekniske Videnskaber' or ATV) funds each student's training programme in cooperation with an industrial partner. Suitable industrial partners are private Danish enterprises with a research and development environment.

The main part of the fellowship programme is a three-year research project at a university leading to the achievement of the PhD degree. The core of the educational scheme is a close and formalised partnership between an enterprise and a university for the conduct of the research project. In carrying out the research project the PhD student applies the knowledge and technology of the university to the benefit of the enterprise, which thereby acquires advanced knowledge and valuable technical skills. The research project is defined in cooperation between the industrial partner, the university and the PhD student.

The general conditions for the Danish Industrial PhD Fellowship Programme are

- The enterprise employs the PhD student for 3 years to work exclusively on the approved project and follow the educational programme defined in the project
- Even distribution of educational period between the enterprise and the university in order to secure the required interaction between research work and practical application of results
- Participation by the PhD student in a business-targeted course, arranged by ATV (corresponds to one month's work)

- Submission of a final study plan to the ATV Committee on Industrial PhD Fellowship Programme six months after the start of the educational programme
- Compliance with the regulations of the university in question
- Approval of the group of external examiners by the ATV Committee on Industrial PhD Fellowship Programme
- Participation of a representative of the ATV Committee on Industrial PhD Fellowship Programme in the dissemination/publication of the results.

1.2 Structure of the thesis

The thesis is divided into four main parts, not including this introduction. The first presents concepts of flow noise quantification, the second a framework for the prediction of the vibroacoustic power flow, and the third experimental quantification of the vibroacoustic power flow. The fourth part discusses the implications of this work and presents some conclusions. A graphical overview of the different parts of this thesis can be seen in figure 1.1.

The first part presents the overall strategy for quantification of flow noise sources, e.g. control valves, connected to water-filled pipes. Two conceptually different quantification methods are discussed: one based on experiments and another based on numerical methods. Both methods are based on the concept of vibroacoustic power flow; if the total vibroacoustic power flow can be quantified in the far field [1] and the absorbtion in the water-filled pipe can be assumed to be small, then the noise produced by e.g. a control valve can be inferred. The main elements of the experimental method are presented in part I, with the detailed measurements deferred to part III. Likewise the main elements of the numerical prediction approach are presented in part I, including the vibroacoustic analogy formulation; the necessary analytical and numerical tools are then developed in detail in part II. The first step in the numerical prediction approach is the calculation of the unsteady flow in the pipe; literature studies and feasibility tests during this work have revealed that the flow calculation is very complicated and worth a PhD study on its own. Discussion is therefore limited to basic concepts, with some remarks on recently published investigations. The second step, the vibroacoustic analogy, is discussed in detail in part I, except for the calculation of the vibroacoustic power flow which is discussed in part II.

Part II brings together published results from several sources, and shows how to calculate the vibroacoustic power flow in an infinite fluid-filled pipe from two simple types of excitation: a point force on the shell wall and a point monopole in the fluid. An all important part of the calculation of the power flow from these sources is the ability to predict the vibroacoustic response at any point (i.e. both the vibration of the pipe wall and the pressure in the contained fluid). Using the prediction model, a parameter

[1] i.e. some distance away from the source along the pipe

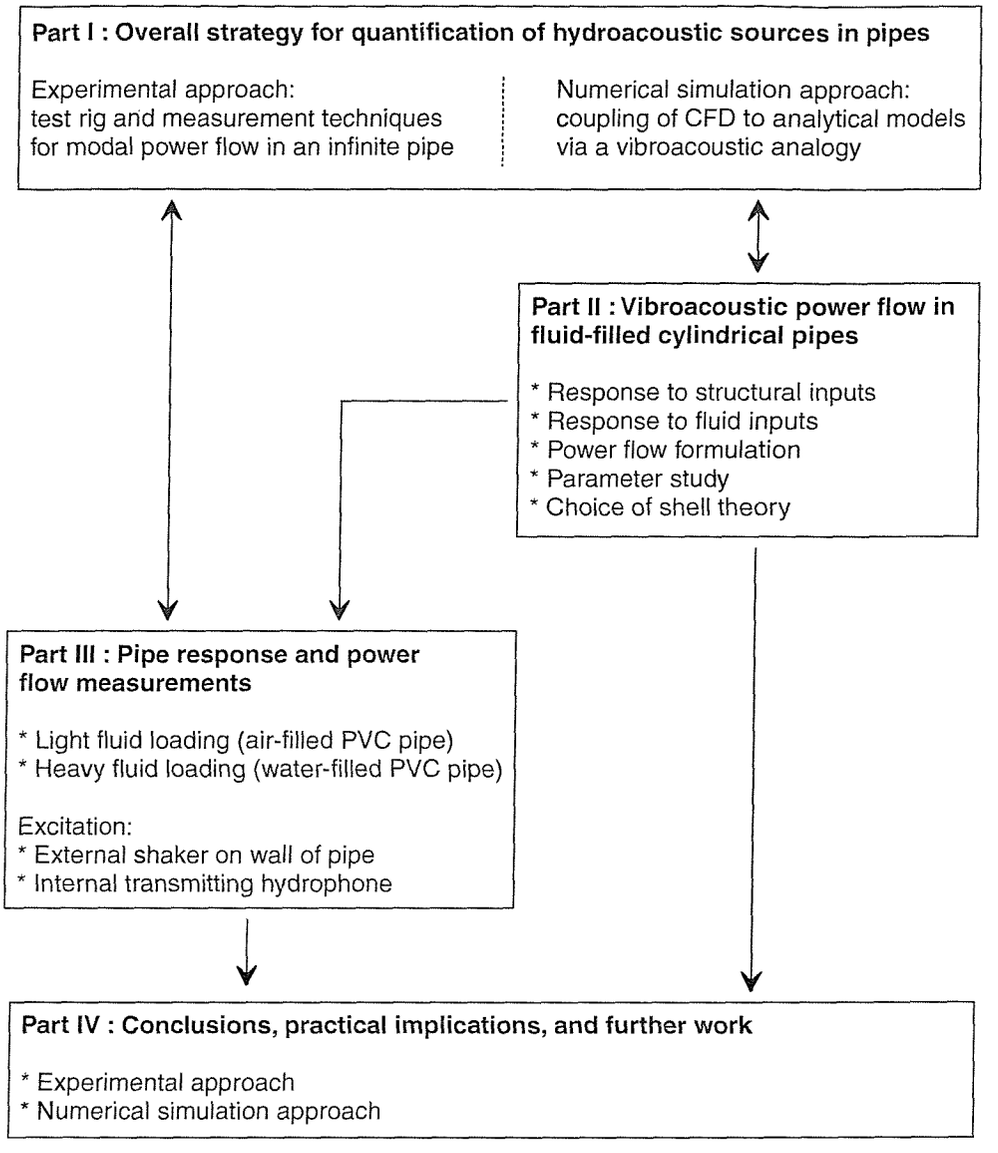

Figure 1.1: Thesis outline in diagrammatic form

study is presented; the study concentrates on the parameter range important for the industrial problem. Included in this parameter study is an assessment of the choice of shell theory in the prediction model. The prediction model is validated against the experiments in part III.

In part III, experiments quantifying the far field vibroacoustic power flow are presented. The experimental principle is first validated on a light fluid loaded pipe: a PVC pipe with air both inside and outside. During these experiments, the vibrational response of the pipe is very close to that of the in vacuo pipe, i.e. the pipe with vacuum both inside and outside. The modal vibrational response of the pipe is measured using modal decomposition of point measurements with an accelerometer. The vibrational response is compared with the prediction model from part II; excellent agreement is demonstrated in the near field and good agreement is demonstrated in the far field. A simple method is presented to infer the far field vibroacoustic power flow from the measured modal response, using the predicted vibrational response and the predicted power flow. The method relies on quite restrictive assumptions that are justified only under special conditions, but the experiments meet these conditions. The same experimental principle is used on a heavy fluid loaded pipe: a PVC pipe with air outside, but water inside. The modal response is measured using both the accelerometer decomposition technique and shaped modal sensors. These sensors are only sensitive to certain modes of vibration and they allow direct measurement of the modal response of a pipe. The modal measurements are compared with each other and with the prediction model, and it is concluded that the agreement is excellent in the near field and good in the far field. Due to the relative softness of the PVC pipe, the vibroacoustic power flow can be inferred from the measurements using the same method as for the light fluid loaded experiments.

Part IV states the main conclusions and discusses the relation between the individual findings. The findings obtained during the PhD project are discussed in the light of the industrial application of the present thesis. Finally are some suggestions for further work stated.

A bibliography is located in the end of the thesis, after the appendices.

1.3 Motivation of the present Industrial PhD project

The industrial sponsor of this project, Danfoss A/S, is one of the world's largest manufacturers of control devices for domestic heating applications. Since the sound quality of domestic appliances is becoming an important factor in consumer choice, one of the prime concerns of Danfoss is the noise output from heating applications including thermostatic radiator valves. Examples of thermostatic radiator valves are shown in figure 1.2.

The main industrial objective of this project is to gain knowledge that can eventually lead to a better design of flow control valves with respect to noise. While the actual design of flow control valves is outside the scope of this project, the methods to quantify

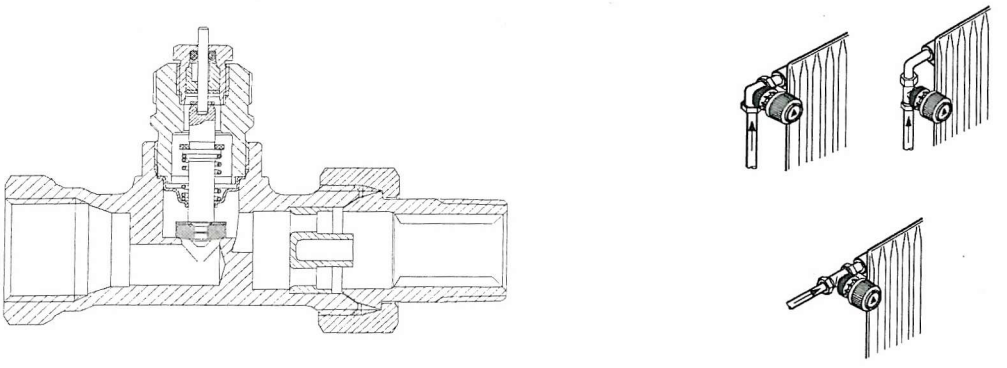

Figure 1.2: Cross section of Danfoss RA-FN 15 valve and application examples.

vibroacoustic power flow presented in this thesis are significant contributions to the general knowledge needed by manufacturers of devices intended for connection to water-filled pipes, if those devices can act as vibroacoustic sources.

Danfoss has for many years worked towards optimisation of control valves using indirect experimental techniques (one of the methods is explained in more detail in the next section). Using indirect measurement methods, valuable insight has been gained over the years, e.g. through a previous Industrial PhD project (Kiil 1982). However, the indirect methods have some drawbacks when used in optimisation cycles of new products. A more direct measurement technique that is able to quantify the noise output from the valve on its own would be a valuable asset in the toolbox of Danfoss.

Virtual product development using advanced Computer Aided Design (CAD) systems and numerical prediction software, allows predictions of many important parameters even before a prototype of the new design exists. Structural finite element programs can reliably predict deformations and stress concentrations of individual components, and other programs are commonly used to simulate the entire mould filling process when producing plastic components. At present Computational Fluid Dynamics (CFD) is a valuable tool in the development of new valves at Danfoss, as it provides insight into the detail of the fluid flow that would be very difficult to establish through experimental techniques.

At Danfoss, the general purpose CFD code Star-CD from Computational Dynamics has been used with great success for several purposes, including some 'virtual prototype' numerical experiments on new designs of valves. So far, the numerical experiments have been concentrated around the control properties of the valve (mainly flow rate as function of pressure drop across the valve, or flow rate as function of valve lift). Experience has shown that this kind of optimisation in some cases can introduce unwanted and unexpected noise problems, that need to be identified and removed using experi-

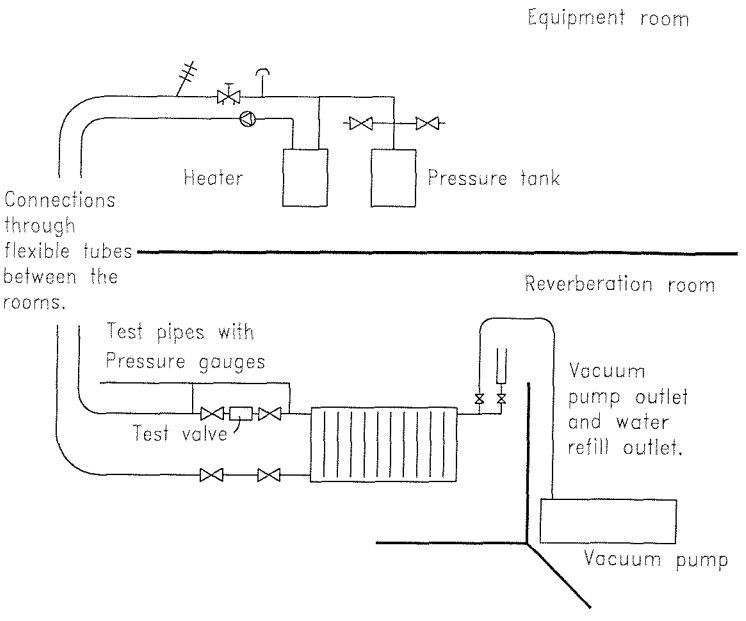

Figure 1.3: Sketch of experimental setup used in the Nordtest method.

mental methods. To be able to use the 'virtual prototype' techniques more efficiently, it would be very useful to be able to predict the acoustical properties of new designs at an early stage without experimental input.

1.3.1 Present experimental method used for noise source quantification

Different approaches exist to quantify the noise output of control valves. Many methods in the public domain are aimed at quantifying the very high noise intensities (with sound pressures up to 120 dB(A)) related to gas pressure reducing valves, e.g. Amini and Owen (1995) or Nakano et al. (1988). Of the measurement methods more relevant to products of Danfoss, all those in current use attempt to replicate the actual application where the control valve is used. While this approach seems sound from an end user point of view, it is problematic when comparing different applications or even individual valves, since the measurement methods rate the entire application and not the valve alone. This is one reason why the otherwise relevant work of Fuchs (1993) regarding generation and control of noise in water supply installations is difficult to apply directly to thermostatic radiator valves.

The method presently used at Danfoss for the noise rating of thermostatic radiator valves is an adapted form of the proposed Nordtest method, (Simmons 1997), 'Radiator valves: Determination of the sound power level in the laboratory'. Figure 1.3 shows the principal parts of the experimental setup. The thermostatic radiator valve to

be tested is mounted rigidly between two test pipes attached to a reference radiator. The reference radiator is suspended elastically inside a reverberation room. A water circulation is enforced by a small and quiet pump outside of the reverberation room. The flow noise generated by the valve is transmitted to the reference radiator through a specified test pipe. The airborne sound radiated from the reference radiator into the test room is measured. By comparison with a reference sound source, or by correction based on the reverberation time and the volume of the test room, the airborne sound power level of the radiator-and-valve assembly is determined.

Even under the best of circumstances (ignoring all problems related to repeatability and reproducibility), the measured sound power is only partly related to the valve itself. The flow noise generated by the valve is transmitted to the pipe, then transmitted from the pipe to the radiator, from the radiator to the air inside the test room and from the test room to the microphones. Experience at Danfoss has shown that this method fails to give results that reliably characterise thermostatic radiator valves, mainly because of problems of repeatability and reproduction. Nonetheless Danfoss is presently using the Nordtest method, as it is – with all its shortcomings – the best method available.

1.3.2 Identification of important parameters for the industrial problem

As noted above, the design of actual thermostatic radiator valves is outside the scope of this project. However, it is appropriate to use the characteristic properties of such a valve as reference properties for the investigations in this present thesis.

Thermostatic radiator valves are mounted on relatively small steel pipes, with diameters up to one inch and with differential pressures across the valve up to one bar. Taking a typical situation, the valve is mounted on a 1" pipe and conveys 1,000 kg/h of hot water. The pipe Reynolds number is in this case $\mathrm{Re}_D = \frac{D \cdot U}{\nu_w} = 13,900$, where D is the diameter of the pipe; $U = Q/A$ is the mean flow velocity in the pipe; ν_w is the kinematic viscosity of water; A is the cross sectional area of the pipe; $Q = M/\rho_w$ is the volumetric flow of water; M is the mass flow; and ρ_w is the density of water. Fully-developed pipe flow is expected to be laminar up to a Reynolds number of approximately 2,300, see e.g. Fox and McDonald (1985), corresponding to a mass flow of 164 kg/h; transition is expected to occur in a Reynolds number range of approximately 2,300-100,000, corresponding to 164-7,100 kg/h; and above this Reynolds number the flow would be fully turbulent. Thus, the flow in the pipe can be everything from laminar at low flow rates, transitional at intermediate flow rates and perhaps fully turbulent at high flow rates. The pipe Mach number in a typical situation is approximately 10^{-3}.

In domestic heating applications that use water as the heat transfer medium and thin-gauge panel radiators as heat exchangers, most of the noise generated by the control valve is transmitted by the pipe to the radiator and emitted from there. The dominant part of the spectrum lies in the approximate range 250 Hz to 10 kHz. Focusing on the noise transmitted by the pipe, the highest frequency range of interest can be normalised with the ring frequency of the pipe, which is seen later to be important for the

transmission of vibroacoustic energy in pipes. This yields a maximum nondimensional frequency of industrial interest:

$$\Omega = \frac{10 \text{ kHz}}{f_{\text{ring}}} = 0.15 \tag{1.1}$$

where Ω is the nondimensional frequency; $f_{\text{ring}} = c_L/2\pi a$ is the ring frequency of the pipe; a is the radius of the pipe; and $c_L = \sqrt{E/\rho(1-\nu^2)}$ is the thin-plate extensional wave speed of the pipe material.

1.4 List of contributions in the thesis

The present thesis is submitted in order to obtain a PhD in accordance with the regulations of the Faculty of Engineering at the University of Southampton. In order to comply with the regulations the present thesis is required to present significant contributions to the existing knowledge.

The major contributions are:

Part I

- Principle of power flow measurements.
- The vibroacoustic analogy formulation.

Part III

- Implementation of the principle of power flow measurements, both for heavy and light fluid loaded pipes.
- Validation of the nondimensional prediction model, both regarding pipe-wall response and vibroacoustic power flow.

Secondary contributions are:

Part II

- Nondimensional prediction model for vibroacoustic response of an infinite fluid-filled circular pipe.

Part III

- Implementation and validation of modal sensors.
- Method of excitation inside the fluid of a fluid-filled pipe.

The objectives of the thesis are presented in part I, which follows next.

Part I

Overall strategy for quantification of hydroacoustic sources in pipes

Chapter 2

Conceptual approach

For noise or vibrational sources connected to water-filled pipes in air, it is quite common to assume that all the noise energy in the system propagates through the acoustic pressure field in the contained water, and that it can be quantified by the internal sound power alone. The underlying assumption is that the walls of the pipe are effectively rigid. This is not necessarily the case for all pipes encountered in industrial applications, as thin or soft walled pipes are used for many different purposes where the density of the contained fluid is not so different from that of the pipe wall material. In these cases, the fluid loading of the contained fluid cannot be neglected and the pipe walls will therefore appear compliant.

When the pipe walls are compliant, any vibration of the shell wall will induce a pressure field in the contained fluid and vice versa. The relative compliance of the pipe walls is dependent on the pipe material, the geometric properties and the contained fluid. The coupled propagation of vibrational and acoustic power (from here onwards called the vibroacoustic power) can be separated into power propagating in the fluid and in the pipe walls, but still they are closely linked; there are some complicated interactions that cannot be interpreted by looking separately at the properties of the fluid or the pipe, respectively.

2.1 Quantification principle

The vibroacoustic power produced by a source (e.g. a thermostatic radiator valve) connected to a complicated system (e.g. a heating system) is transported from the source to the surroundings through different paths, as sketched in figure 2.1. In the simplest possible analysis, vibroacoustic power from the source can either be radiated to the surrounding fluid or it can be transmitted by the connected pipe.

With a control volume placed around the source as sketched in figure 2.1, the vibroacoustic noise generation inside the volume can be quantified by summing the contributions at the boundaries. At each boundary, the vibroacoustic power leaving the volume

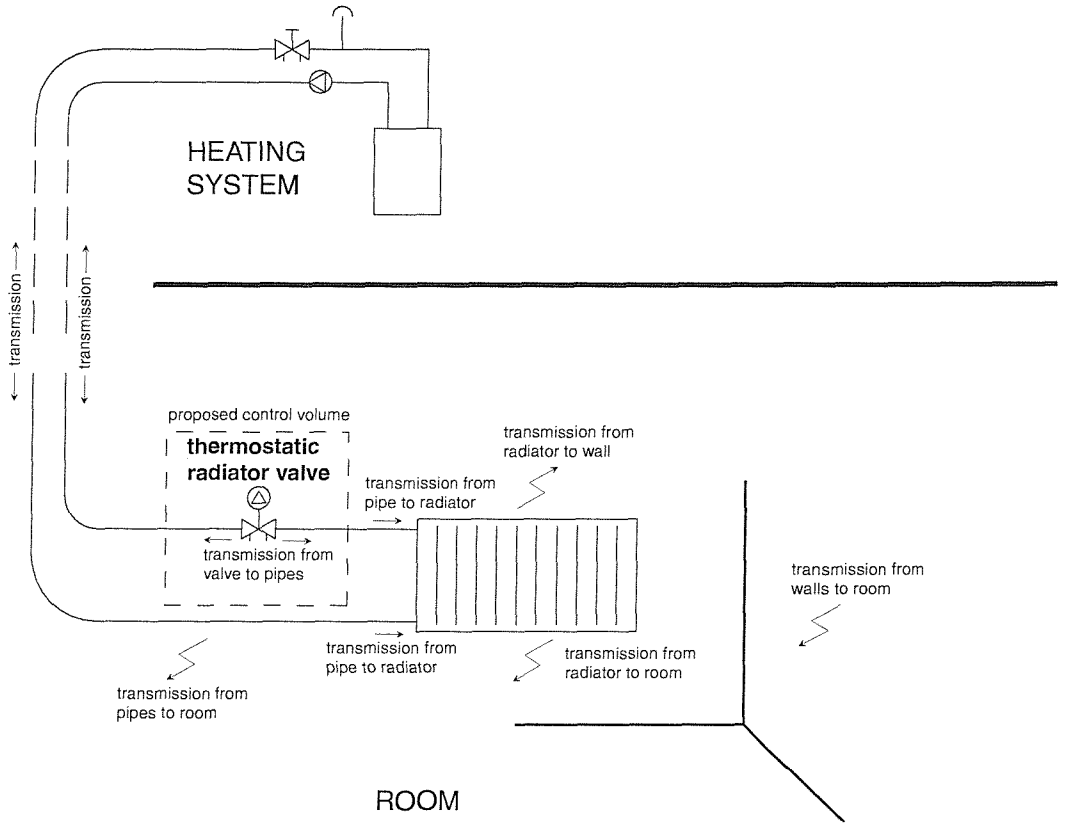

Figure 2.1: Noise transmission paths from a thermostatic radiator valve in a heating system.

gives a positive contribution while power entering the volume gives a negative contribution. Assuming there is little absorption inside the control volume, the vibroacoustic power generated by the source equals the net power leaving the control volume. In the ideal, lossless case the placement of the control volume is arbitrary, as the total power is constant. The amount of power in each of the transmission paths may differ, as e.g. power in the pipe may 'break out' and become airborne.

To simplify the quantification process in the present thesis, it is assumed that the only significant power source is the one under investigation. This means, that the only way power can enter the control volume from outside is through reflection by discontinuities outside the control volume. The reflection of power could effectively be removed if the quantification was performed on an infinite pipe. While this is possible for a numerical method it is not feasible for an experimental method. In this case, a more practical possibility is to devise an anechoic termination of a finite pipe. This anechoic termination is supposed to absorb all incident vibroacoustic power so no reflection is possible. While this is an idealisation, a practical solution would be to have an anechoic termination that makes the reflected power a small proportion of the incident power.

This leaves three paths of power from the source to be quantified: the power emitted into the external fluid from the source surface and the connected pipe, and the coupled transmission of power in the pipe walls and in the internal fluid.

As presented in chapter 1, the industrial application is restricted to air as the external fluid. Intuitively, it seems reasonable to assume that the externally radiated airborne power is significantly smaller that the power transmitted along the fluid-filled pipe. To verify this, an estimate of the radiated power can be found from the equation

$$W_{rad} = \sigma \langle \overline{\dot{w}^2} \rangle S \rho_f c_f \tag{2.1}$$

where σ is the radiation efficiency; $\langle \overline{\dot{w}^2} \rangle$ is the spaced-averaged mean square vibration velocity of the pipe wall; S is the vibrating surface area; and $\rho_f c_f$ is the characteristic acoustic impedance of the external fluid. For exterior radiation from pipes, engineering estimates of the radiation efficiency can be found e.g. from Beranek and Vér (1993). Estimates based on the results from the parameter study in part II show that the externally radiated power for realistic scenarios is several decades smaller than the power transmitted along the pipe.

This leaves only the power transported by the fluid-filled pipe to be quantified. A convenient term for power transmitted in a one-dimensional system is 'power flow', where the word *flow* hints at the transportational property. Vibroacoustic energy leaves the source at a given rate and in a given direction, and this is dubbed the vibroacoustic power flow.

2.2 Objectives of this thesis

For dealing with the industrial problem drawn up in the previous chapter, there are several options. The overall objective of this research programme is to find ways of quantifying hydroacoustic noise sources, such as flow control valves, when they are coupled to fluid-filled pipe systems. Two distinct and complementary approaches are explored in the present thesis: controlled experiments and numerical simulation.

The main steps in the two approaches are:

The experimental approach involves mounting the source in an instrumented pipe system under controlled conditions. Ideally the pipe system is uniform, straight and extends to infinity either side of the source. In practice, anechoic terminations are used to minimise the reflection of structural and fluid-borne sound back towards the source. Special transducers are used to measure the power flow in different circumferential pipe modes. The experimental concept is presented in chapter 3, while the actual investigations under laboratory conditions are presented in part III.

The numerical simulation approach involves 2 stages:

- First, a CFD flow simulation is run to provide a time-accurate solution of the unsteady flow in the source region. It is proposed that this be done with the flow treated as incompressible and the solid boundaries as rigid. Nevertheless, even with these simplifications the task of computing the time-dependent unstable flow through a valve is too difficult for currently available commercial CFD packages: unsteady RANS codes are the subject of active research, but are not yet in widespread use in industry. Actual CFD flow simulations are left out of the present thesis, as the results available from the commercial CFD package used by Danfoss were not of a quality suitable for quantification purposes.

- The second stage requires the unsteady flow solution to be inserted in a vibroacoustic analogy calculation, in order to predict the power flow away from the source along a uniform fluid-filled pipe that extends to infinity on either side of the source. The necessary analytical and numerical tools for this stage of the simulation are assembled in chapter 4, and in part II which deals with the response of fluid-filled pipes to both structural and fluid excitation.

This second stage of the numerical simulation approach represents a major contribution of the present research, along with the development of complementary experimental techniques for the empirical measurement approach.

Chapter 3

A method based on experiments

Measuring the vibroacoustic power flow from a source connected to a fluid-filled pipe is not trivial, as the power flow is not a quantity that can be measured directly. In this thesis, the total vibroacoustic power flow is inferred from measurements of the modal response of the pipe wall.

While this measurement principle is intriguing in its non-intrusive simplicity, its implementation in the form used in the present thesis relies on some quite restrictive assumptions. The most restrictive assumption is that only one branch (wave type) carries the dominant part of the vibroacoustic power flow for each circumferential mode. This is the case for light and heavy fluid loading, but is not necessarily true for any intermediate fluid loading. However, this restriction is not a fundamental flaw of the method, as it can be relaxed to allow for more propagating branches. With only one propagating branch, the measurement task is simplified as that branch accounts for the entire modal response and power flow at a given position. With more sensors it would be possible to decompose multiple branches for a given mode.

3.1 Principle of power flow measurements

As noted in the opening remarks of this chapter, vibroacoustic power flow cannot be measured directly, but several authors have worked with indirect measurements.

For all fluid loadings, the total vibroacoustic power flow can be decomposed into structural and fluid power flows. In the limit of light fluid loading, the coupling between these components can be neglected, and the formulation of the separate terms is relatively simple in terms of in vacuo structural modes and rigid-walled acoustic modes. The structural power flow in the in vacuo case (i.e. no internal or external fluid loading) can be retrieved from the structural intensity, see e.g. Pavic (1976), and the fluid power flow can be retrieved from the acoustic intensity, see e.g. Fahy (1985). The modal power flow in the axisymmetric mode of a light fluid loaded pipe with both fluid and structural excitation was measured by Pinnington and Briscoe (1994). Durant

et al. (1999) presented modal measurements of power flow for a light fluid loaded pipe using a microphone array, excited by boundary layer noise of internal turbulent flow.

When the fluid loading is not light, the coupling between the fluid and the pipe wall becomes significant. In his PhD thesis, Briscoe (1994) presented a method to measure the axisymmetric power flow in a heavy fluid loaded pipe. He also showed results using a special arrangement to excite only the axisymmetric mode of a heavy fluid loaded pipe. No references have been located for general vibroacoustic power flow measurements in heavy fluid loaded pipes.

The power flow measurement method presented here relies on a theoretical prediction of the relation between the total power flow and the vibrational response of the pipe wall. Under special circumstances, the vibrational response for given circumferential mode n is dominated by one branch (or wave) in the vibroacoustic far field, and virtually all the vibroacoustic power flow is carried by this branch. The transmitted vibroacoustic power flow for mode n can then be calculated as

$$P_{n,\text{far}} = |w_{n,\text{meas}}|^2 F_{nb} \tag{3.1}$$

where $P_{n,\text{far}}$ is the far field modal power flow; $w_{n,\text{meas}}$ is the measured modal pipe displacement for mode n; and F_{nb} is a modal power flow factor for the pipe in question. While this equation seems appealingly simple, there are some quite restrictive assumptions that have to be fulfilled for the equation to be valid. These assumptions and the definition of F_{nb} are discussed in more detail in section 8.3.1 for the light fluid loaded case, and in section 9.3.1 for the heavy fluid loaded case.

Standing waves encountered during the measurements of the modal wall response may invalidate equation (3.1). The prediction of the modal response, $w_{n,1}$, and the power flow, $P_{n,1}$ are made for a doubly infinite pipe and to make the ratio of measured and predicted response meaningful, the measurements need to be obtained under essentially the same conditions. In the measurements described below, this is obtained through anechoic terminations at the ends of the pipe. Perfect anechoic terminations are difficult to achieve, but as noted in the previous chapter a significant attenuation of the reflected waves is sufficient. The anechoic termination used consists of several components, each dissipating vibroacoustic energy in a special way for a special type of vibration. The design considerations for the anechoic termination are discussed in section 8.4.1 and section 9.6.2 for the structural and fluid parts, respectively. There is also some advantage in choosing a pipe wall material that has significant damping, and in using long pipes for the experiment: in this way the structural vibrations are attenuated along the length of the pipe before the anechoic termination is reached. At the same time, if the pipe has a significant damping, all measurements should be conducted as close to the source as possible (while still in the far field), as the damping of the structural vibrations reduces the measured response and hence the power flow, thus underestimating the power output of the source.

Equation (3.1) requires three inputs: the measured modal response, $w_{n,\text{meas}}$; the predicted modal response, $w_{n,1}$; and the predicted vibroacoustic power flow, $P_{n,1}$. The necessary tools for making the predictions are covered in detail in part II, while the principle of modal response measurements is discussed in the next section.

3.2 Pipe-wall modal response measurements

Several authors have published measurements of the pipe-wall modal response of fluid-filled pipes. Essentially two different principles have been used: modal decomposition of accelerometer measurements through post-processing, and direct modal measurements using shaped sensors.

Point acceleration data. Feng (1995) presented measurements of the modal response of a heavy fluid loaded pipe. The measurements in this case were done by an accelerometer array and the modal response was obtained through post-processing of the individual accelerometer outputs. Variyart and Brennan (1999) made modal response measurements on a light fluid loaded pipe using wall acceleration data, but in this case a single accelerometer was moved around the circumference; again the modal response was obtained through post-processing. In this thesis, the principle from Variyart and Brennan (1999) is used, mainly because the number of transducers is kept low.

Shaped sensors. As a part of his PhD, Briscoe (1994) developed a modal sensor sensitive to the axisymmetric response of the pipe wall. He then presented measurements of the $n = 0$ pipe-wall response when excited by either (1) an acoustic source radiating into the internal light fluid or (2) an axial $n = 0$ ring force at the pipe end. The sensor is a piezoelectric wire wound around the pipe. Variyart and Brennan (1999) validated a shaped sensor to measure the pipe response of the $n = 2$ mode of a light fluid loaded pipe excited by a radial point force. The shaped sensor is made of patches of thin piezoelectric film cut in sinusoidal shapes. In this thesis, both these principles are used: the piezoelectric wire is used as a modal sensor for $n = 0$, and the shaped sensor principle is taken further as shaped sensors are used for $n = 1$, $n = 2$ and $n = 3$.

3.3 Key results of experiments in this thesis

The principles presented so far in this chapter have been applied to both light and heavy fluid loaded pipes. The experiments are presented in part III. They show that the measurement strategy is valid and workable at least for the cases investigated in this thesis. In part IV, some potential complications are discussed for the case where the fluid loading is neither light nor heavy, but something in between, e.g. water inside an industrial grade steel pipe.

Conceptually, the process of validating the measurement principles can be seen as a number of steps, each including some complicating effects that were not present in the previous step; for example the first experiments for a light fluid loaded pipe were repeated for a heavy fluid loaded pipe. A key part of the entire validation is the comparison of the experiments with the predictions made using the methodology presented in part II of this thesis. As the predictions are made for conditions not

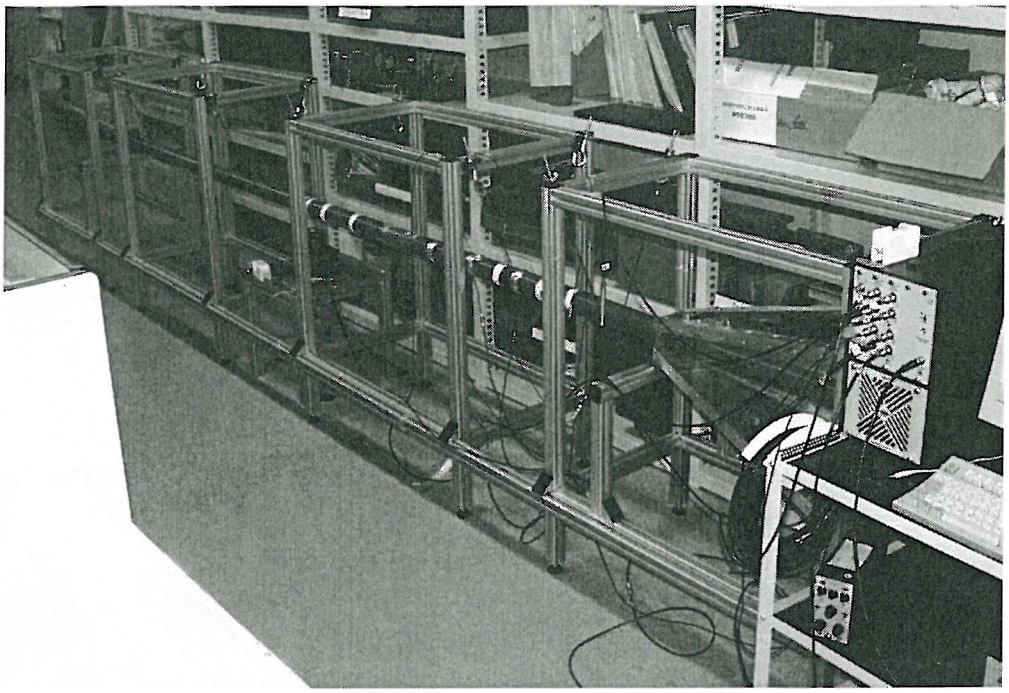

Figure 3.1: Experimental setup used in the light fluid loaded experiments.

obtainable in a laboratory (e.g. infinite pipe and perfect geometry), it is arguable whether the experiments validate the predictions or vice versa. Leaving this discussion aside, the pragmatic approach used in this thesis is that both the experiments and the prediction model are of such a complicated nature, that if they compare well it cannot be a coincidence.

The experiments conducted during this research programme can be divided into three main groups: radial point force excitation of the pipe wall for a light fluid loaded pipe, the same excitation for a heavy fluid loaded pipe, and point monopole excitation of the interior fluid for a heavy fluid loaded pipe.

3.3.1 Structural excitation of a light fluid loaded pipe

The light fluid loaded pipe is not encountered in the industrial applications discussed in chapter 1. However, from a validation point of view, it is the simplest case of interest in this study, as it allows the comparison of experiments with both in vacuo and light fluid loaded predictions, where the fluid-structure coupling is either absent or weak.

The experimental setup is discussed in detail in chapter 8, but figure 3.1 shows a picture. The light fluid loaded pipe measurements were conducted on a 5 m PVC pipe with air both inside and outside. The modal response of the pipe-wall was measured using the accelerometer decomposition method, the input force was measured using a force transducer and the acceleration of the point of excitation was measured using an accelerometer. By post-processing these measurements, the modal accelerance was

obtained for the 6 lowest-order circumferential modes, and also the power supplied by the excitation force. The axial position along the pipe z can be made nondimensional with the pipe radius a to obtain a nondimensional position $s = z/a$.

Point accelerance of the pipe wall. The point accelerance shown in the figures in this chapter is not a directly measured point accelerance, but a synthetic point accelerance formed from the sum of all the decomposed modal accelerances. The main advantage of this procedure is that the point response can be interpreted in terms of individual modal contributions. Comparing the measured (synthetic) point accelerance with the predicted point accelerance, both in the near and far fields, shows excellent overall agreement in the near field at low to intermediate frequencies and good agreement in the far field, as shown in figure 3.2. The only major discrepancies are that the measured accelerance is dominated by distinct but unpredicted peaks at low frequencies and that it rolls off at high frequencies.

The peaks at low frequencies are thought to be caused by axial standing waves, resulting from insufficient attenuation of (especially) the bending mode by the anechoic termination. An investigation of the ratio of incident to reflected waves at the anechoic termination showed a general problem with the low frequency performance of the anechoic termination. This can probably be explained by the relatively small size of the anechoic termination in comparison with the long wavelengths at low frequencies. The roll off at the high frequencies can probably be related to the internal damping of the pipe-wall material, which has a larger effect the more wavelengths are present between the points of excitation and measurement.

Power flow. Figure 3.3 shows the far field total power flow obtained from accelerometer measurements via equation (3.1), compared with the predicted total power flow and the measured input power flow. The predicted power flow is determined by the structural component (compare figure 8.10 on page 113). The agreement is fair, apart from some erratic behaviour at low frequencies. When examining the modal power flows, the erratic behaviour can be related to the $n = 0$ mode, where a large error factor in the accelerance measurement results in a very large error factor in the inferred power flow for that mode, as the error is related to the square of the response measurement.

The large relative error of the acceleration measurement for the $n = 0$ mode has two causes: a radial point force at the pipe wall does not excite the $n = 0$ mode very efficiently (giving a small predicted accelerance for $n = 0$) and the modal discrimination of the accelerometer decomposition method is limited, so that a large response in one mode apparently 'leaks' to other modes. As the radial point force excites the $n = 1$ (beam bending) mode very efficiently, the modal leakage from the bending mode to the $n = 0$ mode is causing the large relative error.

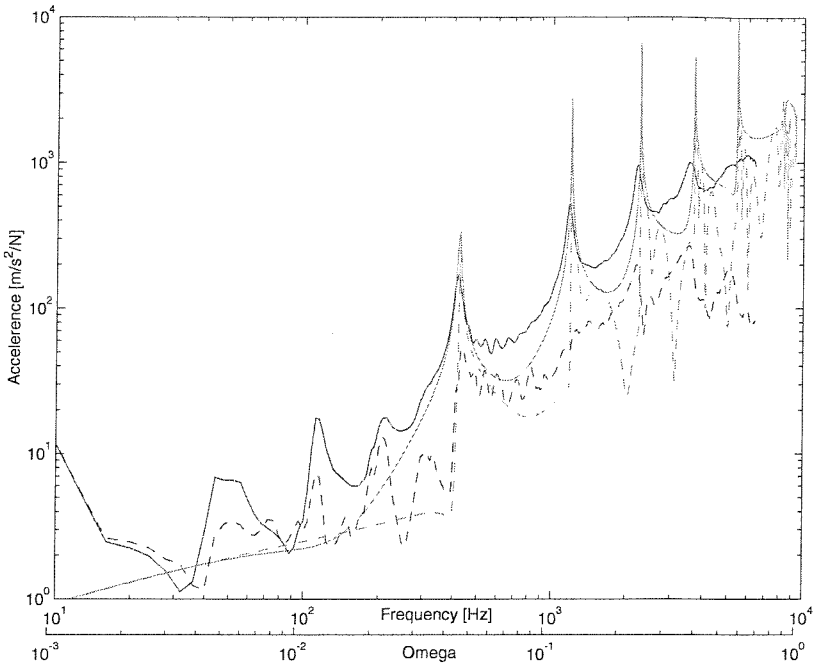

Figure 3.2: Synthetic point accelerance for a pipe with light fluid loading excited by a radial point force. The predicted response is green and the measured red. The solid line is $s = 0.3$ and the dashed line is $s = 14.7$.

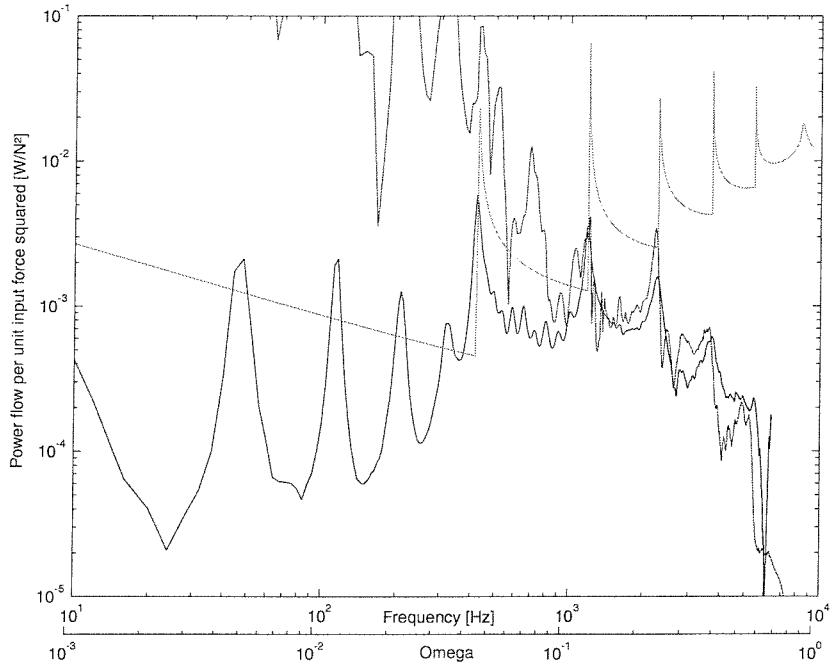

Figure 3.3: Total power flow for a pipe with light fluid loading excited by a radial point force, $s = 14.7$. The predicted power flow is green, the summed modal power flow is red and the input power flow is blue.

3.3.2 Structural excitation of a heavy fluid loaded pipe

The experimental setup in the heavy fluid loaded experiments was identical to the light fluid loaded experiments, apart from the additions necessary to accommodate water inside the pipe and terminate the pipe anechoically. The experimental setup is discussed in chapter 9.

Point accelerance of the pipe wall. The measured and predicted point accelerances for the heavy fluid loaded pipe, excited by a radial point force at the pipe wall, are shown in figure 3.4. The synthesised accelerances shown in the figure were obtained by the accelerometer decomposition method, but modal sensors were also used with good results as shown in chapter 9. The general features are quite similar to the light fluid loaded case. The main difference is that all the cuton frequencies of the higher order modes are shifted to lower frequencies, as predicted by the numerical parameter study in chapter 7. The accelerance magnitude is reduced by approximately a factor of 6, which seems intuitively reasonable as the mass of the fluid-filled pipe is significantly larger when filled with water.

Power flow. Figure 3.5 shows the far field total power flow. Again the general features are quite similar to the light fluid loaded case, but the high frequency roll off is smaller. The reason for this is probably, that the damping in the water (accounting for most of the power flow in the heavy fluid loaded case) is significantly smaller than the damping in the pipe wall material (accounting for most of the power flow in the light fluid loaded case). By using shaped sensors, reasonable agreement with prediction (generally better than 4 dB) is obtained over the frequency range 100 Hz to 3 kHz. This is a much better result than for light fluid loading in figure 3.3.

3.3.3 Fluid excitation of a heavy fluid loaded pipe

To provide acoustic excitation in the fluid, a hydrophone was added to the experimental setup used for the point force excited experiments. When the hydrophone was subjected to a relatively high voltage from a special power amplifier, it transmitted power to the water inside the pipe. The transmission characteristics of the transmitting hydrophone were assumed to be close to those of a point monopole placed in the fluid.

Modal accelerance of the pipe wall. As the experiment was difficult to repeat exactly, it was not possible to use the accelerometer decomposition method and the results presented are obtained using modal sensors. Due to the relatively large size of the sensors (one ring of piezoelectric patches to obtain the cosine part of the response and another to obtain the sine part), it was not possible to fit them all at one axial measurement position. The synthetic point accelerance presented in the last sections is the sum of the modal contributions, and as the modal contributions are not measured

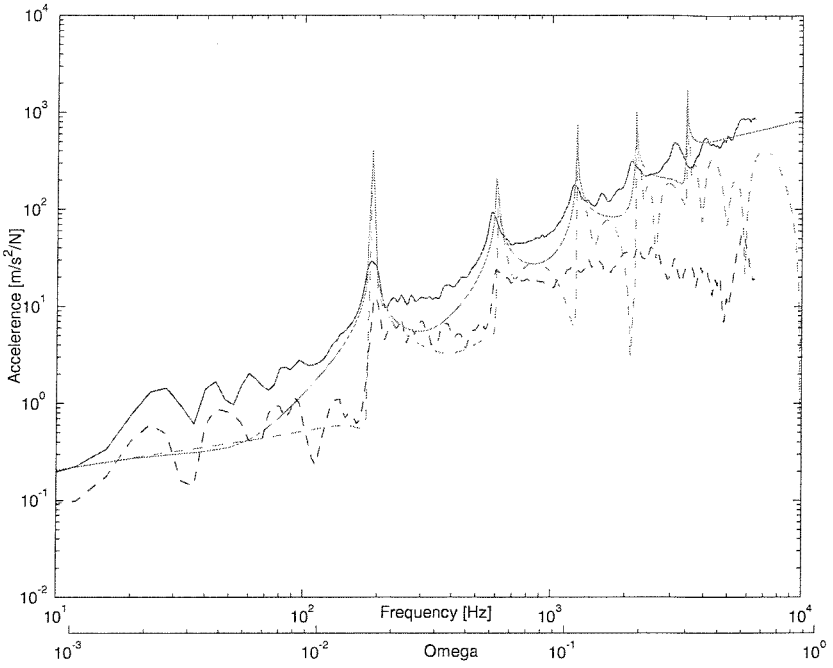

Figure 3.4: Synthetic point accelerance for a pipe with heavy fluid loading excited by a radial point force. The predicted response is green and the measured red. The solid line is $s = 0.3$ and the dashed line is $s = 14.7$.

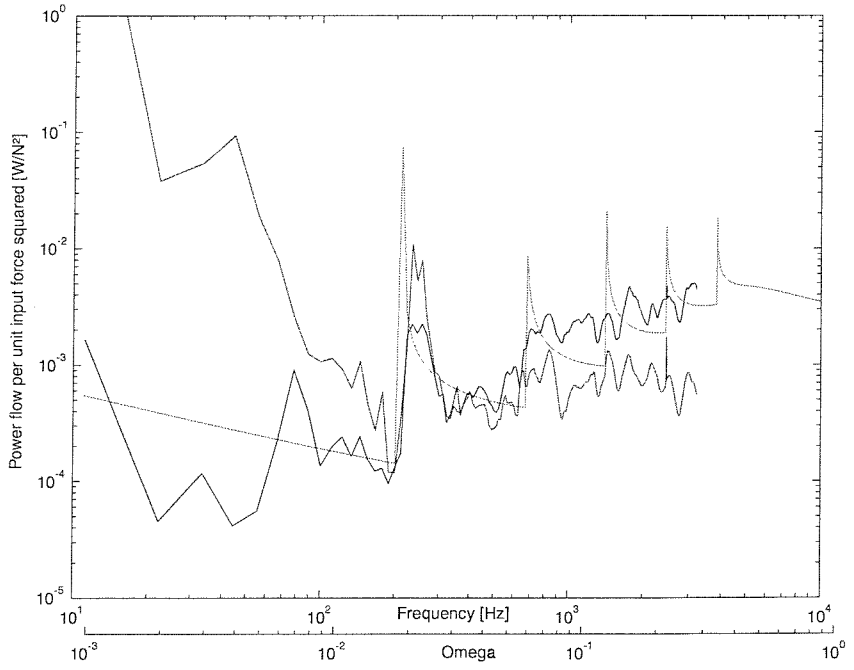

Figure 3.5: Total power flow for a pipe with heavy fluid loading excited by a radial point force, $s = 14.7$. The power flow curves are: predicted power flow (green), measurement using accelerometers (red), and measurement using modal sensors (blue).

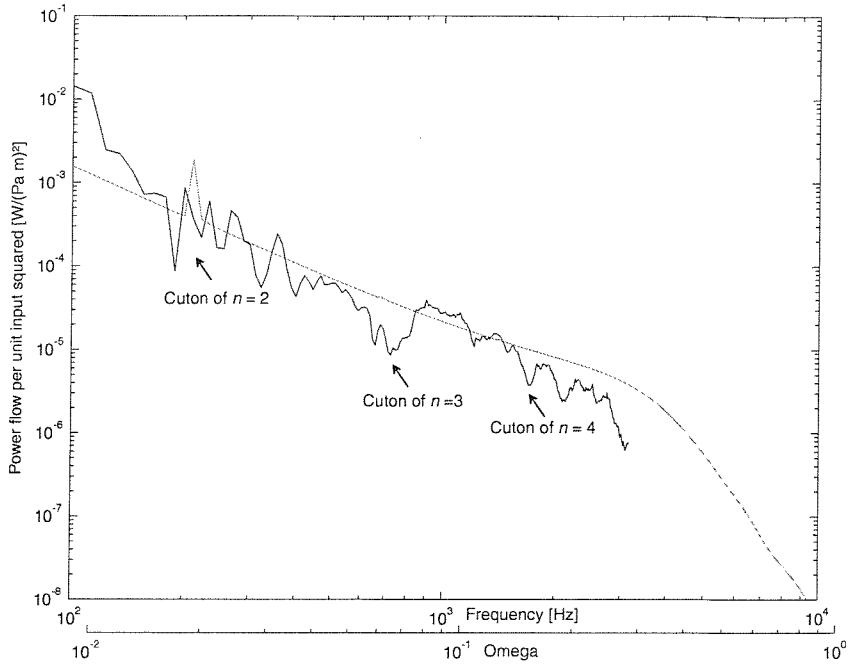

Figure 3.6: Total power flow for a pipe with heavy fluid loading excited by a transmitting hydrophone. The predicted power flow is shown in green and the modal sensor measurement shown in blue.

at the same axial position, it is not reasonable to sum them up. For the individual measurements of modal accelerance (figures shown in section 9.4) the general agreement is worse than for the point force excited experiments, but this was probably to be expected considering the complications involved in getting a transmitting hydrophone inside a pressurised water-filled pipe, where the support of the hydrophone mount significantly changed the properties of the pipe locally.

Power flow. Figure 3.6 shows the far field total power flow. The measured total power flow to the far field is surprisingly close to the predicted power flow, considering the relatively large errors of some of the modal response measurements. However, only two modes contribute significantly to the power flow in the actual case, namely $n = 0$ and $n = 2$, and the measured modal responses of these modes compare relatively well with the predictions.

3.4 Conclusion

The measurement principle suggested at the beginning of this chapter for vibroacoustic power flow has been validated through a number of experiments, which are presented in detail in part III. The power flow measurements are only as good as the measurements of the pipe response, and in using the method the greatest possible care should be taken

to ensure that the conditions for the response measurements are as close as possible to the ideal situation used in the predictions of the power flow. The largest single source of error, in the power flow measurements as presently set up, is probably reflections from inefficient anechoic terminations. Other sources which may be important are geometric imperfections in the pipe (pipe bends, thickness variations, etc.), material imperfections in the pipe (e.g. weld lines and cast defects), and bubbles in the contained fluid.

When using the power flow measurement principle in industrial applications, the internal load impedance of the source should also be considered. It is difficult to predict the pipe impedance characteristics in an industrial application, and the exact conditions of any power flow measurements should thus be stated along with detail of the experimental setup.

It was the original intention also to present in this thesis measurements of the vibroacoustic power flow in a heavy fluid loaded pipe excited by the turbulent fluid flow past a flow obstacle. Unfortunately, problems with the experimental setup made it impossible to obtain a full set of modal response measurements, and time did not allow for another set of measurements once the problems with the experimental setup were taken care off. However, the preliminary results were very encouraging, and no new problems or shortcomings regarding the experimental method were identified during the fluid flow excited experiments.

Chapter 4

A method based on numerical calculations

This chapter presents a novel numerical method to calculate the vibroacoustic power flow in a fluid-filled pipe excited by fluid flow past an obstacle inside the pipe. The method leaves out the airborne transmission path discussed in chapter 2. If this transmission path for some reason cannot be excluded for a given application, the knowledge of the structural vibrations of the pipe wall obtained from the methods in this chapter can be used to include external radiation in the power flow calculations; see e.g. Skelton and James (1997) or Fuller (1986).

The field of numerical calculation of flow generated noise has received a lot of attention in recent years, partly for the same reasons stated in chapter 1 when the industrial motivation of this project was discussed. The entire field of aeroacoustics, as it has been dubbed, began with the original work of Lighthill (1952). In his paper, which described generation and radiation of sound from turbulent fluid motion in a unbounded flow, the acoustic analogy was introduced for the first time. The acoustic analogy is an exact rearrangement of the Navier-Stokes equations producing the linear acoustic wave equation along with some source terms; the latter ensure that the acoustic far-field radiation remains the same. Curle (1955) provided a theoretical expansion of Lighthill's acoustic analogy to allow for the noise generated by interaction between the flow and solid structures. The approach by Lighthill (1952) and Curle (1955) was generalised by Ffowcs Ffowcs Williams and Hawkings (1969) to allow for moving permeable surfaces; they also gave a more general and powerful derivation with the aid of generalised functions. The Ffowcs Williams and Hawkings approach has been used by many later authors, e.g. in the investigation of helicopter rotor noise (Brentner 1996) and in the assessment of noise prediction from wind turbines (Lowson 1982).

In this chapter, the Ffowcs Williams and Hawkings formulation of the acoustic analogy is used to represent the noise generated by a flow obstruction inside a fluid-filled cylindrical pipe by a distribution of equivalent acoustic sources inside the pipe, with the fluid at rest. It is assumed that the vibration of the pipe has no influence on the structure of the flow, which means the flow problem can be solved independently of

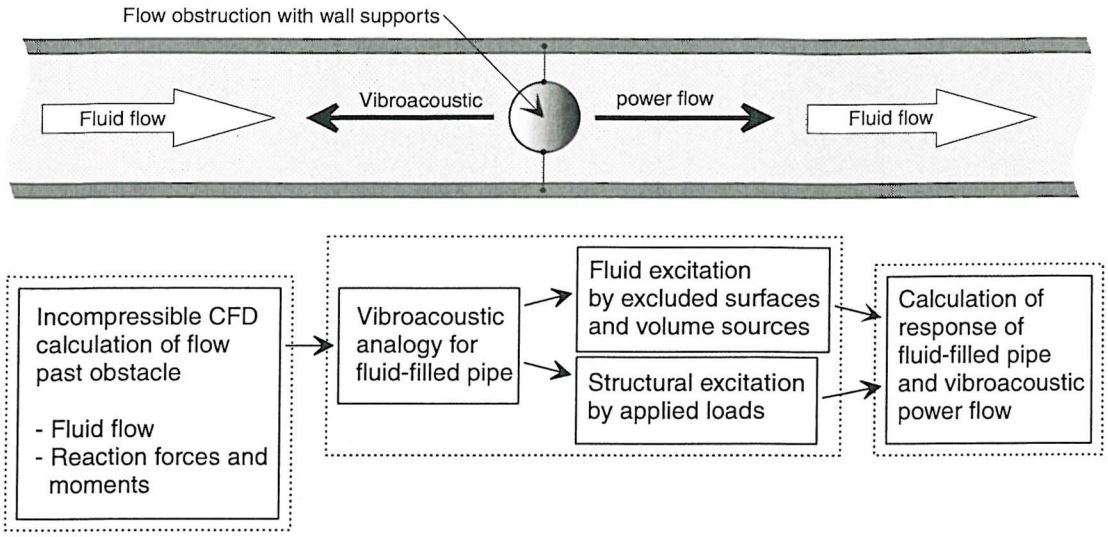

Figure 4.1: Flow diagram showing the steps in numerical quantification of power flow from a flow noise source in a pipe.

the pipe vibrations. It is also assumed that there is no reaction of the internal acoustic pressure field on the flow. Furthermore, it is assumed that the flow Mach number is small enough for wave convection effects to be neglected in the wave propagation. This way, there is no feedback mechanism and the mean flow inside the pipe does not affect the vibroacoustic power flow in the pipe. Under these assumptions, the problem of calculating the vibroacoustic power flow generated by the turbulent flow past a flow obstruction in a fluid-filled pipe is reduced to the problem of calculating the unsteady loading distribution on the obstruction.

4.1 General overview of the method

Sound waves in a fluid are generated in three ways: by the vibration of any solid body in contact with the fluid, by vibratory forces acting directly on the fluid, or by the turbulent motion of the fluid itself. The vibroacoustic analogy presented later in this chapter allows a transformation of the real problem, namely the vibroacoustic excitation of the fluid-filled pipe by the turbulent flow past the flow obstruction, into an equivalent problem of a fluid-filled pipe without fluid flow or flow obstruction, but with a distribution of vibroacoustic point sources providing the excitation in the source region. When the excitation is formulated as vibroacoustic point sources in a fluid-filled pipe, the response of the fluid-filled pipe can be calculated using the prediction model from part II and so can the power flow.

A flow diagram of the method can be seen in figure 4.1. The unsteady fluid flow past the flow obstruction and the reaction forces of the pipe wall are to be calculated using CFD. Using the vibroacoustic analogy, the flow excited fluid-filled pipe is replaced by an identical vibroacoustical situation with a distribution of acoustic point sources of

different types. Knowing the vibroacoustic excitation by the point sources, the response of the fluid-filled pipe can be calculated along with the total vibroacoustic power flow.

In the following, each of these three steps is discussed in more detail.

4.2 CFD calculation of the fluid flow

The compressible Navier-Stokes equations describe both the noise generation and propagation at all flow conditions in hard-walled environments. Unfortunately, these equations are not generally solvable using analytical methods and alternative approaches have been chosen. One approach has been direct numerical simulation (DNS) of the Navier-Stokes equations, but this has only been feasible for very simple problems, as the numerical task of resolving both the smallest eddies and the large scale structures in the flow is enormous, especially as most of the flows of industrial interest in this thesis are turbulent. It is therefore common to decouple the flow problem from the acoustic problem as described in the introduction to this chapter. For low Mach number flows this means calculating the turbulent flow as if it were incompressible.

The calculation of the incompressible flow is also possible using DNS, but the problem remains the same as for the coupled case, so it is only possible for simple cases. To avoid the pitfall of the large differences in spatial and temporal resolution of the flow solution, turbulence modelling is introduced. The idea behind all turbulence modelling is to represent the effects of the smallest scales on the larger scales by some sort of mathematical model. Normally the interest in the smallest scales is only indirect (the high frequency range in aeroacoustic calculations is an exception), and it is the larger scale effects that are important for the flow calculation. If the small scale effects can be represented by a turbulence model and not directly calculated, the flow calculation can disregard the smallest scales and only model the larger, while the flow solution is still valid. It is a generally recognised fact that all existing turbulence models are inexact representations of the physical phenomena involved, as pointed out e.g. by Wilcox (1998). It is also known that the degree of inexactness of a given model depends on the nature of the flow to which it is being applied, and that the characterisation of the circumstances which give rise to 'good' and 'bad' performance must unfortunately be based mainly on experience.

As a feasibility study for this thesis, the general purpose Computational Fluid Dynamics code Star-CD was used to calculate the flow past a square spoiler inside a pipe using the $k-\epsilon$ turbulence model. The square spoiler has been used for benchmarking of Computational Fluid Dynamics (CFD) codes, as the simple geometry yields complex, unsteady flow patterns. The flow shows considerable secondary flow phenomena, like flow separation and recirculation and periodic vortex shedding making up the characteristic von Karman vortex street from bluff bodies. Some experimental results on the flow past a square spoiler are available: Lyn (1992) did LDV-measurements in a water channel and published results of time and phase-averaged velocities, fluctuations and correlations at $\mathrm{Re}_D = 22,000$ (Re_D is the Reynolds number based on the side length

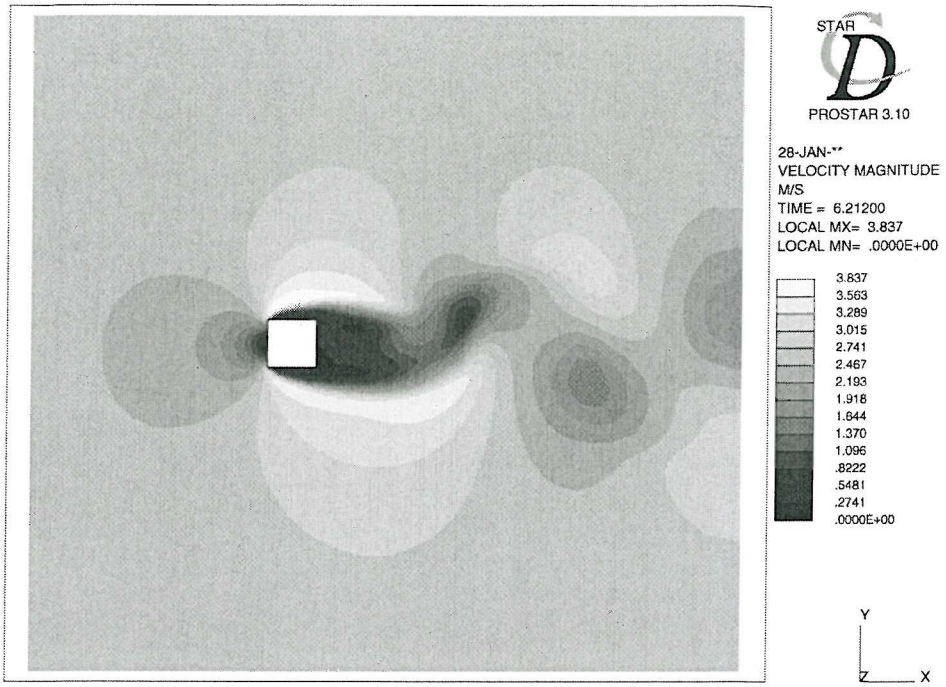

Figure 4.2: Example of CFD calculation: velocity magnitude of the turbulent flow past a square spoiler.

of the square spoiler) and Vickery (1966) measured the fluctuating lift and drag, along with correlation lengths at $\mathrm{Re}_D = 100,000$. The CFD benchmarks use to a large extent these experimental results; Lyn's measurements were used in the second ERCOFTAC-workshop (covering LES turbulence modelling) reported by Rodi et al. (1997), where all CFD-simulations done were on the same set-up. Several other papers were presented in the workshop, all stating results for Lyn's case. Lee (1997) also worked with this set-up, but using $k-\epsilon$ turbulence modelling – unfortunately, his paper is questionable, as the conclusions are beyond the results. Murakami and Mochida (1995) calculated the set-up of Vickery and quoted results for both 2D and 3D LES calculations of the fluctuating lift and drag.

When the results from Star-CD for the square spoiler were compared with the results from literature, they were in reasonable agreement. Unfortunately, the computational resources were inadequate for full 3 dimensional calculations, so all conclusions were based on 2 dimensional calculations. An example of the flow calculation is shown in figure 4.2. The main output parameters were the fluctuating forces (through lift and drag coefficients) and the Strouhal number. During the feasibility study, mesh and time step independence was obtained to within a few percent. When compared with the full 3 dimensional experiment of Vickery (1966), the results were within 15 %. While this was a promising result, the spectral content of the fluctuating forces calculated by Star-CD was qualitatively different from the experimental results, with an almost sinusoidal variation of both lift and drag. This was probably due to the large damping used in the numerical solution to ensure numerical stability of the equations.

The conclusion of the CFD feasibility study was that the overall calculation of the fluid flow past a square cylinder was possible using Star-CD. However, while the time averaged results were in good agreement with experimental results, the spectral content of the fluctuating forces was not of a quality usable for aeroacoustic calculations.

No further CFD-results are presented in this thesis. However, it cannot be concluded that general purpose CFD calculations are unusable for aeroacoustic calculations. During the feasibility study the decision was made to use the code 'as is'. A different choice of turbulence model or even some tweaking with the $k-\epsilon$ model may provide satisfactory results both regarding the time averaged parameters and the spectral content. It was decided that any additional time spent on CFD would not contribute further to this thesis. Unfortunately, the lack of quality CFD results leaves the entire vibroacoustic analogy presented in this chapter in a conceptual form and the originally intended comparison with experimental results is therefore not possible.

4.3 A vibroacoustic analogy for turbulent flow in pipes

4.3.1 Solution of the forced Helmholtz equation using Green functions

Forced acoustic equations can be solved using a number of different techniques. The one presented in the following uses Green functions to solve the forced Helmholtz equation (i.e. single frequency excitation). The procedure is adapted from Morse and Ingard (1968), and relies on the reciprocal property of Green functions in non-moving media.

In an ideal, stationary fluid the frequency domain acoustic pressure satisfies the inhomogeneous Helmholtz equation

$$(\nabla^2 + k_f^2)p_\omega(\mathbf{x}) = -f_\omega(\mathbf{x}) \tag{4.1}$$

where ∇^2 is the Laplacian; $k_f = \omega/c_f$ is the acoustic wavenumber of the fluid; ω is the cyclic frequency; c_f is the fluid speed of sound; and $-f_\omega(\mathbf{x})$ is a frequency domain, distributed source term.

The Green function $G_\omega(\mathbf{x}|\mathbf{y})$ is defined as the solution to the equation

$$(\nabla^2 + k_f^2)G_\omega(\mathbf{x}|\mathbf{y}) = -\delta(\mathbf{x}-\mathbf{y}) \tag{4.2}$$

with a unit point source at $\mathbf{x} = \mathbf{y}$. In general, equation (4.2) is solved subject to specified boundary conditions: Thus the equation is assumed to be valid in a region V_{tot}, bounded by a closed surface S_{tot} (see figure 4.3), and the boundary conditions are applied on S_{tot}. Depending on the boundary conditions, different Green functions are obtained. However, for all linear time-invariant boundaries consisting of stationary fluid or solid regions, the Green function is reciprocal: $G_\omega(\mathbf{y}|\mathbf{x})G_\omega(\mathbf{x}|\mathbf{y})$

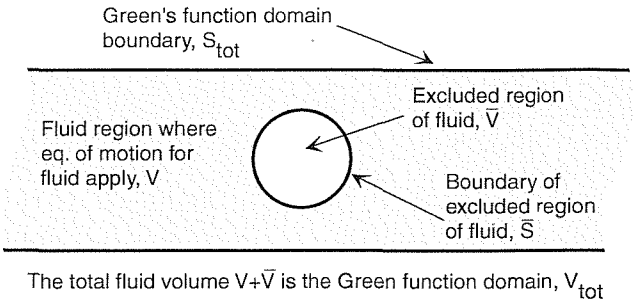

Figure 4.3: Fluid volumes and boundaries of interest for the vibroacoustic analogy.

Given a Green function $G_\omega(\mathbf{x}|\mathbf{y})$, $p_\omega(\mathbf{x})$ can be found by combining equations (4.1) and (4.2) in the following way: (i) replace $\mathbf{x}$ by $\mathbf{y}$ in equation (4.1) and multiply by $G_\omega(\mathbf{y}|\mathbf{x})$, (ii) interchange $\mathbf{x}$ and $\mathbf{y}$ in equation (4.2) and multiply by $p_\omega(\mathbf{y})$, (iii) subtract the two equations, and (iv) integrate with respect to $\mathbf{y}$ over the whole volume of the fluid V_{tot}. The sifting and symmetry properties of the δ-function, along with the reciprocal property and the divergence theorem, give the solution as

$$\begin{aligned} p_\omega(\mathbf{x}) = &\int_{V_{\text{tot}}} f_\omega(\mathbf{y}) G_\omega(\mathbf{x}|\mathbf{y}) dV \\ &+ \int_{S_{\text{tot}}} \left[G_\omega(\mathbf{x}|\mathbf{y}) \frac{\partial}{\partial y_j} p_\omega(\mathbf{y}) - p_\omega(\mathbf{y}) \frac{\partial}{\partial y_j} G_\omega(\mathbf{x}|\mathbf{y}) \right] n_j dS \end{aligned} \tag{4.3}$$

where S_{tot} is the boundary of V_{tot}; n_j is a unit normal vector from S_{tot} pointing outward from V_{tot}; and y_j is a source position coordinate.

Since $G_\omega(\mathbf{x}|\mathbf{y})$ is directly proportional to the pressure at $\mathbf{x}$ due to a source at $\mathbf{y}$, this equation states that the total pressure at $\mathbf{x}$ is the summation of the direct pressure contributions from all the sources in the source distribution at $\mathbf{y}$ plus the pressures reflected by S_{tot}. With an appropriate choice of G_ω (i.e. a G_ω that includes the reflection as part of itself, a so called tailored Green function), the surface integration turns out to be exactly equal to 0, leaving only the volume integral.

4.3.2 The Ffowcs Williams – Hawkings acoustic analogy

With the Ffowcs Williams – Hawkings acoustic analogy (Ffowcs Williams and Hawkings 1969), selected boundaries in the solution domain can be replaced by source and dipole layers.

This has the advantage that so-called 'excluded regions' where the equations of fluid motion do not apply (e.g. a solid body) can nonetheless be included in the solution domain, by treating the excluded region as a continuation of the undisturbed non-moving medium; thus the sound field is identically zero inside the excluded region. The boundaries of any such excluded region are replaced by a distribution of monopoles and dipoles placed at the position of the boundary. Figure 4.3 shows a surface S_{tot}

that corresponds to the wetted surface inside the pipe, a surface $\overline{S}$ that corresponds to the excluded region boundary (the surface of the flow obstruction), a volume $\overline{V}$ that corresponds to the excluded region and a volume V that corresponds to the fluid region where the equations of fluid motion apply. The solution domain V_{tot} is the total volume inside the pipe, that is the sum of V and $\overline{V}$.

Let $f(\mathbf{x}, t)$ be an indicator function such that $f(\mathbf{x}, t) > 0$ in the fluid volume V where the equations of fluid motion apply, $f(\mathbf{x}, t)$ vanishes on S and $\overline{S}$, and $f(\mathbf{x}, t) < 0$ in the excluded region. The indicator function can then be introduced in the Heaviside unit function $\mathrm{H}(f)$, such that $\mathrm{H}(f) = 1$ for $f > 0$ and $\mathrm{H}(f) = 0$ for $f \leq 0$.

Using these functions, Howe (1997) states the differential form of the Ffowcs Williams – Hawkings equation as

$$\left(\frac{1}{c_f^2}\frac{\partial^2}{\partial t^2} - \nabla^2\right)\left[\mathrm{H}c_f^2(\rho - \rho_f)\right] = \frac{\partial^2(\mathrm{H}T_{ij})}{\partial x_i \partial x_j} - \frac{\partial}{\partial x_i}\left(\left[\rho v_i(v_j - \overline{v}_j) + p'_{ij}\right]\frac{\partial \mathrm{H}}{\partial x_j}\right) + \frac{\partial}{\partial t}\left(\left[\rho(v_j - \overline{v}_j) + \rho_f \overline{v}_j\right]\frac{\partial \mathrm{H}}{\partial x_j}\right) \quad (4.4)$$

where subscript $_f$ refers to quantities in the undisturbed fluid at rest. Thus c_f is the speed of sound in the undisturbed fluid, and $\rho - \rho_f$ is the acoustic density perturbation. The first term on the right hand side is a fluid quadrupole term, the second is a surface dipole term and the last is a surface monopole term. The quadrupole term can be decomposed as $T_{ij} = \rho v_i v_j - \tau_{ij} + ([p - p_f] - c_f^2[\rho - \rho_f])\delta_{ij}$ where the first part of T_{ij} are the Reynolds stesses, the second part the viscous stresses and the last part is related to entropy and fluid inhomogeneity. The first part of the dipole term is the flux of momentum across S ($\overline{v}_j$ being the velocity of the surface S), while the last part is the force per unit area applied at S (with $p'_{ij} = (p - p_f)\delta_{ij} - \tau_{ij}$). The first part of the surface monopole term is the mass flow through the surface and the other part is the equivalent mass flux due to surface motion. Due to the properties of the generalised function $\mathrm{H}(f)$, equation (4.4) is valid throughout the whole of space.

In the following, the surfaces are assumed to be impenetrable, so the first part disappears in each of the surface terms. The term $c_f^2(\rho - \rho_f)$ tends to the acoustic pressure far away from the source region, and the frequency-domain version of the Ffowcs Williams – Hawkings equation can be solved for $p_\omega(\mathbf{x})$ using the method from the previous section. Assuming a tailored Green function, the solution to equation (4.4) can be found directly from equation (4.3):

$$\mathrm{H}p_\omega(\mathbf{x}) = \int_{V_{\text{tot}}} \left[\frac{\partial^2(\mathrm{H}T_{ij})}{\partial y_i \partial y_j} - \frac{\partial}{\partial y_i}\left(p'_{ij}\frac{\partial \mathrm{H}}{\partial y_j}\right) + \frac{\partial}{\partial t}\left(\left[\rho_f \overline{v}_j\right]\frac{\partial \mathrm{H}}{\partial y_j}\right)\right] G_\omega(\mathbf{x}|\mathbf{y})\, dV \quad (4.5)$$

To simplify this solution, the first two terms are integrated by parts. The dipole term is rewritten as

$$-G_\omega(\mathbf{x}|\mathbf{y})\frac{\partial}{\partial y_i}\left(p'_{ij}\frac{\partial \mathrm{H}}{\partial y_j}\right) = -\frac{\partial}{\partial y_i}\left(G_\omega(\mathbf{x}|\mathbf{y})p'_{ij}\frac{\partial \mathrm{H}}{\partial y_j}\right) + \frac{\partial G_\omega(\mathbf{x}|\mathbf{y})}{\partial y_i}\left(p'_{ij}\frac{\partial \mathrm{H}}{\partial y_j}\right) \quad (4.6)$$

and the quadrupole term is rewritten as

$$G_\omega(\mathbf{x}|\mathbf{y})\frac{\partial^2(\mathrm{H}T_{ij})}{\partial y_i \partial y_j} = -\frac{\partial^2}{\partial y_i \partial y_j}\left(G_\omega(\mathbf{x}|\mathbf{y})T_{ij}\mathrm{H}\right) + 2\frac{\partial}{\partial y_i}\left(G_\omega(\mathbf{x}|\mathbf{y})\frac{\partial(T_{ij}\mathrm{H})}{\partial y_j}\right) + \frac{\partial^2 G_\omega(\mathbf{x}|\mathbf{y})}{\partial y_i \partial y_j}(\mathrm{H}T_{ij}) \tag{4.7}$$

Using the rewritten forms of the quadrupole and dipole terms, the volume integral of equation (4.5) can be rewritten as

$$\begin{aligned} \mathrm{H}p_\omega(\mathbf{x}) = \int_{V_{\mathrm{tot}}} \Bigg[\Bigg(& -\frac{\partial^2}{\partial y_i \partial y_j}\left(G_\omega(\mathbf{x}|\mathbf{y})T_{ij}\mathrm{H}\right) + 2\frac{\partial}{\partial y_i}\left(G_\omega(\mathbf{x}|\mathbf{y})\frac{\partial(T_{ij}\mathrm{H})}{\partial y_j}\right) \\ & + \frac{\partial^2 G_\omega(\mathbf{x}|\mathbf{y})}{\partial y_i \partial y_j}(\mathrm{H}T_{ij})\Bigg) \\ & - \frac{\partial}{\partial y_i}\left(G_\omega(\mathbf{x}|\mathbf{y})p'_{ij}\frac{\partial \mathrm{H}}{\partial y_j}\right) + \frac{\partial G_\omega(\mathbf{x}|\mathbf{y})}{\partial y_i}\left(p'_{ij}\frac{\partial \mathrm{H}}{\partial y_j}\right) \\ & + \frac{\partial}{\partial t}\left([\rho_f \overline{v}_j]\frac{\partial \mathrm{H}}{\partial y_j}\right)G_\omega(\mathbf{x}|\mathbf{y})\Bigg] dV \end{aligned} \tag{4.8}$$

Applying the divergence theorem, see e.g. Kreyzig (1998), to equation (4.8) transforms some of the volume integral terms into surface integral terms and the solution to the Ffowcs Williams – Hawkings equation is then

$$\begin{aligned} \mathrm{H}p_\omega(\mathbf{x}) = & \int_{V_{\mathrm{tot}}} \left[\frac{\partial^2 G_\omega(\mathbf{x}|\mathbf{y})}{\partial y_i \partial y_j}(\mathrm{H}T_{ij}) + \frac{\partial G_\omega(\mathbf{x}|\mathbf{y})}{\partial y_i}\left(p'_{ij}\frac{\partial \mathrm{H}}{\partial y_j}\right)\right. \\ & \left. + G_\omega(\mathbf{x}|\mathbf{y})\frac{\partial}{\partial t}\left([\rho_f \overline{v}_j]\frac{\partial \mathrm{H}}{\partial y_j}\right)\right] dV \\ & + \int_{S_{\mathrm{tot}}} \left[-\frac{\partial}{\partial y_j}\left(G_\omega(\mathbf{x}|\mathbf{y})\mathrm{H}T_{ij}\right) + 2G_\omega(\mathbf{x}|\mathbf{y})\frac{\partial(\mathrm{H}T_{ij})}{\partial y_j} - G_\omega(\mathbf{x}|\mathbf{y})p'_{ij}\frac{\partial \mathrm{H}}{\partial y_j}\right] n_i dS \end{aligned} \tag{4.9}$$

where n_i are the components of the unit normal pointing out of the domain from S_{tot}.

The properties of the Heaviside unit function allow equation 4.9 to be simplified, noting that $\mathrm{H} = 1$ in V and $\mathrm{H} = 0$ in $\overline{V}$. The last two terms of the volume integral in equation (4.9) can be evaluated as a surface integral over $\overline{S}$, since $\partial \mathrm{H}/\partial y_j = 0$ except at $\overline{S}$ where $\partial \mathrm{H}/\partial y_j$ is equivalent to $\overline{n}_j \delta(\xi)$.

Here $\overline{n}_j$ are the components of the unit normal to $\overline{S}$ pointing out of $\overline{V}$ into V; in terms of the indicator function $f(\mathbf{x}, t)$, $\overline{\mathbf{n}} = (\nabla f/|\nabla f|)_0$, and $\xi = f/|\nabla f|_0$ (subscript 0 denotes evaluation on $\overline{S}$). The delta function variable (ξ) is the local coordinate normal to $\overline{S}$, with $\xi = 0$ on $\overline{S}$.

Further simplification results from the fact that S_{tot} lies entirely outside $\overline{S}$ (figure 4.3); thus in the surface integral over S_{tot}, H can be replaced by 1 and $\partial \mathrm{H}/\partial y_j$ by 0. The

final form of the solution in region V is then

$$p_\omega(\mathbf{x}) = \int_V \frac{\partial^2 G_\omega(\mathbf{x}|\mathbf{y})}{\partial y_i \partial y_j} T_{ij}\, dV + \int_{\overline{S}} \left[\frac{\partial G_\omega(\mathbf{x}|\mathbf{y})}{\partial y_i} p'_{ij} + G_\omega(\mathbf{x}|\mathbf{y}) \frac{\partial}{\partial t} \left([\rho_f \overline{v}_j] \right) \right] \overline{n}_j dS + \int_{S_{\text{tot}}} \left[\frac{\partial G_\omega(\mathbf{x}|\mathbf{y})}{\partial y_j} T_{ij} - G_\omega(\mathbf{x}|\mathbf{y}) \frac{\partial T_{ij}}{\partial y_j} \right] n_i dS \tag{4.10}$$

In this equation, all source terms are evaluated at $\mathbf{y}$ and the volume and surface integrals are with respect to position $\mathbf{y}$.

4.3.3 Interpretation of the vibroacoustic analogy

While equation (4.10) is perfectly valid, it needs some interpretation to become usable in this context as part of the vibroacoustic analogy.

The integrand of the volume integral takes the form of an acoustic quadrupole. This is thus the noise generated by free turbulence in the fluid. The first of the $\overline{S}$ surface terms takes the form of an acoustic dipole and thus is the noise generated by the fluctuating forces on the flow obstruction. The second term of the $\overline{S}$ integral is an acoustic monopole and is related to the surface vibration of the flow obstruction. The entire S_{tot} integral is fairly difficult to interpret in the form presented, but it is a layer of monopoles and dipoles at the pipe wall, related to the noise generation in the wall boundary layer.

So far, the acoustic analogy has been presented as a classic acoustic analogy, formulated with tailored Green functions. However, it is possible to add in an extra complicating effect to make it a true vibroacoustic analogy. In the case of a flow obstruction in a fluid-filled pipe, there will be a structural connection between the obstruction and the pipe wall. The flow forces on the obstruction generates reaction forces at the connection with the shell wall. The inclusion of these forces in the modelling framework makes it a true vibroacoustic analogy, as laid out in principle in figure 4.1. In a mathematical formulation, the structural excitation could be included in the modelling by cutting the surface $\overline{S}$ just outside the pipe wall so the flow obstruction is completely surrounded by fluid. The stresses could then be integrated at the cut and an equivalent distributed reaction force could be applied to the shell. However for purposes of this thesis, no additional mathematical modelling will be attempted concerning the structural reaction, as the purpose is mainly to introduce the concept.

This leaves the important question of whether all the terms of equation (4.10) are equally important in the industrial application. Scaling laws in aeroacoustics are commonly based on the free-field acoustic analogy, where the relative scaling of far-field pressures from monopole/dipole/quadrupole sources is 1:He:He^2 (He $= \omega L/c$ is the Helmholtz number, where L is a typical length scale) in the compact limit (He $\ll 1$). The purpose of the scaling laws is to reduce the number of sources to include in the calculation: if one source type is dominating the others, the calculations can be significantly simplified by leaving out the other source types without any major impact on the precision of the prediction. Another important aeroacoustic scaling parameter

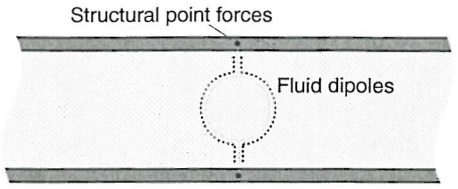

Figure 4.4: Equivalent source distribution for the vibroacoustic analogy applied on a rigid flow obstruction connected to the pipe wall. Compare with figure 4.1

is the Mach number of the flow (Ma= $\overline{u}/c$, where $\overline{u}$ is the mean flow velocity) and normally a dipole scales with a higher power than a monopole and a quadrupole with a higher power than a dipole. In the industrial application, the Mach number is very low (approximately 0.001) and according to the 'free-field logic', it would only be necessary to include the lowest order source type (e.g. monopole), as the scaling laws suggest that the higher order sources should be comparatively ineffective in generating noise at such low Mach numbers. However, there are cases (e.g. near a sharp edge of a plate (Ffowcs Williams and Hall (1970) and Crighton and Leppington (1971)) where the normal scaling laws do not apply. To investigate the scaling effect inside a fluid-filled pipe, monopole, dipole and quadrupole excitation are compared over a range of frequencies in section 4.3.6. The conclusion of this section is that the expected scaling applies: the monopole is more efficient than a dipole, and a dipole is more efficient than a quadrupole at the very low Mach numbers of the industrial application.

Knowing this, it is possible to formulate a true vibroacoustic analogy. In the industrial application, the flow obstructions are metallic and they can therefore be assumed to be very rigid. There is thus no monopole excitation at $\overline{S}$. As the flow past blunt objects is unsteady (at anything but the very lowest Reynolds numbers), there will be fluctuating forces on the flow obstruction and thus dipole excitation at $\overline{S}$. When there is dipole excitation at $\overline{S}$, this will dominate in the far field and there is therefore no reason to include quadrupole excitation, so the volume integration can be left out. The boundary layer noise generated by the S_{tot} integral in equation (4.10) is difficult to estimate. The two terms involving T_{ij} contain a product of two velocities in the Reynolds stress term; however, as the surface S is placed just in the fluid next to the wall, there are no slip velocities, so they are equal to the wall vibration velocities in the respective directions. If this is to be used in the calculation of the boundary layer noise, it should be noted that the shell theory used for the calculation of the wall vibration in this thesis is linear and does not contain any quadratic terms. Intuitively, it seems reasonable that the boundary layer noise due to surface sources on the pipe wall will be small compared to the radiation from structurally-excited wall vibration. The source terms representing the boundary layer noise are therefore disregarded.

The pressure at a far field observation point inside the pipe can under these circumstances be calculated from the vibroacoustic analogy as (see also figure 4.4),

$$p_\omega(\mathbf{x}^f) \approx \int_{\overline{S}} \frac{\partial G_\omega(\mathbf{x}^f|\mathbf{y}^f)}{\partial y_i} p'_{ij}\, \bar{n}_j dS + \sum_{j=1}^{N} S^i_{s,j} G^i_s(\mathbf{x}^f|\mathbf{y}^s_j) \tag{4.11}$$

where N is the number of reaction points; $S^i_{s,j}$ is the strength of the j'th structural reaction force in direction i and G^i_s is the structural Green function in direction i, giving the point pressure response at a fluid receiver point for unit excitation in direction i at the pipe wall. The different types of Green functions and source and receiver points are discussed in more detail in the next section.

4.3.4 Tailored Green functions for fluid-filled compliant pipes

The tailored Green functions that appear in equation (4.11) are designed to incorporate the effect of the wall vibrations. Part II of this thesis deals with a prediction model of point to point response functions for a fluid-filled cylindrical shell. The excitation in the prediction model is either in the form of a structural point force acting on the shell or a point monopole in the contained fluid. The receiver point can either be in the fluid or in the shell wall.

The tailored Green functions can be derived from the results of part II. The fluid Green function G_ω used in the vibroacoustic analogy is closely linked to the pressure response when the fluid-filled shell is excited by a monopole, as defined in equation (6.43). This pressure response is the sum of (a) the pressure from a free-field monopole, (b) the pressure arising from the scattering from hard boundaries inside the pipe and (c) the pressure in the fluid originating from the wall motion induced by the monopole. To formulate the same pressure using Green functions, the pressure response in a receiver point in the fluid $\mathbf{x}^f$ from a fluid monopole at a point in the fluid $\mathbf{y}^f$ is written as

$$p(\mathbf{x}^f) = S_f G_f(\mathbf{x}^f|\mathbf{y}^f) \tag{4.12}$$

where S_f is the source strength of the monopole and $G_f(\mathbf{x}^f|\mathbf{y}^f)$ is the fluid Green function. The fluid Green function $G_f(\mathbf{x}^f|\mathbf{y}^f)$ is thus proportional to the complex pressure produced at $\mathbf{x}^f$ due to a harmonic point monopole source of unit strength at $\mathbf{y}^f$. G_ω is then identical to G_f. Equating the two different approaches gives an expression for the fluid Green function,

$$\begin{aligned} &G_f\big((r,\theta,s)|(r_o,\theta_o,s_o)\big) \\ &= \sum_{n=0}^{\infty}\sum_{b=1}^{\infty} i\frac{2\varepsilon_n\Omega^2}{h\alpha_{nb}J_n'(\alpha_{nb})}\frac{\rho_f}{\rho_s}\mathrm{Res}^m_{nb}\cos(n(\theta-\theta_o))J_n(\alpha_{nb}r)e^{i\kappa_{nb}(s-s_o)} \qquad (s>s_o) \end{aligned} \tag{4.13}$$

where the different symbols are to be defined in Part II.

As the structural response is also a part of the vibroacoustic problem, the formulation of the Green function for a fluid-filled pipe is more complicated than for Green functions in hard-walled environments.

The fluid Green function can also be extended to include the associated structural response,

$$u^i(\mathbf{x}^s) = S_f G^i_f(\mathbf{x}^s|\mathbf{y}^f) \tag{4.14}$$

where u^i is the complex displacement of the shell wall in any of the three coordinate directions and $\mathbf{x}^s$ is a receiver point in the structure.

The structural Green function $G_s^i(\mathbf{x}|\mathbf{y}^s)$ is a reversal of this concept, giving the pressure at a fluid receiver point due to a structural point input:

$$p(\mathbf{x}^f) = S_s^i G_s^i(\mathbf{x}^f|\mathbf{y}^s) \tag{4.15}$$

Here S_s^i is the strength of the input force in any of the coordinate directions and $G_s^i(\mathbf{x}^f|\mathbf{y}^s)$ is the structural Green function giving the pressure in the fluid at a fluid receiver point $\mathbf{x}^f$ from a structural point force of unit strength in direction i. The structural response from a structural point force can be defined in a corresponding manner.

4.3.5 Definition of multipole sources using Green functions

Having defined the fluid Green function G_f in terms of the pressure response to a fluid monopole, the point dipole and point quadrupole Green functions are introduced.

Fluid dipole If two simple point sources of opposite phases but equal magnitudes are put close together, the fluid ejected from one of the sources is sucked in by the other and vice versa, as though it were simply being moved from the one source point to the other. Such a source is called a dipole source. A number of textbooks present the construction of a point dipole from two closely spaced point monopoles of opposite phases, e.g. Fahy and Walker (1998).

The net complex response (e.g. pressure or displacement) from a point dipole, at any receiver point $\mathbf{x} = (r, \theta, s)$, is the sum of the individual responses of two closely spaced monopoles with strengths $-S$ and $+S$, respectively. In the limit where the vector separation $|\mathbf{d}| \to 0$, the product of strength and separation is held constant $S\mathbf{d} = \mathbf{D}$ and the pressure field from the point dipole emerges as

$$p^d(\mathbf{x}) = \mathbf{D} \cdot \nabla_{\mathbf{y}} G_f(\mathbf{x}|\mathbf{y}) = D_i \frac{\partial G_f(\mathbf{x}|\mathbf{y})}{\partial y_j} \tag{4.16}$$

where $G_f(\mathbf{x}|\mathbf{y})$ is the same monopole Green function derived in the last section; the index $\mathbf{y}$ denotes differentiation with respect to the source coordinates $\mathbf{y} = (r_o, \theta_o, s_o)$; and the gradient operator in nondimensional cylindrical coordinates is

$$\nabla_{\mathbf{y}} f = \left(\frac{\partial f}{\partial r} \frac{\partial r}{\cdot a \partial r_o}, \frac{1}{r} \frac{\partial f}{\partial \theta_o}, \frac{\partial f}{\partial s_o} \frac{\partial s}{\partial z} \right) = \left(\frac{1}{a} \frac{\partial f}{\partial r_o}, \frac{1}{r} \frac{\partial f}{\partial \theta}, \frac{1}{a} \frac{\partial f}{\partial s} \right) \tag{4.17}$$

The dipole can have three different orientations, aligned radially, tangentially or axially. Any dipole not aligned with the axes can be constructed using the three fundamental forms. The axial and tangential dipole pressure response have essentially the same form as the Green function, apart from multiplying factors κ_{nb} and n, while the radial dipole is more complicated as it involves differentiation of the Bessel function. Nonetheless, the construction of the dipole from equations (4.13) and (4.16) is straightforward and will not be stated here.

Using essentially the same concept, the structural response to a point dipole in the fluid can be derived as

$$u^{i,d} = \mathbf{D} \cdot \nabla_{\mathbf{y}} G_s^i(\mathbf{x}|\mathbf{y}) \tag{4.18}$$

where index i indicates the displacement can be either of the displacement directions u, v and w.

Fluid quadrupoles In the case of two point dipoles of strength $-\mathbf{D}$ and $+\mathbf{D}$ with a vector separation $\mathbf{d}'$, the result of taking the limit $|\mathbf{d}'| \to 0$ with the product of strength and separation held constant, $\mathbf{D} : \mathbf{d}' = \mathbf{Q}$, a point quadrupole emerges,

$$p^q(\mathbf{x}) = \mathbf{Q} : \nabla_{\mathbf{y}} \nabla_{\mathbf{y}} G_f(\mathbf{x}|\mathbf{y}) = Q_{ij} \frac{\partial^2 G_f(\mathbf{x}|\mathbf{y})}{\partial y_i \partial y_j} \tag{4.19}$$

where Q_{ij} is the strength tensor.

Each of the two dipoles can have three different orientations, making a total of nine different combinations. Because of symmetry, only six of these are unique. Each of these can be derived from equations (4.13) and (4.19).

The structural response to the fluid quadrupole can be defined using the same concept as for the fluid dipole.

4.3.6 Relative scaling of pressure response of multipole sources

As noted in section 4.3.3 above, the relative scaling of multipole sources may allow a simplification of the vibroacoustic analogy. In free fields there is a well established expectation regarding the relative scaling of monopole, dipole, and quadrupole type aeroacoustic sources (Howe 1997). If the Mach number is sufficiently low the radiated power in the free field for each type scales as: 1:Ma^2:Ma^4. However, the environment of the source may affect the radiation; this is for example the case near a sharp edge of a large plate ((Ffowcs Williams and Hall 1970) and (Crighton and Leppington 1971)) where the relative importance of the quadrupole sources is increased. The purpose of this section is to investigate whether the relative scaling laws from the free-field also apply inside a fluid-filled pipe.

Since each of the source types drives the fluid-filled pipe in a fundamentally different way, they are not directly comparable. To circumvent this problem a dimensionless pressure ratio is introduced, such that the in-pipe pressure amplitude of a given source type is related to the free far-field pressure amplitude of the same source type. In the case of the directional source types, the directional peak pressure amplitude is used, as the pressure perpendicular to the dipole axis is, for example, identical to zero. The dimensionless pressure ratio is defined as:

$$\Lambda_{\mathrm{pres}}(r, r_o; \theta - \theta_o; s - s_o) = \left| \frac{p_{\mathrm{pipe}}}{\frac{D}{a} \cdot p_{\mathrm{free,peak}}} \right| \tag{4.20}$$

where p_{pipe} is the in-pipe pressure amplitude; $p_{\text{free,peak}}$ is the free-field directional peak pressure amplitude at distance D; (r, θ, s) is the receiver point; and (r_o, θ_o, s_o) is the source point.

The numerical prediction model from chapter 6 is used along with the definition of the multipole sources from section 4.3.5 to predict the in-pipe pressure. The free-field pressure is calculated standard theory (Morse and Ingard 1968). As a special case, the dimensionless pressure ratio in a hard-walled circular duct can be predicted analytically for each type; a simple result is obtained in the limit of low Helmholtz numbers (He = $k_f a = 2\pi f a / c_f$), where the far-field in-pipe pressure response is restricted to plane waves.

Figure 4.5 shows the dimensionless pressure ratios for a pipe with light fluid loading (PVC pipe with air inside and outside, corresponding to the experimental setup of chapter 8) excited by monopole, axial dipole, and axial-axial quadrupole sources. Below cuton of the higher order duct modes at He = 1.84, the curves in the figure are virtually identical to those predicted by the low-frequency theory mentioned above: in a hard-walled circular duct below He = 1.84 each of the source types is represented by a 2/He curve. Above He = 1.84 there is multimode excitation, and the curves become more complex.

Figure 4.6 shows similar curves for a light fluid loaded pipe excited by monopole, radial dipole, and radial-radial quadrupole sources. The theoretical hard-walled prediction in this case is that the monopole should follow 2/He (no change from figure 4.5), while neither the radial dipole nor the radial-radial quadrupole should drive the plane-wave mode and therefore their contributions should disappear once the lowest transverse mode is cut off, below He = 1.84. However, as seen in the figure, there is a small response for both the radial dipole and the radial-radial quadrupole. This reason for this is simply that the pipe walls are slightly compliant even for light fluid loading, but the response is relatively insignificant.

The conclusion to draw from figures 4.5 and 4.6 is that in the light fluid loaded case the relative ranking of monopole, axial-dipole, and axial-axial quadrupole radiation remains unaltered inside the pipe for low He, compared to the free-field situation. The radiation from radial dipoles and quadrupoles are small by comparison. As no augmentation takes place, the free-field Mach number scaling still applies for low Mach numbers. Davies and Ffowcs Williams (1968) present the same conclusion for quadrupoles inside an infinite hard-walled duct.

Figure 4.7 shows the dimensionless pressure ratios for the axial source types, for a pipe with heavy fluid loading (PVC pipe with air outside and water inside, corresponding to the experiments in chapter 9). At low He the curves are all approximately parallel with a 1/He slope, but not coincident. Apparently each of the source types differs from the next by a constant factor: the dimensionless pressure ratio from the axial dipole is approximately a factor of 5 larger than from the monopole, and likewise there is a factor of 5 between the axial-axial quadrupole and the axial dipole. From the fact that the curves in figure 4.7 are approximately parallel at low He, it can be concluded that the free-field Mach number scaling also applies for heavy fluid loading.

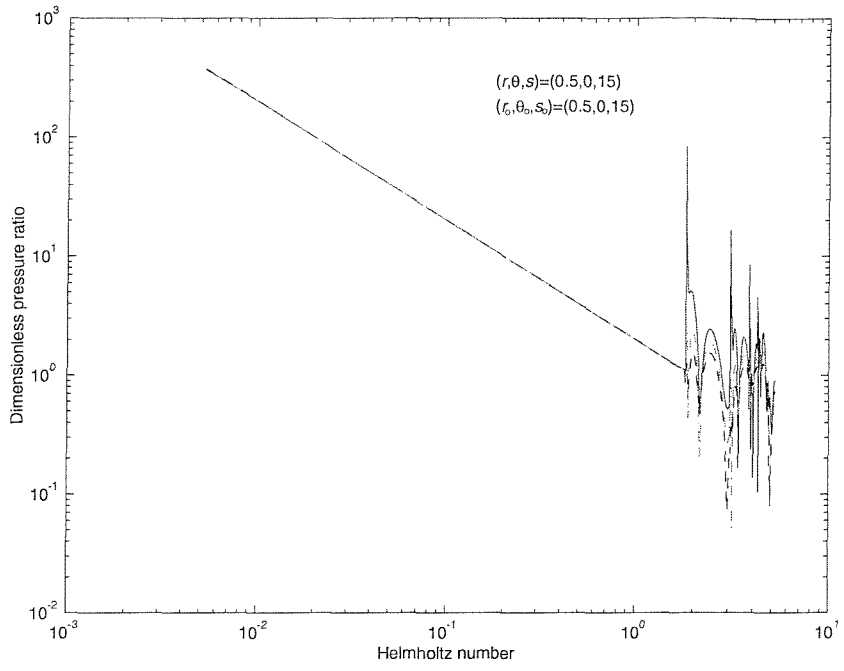

Figure 4.5: Dimensionless ratio of in-pipe to free-field pressure response. Pipe with light fluid loading: monopole(red), axial dipole(green) and axial-axial quadrupole(blue).

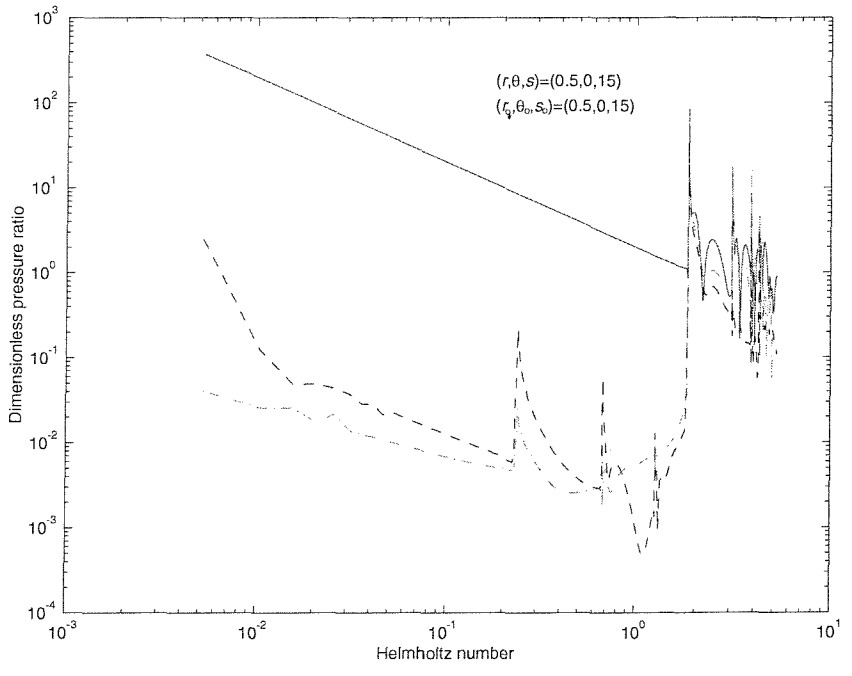

Figure 4.6: Dimensionless ratio of in-pipe to free-field pressure response. Pipe with light fluid loading: monopole(red), radial dipole(green) and radial-radial quadrupole(blue).

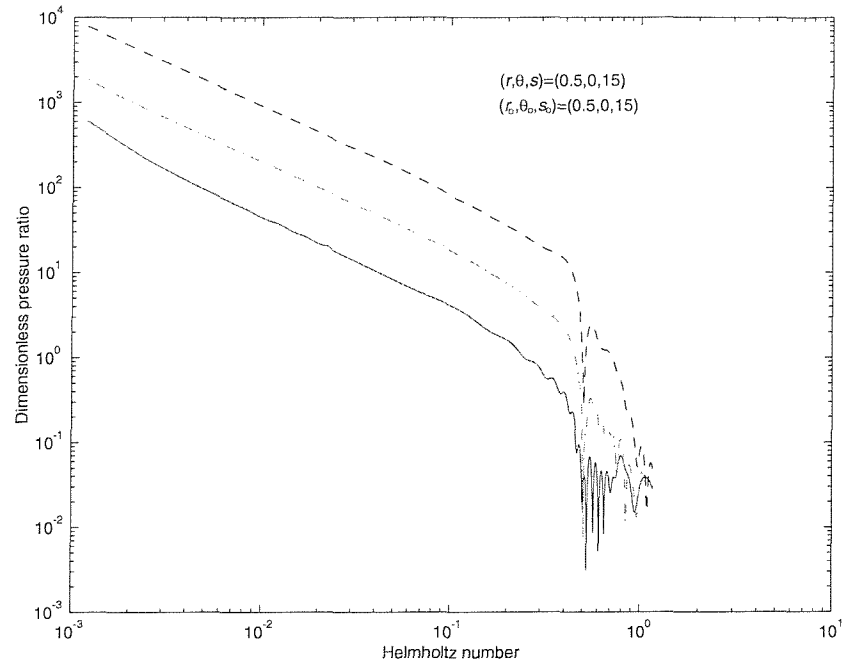

Figure 4.7: Dimensionless ratio of in-pipe to free-field pressure response. Pipe with heavy fluid loading: monopole(red), axial dipole(green) and axial-axial quadrupole(blue).

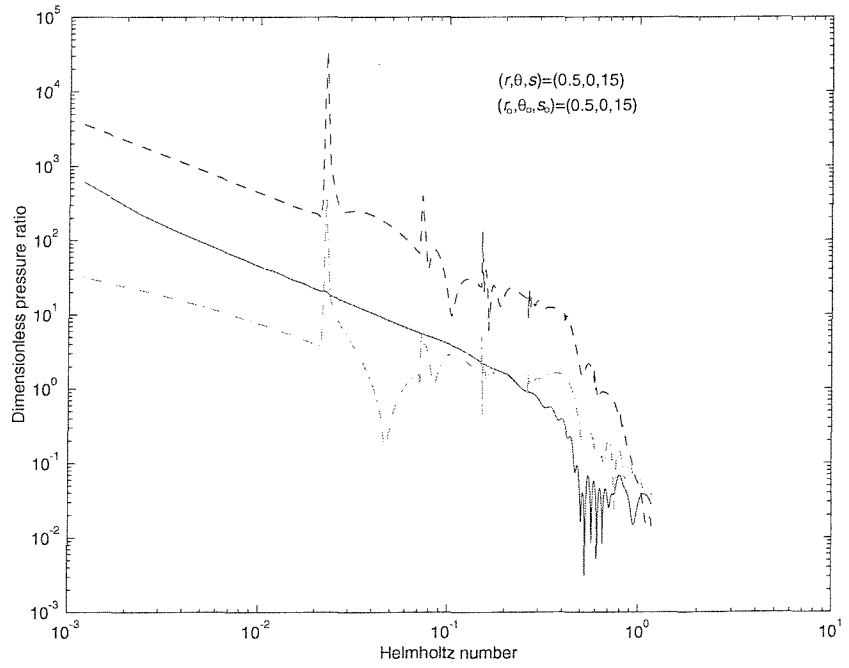

Figure 4.8: Dimensionless ratio of in-pipe to free-field pressure response. Pipe with heavy fluid loading: monopole(red), radial dipole(green) and radial-radial quadrupole(blue).

However, the implied dominance of monopoles at low Mach numbers (or of dipoles, if no monopoles are present) is only the case below a certain problem-dependent Mach number. If the Mach number is higher than the so-called cross-over Mach number, then the multipoles will dominate the monopole. The cross-over Mach number is affected by the constant factor between the curves in figure 4.7; for example, the cross-over Mach number between the axial dipoles and axial quadrupole is reduced by a factor of approximately 5 relative to free-field radiation.

The dimensionless pressure ratios for the radial source types in a pipe with heavy fluid loading are plotted in figure 4.8. If one compares this figure with the light fluid loading case (figure 4.6) the overall appearance is different, as the curves for both the radial dipole and radial-radial quadrupole (particularly the latter) are now of comparable magnitude with the monopole. The reason for this is the significantly larger excitation of the pipe with heavy fluid loading below He = 1.84, due to the relatively larger flexibility of the pipe wall. The in-pipe pressure response to the radial dipole is dominated by the structural $n = 1$ mode (beam bending), while both the monopole and the radial-radial quadrupole are dominated by the $n = 0$ mode. The curves remain approximately parallel at low He and the free-field Mach number scaling rules therefore apply. However there is a factor of approximately 100 between the dipole and the quadrupole ratios, and the cross-over Mach number between these sources is therefore significantly affected as discussed below.

No significant changes in the trends discussed above occur when either the point of excitation or the receiver point are moved along the radius. The reason for this is that the pressure response at low He in each of the cases is dominated by low n (the modal pressure field for $n = 0$ and $n = 1$ does not depend strongly on radial location), and therefore (by reciprocity) the monopole response of these modes are largely unaffected by the radial position of the source. There are some minor changes at higher He where the higher order modes have significant contributions, but the overall trends are unchanged.

In the interpretation of the vibroacoustic analogy in section 4.3.3 it was argued that there was no monopole contribution in the industrial application. This leaves dipole and quadrupole contributions. In the free-field scaling laws, a rule of thumb for turbulent flow noise with solid boundaries says that the cross-over Mach number where quadrupoles tend to dominate over dipoles is approximately 1. As the dimensionless pressure ratio for dipoles and quadrupole differs approximately by a factor of 5 in the axial case and a factor of 100 in the radial case, the radial case is most critical. However, the cross-over Mach number is approximately 0.01 in this case and as the Mach number in the industrial application is of the order 0.001, the dipole excitation will dominate the pressure response in the vibroacoustic analogy calculation.

4.3.7 Power flow calculation from the vibroacoustic analogy

Once the input excitation is calculated from the vibroacoustic analogy, the response of the fluid-filled cylindrical shell can be predicted. In Part II of this thesis a prediction

model is presented; this model enables prediction of the shell vibration, the internal fluid pressure, and the total vibroacoustic power flow in the axial direction. The excitation presented in Part II is limited to a point force at the shell wall or a point monopole in the fluid, but as shown in the previous sections it is quite simple to expand the excitation to include source distributions of multipole order, for which the response is determined by taking derivatives of the point monopole Green function.

Eventually, it is expected that the necessary inputs will come from a CFD simulation of the unsteady flow. Any input to the vibroacoustic analogy provided by a numerical flow calculation is not continuous, as the equations of fluid motion are discretised in both space and time. The temporal discretisation is not a problem, if the analysis is conducted carefully, as the time steps can be chosen to be significantly smaller than the smallest time scale of interest in the fluid. The spatial discretisation is not a problem either, if the calculation is conducted carefully. The spatial scales of the vibroacoustic problem (e.g. the wavelength of the bending modes) are significantly larger than the spatial scales of the flow calculations, as small eddies need to be resolved, even when using a turbulence model. A key part of the spatial discretisation in the flow calculation is the meshing of the fluid volumes. Any surfaces in contact with the fluid are also meshed in patches. When solving the unsteady fluid flow, the fluctuating forces on each patch becomes known. If the time series are long enough, the fluctuating force on each patch can be Fourier transformed. Knowing the surface normal of the patch, the dipoles of the $\overline{S}$ integral in equation (4.11) can be constructed. The reaction forces from the flow obstruction on the pipe wall can also be extracted from the flow solution.

Due to the coupled nature of the fluid-filled shell, the structural excitation by the reaction forces leads both to vibration of the shell wall and pressure fluctuations in the fluid. Since the different excitation processes have a common generation mechanism in the fluid flow, it cannot be generally assumed that the excitations are incoherent. Their power flow contributions then need to be added modally. While modal addition may be troublesome, there are standard methods for dealing with the problem; see e.g. Norton (1989).

4.4 Conclusion

The concept of numerical calculation of vibroacoustic power flow from a flow obstruction in a fluid-filled pipe has been presented in this chapter. The method is general and does not put any constraints on the geometry of the flow obstruction. The calculation involves three steps:

i) Solution of the incompressible unsteady flow around a flow obstruction inside the pipe using Computational Fluid Dynamics.

ii) Construction of a vibroacoustic analogy that transforms the vibroacoustic excitation of the flow past the flow obstruction into an equivalent problem with vibroacoustic excitation by point sources in a fluid-filled pipe without flow and flow obstruction.

iii) Calculation of the vibroacoustic power flow from the equivalent point sources.

The second part involving the vibroacoustic analogy is one of the main contributions in this thesis and it is therefore discussed in some detail. The CFD solution of the fluid flow has been left out, as it is very complicated to obtain a unsteady time-resolved solution of the fluid flow. Only a few remarks have been posed regarding the numerical calculation of the vibroacoustic power flow, as it is presented in detail in part II of this thesis.

Part II

Prediction of vibroacoustic power flow in mechanically and acoustically excited pipes

Chapter 5

Review of analytical models for fluid-filled infinite cylindrical shells

This chapter is a review of analytical models for small-amplitude vibrations of infinite cylindrical shells, excited by point forces at the shell wall and monopoles in the contained fluid. The dimensional formulation of the equations presented in this chapter is not used explicitly in later chapters. Instead, in chapter 6 they are reformulated in nondimensional form and the nondimensional form is used throughout the rest of the thesis. The equations in this chapter are therefore not discussed in depth, as many of the comments and interpretations are put more appropriately in the later chapters.

The modelling of infinite cylindrical shells has received quite a bit of research in the last century. The main focus at first was predicting the in vacuo shell vibrations excited by structural forces, e.g. Donnell (1933) and Flügge (1962), but later work included the effects of internal and external fluids. Most of the relevant background theory on cylindrical shells can be found in the reference work by Leissa (1973). A key omission in Leissa (1973) is the lack of any excitation of the shell by the fluid. While some confidential research was done on this topic by J. M. James (parts quoted by Fuller (1984) and Skelton and James (1997)), the first publicly available paper to examine in depth the behaviour of cylindrical shells excited by internal and external monopoles was by Fuller (1984). This reference was part of a sequence of papers by Fuller investigating different properties of the cylindrical shell.

The review in this chapter follows the framework set out in 'Theoretical acoustics of underwater structures' by Skelton and James (1997). The framework includes the general modelling of infinite cylindrical shell with internal and external fluid loading. The excitation in this review is restricted to point forces at the shell wall and point monopoles placed in the interior fluid. Skelton and James (1997) use the Goldenveizer-Novozilov shell theory, but as the main shell theory used in the present thesis is the Flügge shell theory (Flügge 1962), the Flügge equations are presented in the following. A closer examination of the influence of the shell theory on relevant vibroacoustic aspects can be found in chapter 7, where the Flügge, Goldenveizer-Novozhilov and Donnell-Mushtari shell theories are compared. The solution of the equations of motion

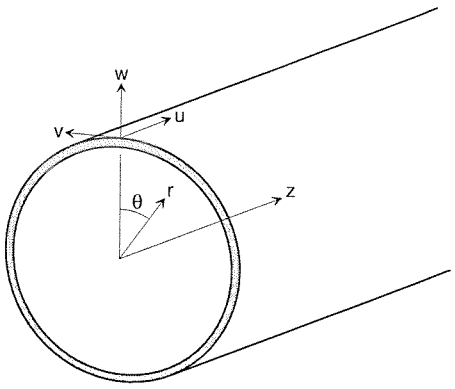

Figure 5.1: Coordinate system for infinite cylindrical shell

is not presented in this chapter. Instead this is presented in chapter 6 along with the nondimensional prediction model.

5.1 Equations of motion

Consider a uniform thin cylindrical shell of thickness h and mean radius a. The mid-surface of the shell is described in a (r, θ, z) cylindrical coordinate system, as shown is figure 5.1. If $u(\theta, z)$, $v(\theta, z)$ and $w(\theta, z)$ represent the components of displacement from the equilibrium state in the axial, circumferential, and radial directions, respectively, the equations of motion for the shell can be written as

$$\begin{aligned} Q_{11}u(\theta,z) + Q_{12}v(\theta,z) + Q_{13}w(\theta,z) &= E^z(\theta,z) \\ Q_{21}u(\theta,z) + Q_{22}v(\theta,z) + Q_{23}w(\theta,z) &= E^\theta(\theta,z) \\ Q_{31}u(\theta,z) + Q_{32}v(\theta,z) + Q_{33}w(\theta,z) &= E^r(\theta,z) \end{aligned} \tag{5.1}$$

where the Q-elements are differential operators acting on the displacements; $E^z(\theta, z)$, $E^\theta(\theta, z)$, and $E^r(\theta, z)$ are the orthogonal components of mechanical excitation of the shell wall per unit area (the tractions) in the positive coordinate directions. The differential operators are, according to the Flügge shell theory (Flügge 1962),

$$\begin{aligned} Q_{11} &= -D\left(\frac{\partial^2}{\partial z^2} + \frac{(1-\nu)(1+\beta^2)}{2a^2}\frac{\partial^2}{\partial\theta^2}\right) + \rho_s h\frac{\partial^2}{\partial t^2} \qquad Q_{12} = -D\frac{1+\nu}{2a}\frac{\partial^2}{\partial z\partial\theta} \\ Q_{13} &= -D\left(\frac{\nu}{a}\frac{\partial}{\partial z} - a\beta^2\frac{\partial^3}{\partial z^3}\right) + \frac{(1-\nu)\beta^2}{2a}\frac{\partial^3}{\partial z\partial\theta^2} \qquad Q_{21} = Q_{12} \\ Q_{22} &= -D\left(\frac{1-\nu}{2}\frac{\partial^2}{\partial z^2} + \frac{1}{a^2}\frac{\partial^2}{\partial\theta^2} + \frac{3(1-\nu)\beta^2}{2}\frac{\partial^2}{\partial z^2}\right) + \rho_s h\frac{\partial^2}{\partial t^2} \\ Q_{23} &= -D\left(\frac{1}{a^2}\frac{\partial}{\partial\theta} - \frac{(3-\nu)\beta^2}{2}\frac{\partial^2}{\partial z^2}\right) \qquad Q_{31} = -Q_{13} \qquad Q_{32} = -Q_{23} \\ Q_{33} &= D\left(\frac{1}{a^2} + \beta^2\left(a^2\frac{\partial^4}{\partial z^4} + \frac{1}{a^2}\frac{\partial^4}{\partial\theta^4} + 2\frac{\partial^4}{\partial z^2\partial\theta^2}\right)\right) + \rho_s h\frac{\partial^2}{\partial t^2} \end{aligned} \tag{5.2}$$

Here $D = Eh/(1-\nu^2) = \rho_s c_L^2 h$ is the extensional rigidity also called the membrane stiffness; $c_L = \sqrt{E/\rho(1-\nu^2)}$; ν is the Poisson's ratio of the shell; E is the Young's modulus of the shell; ρ_s is the material density of the shell; $\beta^2 = h^2/12a^2$ is a thickness ratio.

Representing field quantities in the cylindrical coordinate system by a Fourier integral transform in the z direction and a Fourier series in the θ direction, yields

$$f(r,\theta,z) = \frac{1}{2\pi}\sum_{n=-\infty}^{\infty} e^{in\theta}\int_{-\infty}^{\infty} f(r,n,k)e^{ikz}\mathrm{d}k \tag{5.3}$$

and the inverse transform

$$f(r,n,k) = \frac{1}{2\pi}\int_0^{2\pi} e^{-in\theta}\mathrm{d}\theta\int_{-\infty}^{\infty} f(r,\theta,z)e^{-ikz}\mathrm{d}z \tag{5.4}$$

where $f(r,\theta,z)$ is the field quantity; $f(r,n,k)$ is the spectral field quantity; n is the circumferential mode order and k is the wavenumber in the axial direction.

From the shell equations it follows that the tangential displacement component generally is $\pi/2$ radians out of phase with the axial and radial displacement components. The displacement components could be formulated using complex exponential functions as in equation (5.3), but it is more convenient to use displacements of the form

$$\begin{aligned} u(t,\theta,z) &= U\cos(n\theta)e^{i\left(kz-\omega t+\frac{\pi}{2}\right)} \\ v(t,\theta,z) &= V\sin(n\theta)e^{i(kz-\omega t)} \\ w(t,\theta,z) &= W\cos(n\theta)e^{i(kz-\omega t)} \end{aligned} \tag{5.5}$$

with unknown displacement amplitudes U, V and W. The $\pi/2$ in the u-displacement is by convention added to avoid imaginary components of the following S-matrix. It is convenient to consider single-frequency solutions with time factor $e^{i\omega t}$. Accordingly in the reminder of this thesis, all displacements, pressures, and input forcing terms are represented by their complex amplitudes, with the $e^{i\omega t}$ factor suppressed.

The differential equations of motion can then be expanded as transforms. Using a matrix representation, the spectral equations of motion are

$$\begin{bmatrix} S_{11}(n,k) & S_{12}(n,k) & S_{13}(n,k) \\ S_{21}(n,k) & S_{22}(n,k) & S_{23}(n,k) \\ S_{31}(n,k) & S_{32}(n,k) & S_{33}(n,k) \end{bmatrix} \begin{bmatrix} u(n,k) \\ v(n,k) \\ w(n,k) \end{bmatrix} = \begin{bmatrix} E^z(n,k) \\ E^\theta(n,k) \\ E^r(n,k) \end{bmatrix} \tag{5.6}$$

where $E^z(n,k)$, $E^\theta(n,k)$ and $E^r(n,k)$ are the spectral excitation tractions (force per unit area); and the elements of the S matrix are found by using the assumed form of the displacements in equation (5.5) in the definition of the Q-matrix from equation

(5.1). This yields

$$S_{11} = D\left(k^2 + n^2\frac{(1-\nu)(1+\beta^2)}{2a^2}\right) - \omega^2\rho_s h \qquad S_{12} = D(1+\nu)\frac{nk}{2a}$$

$$S_{13} = -D\left(\nu\frac{k}{a} + a\beta^2k^3 - \frac{(1-\nu)\beta^2n^2k}{2a}\right) \qquad S_{21} = S_{12}$$

$$S_{22} = D\left((1-\nu)\frac{a^2}{2} + \frac{n^2}{a^2} + \frac{3(1-\nu)}{2}\beta^2\kappa^2\right) - \omega^2\rho_s h$$

$$S_{23} = D\left(\frac{n}{k} + \frac{(3-\nu)\beta^2nk^2}{2}\right) \qquad S_{31} = -S_{13}$$

$$S_{32} = -S_{23} \qquad S_{33} = D\left(\frac{1}{a^2} + \beta^2\left(a^2k^4 + \frac{n^4}{a^2} + 2k^2n^2\right)\right) - \omega^2\rho_s h$$

5.2 Structural point excitation and fluid loading

If the shell is not in vacuo, but filled with an internal fluid and submerged in an external fluid, the effect of the fluids can be accounted for through a fluid loading term. The combined effect of (1) a mechanical point force vector (F^z, F^θ, F^r), located on the pipe wall at the coordinates (a, θ_o, z_o), and (2) fluid loading pressures p_i, p_e on the internal and external walls, is represented by the tractions

$$\begin{bmatrix} E^z(\theta,z) \\ E^\theta(\theta,z) \\ E^r(\theta,z) \end{bmatrix} = \begin{bmatrix} F^z\delta(z-z_o)\delta(\theta-\theta_o)/a \\ F^\theta\delta(z-z_o)\delta(\theta-\theta_o)/a \\ F^r\delta(z-z_o)\delta(\theta-\theta_o)/a - p_e(a,\theta,z) + p_i(a,\theta,z) \end{bmatrix} \tag{5.7}$$

where F^z, F^θ and F^r are the axial, tangential and radial components of local force acting on the shell mid-surface, being positive in the directions of the coordinate axes. Both the internal and external fluid are assumed to be inviscid.

The related pressure fields satisfy the acoustic wave equation. Solutions are conveniently expressed in spectral (n,k) form rather than in physical (θ,z) space. The interior spectral pressure p_i^w driven by vibration of the shell wall has the following form, as it is a solution to the Helmholtz equation in cylindrical coordinates which is finite at the origin,

$$p_i^w = A_n \mathrm{J}_n(k_i^r r) \tag{5.8}$$

where A_n is an amplitude coefficient to be determined; $k_i^r = +\sqrt{k_i^2 - k^2}$ is the interior radial wavenumber; $k_i = \omega/c_f^i$ is the interior acoustic wavenumber; c_f^i is the sound speed of the interior fluid ; and J_n is the Bessel function of the first kind of order n. A boundary condition requiring the fluid to stay in contact with the shell wall can be applied, coupling the radial shell displacement and the internal pressure field. Applying the boundary condition at $r = a$ to solve for A_n gives

$$\left.\frac{\partial p_i^w}{\partial r}\right|_{r=a} = \rho_i\omega^2 w \tag{5.9}$$

where ρ_i is the interior fluid density; the interior spectral pressure is then found to be

$$p_i^w = \rho_i \omega^2 w \frac{\mathrm{J}_n(k_i^r r)}{k_i^r \mathrm{J}_n'(k_i^r a)} \tag{5.10}$$

where J_n' is the derivative of the Bessel function with respect to the argument. Equation (5.10) is a key equation that links the modal pressure response in the interior fluid to the modal radial-displacement response of the pipe wall. It is (in the form of a fluid loading term) used in the structural response solution in equation (5.14) below, and also in the response calculations in chapter 6.

The vibrations of the shell wall also gives rise to an external pressure field when the shell is surrounded by an external fluid. The exterior spectral pressure must be a solution to the Helmholtz equation in cylindrical coordinates which satisfies the radiation condition at infinity. Thus,

$$p_e^w = B_n \mathrm{H}_n(k_e^r r) \tag{5.11}$$

where B_n is an amplitude coefficient to be determined; $\mathrm{H}_n = \mathrm{J}_n + i\mathrm{Y}_n$ is the Hankel function of order n (commonly written $\mathrm{H}_n^{(1)}$); $k_e^r = +\sqrt{k_e^2 - k^2}$ is the exterior radial wavenumber; $k_e = \omega / c_f^e$ is the exterior acoustic wavenumber; and c_f^e is the sound speed of the exterior fluid. Using the same boundary condition argument as before to solve for B_n gives

$$\left. \frac{\partial p_e^w}{\partial r} \right|_{r=a} = \rho_e \omega^2 w \tag{5.12}$$

where ρ_e is the exterior fluid density; the exterior spectral pressure is then found to be

$$p_e^w = \rho_e \omega^2 w \frac{\mathrm{H}_n(k_e^r r)}{k_e^r \mathrm{H}_n'(k_e^r r)} \tag{5.13}$$

The fluid loading can therefore be included in the equations of motion for a shell driven by a point force, as

$$\begin{bmatrix} S_{11}(n,k) & S_{12}(n,k) & S_{13}(n,k) \\ S_{21}(n,k) & S_{22}(n,k) & S_{23}(n,k) \\ S_{31}(n,k) & S_{32}(n,k) & S_{33}(n,k) + f_l \end{bmatrix} \begin{bmatrix} u(n,k) \\ v(n,k) \\ w(n,k) \end{bmatrix} = \begin{bmatrix} F^z \delta(z - z_o)\delta(\theta - \theta_o)/a \\ F^\theta \delta(z - z_o)\delta(\theta - \theta_o)/a \\ F^r \delta(z - z_o)\delta(\theta - \theta_o)/a \end{bmatrix} \tag{5.14}$$

where the (3,3) matrix element includes a term

$$f_l = \rho_e \omega^2 \frac{\mathrm{H}_n(k_e^r a)}{k_e^r \mathrm{H}_n'(k_e^r a)} - \rho_i \omega^2 \frac{\mathrm{J}_n(k_i^r a)}{k_i^r \mathrm{J}_n'(k_i^r a)} \tag{5.15}$$

that accounts for the fluid loading by the internal and external fluids at the shell wall.

5.3 Fluid monopole excitation

When the excitation of the shell is by an interior monopole, located at $\mathbf{y} = (r_o, \theta_o, z_o)$, it is convenient to express the interior spectral pressure as a sum of separately identifiable contributions as follows:

$$p_i = p_i^m + p_i^r + p_i^w \tag{5.16}$$

Here p_i^m is the free-field spectral pressure of a monopole; p_i^r is the interior spectral pressure scattered as though the boundary was hard; and p_i^w is the interior spectral pressure due to the shell wall vibrations.

The free-field pressure at a position $\mathbf{x} = (r, \theta, z)$ of the interior monopole is written as

$$p_i^m(\mathbf{x}, \mathbf{y}) = S\frac{e^{ik_i|D|}}{|D|} \tag{5.17}$$

where $|D| = \sqrt{r^2 + r_o^2 - 2rr_o\cos(\theta - \theta_o) + (z - z_o)^2}$ is the distance from the monopole to the observation point and S is the strength of the monopole, having units of force per length. The spectral free-field pressure from the monopole is then

$$p_i^m(r) = -i\pi S\cos(n(\theta - \theta_o))e^{-ik(z-z_o)}\begin{cases} \mathrm{J}_n(k_i^r r_o)\mathrm{H}_n(k_i^r r) & \text{for} \quad r \geq r_o \geq 0 \\ \mathrm{J}_n(k_i^r r)\mathrm{H}_n(k_i^r r_o) & \text{for} \quad r_o \geq r \geq 0 \end{cases} \tag{5.18}$$

The interior spectral pressure p_i^r scattered as though the boundary were hard is found by solving for the total spectral pressure p_{ih} inside a shell with a hard boundary. The general solution for p_{ih} is obtained by adding a solution of the homogeneous wave equation to the monopole free-field expression above; thus

$$p_{ih}(r) = p_i^m(r) + p_i^r(r) = p_i^m(r) + C_n\mathrm{J}_n(k_i^r r) \tag{5.19}$$

The constant C_n is found using the boundary condition $\partial p_{ih}/\partial r = 0$ at $r = a$, giving

$$p_i^r(r) = -i\pi S\cos(n(\theta - \theta_o))e^{-ik(z-z_o)}\frac{\mathrm{J}_n(k_i^r r_o)\mathrm{H}_n'(k_i^r a)}{\mathrm{J}_n'(k_i^r a)}\mathrm{J}_n(k_i^r r) \tag{5.20}$$

At the surface of the shell at $r = a$, the blocked interior spectral pressure is written in the following simplified form, using the Wronskian relation $\mathrm{J}_n(z)\mathrm{H}_n'(z) - \mathrm{H}_n(z)\mathrm{J}_n'(z) = 2i/\pi z$:

$$p_i^m(a) + p_i^r(a) = 2S\cos(n(\theta - \theta_o))e^{-ik(z-z_o)}\frac{\mathrm{J}_n(k_i^r r_o)}{(k_i^r a)\mathrm{J}_n'(k_i^r a)} \tag{5.21}$$

The interior spectral pressure on the inner wall $r = a$ can now be expanded using equations (5.16) and (5.21):

$$p_i(a) = 2S\cos(n(\theta - \theta_o))e^{-ik(z-z_o)}\frac{\mathrm{J}_n(k_i^r r_o)}{(k_i^r a)\mathrm{J}_n'(k_i^r a)} + p_i^w(a) \tag{5.22}$$

The pressure contributed at the inner wall from the fluid impedance presented to the shell motion is included in the fluid loading term in equation (5.15), and the equations of motion for a infinite cylindrical shell excited by a fluid monopole can then be written as

$$\begin{bmatrix} S_{11} & S_{12} & S_{13} \\ S_{21} & S_{22} & S_{23} \\ S_{31} & S_{32} & S_{33} + f_l \end{bmatrix}\begin{bmatrix} u \\ v \\ w \end{bmatrix} = \begin{bmatrix} 0 \\ 0 \\ 2S\cos(n(\theta - \theta_o))e^{-ik(z-z_o)}\frac{\mathrm{J}_n(k_i^r r_o)}{(k_i^r a)\mathrm{J}_n'(k_i^r a)} \end{bmatrix} \tag{5.23}$$

Solutions of this equation, and of the corresponding equation (5.14) for mechanical excitation by a point force, are discussed in chapter 6.

5.4 Conclusion

Using the Flügge shell theory, the equations of motion for the forced vibroacoustic problem of an infinite cylindrical shell, filled with an internal fluid and submerged in an external fluid, have been formulated for two different types of excitation: mechanical (via the structure) and acoustical (via the fluid). The structural excitation is assumed to be in the form of a point force applied to the shell, while the fluid excitation is in the form of a point monopole in the interior fluid.

The equations presented in this chapter are included to provide a foundation for the nondimensional prediction model in the next chapter. This way, the presentation of the prediction model can be smoother, as the equations in this chapter can be referenced instead of references to the literature.

Chapter 6

Prediction of response functions and power flow

In this chapter, a complete numerical model of the vibroacoustic problem is presented along with expressions for calculations of the power flow in the system. The starting point for the numerical model is the equations presented in the previous chapter.

In a series of papers, C. R. Fuller has worked his way through the characteristics of wave propagation in infinite circular shells, from the transmission of flexural waves through discontinuities in in vacuo shells to monopole excitation of fluid-filled shells. Fuller (1981) investigated the transmission of flexural waves through some discontinuities with the use of Flügge's theory of thin cylindrical shells, but for in vacuo shells alone. Along with Fahy (Fuller and Fahy 1982), the complicating effects of fluid loading on the inside of the shell were analysed in depth, using the theoretical framework of Donnell-Mushtari, which is a less complicated subset of the Flügge theory. This work investigated the dispersion behaviour of free waves in thin-walled cylindrical shells, and some aspects of the variation with frequency and material parameters were highlighted. On top of this work Fuller (1983) investigated the forced response of the shell from mechanical excitation in the form of line and point forces, via the input mobility of the fluid-filled shell. The same methodology was used to examine the forced response to fluid excitation by a point monopole (Fuller 1984).

Several other researchers have also worked with fluid-filled cylindrical shells, using different methods for different purposes, mainly Pavic (1990), Feng (1994) and Finnveden (1997a), (Finnveden 1997b) and (Finnveden 1997c). The first two used a similar analytical formulation to that of Fuller (Pavic used a series expansion of key elements for faster calculation, while Feng used the Flügge equations for added precision), but Finnveden used FE-methodology for his work. While Finnveden's method is very efficient from a numerical point of view and also almost as precise as the analytical formulation, its physical meaning is obscured by the use of FE. In the present thesis, physical understanding is rated higher than numerical efficiency and therefore the analytical formulation is used.

The starting point of this chapter is the Flügge equations of motion from chapter 5, but in this chapter they are nondimensionalised to reduce the number of variables needed to address the vibroacoustic problem. No further reductions of the equations are done even though the frequency range of interest in the present thesis is relatively low compared with the ring frequency of the shell. Some authors dealing with low frequency vibrations tend to make a low frequency approximation of the shell theory, e.g. Cremer et al. (1988) and Variyart and Brennan (1999). While this is feasible for in vacuo investigations, it is more difficult for fluid loaded problems, as the fluid loading terms in the equations tend to be strongly frequency dependent without any direct connection to the ring frequency of the shell. A low frequency approximation of a fluid loaded problem would therefore imply low frequency both in relation to the ring frequency and the fluid loading. The relation to the ring frequency can easily be established, and this is certainly the case for the problems investigated in this thesis, whereas the relation to the fluid loading is dependent both on the shell geometry and the material parameters involved. Both for the industrial problem and the experimental investigations in part III a low frequency approximation is not easy to make, and the full equations are therefore used.

6.1 Nondimensional matrix formulation

A total of 11 input parameters completely identify the problem drawn up in chapter 5, namely $h, a, \omega, n, \nu, c_L, \rho_s, c_f^i, \rho_i, c_f^e, \rho_e$. In the industrial application of this PhD project there will always be air on the outside of the pipe. It is shown in section 7.2.2 that from a vibroacoustic point of view, the influence of air as the external fluid is almost indistinguishable from vacuum in the frequency range of interest. The external fluid loading is therefore left out of the entire prediction model.

The output variables take the form of various frequency response functions which will be specified later.

It is convenient to introduce a nondimensional form of the equations in chapter 5 using the Buckingham Π theorem, see e.g. Fox and McDonald (1985). The Π theorem states that $9 - 3 = 6$ nondimensional groups are necessary in this case to completely specify the problem. Following the Π theorem, 3 parameters are chosen as repeating parameters, covering the 3 primary dimensions length, time and mass. For this problem, a, c_L and ρ_s are chosen, with the dimensions $[L]$, $[LT^{-1}]$ and $[ML^{-3}]$. This results in the following six nondimensional input groups: $\Omega = \omega a/c_L, n, \nu, h/a, \rho_f/\rho_s, c_f/c_L$. The entire formulation in this chapter makes use of these input groups. In addition, nondimensional axial and radial coordinates are introduced: $s = z/a$ and $r = r_{dim}/a$ where r_{dim} is the dimensional radius.

6.1.1 Point excitation of fluid-filled cylindrical shell

For single frequency forced vibration, it is convenient to express the shell displacements of equation (5.5) as Fourier transforms. If $u(\theta, s, t) = \tilde{u}e^{-i\omega t}$, then the complex displacement amplitudes $\tilde{u}$, $\tilde{v}$ and $\tilde{w}$ can be expressed as (compare equation (5.5))

$$\begin{aligned}
\tilde{u}(\theta, s) &= \frac{1}{2\pi}\int_{-\infty}^{\infty}\sum_{n=0}^{\infty}\varepsilon_n \cos(n(\theta-\theta_o))a\tilde{U}_n(\kappa)e^{i\left(\kappa(s-s_o)+\frac{\pi}{2}\right)}\mathrm{d}\kappa \\
\tilde{v}(\theta, s) &= \frac{1}{2\pi}\int_{-\infty}^{\infty}\sum_{n=0}^{\infty}\varepsilon_n \sin(n(\theta-\theta_o))a\tilde{V}_n(\kappa)e^{i\kappa(s-s_o)}\mathrm{d}\kappa \\
\tilde{w}(\theta, s) &= \frac{1}{2\pi}\int_{-\infty}^{\infty}\sum_{n=0}^{\infty}\varepsilon_n \cos(n(\theta-\theta_o))a\tilde{W}_n(\kappa)e^{i\kappa(s-s_o)}\mathrm{d}\kappa
\end{aligned} \tag{6.1}$$

where $\tilde{U}_n(\kappa)$, $\tilde{V}_n(\kappa)$ and $\tilde{W}_n(\kappa)$ are the respective modal displacement transforms; $s = z/a$ is the nondimensional axial position; $\kappa = ka$ is the nondimensional axial wavenumber; and ε_n is used to transform the doubled sided spectrum into a single sided, as

$$\sum_{n=-\infty}^{\infty} f(n) = \sum_{n=0}^{\infty}\varepsilon_n f(n) \tag{6.2}$$

where $f(n)$ is an arbitrary even function of n; $\varepsilon_n = 1$ for $n = 0$ and $\varepsilon_n = 2$ for all other cases. It is assumed that the excitation is symmetric about the diameter containing $\theta = \theta_o$.

The pressure inside the pipe can likewise be formulated as

$$\tilde{p}(r, \theta, s) = \frac{1}{2\pi}\sum_{n=0}^{\infty}\int_{-\infty}^{\infty}\varepsilon_n \cos(n\theta)\mathrm{J}_n(\alpha r)\tilde{P}_n(\kappa)e^{i\kappa s}\mathrm{d}\kappa \tag{6.3}$$

where $r = r_{\mathrm{dim}}/a$ is the nondimensional radius (r_{dim} is the dimensional radius), and α is the nondimensional radial acoustic wavenumber, related to the axial wavenumber by

$$\alpha = \pm\sqrt{\Omega^2\left(\frac{c_L}{c_f}\right)^2 - \kappa^2} \tag{6.4}$$

where c_f (formerly written as c_f^i) is the free wave speed in the fluid. As discussed in section 5.2, the pressure transform for a source-free fluid is linked to the radial displacement transform as

$$\tilde{P}_n = \frac{a^2\omega^2\rho_f}{\alpha \mathrm{J}_n'(\alpha)}\tilde{W}_n \tag{6.5}$$

The equations of motion in equation (5.6) of chapter 5 can be nondimensionalised, as follows: on the left of equation (5.6), the elements of the S matrix are divided by $D/a^2 = \rho_s c_L^2 h/a^2$; the displacements (u, v, w) are divided by a; and the right hand

side is divided through by $D/a = \rho_s c_L^2 h/a$. This gives the nondimensional spectral equations of forced motion as

$$\begin{bmatrix} L_{11} & L_{12} & L_{13} \\ L_{21} & L_{22} & L_{23} \\ L_{31} & L_{32} & L_{33} \end{bmatrix} \begin{bmatrix} \frac{u}{a} \\ \frac{v}{a} \\ \frac{w}{a} \end{bmatrix} = \begin{bmatrix} E^s \\ E^\theta \\ E^r \end{bmatrix} \tag{6.6}$$

where E^s, E^θ and E^r are the excitations in the directions indicated by the superscript and the elements in the L-matrix are

$$L_{11} = -\Omega^2 + \kappa^2 + \frac{1}{2}(1-\nu)(1-\beta^2)n^2 + \frac{1}{2}(1-\nu)\beta^2 \qquad L_{12} = \frac{1}{2}(1+\nu)n\kappa$$

$$L_{13} = \nu\kappa - \frac{1}{2}(1-\nu)\beta^2 n^2 \kappa + \beta^2\kappa^3 \qquad L_{21} = L_{12}$$

$$L_{22} = -\Omega^2 + \frac{1}{2}(1-\nu)\kappa^2 + n^2 + \frac{3}{2}(1-\nu)\beta^2\kappa^2 \qquad L_{23} = +n + \frac{1}{2}(3-\nu)n\beta^2\kappa^2$$

$$L_{31} = -L_{13} \qquad L_{32} = -L_{23} \qquad L_{33} = -\Omega^2 + 1 + \beta^2\left(\left(\kappa^2 + n^2\right)^2 + 1 - 2n^2\right) - \mathcal{F}$$

The nondimensional fluid loading term $\mathcal{F}$ is given by

$$\mathcal{F} = \Omega^2 \left(\frac{\rho_f}{\rho_s}\right)\left(\frac{h}{a}\right)^{-1} \frac{\mathrm{J}_n(\alpha)}{\alpha \mathrm{J}_n'(\alpha)} \tag{6.7}$$

where ρ_s is the density of the shell material. As noted by Fuller (1983), $\mathcal{F}$ is an even function of α and thus the fluid loading is independent of the sign of the square root in equation (6.4). This feature will later be seen to simplify the solution of the forced response of the system, as it ensures a particular integrand is single valued.

The two following sections present the response of the coupled system to two fundamentally different forms of excitation, namely a point force at the shell wall and a monopole in the interior fluid. While there is a fundamental difference between the two types of excitation, the solution method is the same for both cases: a nondimensional forcing is implemented in the forced equations of motion. When solving the equations of motion, the response in each of the coordinate directions includes a wavenumber integral. In the present thesis, the wavenumber integral is solved using the method of residues, but other integration methods could alternatively be used. With the method of residues, the modal response of both the shell and the fluid is formulated as a sum involving the wavenumbers of free propagation in the coupled system.

6.1.2 Point force excitation of the shell

The presentation in this section is split into two subsections. The first subsection presents in some detail how to predict the vibroacoustic response when the shell is excited by a radial point force. The second subsection states the results for tangential and axial excitation of the shell, since the steps involved in the derivation are exactly the same as for the radial point force.

6.1.2.1 Radial point force excitation

According to equation (5.7), a radial point force F^r (with dimension of force) applied at the surface of the shell, can be specified as a nondimensional force distribution on the shell (using the same normalisation procedure as in section 6.1.1):

$$\tilde{E}^r(s,\theta) = \frac{F^r}{c_L^2 \rho_s h a}\delta(\theta-\theta_o)\delta(s-s_o) = \frac{\Omega^2}{\omega^2}\frac{F^r}{\rho_s h a^3}\delta(\theta-\theta_o)\delta(s-s_o) \tag{6.8}$$

The r superscript will be used in what follows to denote the response to a radial point force.

As the circumferential wavenumbers are discrete and the axial wavenumbers are continuous, the delta functions of equation (6.8) may be expressed as

$$\begin{aligned}\delta(\theta-\theta_o) &= \frac{1}{2\pi}\sum_{n=0}^{\infty}\varepsilon_n \cos(n(\theta-\theta_o)) \\ \delta(s-s_o) &= \frac{1}{2\pi}\int_{-\infty}^{\infty} e^{i\kappa(s-s_o)}\mathrm{d}\kappa\end{aligned} \tag{6.9}$$

Using this, the radial point force can then be described in the wavenumber domain as

$$\tilde{E}^r = \sum_{n=0}^{\infty}\int_{-\infty}^{\infty}\varepsilon_n \frac{\Omega^2 F^r}{4\pi^2\omega^2\rho_s h a^3}\cos(n(\theta-\theta_o))e^{i\kappa(s-s_o)}\mathrm{d}\kappa \tag{6.10}$$

revealing the point force as an infinite sum of ring forces with increasing circumferential mode order. Combining this result with the modal representation of the displacements from equation (6.1), the spectral equations of motion for a fluid-filled pipe excited by an externally applied radial point force can be formulated and the solution is

$$\begin{bmatrix}\tilde{U}_n^r \\ \tilde{V}_n^r \\ \tilde{W}_n^r\end{bmatrix} = \begin{bmatrix}I_{11} & I_{12} & I_{13} \\ I_{21} & I_{22} & I_{23} \\ I_{31} & I_{32} & I_{33}\end{bmatrix}\begin{bmatrix}0 \\ 0 \\ \frac{\Omega^2 F^r}{2\pi\omega^2\rho_s h a^3}\end{bmatrix} \tag{6.11}$$

where matrix I is the inverse of the L-matrix in equation (6.6). The spectral displacement amplitude of each of the directions of motion can be extracted using standard matrix algebra operations,

$$\tilde{U}_n^r = \frac{\Omega^2 F^r}{2\pi\omega^2\rho_s h a^3} I_{13} \tag{6.12}$$

$$\tilde{V}_n^r = \frac{\Omega^2 F^r}{2\pi\omega^2\rho_s h a^3} I_{23} \tag{6.13}$$

$$\tilde{W}_n^r = \frac{\Omega^2 F^r}{2\pi\omega^2\rho_s h a^3} I_{33} \tag{6.14}$$

where the element I_{pq} of the inverted matrix are found using matrix algebra; e.g. the term I_{33} is given by

$$I_{33} = \frac{L_{11}L_{22} - L_{12}L_{21}}{\det(L)} \tag{6.15}$$

Equation (6.14) can be re-substituted into equation (6.1) and application of the inverse transform gives the nondimensional radial displacement in response to a radial point force for a particular mode as

$$\frac{\tilde{w}_n^r(s,\theta)}{a} = \frac{\varepsilon_n \Omega^2 F^r}{4\pi^2 \omega^2 \rho_s h a^3} \cos(n(\theta - \theta_o)) \int_{-\infty}^{\infty} I_{33} e^{i\kappa(s-s_o)} \mathrm{d}\kappa \tag{6.16}$$

This integral in the wavenumber domain can be evaluated numerically using a number of different techniques. In an early paper Fuller (1981) suggested integration using the method of residues, which is a complex integration method. In a later paper, Fuller (1984) showed that the integration could be done straightforwardly, integrating along the real axis. Xu and Zhang (1998) used the same approach, except that the integration was performed along the imaginary axis. Xu and Zhang (1998) have shown that the different integration techniques converge numerically, and they therefore all are usable for this purpose.

For the numerical evaluation of a single integral, the method of residues is relatively time consuming, as it requires the wavenumbers of free propagation of the coupled system to be identified before the integration, while either of the two other integration techniques performs the integration straight away. The method of residues is nonetheless chosen for the present thesis, as it uses a very efficient algorithm once a table of free wavenumbers is established, while the other methods rely on direct evaluation of every single integral. The table of free wavenumbers is calculated for each different coupled shell-fluid configuration (geometry and material properties for the shell and fluid) and then stored for later use, as explained in section 6.2.1.

The denominator of equation (6.15) suggests the complex integral of equation (6.16) can be evaluated by using the method of residues for simple poles (Kreyzig 1998). The residue theorem (Kreyzig 1998) states that the integral of a given form of complex functions is the sum of the singular points inside a simple closed path, i.e.

$$\oint_C f(z)dz = 2\pi i \sum_{j=1}^{k} \mathrm{Res}\, f(z = z_j) \tag{6.17}$$

where the function $f(z) = p(z)/q(z)$, has k simple poles at $z = z_j$. The residue is then $\mathrm{Res}\, f(z_j) = p(z_j)/q'(z_j)$.

Assuming $s - s_o$ is positive, equation (6.16) can be expressed using the method of residues as

$$\frac{\tilde{w}_n^r(s,\theta)}{a} = i\frac{\varepsilon_n \Omega^2 F^r}{2\pi \omega^2 \rho_s h a^3} \cos(n(\theta - \theta_o)) \sum_{b=1}^{\infty} \mathrm{Res}_{nb}^r e^{i\kappa_{nb}(s-s_o)} \qquad (s > s_o) \tag{6.18}$$

where κ_{nb} is the wavenumber giving rise to the b'th singular point of the L-matrix in equation (6.6) with given n and Ω. In what follows, a related sequences of wavenumbers as a function of frequency is referred to as a branch, because when plotted in a dispersion plot the wavenumbers have a characteristic appearance, see e.g. figure 7.2 on page 75.

The residue in equation (6.18) is defined as

$$\mathrm{Res}^r_{nb} = \left[\frac{L_{11}L_{22} - L_{12}L_{21}}{\partial \det(L)/\partial\kappa}\right]_{nb} \tag{6.19}$$

To ensure that only the poles related to the positive direction of propagation are included in the integration of equation (6.16), the integration path is chosen as a semicircle of infinite radius in the upper complex wavenumber half plane ($\mathrm{Im}(\kappa) > 0$). Conceptually, adding an infinitesimal amount of damping will shift any real poles of equation (6.16) into the complex domain by introduction of a infinitesimal positive imaginary part. The damping will not affect the result if it is chosen to be small enough, but it will move the poles connected to propagation in the positive z-direction into the upper wavenumber half plane, and vice versa for the negative axial direction. The poles contained in the integration path will be the zeros of the determinant of the matrix L; i.e. the free wavenumbers from the dispersion equation,

$$\det(L) = 0 \tag{6.20}$$

By summing equation (6.18) over all circumferential modes, the nondimensional radial displacement due to a radial point force can be expressed in the compact form

$$\frac{\tilde{w}^r(\theta, s)}{a} = \sum_{n=0}^{\infty}\sum_{b=1}^{\infty} W^r_{nb}\cos(n(\theta - \theta_o))e^{i\kappa_{nb}(s-s_o)} \qquad (s > s_o) \tag{6.21}$$

where the modal displacement amplitude W^r_{nb} follows from equation (6.18) as

$$W^r_{nb} = i\frac{\varepsilon_n\Omega^2 F^r}{2\pi\omega^2\rho_s h a^3}\mathrm{Res}^r_{nb} \tag{6.22}$$

Similarly, the displacements in the axial and tangential directions, respectively, can be formulated as

$$\frac{\tilde{u}^r(a, \theta, s)}{a} = \sum_{n=0}^{\infty}\sum_{b=1}^{\infty} U^r_{nb}\cos(n(\theta - \theta_o))e^{i(\kappa_{nb}(s-s_o)+\pi/2)} \qquad (s > s_o) \tag{6.23}$$

$$\frac{\tilde{v}^r(a, \theta, s)}{a} = \sum_{n=0}^{\infty}\sum_{b=1}^{\infty} V^r_{nb}\sin(n(\theta - \theta_o))e^{i\kappa_{nb}(s-s_o)} \qquad (s > s_o) \tag{6.24}$$

The axial and tangential displacement amplitudes are found using their respective ratios to the radial displacement, according to equations (6.12)-(6.14). Thus, $U^r_{nb} = R_{a,nb}W^r_{nb}$ and $V^r_{nb} = R_{t,nb}W^r_{nb}$, where the axial amplitude ratio is defined as

$$R_{a,nb} = \frac{U^r_{nb}}{W^r_{nb}} = \frac{I_{13}}{I_{33}} = \frac{L_{12}L_{23} - L_{13}L_{22}}{L_{11}L_{22} - L_{12}L_{21}} \tag{6.25}$$

and the tangential amplitude ratio is defined as

$$R_{t,nb} = \frac{V^r_{nb}}{W^r_{nb}} = \frac{I_{23}}{I_{33}} = \frac{L_{13}L_{21} - L_{23}L_{11}}{L_{11}L_{22} - L_{12}L_{21}} \tag{6.26}$$

Finally, using the same methodology, the pressure inside the shell is expressed as

$$\tilde{p}^r(r,\theta,s) = \sum_{n=0}^{\infty}\sum_{b=1}^{\infty} P^r_{nb}\cos(n(\theta-\theta_o))J_n(\alpha_{nb}r)e^{i\kappa_{nb}(s-s_o)} \qquad (s > s_o) \tag{6.27}$$

and equations (6.5) and (6.22) give the pressure amplitude as

$$P^r_{nb} = \frac{a^2\omega^2\rho_f}{\alpha_{nb}\mathrm{J}'_n(\alpha_{nb})}W_{nb} = i\frac{\varepsilon_n\Omega^2F^r}{2\pi ha}\frac{\rho_f}{\rho_s}\frac{\mathrm{Res}^r_{nb}}{\alpha_{nb}J'_n(\alpha_{nb})} \tag{6.28}$$

6.1.2.2 Axial and tangential point force excitation

The modal response produced by a tangential point force F^θ or a axial point force F^a located at (θ_o, s_o) (the superscripts refer to the direction of excitation) can be derived using the same methodology as for the radial point force excitation.

After summation over modes, the total radial displacement in response to a tangential or axial point force can be written as, respectively

$$\frac{\tilde{w}^\theta(a,\theta,s)}{a} = \sum_{n=0}^{\infty}\sum_{b=1}^{\infty} W^\theta_{nb}\cos(n(\theta-\theta_o))e^{i\kappa_{nb}(s-s_o)} \qquad (s > s_o) \tag{6.29}$$

$$\frac{\tilde{w}^a(a,\theta,s)}{a} = \sum_{n=0}^{\infty}\sum_{b=1}^{\infty} W^a_{nb}\cos(n(\theta-\theta_o))e^{i\kappa_{nb}(s-s_o)} \qquad (s > s_o) \tag{6.30}$$

The modal displacement amplitudes will have the same form as the displacement amplitude for radial excitation in equation (6.22), apart from the residue term. The tangential and axial residues are defined as, respectively

$$\mathrm{Res}^\theta_{nb} = -\left[\frac{L_{11}L_{33} - L_{31}L_{31}}{\partial\det(L)/\partial\kappa}\right]_{nb} \tag{6.31}$$

$$\mathrm{Res}^a_{nb} = \left[\frac{L_{22}L_{33} - L_{23}L_{32}}{\partial\det(L)/\partial\kappa}\right]_{nb} \tag{6.32}$$

The displacements in the other directions can be derived from the radial displacements using the amplitude ratios of equations (6.25) and (6.26).

The pressure response for these two directions of point excitation can be derived using the same methodology as in equations (6.27) and (6.28).

6.1.3 Monopole excitation of the interior fluid

The response of the coupled system when excited by a fluid monopole can be solved using the same methodology as for the point force. The steps in the solution process correspond closely to the point force: first the excitation is defined in nondimensional

form and the equations of motion are solved for each of the coordinate directions. Then the response expressed is in summation form using the method of residues.

In accordance with equation (5.17), a monopole source of strength S_o (with dimension of force per length) located in located in the fluid at $(r_{o,dim}, \theta_o, z)$ has a nondimensional free pressure field of the form

$$\tilde{p}^m(r,\theta,s) = \frac{S_o}{c_L^2 \rho_s h} \frac{e^{i(\kappa_f \frac{D}{a} - \omega t)}}{\frac{D}{a}} = \frac{\Omega^2}{\omega^2} \frac{S_o}{\rho_s h a^2} \frac{e^{i(\kappa_f \frac{D}{a} - \omega t)}}{\frac{D}{a}} \tag{6.33}$$

where superscript m refers to monopole excitation; D is the distance from the monopole to the receiver point; and $\kappa_f = \omega a / c_f$ is the nondimensional fluid acoustic wavenumber. See section 6.1.1) for the normalisation procedure.

Following the same arguments presented in section 5.3, the solution to the spectral equations of motion can be written as

$$\begin{bmatrix} \tilde{U}_n^m \\ \tilde{V}_n^m \\ \tilde{W}_n^m \end{bmatrix} = \begin{bmatrix} I_{11} & I_{12} & I_{13} \\ I_{21} & I_{22} & I_{23} \\ I_{31} & I_{32} & I_{33} \end{bmatrix} \begin{bmatrix} 0 \\ 0 \\ 2\frac{\varepsilon_n \Omega^2 S_o}{\rho_s h \omega^2 a^2} \frac{\mathrm{J}_n(\alpha r_o)}{\alpha \mathrm{J}_n'(\alpha)} \end{bmatrix} \tag{6.34}$$

where $r_o = r_{o,dim}/a$ is the nondimensional radial source position.

Matrix algebra gives the radial displacement amplitude as

$$\tilde{W}_n^m = \frac{2\varepsilon_n \Omega^2 S_o}{\rho_s h \omega^2 a^2} \frac{\mathrm{J}_n(\alpha r_o)}{\alpha \mathrm{J}_n'(\alpha)} I_{33} \tag{6.35}$$

where I_{33} is defined in equation (6.15). Application of the inverse transform gives the radial displacement for a particular mode n as

$$\frac{\tilde{w}_n^m(\theta,s)}{a} = \frac{\varepsilon_n \Omega^2 S_o}{\pi \rho_s h \omega^2 a^2} \int_{-\infty}^{\infty} \cos(n(\theta - \theta_o)) \frac{\mathrm{J}_n(\alpha r_m)}{\alpha \mathrm{J}_n'(\alpha)} I_{33} e^{i\kappa(s-s_o)} \mathrm{d}\kappa \tag{6.36}$$

The discussion regarding the method of residues from the last section also applies here. However, it should be noted that although the denominator of equation (6.36) is more complicated than the corresponding equation (6.18) in the case of the point force, it still has simple poles. The method of residues can therefore be applied. By integration of equation (6.36) using the method of residues, the radial modal displacement in response to a fluid monopole can therefore be written as

$$\frac{\tilde{w}_n^m(\theta,s)}{a} = \frac{i2\varepsilon_n \Omega^2 S_o}{\rho_s h \omega^2 a^2} \cos(n(\theta - \theta_o)) \sum_{b=1}^{\infty} \mathrm{Res}_{nb}^m e^{i\kappa_{nb}(s-s_o)} \qquad (s > s_o) \tag{6.37}$$

where the residue connected to the fluid monopole is

$$\mathrm{Res}_{nb}^m = \left[\frac{\mathrm{J}_n(\alpha r_o)(L_{11}L_{22} - L_{12}L_{21})}{\partial(\alpha \mathrm{J}_n'(\alpha) \det(L))/\partial\kappa} \right]_{nb} \tag{6.38}$$

After summation over modes, the nondimensional radial displacement in response to a fluid monopole can be written as

$$\frac{\tilde{w}^m(a,\theta,s)}{a} = \sum_{n=0}^{\infty}\sum_{b=1}^{\infty} W_{nb}^m \cos(n(\theta-\theta_o))e^{i\kappa_{nb}(s-s_o)} \qquad (s>s_o) \tag{6.39}$$

with all other terms collected in the radial modal displacement amplitude W_{nb}^m:

$$W_{nb}^m = \frac{2i\varepsilon_n\Omega^2 S_o}{\rho_s h\omega^2 a^2}\mathrm{Res}_{nb}^m \tag{6.40}$$

As in equations (6.23) and (6.24), the radial and tangential displacements can be formulated as, respectively

$$\frac{\tilde{u}^m(a,\theta,s)}{a} = \sum_{n=0}^{\infty}\sum_{b=1}^{\infty} U_{nb}^m \cos(n(\theta-\theta_o))e^{i(\kappa_{nb}(s-s_o)+\pi/2)} \qquad (s>s_o) \tag{6.41}$$

$$\frac{\tilde{v}^m(a,\theta,s)}{a} = \sum_{n=0}^{\infty}\sum_{b=1}^{\infty} V_{nb}^m \sin(n(\theta-\theta_o))e^{i\kappa_{nb}(s-s_o)} \qquad (s>s_o) \tag{6.42}$$

where the axial and tangential displacement amplitudes are found as before using the displacement ratios in equations (6.25) and (6.26): $U_{nb}^m = R_{a,nb}W_{nb}^m$ and $V_{nb}^m = R_{t,nb}W_{nb}^m$.

Finally, the pressure inside the shell due to a point monopole in the interior fluid is expressed as

$$\tilde{p}^m(r,\theta,s) = \sum_{n=0}^{\infty}\sum_{b=1}^{\infty} P_{nb}^m \cos(n(\theta-\theta_o))J_n(\alpha_{nb}r)e^{i\kappa_{nb}(s-s_o)} \qquad (s>s_o) \tag{6.43}$$

and equations (6.5) and (6.40) give the modal pressure amplitude as

$$P_{nb}^m = \frac{a^2\omega^2\rho_f}{\alpha_{nb}\mathrm{J}_n'(\alpha_{nb})}W_{nb} = i\frac{2\varepsilon_n\Omega^2 S_o}{h\alpha_{nb}J_n'(\alpha_{nb})}\frac{\rho_f}{\rho_s}\mathrm{Res}_{nb}^m \tag{6.44}$$

6.1.4 Power flow formulation

Each branch couples the 3 directions of motion (u, v and w) and the pressure field inside the shell in a different way, but in essence excitation in the fluid will always excite vibrations in the wall and vice versa. This leads to a distribution of vibrational energy between the shell and the contained fluid.

The total power flow of the coupled system for a given free-wave branch number b can be found as the sum of the power carried by each of the three fundamental types of vibration in the structure (flexure, extension and torsion) and the power carried by the fluid,

$$P_\kappa = P_{be} + P_{ex} + P_{to} + P_f \tag{6.45}$$

It should be noted that it is not possible to quantify the power flow in the structure and the fluid individually, as the actual distribution of power between the shell and the fluid is spatially dependent.

In this section, it is shown how the total power flow can be quantified. To avoid too much confusion by the complications introduced from cross-terms, the power flow from a single branch (i.e. given n and b) is presented first. This result is then expanded to include all branches for a given n, and finally the total power flow is presented. Before this, power flow is defined in the next subsection.

6.1.4.1 Definition of power flow

Power is defined as the rate at which work is done. For example, the instantaneous structural power input to a system from a point force is given by the relationship

$$P_I = F_I V_I \tag{6.46}$$

where F_I and V_I are the physical instantaneous values of force and velocity at the input point. For steady-state excitation, the average power transmission or power flow is more useful.

For complex harmonic excitation, $F_i = F\mathrm{e}^{-i\omega t}$ and $V_i = V\mathrm{e}^{-i\omega t}$, the time average structural power flow can be written as

$$\langle P \rangle = \frac{1}{T}\int_0^T \mathrm{Re}(F\mathrm{e}^{-i\omega t})\mathrm{Re}(V\mathrm{e}^{-i\omega t})dt = \frac{1}{2}\mathrm{Re}(FV^*) \tag{6.47}$$

where the asterisk * denotes complex conjugate; Re denotes the real part of a complex quantity; the period $T = 2\pi/\omega$ and $\langle \quad \rangle$ indicates average with respect to time. As all the following equations are time averaged, the brackets for time averaging are left out.

The same methodology can be applied to calculate the time averaged power flow due to structural rotation (involving rotational velocity and moment) and the time averaged power flow in the fluid (involving fluid pressure and velocity).

6.1.4.2 Force and moment resultants in the shell

If the input force and response velocity of any structural point can be retrieved, then the time averaged power input of that point can be calculated using the above expressions. This fact will be used later as a check on the overall power balance for a fluid-filled pipe. However, the structural power density (power flow per unit circumference across any pipe cross-section) can be expressed in a similar manner by combining the shear force (per unit circumference) with the displacement in the corresponding direction, and the bending moment with the shell rotation. The resulting power flow expressions for any cross-section of the pipe, expressed in modal form, will be used extensively in what follows. Details of the derivation are given below.

According to Flügge's shell theory, the force resultants in the coordinate directions at any point on the shell can be formulated by integration through the thickness of the shell (Flügge 1962). All the following resultants are per unit length of circumference, i.e. they have to be integrated around the circumference of the shell.

The bending moment in the z-direction is in Flügge's formulation (Flügge 1962) given by

$$M_z = K\left(\frac{\partial^2 w}{\partial z^2} + \frac{\nu}{a^2}\frac{\partial^2 w}{\partial \theta^2} - \frac{1}{a}\frac{\partial u}{\partial z} - \frac{\nu}{a}\frac{\partial v}{\partial \theta}\right) \tag{6.48}$$

where $K = Eh^3/12(1-\nu^2)$ is the bending stiffness. The transverse shear force is given by

$$\begin{aligned} Q_z = -K&\left(\frac{\partial^3 w}{\partial z^3} + \frac{\nu}{a^2}\frac{\partial^3 w}{\partial z \partial \theta^2} - \frac{1}{a}\frac{\partial^2 u}{\partial z^2} - \frac{\nu}{a^2}\frac{\partial^2 v}{\partial \theta \partial z}\right) \\ +K(1-\nu)&\left(\frac{1}{a^2}\frac{\partial^3 w}{\partial z \partial \theta^2} + \frac{1}{2a^3}\frac{\partial^2 u}{\partial \theta^2} - \frac{1}{2a^2}\frac{\partial^2 v}{\partial z \partial \theta}\right) \end{aligned} \tag{6.49}$$

The torsional shear force is given by

$$N_{z\theta} = \frac{D(1-\nu)}{2}\left(\frac{1}{a}\frac{\partial u}{\partial z} + \frac{\partial v}{\partial z}\right) + \frac{K(1-\nu)}{2a^2}\left(\frac{\partial v}{\partial z} - \frac{\partial^2 w}{\partial z \partial \theta}\right) \tag{6.50}$$

where $D = Eh/(1-\nu^2)$ is the membrane stiffness. Finally the axial force is given by

$$N_z = \frac{D}{a}\left(a\frac{\partial u}{\partial z} + \nu\frac{\partial v}{\partial \theta} + \nu w\right) - \frac{K}{a}\frac{\partial^2 w}{\partial z^2} \tag{6.51}$$

6.1.4.3 Power flow for a given branch

For a branch with given n and b, there are no cross branch contributions to the power flow and the power flow can therefore be separated in the individual parts of equation (6.45) without introducing any cross terms.

Assuming the excitation to be symmetric about $\theta = 0$ and $s_o = 0$, the displacements of the shell can be formulated as

$$\begin{aligned} \tilde{u}_{nb} &= aU_{nb}\cos(n\theta)e^{i(\kappa_{nb}s+\pi/2)} \\ \tilde{v}_{nb} &= aV_{nb}\sin(n\theta)e^{i\kappa_{nb}s} \\ \tilde{w}_{nb} &= aW_{nb}\cos(n\theta)e^{i\kappa_{nb}s} \end{aligned} \tag{6.52}$$

where the displacement amplitudes U_{nb}, V_{nb} and W_{nb} are determined for point excitation in sections 6.1.2 and 6.1.3. The complex conjugates of the displacements are

$$\begin{aligned} \tilde{u}^*_{nb} &= aU^*_{nb}\cos(n\theta)e^{-i(\kappa^*_{nb}s+\pi/2)} \\ \tilde{v}^*_{nb} &= aV^*_{nb}\sin(n\theta)e^{-i\kappa^*_{nb}s} \\ \tilde{w}^*_{nb} &= aW^*_{nb}\cos(n\theta)e^{-i\kappa^*_{nb}s} \end{aligned} \tag{6.53}$$

The flexural (or bending) part of the power flow is found as the circumferential integral of the power density (structural intensity). It has a contribution from rotation of the shell element as well as from radial flexure, thus

$$P_{be} = \frac{1}{2}\int_0^{2\pi} \left[\mathrm{Re}(M_z \dot{w}'^*) + \mathrm{Re}(Q_z \dot{w}^*)\right] a \mathrm{d}\theta \tag{6.54}$$

where the dot implies differentiation with respect to time and the prime implies differentiation with respect to the axial coordinate; thus $\dot{w}' = \partial^2 w/\partial t \partial z$ is the angular rotation of the shell element in the z-direction. Inserting the displacements in the force and moment resultants, multiplying by the complex conjugates of the displacements and integrating around the circumference produces the power flow in a single branch due to flexure of the shell:

$$\begin{aligned} P_{be,nb} = -\frac{1}{2}\mathrm{Re}\Bigg(\eta_n \frac{\pi\omega E h^3 W_{nb}^*}{24(1-\nu^2)} \big[& 2\kappa^2\kappa_{nb}^* W_{nb} + 2\nu n^2 \kappa_{nb}^* W_{nb} - 2\kappa_{nb}\kappa_{nb}^* U_{nb} + 2\nu n \kappa_{nb}^* V_{nb} - 2\kappa_{nb}^3 W_{nb} \\ & + 2\kappa_{nb}^2 U_{nb} - \nu n \kappa_{nb} V_{nb} - 2n^2 \kappa_{nb} W_{nb} - n^2 U_{nb} - n\kappa_{nb} V_{nb} + \nu n^2 U_{nb} \big] e^{i(\kappa_{nb} - \kappa_{nb}^*)s} \Bigg) \end{aligned} \tag{6.55}$$

where $\eta_n = 2$ for $n = 0$ and $\eta_n = 1$ otherwise.

Likewise the extensional and torsional contributions to the power flow can be found as, respectively

$$\begin{aligned} P_{ex} =& \frac{1}{2}\int_0^{2\pi} \mathrm{Re}(N_z \dot{u}^*) a \mathrm{d}\theta \\ =& \frac{1}{2}\mathrm{Re}\Bigg(\eta_n \frac{\pi\omega E h a^2 U_{nb}^*}{(1-\nu^2)} \big[\kappa_{nb} U_{nb} - \nu n V_{nb} - \nu W_{nb} \\ & - \frac{h^2}{12a^2}\kappa_{nb}^2 W_{nb} \big] e^{i\kappa_{nb} - \kappa_{nb}^*)s} \Bigg) \end{aligned} \tag{6.56}$$

$$\begin{aligned} P_{to} =& -\frac{1}{2}\int_0^{2\pi} \mathrm{Re}(N_{z\theta} \dot{v}^*) a \mathrm{d}\theta \\ =& -\frac{1}{2}\mathrm{Re}\Bigg(\eta_n \frac{\pi\omega E h V_{nb}^*}{24(1+\nu)} \big[h^2 n \kappa_{nb} W_{nb} - 12a^2 n U_{nb} \\ & + 12a^2 \kappa_{nb} V_{nb} + h^2 \kappa_{nb} V_{nb} \big] e^{i(\kappa_{nb} - \kappa_{nb}^*)s} \Bigg) \end{aligned} \tag{6.57}$$

The expressions for the power flow are conveniently simplified by introducing the ratios of the displacement amplitudes defined in equations equations (6.25) and (6.26): $U_{nb} = R_{a,nb} W_{nb}$ and $V_{nb} = R_{t,nb} W_{nb}$. Using these substitutions, the total structural power flow

from a single branch is

$$P_{s,\kappa} = -\frac{1}{2}\mathrm{Re}\Bigg(\eta_n \frac{\pi\omega E W_{nb} W^*_{nb}}{(1-\nu^2)}\Bigg[\frac{h^3}{24}(2\kappa^2_{nb}\kappa^*_{nb} + 2\nu n^2\kappa^*_{nb} - 2\kappa_{nb}\kappa^*_{nb}R_{a,nb} + 2\nu n\kappa^*_{nb}R_{t,nb} \\ - 2\kappa^3_{nb} + 2\kappa^2_{nb}R_{a,nb} - \nu n\kappa_{nb}R_{t,nb} - 2n^2\kappa_{nb} - n^2R_{a,nb} - n\kappa_{nb}R_{t,nb} + \nu n^2R_{a,nb}) \\ - h^3\frac{R^*_{t,nb}(\nu-1)}{24}(n\kappa_{nb}W_{nb} - 12\frac{a^2}{h^2}nR_{a,nb} + 12\frac{a^2}{h^2}\kappa_{nb}R_{t,nb} + \kappa_{nb}R_{t,nb}) \\ + \frac{hR^*_{a,nb}}{12}(12a^2\kappa_{nb}R_{a,nb} - 12a^2\nu nR_{t,nb} - 12a^2\nu - h^2\kappa^2_{nb})\Bigg]e^{i(\kappa_{nb}-\kappa^*_{nb})s}\Bigg) \tag{6.58}$$

Finally, to obtain the total power flow for a single branch, the power flow carried by the interior fluid needs to be added. The fluid power flow is found by integration of the acoustic intensity over the pipe cross-section, as

$$P_f = \frac{1}{2}\int_0^{2\pi}\int_0^1 \mathrm{Re}(pu^*)r\mathrm{d}r\mathrm{d}\theta \tag{6.59}$$

where p is the pressure and u is the acoustic particle velocity in the axial direction. For symmetric excitation, the pressure at an observation point (r, θ, s) is expressible as

$$\tilde{p}_{nb}(r,\theta,s) = P_{nb}\cos(n\theta)\mathrm{J}_n(\alpha_{nb}r)e^{i\kappa s} \tag{6.60}$$

where the pressure amplitude P_{nb} is determined for point excitation in sections 6.1.2 and 6.1.3. The complex conjugate of the particle velocity can be found from the momentum relation as

$$\tilde{u}^*(r,\theta,s) = -\frac{1}{ia\rho_f\omega}\frac{\partial\tilde{p}^*}{\partial s} = -\frac{1}{ia\rho_f\omega}P^*_{nb}\cos(n\theta)\mathrm{J}_n(\alpha^*_{nb}r)(-i\kappa^*_{nb})e^{-i\kappa^*_{nb}s} \tag{6.61}$$

Using this, it is possible to calculate the fluid-borne power flow as

$$P_f = \frac{1}{2}\mathrm{Re}\left(\frac{\pi}{a\omega\rho_f}\eta_n P_{nb}P^*_{nb}\kappa^*_{nb}e^{i(\kappa_{nb}-\kappa^*_{nb})s}\int_0^1 \mathrm{J}_n(\alpha_{nb}r)\mathrm{J}_n(\alpha^*_{nb}r)r\mathrm{d}r\right) \tag{6.62}$$

The integral involving the Bessel functions is called Lommel's integral (Kreyzig 1998) and the solution is

$$\int z\mathrm{J}_p(\alpha z)\mathrm{J}_p(\beta z)\mathrm{d}z \\ = \frac{1}{\alpha^2-\beta^2}\Big[\beta z\mathrm{J}_p(\alpha z)\mathrm{J}_{p-1}(\beta z) - \alpha z\mathrm{J}_{p-1}(\alpha z)\mathrm{J}_p(\beta z)\Big] \qquad (\alpha \neq \beta) \tag{6.63}$$

and

$$\int z\mathrm{J}^2_p(\alpha z)\mathrm{d}z = \frac{1}{2}z^2\Big[\mathrm{J}^2_p(\alpha z) - \mathrm{J}_{p-1}(\alpha z)\mathrm{J}_{p+1}(\alpha z)\Big] \tag{6.64}$$

The total power flow carried by a single branch can be found by summing the structural contribution from equation (6.58) and the fluid contribution from equation (6.55).

6.1.4.4 Modal power flow

For a circumferential mode n, the vibroacoustic response consists of the combined response of all branches for that mode. In the case of a fluid-filled shell, there is an infinite number of branches, as discussed in section 6.2. When more than one branch participates in the transport of energy, there will be cross couplings between the different branches that will also contribute to the energy transport. Therefore a simple summation of the power flow due to each of the branches will produce an incorrect total power flow, as it leaves out the power flow due to the cross couplings.

To account for this, all the branches need to be included in the power flow formulation. For given n, the total modal displacement can be formulated as

$$\begin{aligned}
\tilde{u}_n &= \sum_{b=1}^{\infty} aU_{nb}\cos(n\theta)e^{i(\kappa_{nb}s+\pi/2)} \\
\tilde{v}_n &= \sum_{b=1}^{\infty} aV_{nb}\sin(n\theta)e^{i\kappa_{nb}s} \\
\tilde{w}_n &= \sum_{b=1}^{\infty} aW_{nb}\cos(n\theta)e^{i\kappa_{nb}s}
\end{aligned} \tag{6.65}$$

Substituting the displacements and their corresponding complex conjugates in the total structural power flow equation from the previous section produces the power flow for a given n, including all cross-term contributions. Using the relation

$$\sum_i (a_i)\sum_j (b_j) = \sum_i \sum_j (a_i b_j) \tag{6.66}$$

the total structural power flow for a given circumferential mode can be written as

$$\begin{aligned}
P_{s,n} = -\frac{1}{2}\mathrm{Re}\Bigg(\eta_n \frac{\pi\omega E}{(1-\nu^2)} \sum_{b=1}^{\infty}\sum_{c=1}^{\infty} W_{nb}W_{nc}^* \Bigg[\\
\frac{h^3}{24}(2\kappa_{nb}^2\kappa_{nc}^* + 2\nu n^2\kappa_{nc}^* - 2\kappa_{nb}\kappa_{nc}^* R_{a,nb} + 2\nu n\kappa_{nc}^* R_{t,nb} - 2\kappa_{nb}^3 + 2\kappa_{nb}^2 R_{a,nb} \\
- \frac{R_{t,nc}^*(\nu-1)}{24}(h^2 n\kappa_{nb} - 12a^2 nR_{a,nb} + 12a^2\kappa_{bc}R_{t,nb} + h^2\kappa_{nb}R_{t,nb}) \\
- \nu n\kappa_{nb}R_{t,nb} - 2n^2\kappa_{nb} - n^2 R_{a,nb} - n\kappa_{nb}R_{t,nb} + \nu n^2 R_{anb}) \\
+ \frac{hR_{a,nc}^*}{12}(12a^2\kappa_{nb}R_{a,nb} - 12a^2\nu nR_{t,nb} - 12a^2\nu - h^2\kappa_{nb}^2)\Bigg] e^{i(\kappa_{nb}-\kappa_{nc}^*)s}\Bigg)
\end{aligned} \tag{6.67}$$

and the corresponding fluid-borne power flow is

$$P_{f,n} = \frac{1}{2}\mathrm{Re}\left(\frac{\pi}{a\omega\rho_f}\eta_n \sum_{b=1}^{\infty}\sum_{c=1}^{\infty} P_{nb}P_{nc}^*\kappa_{nc}^* \int_0^1 J_n(\alpha_{nb}r)J_n(\alpha_{nc}^* r)e^{i(\kappa_{nb}-\kappa_{nc}^*)s} r\mathrm{d}r\right) \tag{6.68}$$

It should be noted that the above power flow expressions do not imply any restrictions on the branches. Therefore these expressions are valid in the vibroacoustic near field,

as well as in the far field (as long as the waves are progressive, i.e. away from the source only). This can e.g. prove useful when analysing the near-field behaviour of a given point source, where vibrational energy is redistributed from evanescent branches in the near field to the propagating branches in the far field. Unfortunately, time has not allowed any detailed examination of this phenomenon, but it may be important for the industrial application where radiators are placed in the vibroacoustic near field of the source. If this is the case, then some surprising effects may occur, as the evanescent branches may play a significant role in the energy transfer to the radiator. This could be part of the explanation why the traditional noise control techniques to reduce noise transmission from the valve to the radiator fail in some situations.

6.1.4.5 Total power flow

The total power flow in one direction of propagation can be found as the sum over all circumferential modes of the combined structural and fluid power flows,

$$P_{tot} = \sum_{n=0}^{\infty} (P_{s,n} + P_{f,n}) \tag{6.69}$$

Is should be noted that in a lossless system, the power flow is the same across all cross sections. The input power flow is therefore the same as the transmitted power flow. This can be useful if the input power flow for some reason is impossible or difficult to quantify, as any quantification of e.g. the far field power flow then implies the quantification of the input power flow. This is also the case for the individual modal power flows, but not for the distributions of power flow between branches and between media. Fuller (1986) notes that while the total modal power flow remains constant at different axial positions, the distribution of power flow between the structure and the internal fluid varies with the axial position. The extent of this redistribution is both parameter and frequency dependent, but it has not been significant for any of the cases investigated in the present thesis.

6.2 Solution of the dispersion equation

The vibroacoustic response of the fluid-filled infinite pipe to various types of point input was given by solving the wavenumber integrals in sections 6.1.2 and 6.1.3 by the method of residues. This process introduced a summation over the free propagation wavenumbers of the coupled system. The solution of the dispersion equation, leading to the free wavenumbers needed for the forced response calculation, is discussed in detail below.

The dispersion equation was stated in section 6.1.2 as equation (6.20),

$$\det(L) = 0$$

It is not possible to find the free wavenumbers of a fluid-filled cylindrical shell analytically, and instead a mainly numerical solution technique will be employed, as discussed in the next subsection. The solutions of the dispersion equation can be divided into three different categories:

- Pure real roots
- Pure imaginary roots
- Complex roots.

The first two correspond to the usual type of wave in a lossless medium, where the phase and amplitude respectively change with distance; while the last one is a near field phenomenon, related to the local deflections of the shell in the close vicinity of a discontinuity, e.g. a forcing point. It is not caused by the coupling between the fluid and the shell, since the in vacuo shell equations exhibit the same behaviour.

Whereas the purely imaginary roots represent evanescent wave motion, which propagates no energy along the pipe, the other waves do carry energy along the pipe. In other areas of acoustics, complex wavenumbers usually imply a propagating wave which attenuates with distance from the source, i.e. it carries energy, some of which is dissipated through damping as it travels. However as the shells in the present thesis are considered lossless, there can be no energy lost through damping, so another explanation is needed for this phenomenon. When the equations for the coupled system are solved, the complex roots for the axial wavenumber occur in combinations of $\pm(\alpha \pm i\beta)_{nb}$. According to Fuller (1980), this corresponds to two pairs of complex roots, where a pair of complex roots $(\pm\alpha + i\beta)_{nb}$ can be interpreted as one wave propagating and decaying in the positive z-direction and another one that appears to propagate in the negative z-direction while still decaying in the positive z-direction. When combined with equal amplitudes for each wave, the pair represents an attenuated standing wave in the axial direction, not propagating any energy. Such pairs of waves are only excited near points of discontinuity, where they account for local shell deflections, without any net energy propagation along the axial direction.

It has already been mentioned that an infinite number of branches exist for each circumferential mode, corresponding to an infinite number of radial nodal points in the fluid along a radius of the shell. At low frequencies, most of these branches have a negligible effect on the vibroacoustic behaviour of the coupled system. During the parameter study in chapter 7, the effect of excluding these branches from the calculations was investigated. When calculating the input power flow at a point of excitation, all branches participate as discussed in the previous section. Leaving out branches therefore corresponds to leaving out input power flow, but this effect is purely theoretical. It was found in all cases that leaving out branches far from cuton had no effect on the vibroacoustic power input to the system, within the numerical resolution of Matlab. Therefore all branches having a nondimensional imaginary wavenumber of more than $10i$ were kept out of the calculations. In most cases, this corresponds to around three imaginary branches being included in the calculations.

A word of caution should perhaps be introduced at this point. As the combination of a solid shell and a contained fluid is a coupled system from a vibroacoustic point of view, it is not possible to separate the vibroacoustic response into a structural part and a fluid part. Any pressure fluctuations in the fluid will have some corresponding vibration in the shell wall and vice versa. Nonetheless, as will become evident later in this thesis, it is very difficult to explain the effect of some parameter appealing to a few simplifying concepts. Therefore expressions such as 'the fluid branch' may be used, but it should be kept in mind that no clear-cut distinction is really possible.

6.2.1 Numerical solution technique

A complete numerical solution of all the equations arising from the nondimensional matrix formulation in section 6.1 has been coded in Matlab. Owing to the use of the method of residues to evaluate the fluid loaded system response, all calculations are based on the free wavenumbers of the coupled system.

The free wavenumbers are found as roots to the dispersion equation (6.20), but as they are quite time-consuming to locate, they are stored and kept in a table for later use. This approach is quite slow for the first pass compared to e.g. finite element or boundary element methods (time measured in hours, using a 600 MHz Athlon equipped PC); but for subsequent calculations it is quite fast, using only a few seconds for a modal mobility calculation up to the ring frequency with a frequency resolution of 0.001 Ω. The numerical results in the present thesis were generated by first calculating the free wavenumbers for all the cases to be presented, using a few days of CPU time. Then all later calculations reused the free wavenumbers when needed, providing results fast.

The purely real and imaginary roots are found by a simple stepping technique, where pairs of (Ω, κ_{nb}) are found by setting Ω to the highest nondimensional frequency wanted and then making relatively small steps along the relevant axis (real or imaginary wavenumber) in order to find the roots of equation (6.20) with a numerical zero-finding solution algorithm. With this stepping technique, the Matlab based Newton-solver written by Kelley (1994) finds all real roots of the desired type without too much effort. Once the free wavenumbers are found at the maximum nondimensional frequency of interest, the wavenumbers are traced down through the nondimensional frequencies, using extrapolations of the roots already found. This ensures that the roots are found using only a few iterations and thus limiting the computational effort.

In the case of complex solutions, the same solution procedure is used, but here the main problem is to provide a reasonable starting guess to find the desired root. The solver used is globally convergent and will – if the function is just a little bit well behaved – always converge to a solution. If the starting guess is too far away from the wanted root, however, the chances are that the solution found is different from that wanted. A simple method to deal with this is to take advantage of the frequency-dependent properties of the fluid loading term. For the lowest desired Ω, a starting guess is found from the in vacuo solution, i.e. without any fluid loading. Using this guess as input to the Newton-solver, the root is found with relative ease, as the system is not too much

affected by the presence of a even a heavy internal fluid at low frequencies. Then when stepping up in Ω, extrapolation of the already established complex roots is used as a starting guess. If the steps are kept small enough, then the complex solution is traced like the purely real or imaginary ones.

Numerical problems always occur when one type of solution (e.g. imaginary) changes to another (e.g. real, in case of a wave cutting on, as frequency is increased). Using the extrapolation technique can lead to spurious solutions, as the Newton-solver converges to another branch than the one originally traced. This means that it is difficult to trace branches successfully and some jumping around between different branches may be the result, calling for a subsequent sorting.

In special cases, the discontinuities of the fluid loading term in equation (6.7) may trick the Newton-solver into a loop, where a fluid loading discontinuity is interpreted as a root. Therefore a sorting and conditioning algorithm has been used, testing whether the solution from the Newton-solver is truly a root of the dispersion equation, simply by putting the solution into the dispersion relation and checking that the result is small (e.g. smaller than 10^{-10}). Because the internal representation of numbers in Matlab is only double precision, corresponding to approximately 16 significant digits, some of the true roots of the dispersion equations may be rejected by the algorithm, as some of the equations solved are badly conditioned. While this normally happens only for large imaginary wavenumbers, which are far from cuton and thus of limited interest in the vibroacoustic far field, these types of error are easily spotted in the dispersion plots, as they appear as 'holes' in the branches.

6.3 Conclusion

In this chapter, a prediction model of the vibroacoustic response and power flow has been presented. The prediction model is nondimensionalised to reduce the number of input groups to a minimum. The influence of some of the input parameters is examined in the parameter study presented in the next chapter. The prediction model is validated against experimental results in chapter 8 for a light fluid loading case and in chapter 9 for a heavy fluid loading case.

The prediction model presented in this chapter includes two different types of excitation: structural point force excitation of the shell wall and acoustic point monopole excitation of the contained fluid. As shown in section 4.3.4, the response of the infinite fluid-filled pipe to a point monopole can be interpreted as a Green function. Knowing the Green function, it is relatively easy to construct the response functions of the fluid-filled pipe to point dipoles and point quadrupoles as dipole and quadrupole Green functions. This is demonstrated in section 4.3.5 for the internal pressure response, but it could easily be expanded to the pipe wall response as well. Finally, the formulation of the multipole responses as modal displacement amplitudes (as in equation (6.40) for the point monopole), would allow predictions of the vibroacoustic power flow from the point multipoles.

Chapter 7

Parameter study and investigation of shell theories

The vibroacoustic behaviour of cylindrical shells is quite complicated and the purpose of this chapter is to examine the influence of some of the parameters that are important for the industrial problem.

As an aid to understanding the dispersion behaviour of fluid-filled cylindrical shells, the first section of this chapter introduces the limiting cases of the fluid-filled cylindrical shell: namely the in vacuo shell, the hard-walled duct and the pressure-release duct. These correspond to no fluid loading, infinitely stiff walls and infinitely soft walls. The next section discusses the effect of changing some of the modelling parameters: the properties of the shell wall material and the interior fluid, and the wall thickness ratio h/a. The last section investigates the differences of three different shell theories: Donnell-Mushtari, Goldenveizer-Novizhilov and Flügge.

7.1 Basic tools for interpretation of results

In the case of light fluid loading, the cylindrical shell is largely unaffected by the presence of any internal or external fluid. The limiting case of the in vacuo cylindrical shell can then shed some light on the structural part of the coupled system. Likewise an understanding of the acoustic modes of a hard-walled circular duct can be helpful for light fluid loading or low frequencies, where the duct appears rigid due to the relatively high wall impedance compared with $\omega\rho a$. The acoustic modes of the pressure-release duct can also add to the understanding of the coupled system at certain frequencies, where the contribution from the fluid loading term is relatively large, e.g. at the cuton frequencies of higher order modes in the coupled system.

7.1.1 Solution of the in vacuo dispersion equation

In the case of a shell with neither external nor internal fluid loading (an in vacuo shell), the dispersion equation can be solved with relative ease by expansion of the dispersion equation (6.20) with the fluid loading term set equal to zero. The explicit solution can then expressed in the form

$$C_8(\kappa_{nb})^8 + C_6(\kappa_{nb})^6 + C_4(\kappa_{nb})^4 + C_2(\kappa_{nb})^2 + C_0 = 0 \tag{7.1}$$

where the C_n terms can be found from expanding the determinant of the matrix of equation (6.6). In contrast to the dispersion equation (6.20) for a fluid loaded shell, equation 7.1 can be solved analytically, as it is an eighth order polynomial with no odd orders. Thus, it has eight different roots for each circumferential mode; for each direction of propagation there are four roots, corresponding to four different branches in the dispersion plot.

Re-substitution of the roots of the dispersion equation, κ_{nb}, back into the equation of motion and elimination of one variable by dividing the equations by W_{nb} gives axial and tangential amplitude ratios $R_{a,nb}$ and $R_{t,nb}$ (defined in equations (6.25) and (6.26)) for each particular circumferential mode and eigensolution of the shell characteristic equation. The amplitude ratio reveals the propagation characteristics of a particular branch, for example whether it is flexural, extensional, torsional or combinations of these. The propagation characteristics for a given branch can vary with frequency, such that a branch that is extensional at low frequencies may become flexural at higher frequencies.

7.1.2 Solution of the duct dispersion equations

The dispersion relations for both the hard-walled circular duct and the pressure-release duct are given by equation (7.2) below:

$$\kappa_{nm} = \pm\sqrt{\Omega^2\left(\frac{c_L}{c_f}\right)^2 - \kappa^2} \tag{7.2}$$

Here n refers to the circumferential mode in the duct, and the mode transverse wavenumbers κ_{nm} are the m'th successive solution of $\mathrm{J}'_n(\kappa) = 0$ in the case of the hard-walled duct, and of $\mathrm{J}_n(\kappa) = 0$ in the case of the pressure-release duct.

7.1.3 Dispersion of in vacuo shell and duct solutions

The dispersion curves for an in vacuo steel shell are plotted in figure 7.1. Pure real roots are plotted using dots ($\cdot$); pure imaginary roots are plotted using plus-signs ($+$); and complex roots are plotted using crosses ($\times$).These symbols will be used throughout this chapter, and no special reference will be made to them in the individual figures. It should be noted that the figure is really a folded-out plot of the projections of the

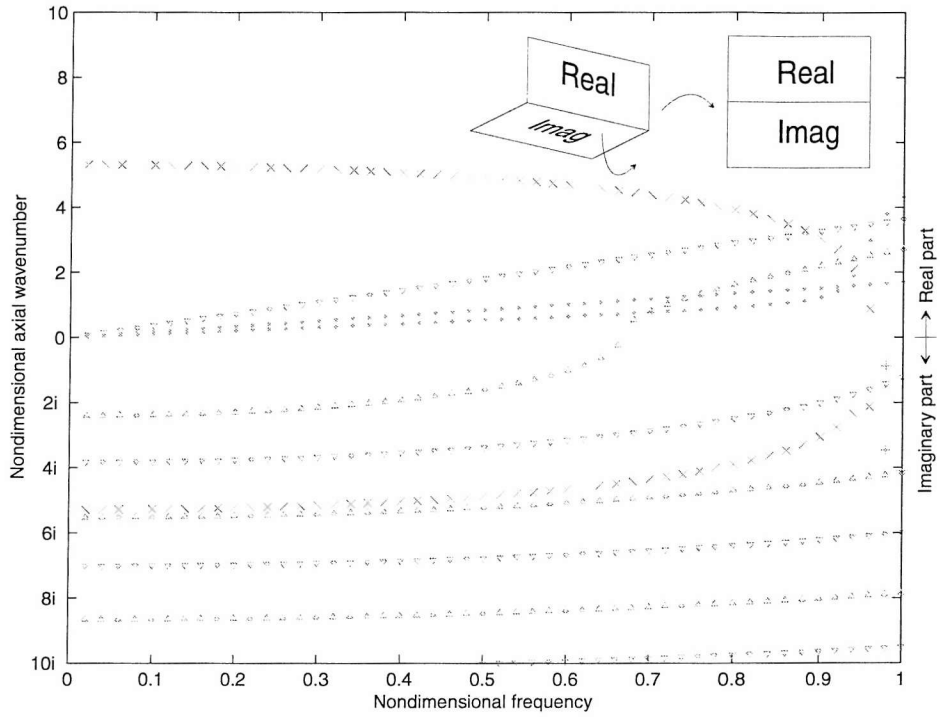

Figure 7.1: Dispersion of in vacuo shell and duct solutions. $h/a = 0.059$, $n = 0$. The real part of the wavenumbers are plotted in the upper half of the figure and the imaginary wavenumbers are plotted in the lower half. The in vacuo dispersion curves are plotted using the following symbols: ($\cdot$) pure real roots ; ($+$) pure imaginary roots; and ($\times$) complex roots . The hard-walled duct solutions are plotted using down-triangles (∇), and the pressure-release solutions are plotted using up-triangles (Δ).

dispersion curves on the real and imaginary planes, as sketched at the top of the figure. When plotted this way, a branch crossing the line connecting the real and imaginary planes corresponds to cuton of a given wave.

The in vacuo dispersion curves in figure 7.1 will be used to compare and interpret the fluid-loaded dispersion curves below. It is also useful to show the fluid-mode limiting cases: here wave speeds for air and steel are used in equation (7.2). The hard-walled duct solutions are plotted using down-triangles (∇), and the pressure-release solutions are plotted using up-triangles (Δ).

In the dispersion plot there are a number of branches, each related to a different root of the dispersion relation for a given Ω. In some cases where it is of importance to discuss the branches, they have been assigned a number. The numbering of the dispersion curves is purely arbitrary. In the present thesis, they are numbered from $b = 1$ starting in the upper right corner.

All dispersion curves in the present thesis are plotted with the symbols and methodology of figure 7.1.

7.2 Parameter study

It was shown in section 6.1 that 6 dimensionless input parameters were necessary to address the coupled problem of a cylindrical shell with an internal fluid. This leaves quite a number of different parameter combinations to be investigated to cover the entire parameter space in detail. Instead of trying to cover all parameters evenly, the present investigation is concentrated on parameter values important for the industrial application.

Specifically, the influence of fluid loading is investigated by comparing in vacuo shells with air and water-filled shells. The influence of the shell material is investigated by comparing dispersion curves and point mobility for steel, PVC and rubber shells. The geometric properties are investigated by variation of the thickness ratio of the shell.

All the cases investigated in this section can be found in table 7.1; the material properties are shown in table 7.2 and the geometric properties are shown in table 7.3. The mean radius a is defined to be the distance from the pipe axis to the geometric midpoint of the shell, $a = (D_o + D_i)/4$, where D_o is the outer diameter of the pipe; D_i is the inner diameter of the pipe; and $h = (D_o - D_i)/2$ is the thickness of the shell.

7.2.1 Variation of shell material

As steel pipes are used in the industrial application and the experiments presented in part III use PVC pipes and rubber hoses, these materials are compared in this section, keeping other parameters constant. The contained fluid is water, and the shell geometry (A in table 7.3) corresponds to the experimental setup used in part III.

Case no.	Shell material	Shell geometry from table 7.3	Internal fluid	Resulting fluid load	Ring frequency [kHz]
1	PVC	A	Water	Heavy	9.25
2	PVC	A	None	None	9.25
3	PVC	A	Air	Light	9.25
4	Steel	A	Water	Intermediate	28.3
5	Rubber	A	Water	Heavy	5.55
6	PVC	B	Water	Heavy	9.25
7	PVC	C	Water	Heavy	9.25

Table 7.1: Cases investigated in the parameter study.

Material	Young's modulus [N/m^2]	Poisson's ratio	Density [kg/m^3]	Wave speed (c_L or c_f) [m/s]
Steel	2.1×10^{11}	0.30	7800	5439
PVC	3.8×10^{9}	0.40	1360	1786
Rubber	1.0×10^{9}	0.45	1100	1068
Water	—	—	997	1480
Air	—	—	1.2	340

Table 7.2: Material properties for pipe materials and internal fluids.

Name	Outer dia. D_o [mm]	Inner dia. D_i [mm]	Mean radius a [mm]	Thickness h [mm]	h/a
A. PVC pipe	63.0	59.4	30.60	1.80	0.059
B. PVC pipe, medium	64.2	58.2	30.60	3.00	0.098
C. PVC pipe, heavy	68.2	54.2	30.60	7.00	0.228
D. Rubber hose	79.2	76.0	38.80	1.60	0.041
E. 1" standard pipe	33.7	27.2	15.23	3.25	0.214
F. 1" light pipe	33.7	28.5	15.55	2.60	0.167
G. 1" PVC pipe	31.8	28.6	15.10	1.60	0.106

Table 7.3: Geometrical properties for relevant pipes of industrial interest.

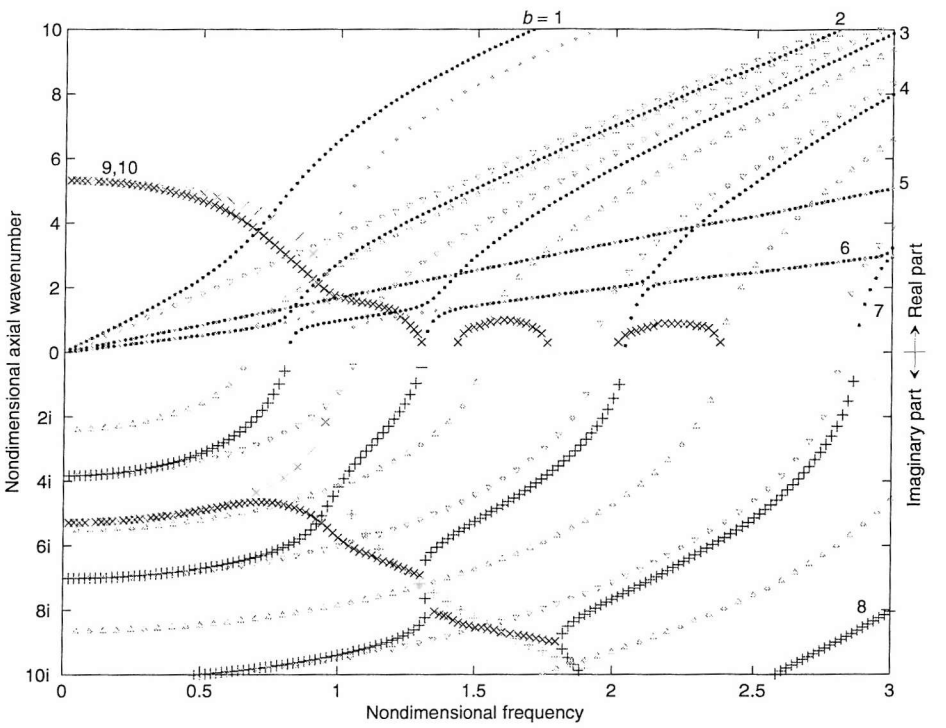

Figure 7.2: Dispersion curves for case 4, water-filled steel shell (same geometry as figure 7.1). $n = 0$. Case 4 is plotted with red symbols, and the cyan symbols correspond to figure 7.1.

The steel shell has been investigated by several authors in literature, e.g Fuller and Fahy (1982), Pavic (1990) and Feng (1994). To assist any comparison of the present thesis with these authors the steel shell is presented in some detail first. Then the three materials steel, PVC and rubber are compared.

7.2.1.1 Water-filled steel shell

The prime material in the industrial application is steel, so the features of the dispersion curves will be discussed in detail for this material. The dispersion curves are shown using the same format and symbols as for figure 7.1, with the real wavenumber component in the upper half of the plot and the imaginary wavenumber component in the lower half.

Dispersion curves are presented below for $n = 0$, $n = 1$ and $n = 2$.

The breathing mode, $n = 0$**.** Figure 7.2 shows the dispersion curves of axial wavenumber versus nondimensional frequency for the breathing mode, i.e. waves of circumferential order n=0.

- **The real branches.** Only three real branches exist at low frequencies. The

first branch is close to a plane fluid wave in a rigid walled cylindrical duct at low frequencies, while the wavenumbers at higher frequencies are larger than the rigid duct solution. The second branch is the torsional shell wave, which is completely uncoupled from the fluid and thus identical to the in vacuo torsional wave. The third branch is very close to the in vacuo shell extensional wave at low frequencies.

Some of the effects of fluid loading from the contained fluid can be seen directly from a plot of the fluid loading term $\mathcal{F}$ in equation (6.7). The fluid loading equation is restated here for convenience:

$$\mathcal{F} = \Omega^2 \left(\frac{\rho_f}{\rho_s}\right) \left(\frac{h}{a}\right)^{-1} \frac{\mathrm{J}_n(\alpha)}{\alpha \mathrm{J}_n'(\alpha)}$$

At very low frequencies ($\Omega \to 0$) the fluid loading term is relatively small compared to the very high stiffness of the shell for waves with long axial wavelength, and therefore the effect on shell waves is quite small; one would expect the fluid-filled shell response to be close to that of an in vacuo shell (see branches $b = 2$, 9 and 10 in figure 7.2). Similarly at the poles of $\mathcal{F}$, when $\mathrm{J}_n'(\alpha) \to 0$, the fluid loading is extremely large and the coupled system response will approach that of an acoustic wave in a pressure release duct. This effect is not clearly visible in figure 7.2 where the stiffness of the steel shell is relatively high also at higher frequencies, but some effect can be seen on the cuton of the $b = 3$ branch.

From figure 7.2, it can be seen that a third branch ($b = 3$) cuts on at $\Omega \approx 0.82$. In a hard-walled duct, this would be the first duct wave (note that the red plus-signs and the cyan down triangles overlaps at low frequencies near $4i$), but with heavy fluid loading the cuton frequency of the branch is shifted towards the first pressure release duct wave. Furthermore the $b = 3$ branch changes shortly after cuton from a mainly fluid wave to a mainly structural wave, resembling the extensional shell wave. The branch that had the characteristics of the extensional shell wave at low frequencies ($b = 2$), changes near the cuton frequency of the $b = 3$ branch to have the characteristics of a mainly fluid wave. Near the cuton frequency of the $b = 3$ branch, the two branches $b = 2$ and 3 interchanges their main characteristics.

All higher branches cut on as fluid waves and then quickly change their behaviour to that of shell waves, while the previous shell type branch converts to a fluid wave. At the higher frequencies, cuton of the modes occurs near rigid walled duct cuton frequencies. The behaviour can be explained by considering the coincidence of an extensional shell wave and a fluid wave in a duct with only slightly compliant walls. At the point where one branch enters a plateau and the other branch leaves it, free motion can exist independently both in the fluid and the shell wall. The shell vibrates largely as in vacuo due to the extensional nature of the motion, and correspondingly the shell appears rigid to the fluid. However due to the Poisson's ratio effect, there will be some coupling between the shell and fluid motion. As the frequency is increased along a plateau to the point of coincidence of free shell and fluid waves, the pressure field 'forced' in the fluid by the shell subsequently encounters a region of free fluid propagation, and the system behaviour changes to a fluid type wave. Similarly a 'forced' shell wave, driven by the fluid pressure

field for the next branch, encounters a free propagation region for shell waves at the same coincidence point, and its behaviour changes therefore to a shell wave.

The fluid loading has no effect at all on the torsional branch ($b = 5$), as there is no radial component of displacement; since the fluid is modelled as inviscid, it cannot affect the pure torsional motion of the pipe.

- **The imaginary branches.** At low frequencies the wavenumber solutions are almost identical to hard-walled duct modes below cut-off, owing to the rigidity of the shell wall. Therefore there are an infinite number of branches, corresponding to modes with an increasing number of radial nodes. As the frequency is increased, the stiffness of the shell in the radial direction becomes smaller and the branches fall between the hard-walled and pressure-release solutions for a cylindrical duct, as discussed above.

- **The complex branches.** The complex wavenumber solutions ($b = 9$ and 10) are very close at low frequencies to those obtained from an in vacuo shell, owing to the low coupling to the fluid, as discussed for the real branches. At zero frequency, the two branches have non-zero complex values of the same absolute magnitude, with real parts of opposite sign. The real parts of these solutions reduce with increasing frequency, and the two complex branches become imaginary at $\Omega \approx 1.20$.

  Typically a fluid-type branch is imaginary at low frequencies, becomes complex over a small frequency range near the occurrence of a 'meander', becomes purely imaginary near the next 'meander', and eventually cuts on. Likewise a branch which is close to the in vacuo shell branch is complex at low frequencies, and progresses with increasing frequency as a series of complex and imaginary sections.

The real part of the dispersion plot has a distinct appearance, as three different groups of curve slopes are represented in the curves: i) the mainly fluid wave (e.g. $b = 1$, 2 and 3), ii) the torsional shell wave, where the red and the blue dots overlap exactly ($b = 5$), and iii) the flat curve for the mainly extensional shell wave where the blue curve is continuous, while the red curves are discontinuous (e.g. $b = 2$, 3, 4 and 6 just after cuton).

The slope of the dispersion curves is related to the group speed of the branch. The slope of group i) asymptotically approaches the sound speed of the internal fluid c_f. The slope of group ii) is the torsional wave speed. The slope of group iii) is the extensional wave speed of a circular shell. Curiously, there is a difference of approximately 0.5 % between the extensional group speed for a circular shell (deduced from the slope of the numerical dispersion curve) and c_L (the thin-plate extensional group speed) with the actual parameters used in the calculation. Apparently, this discrepancy is not reduced as Ω is increased, but no plausible explanation has been found.

The beam mode, $n = 1$. Figure 7.3 presents the dispersion curves of the fluid-filled shell vibrating in the circumferential mode of order $n = 1$, the beam mode. The dispersion curves are similar to those discussed for the breathing mode, apart from a

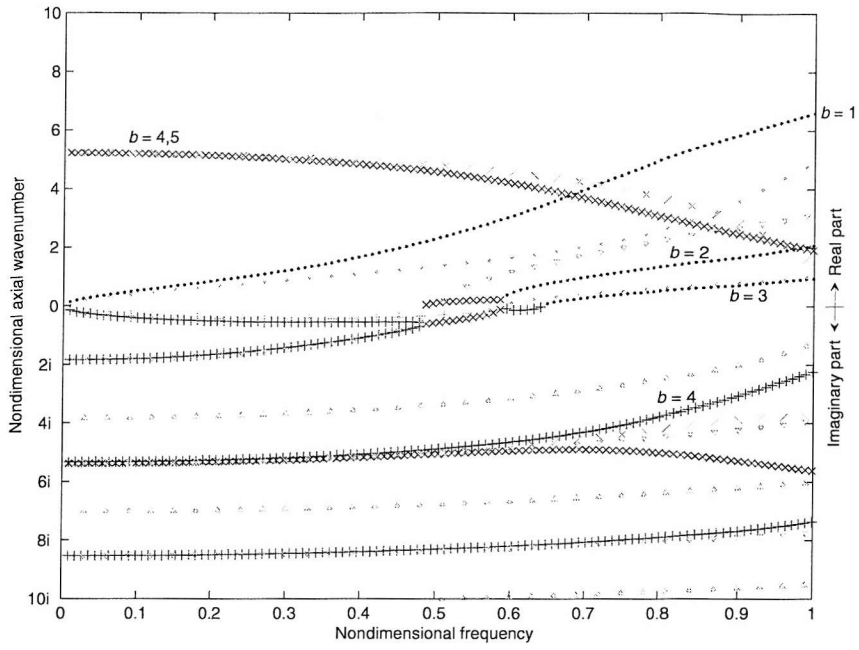

Figure 7.3: Dispersion curves for case 4, water-filled steel shell. $n = 1$. Case 4 is plotted with red symbols, and the cyan symbols correspond to figure 7.1.

few differences. At low frequencies, there exists only one branch ($b = 1$), corresponding to the beam type shell motion. This wave is acoustically slow, with a purely imaginary radial wavenumber. Thus the 'forced' acoustic motion in the contained fluid consists of a pressure field decaying away from the shell wall. At $\Omega \approx 0.6$ the second branch cuts on, and this branch corresponds to the lowest $n = 1$ rigid walled duct wave. At a slightly higher frequency a third branch cuts on. This branch is predominantly a torsional shell wave and behaves as such until it encounters the next branch ($b = 4$), where its characteristics change to a fluid-type wave, as for the $n = 0$ branches.

As well as the complex branches already demonstrated in the case of the breathing mode (b=4 and 5), there appears for the $n = 1$ mode an additional pair of complex branches in the imaginary region near $\Omega = 0.5$, linking together the branches $b = 2$ and $b = 3$ in the evanescent region by some sort of complex transition just below the cuton frequency of the second branch.

Higher order modes, $n > 1$. In figure 7.4, the dispersion curve is shown for the same water-filled steel shell with a mode order of $n = 2$.

For these waves of higher circumferential modal number ($n > 1$) the dispersion characteristics are similar to those of the beam mode, except that the fundamental shell type wave has a non-zero cuton frequency and the points of coincidence are shifted to higher frequencies. For these modes there are two series of plateaux arising from coincidence

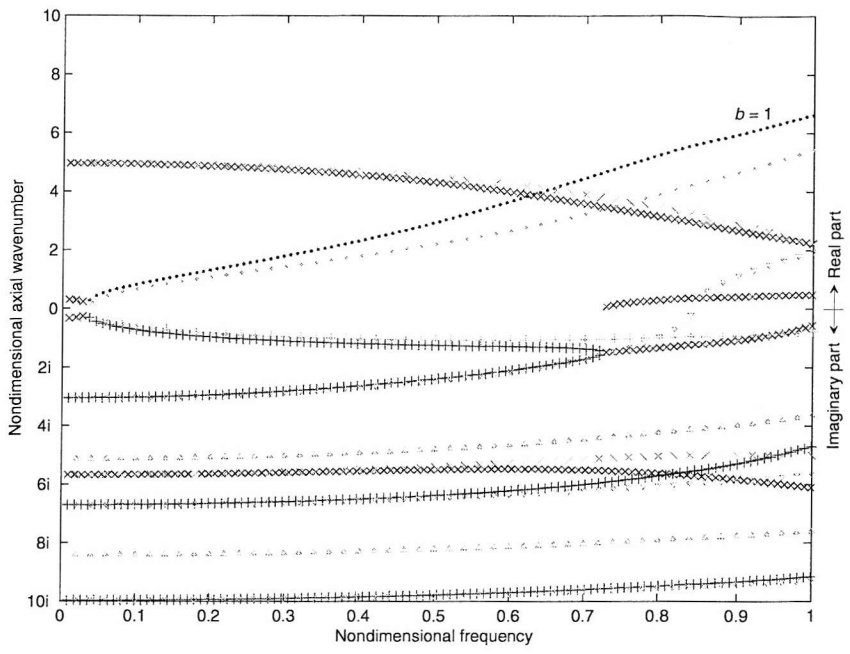

Figure 7.4: Dispersion curves for case 4, water-filled steel shell. $n = 2$. Case 4 is plotted with red symbols, and the cyan symbols correspond to figure 7.1.

of torsional and extensional shell waves with duct type waves.

The cuton of the first $n = 2$ wave happens at $\Omega \approx 0.03$, which is a little more than half the frequency of the cuton of the similar in vacuo wave. This is a common feature for the cuton frequencies for the fluid loaded shell in comparison with the in vacuo shell. As discussed in section 7.2.2, the reason for this is probably that the added mass of the water reduces the effective stiffness of the shell wall, leading to a lower cuton frequency. It should be noted that the fluid loading does not affect the ring frequency of the shell, so the explanation for the lower cuton frequency is not a change in the ring frequency.

Point mobility The combined effect of the different modal dispersion relations can be seen through the point mobility, as calculated for a radial point input force and a receiving point on the shell wall in the far field. The shell is excited by a point force 20 radii (corresponding to 0.61 m) from the receiver point, with no angular separation between the two points. In figure 7.5, the magnitude of the radial point mobility is shown for a water-filled steel shell excited by a radial point force.

The radial point mobility relates the radial velocity of the shell wall to a point unit input force. A peak in the mobility plot can thus be interpreted as resonant behaviour of the shell. All the peaks in the mobility plot are the points of cuton of higher order modes. The first peak, at $\Omega \approx 0.03$, corresponds to the cuton of the $n = 2$ mode; the one at $\Omega \approx 0.1$ corresponds to the $n = 3$ mode. This sequence continues up to $\Omega \approx 0.7$

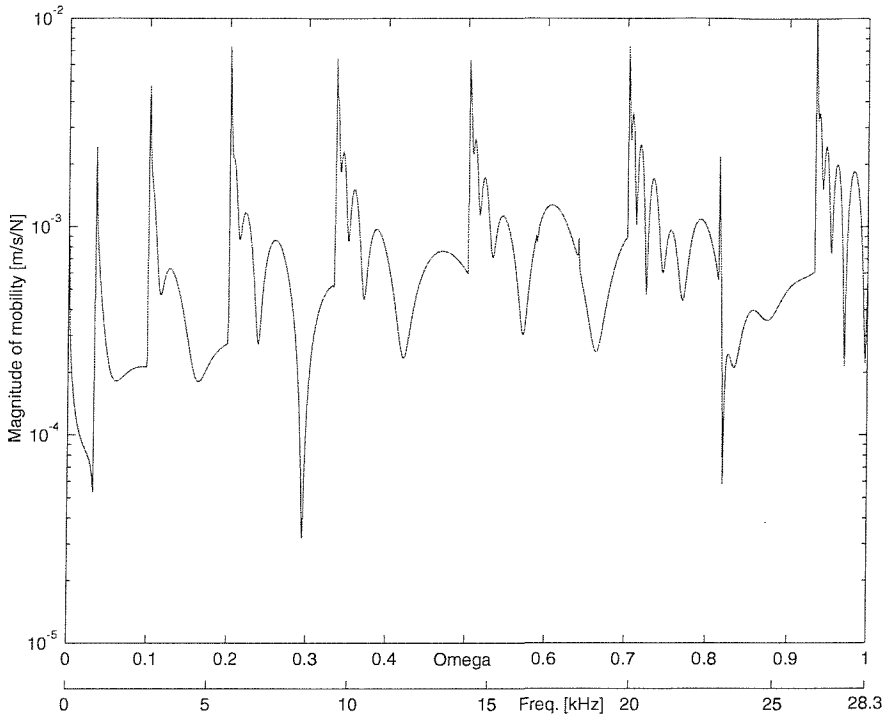

Figure 7.5: Point mobility of case 4, water-filled steel shell. $s = 20$, $\theta_o = 0$.

where the second propagating $n = 2$ branch cuts on. The $n = 7$ mode is the last to cut on below the ring frequency, at $\Omega \approx 0.8$.

The high mobility, at cuton, of higher order modes, is viewed in some industrial applications (not the ones relevant to this thesis, though) as an important problem in relation to fatigue fractures in pipes. Pipes designed to survive an infinite number of vibrational cycles are seen to fail, due to fatigue fractures that can probably be related to cuton of higher order modes. From figure 7.5 it is evident that if the frequency-average mobility is used as design limit for fatigue, then a pipe designed to survive an infinite number of cycles with a safety factor of 5 (or a would-be safety factor of 5 if the underlying assumptions were correct) would be in danger of failing due to fatigue, as the peaks are more than one order of magnitude higher than the average level.

7.2.1.2 Comparison of PVC, steel and rubber shells

The materials investigated in this section are PVC, steel and rubber, and the shell geometry corresponds to the experiments in part III with water as the internal fluid. This corresponds to case 1, 4 and 5 in table 7.1.

The steel shell presented in the previous section has a c_L of approximately 3.6 times the speed of sound in water, and a density ratio ρ_f/ρ_s of approximately 0.129. For the PVC shell filled with water the corresponding ratios are approximately 1.20 and 0.74, and for the rubber shell the ratios are 0.71 and 0.91 (see table 7.2 on page 74). For the given

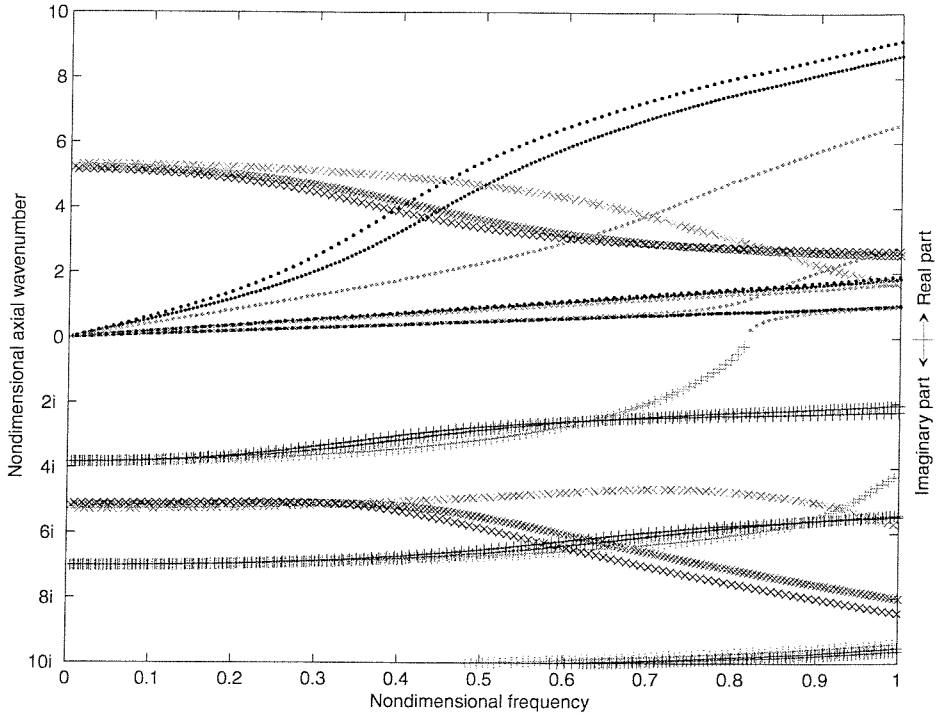

Figure 7.6: Dispersion curves for case 1(red), 4(green) and 5(blue). $n = 0$.

geometry the ring frequency for the PVC shell is 9,251 Hz, for the steel shell it is 28,290 Hz and for the rubber shell it is 5,553 Hz. Another important difference between the three materials relates to Poisson's ratio. The low $\nu = 0.3$ for steel makes the coupling between the fluid and the mainly extensional branches in the shell relatively small, while the large $\nu = 0.45$ for rubber makes the coupling in the case of rubber relatively large.

Dispersion plots for $n = 0$ are shown in figure 7.6 for the three different shells. The colours are red for the PVC shell, green for the steel shell and blue for the rubber shell. The dispersion curves are very similar, considering the large differences in the material properties. However, this is not surprising as the nondimensional formulation tends to collapse the situations, making comparisons more straightforward. The main difference between the curves is the appearance of a fluid wave cut on in the case of the steel shell, but not in the other two cases. This is due to one of the shortcomings of the chosen form of collapsing the different shells, as the cuton of fluid waves is not related purely to the material properties and the thickness ratio of the shells: the cuton of mainly fluid waves is dependent on the Helmholtz number, rather than the ring frequency of the shell. The dispersion plots highlight what was hinted at by the material parameters: the rubber and PVC shells are more similar to each other than to the steel shell.

The dispersion curves for $n = 1$ are plotted the same way in figure 7.7. The three shells are quite close, but again the steel shell is a bit off the other two. An interesting feature is the cuton of two branches of the steel shell at Ω between 0.5 and 0.7, but only one for the each of the other two. Closer examination of figures 7.3 and 7.7, reveals the

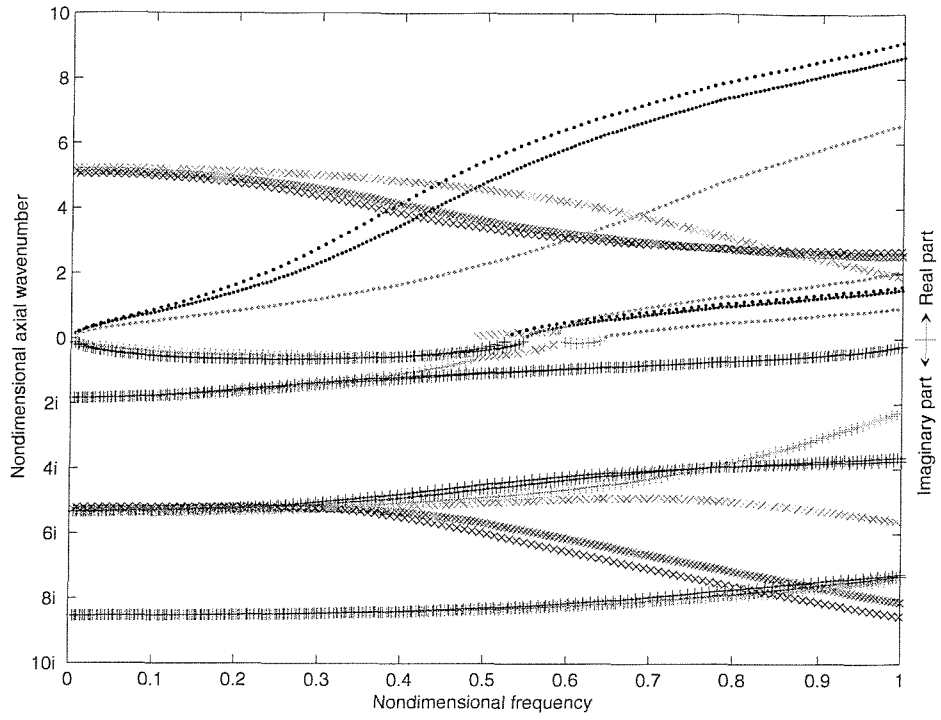

Figure 7.7: Dispersion curves for case 1(red), 4(green) and 5(blue). $n = 1$.

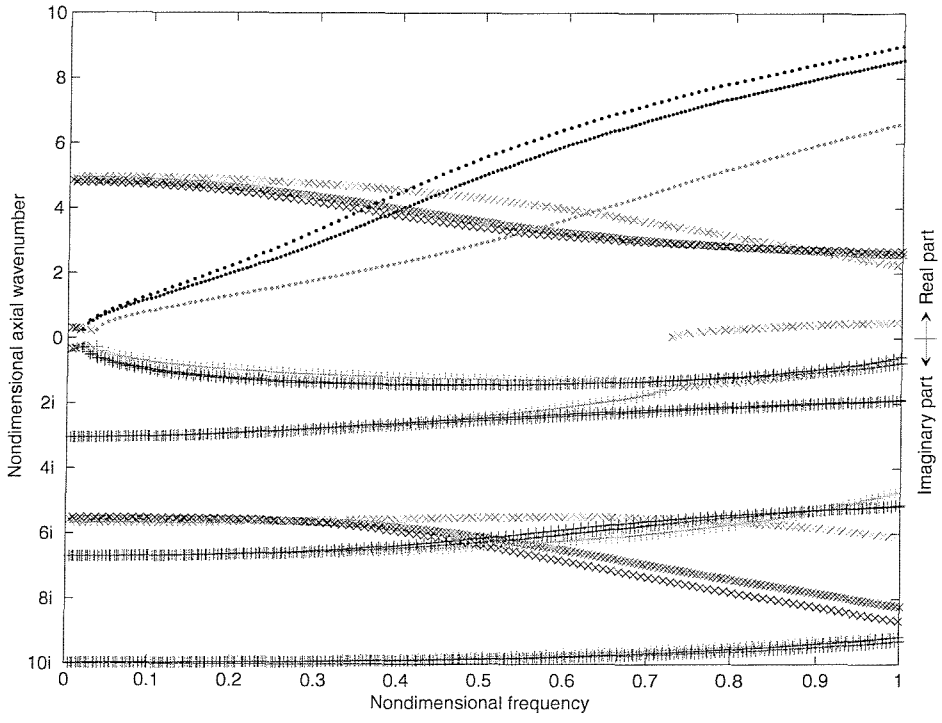

Figure 7.8: Dispersion curves for case 1(red), 4(green) and 5(blue). $n = 2$.

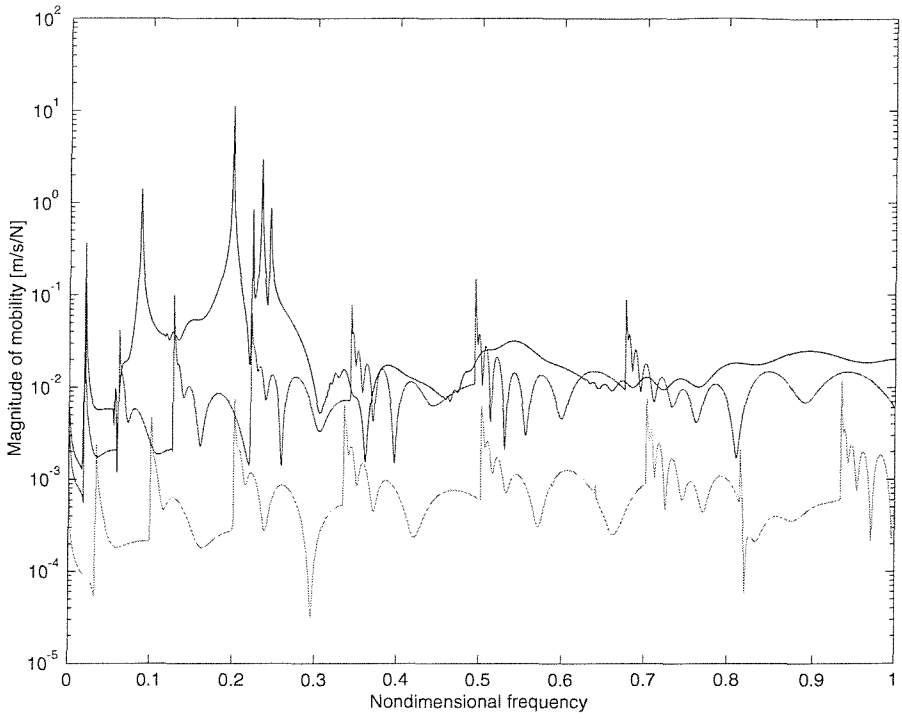

Figure 7.9: Point mobility for case 1(red), 4(green) and 5(blue). $s = 20$, $\theta_o = 0$.

cuton of a mainly fluid wave in the steel shell, at approximately the same frequency as the cuton of a mainly shell wave.

Figure 7.8 shows dispersion curves for $n = 2$. The main difference from the dispersion curves for $n = 0$ and $n = 1$ is the non-zero cuton frequency of the first propagating branch. Again the difference between the steel shell and the other two is highlighted, as the first nondimensional cuton frequency of the steel shell (at $\Omega = 0.03$) is significantly higher than the other two. The branch cutting on is a mainly shell wave, so the cuton frequency is expected to be largely unaffected by the Helmholtz number. Instead the difference seems to be caused by the fluid loading, as a light fluid loading results in a relatively high cuton frequency (very close to that of an in vacuo shell, as seen in section 7.2.2), while a heavy fluid loading results in a relatively low cuton frequency. The water-filled steel shell in question can thus be seen as some sort of intermediate fluid loading case, neither heavy nor light. This is discussed in more detail in chapter 11 of part IV.

The point mobility for the 3 different wall materials is plotted in figure 7.9 the same way as in figure 7.5. Again there are close similarities between the PVC and rubber shells, while the steel shell has a significantly lower mobility. The peaks from the cuton of higher order modes are a prominent feature for all three shells at low frequencies, but at higher frequencies the rubber shell looks different without any distinct peaks. This is certainly not due to any damping, as the modelling is lossless, but no good explanation for this phenomenon has been found. Somehow the result seems intuitively correct – perhaps because of the 'feel' when tapping rubber (but this is probably due to the high

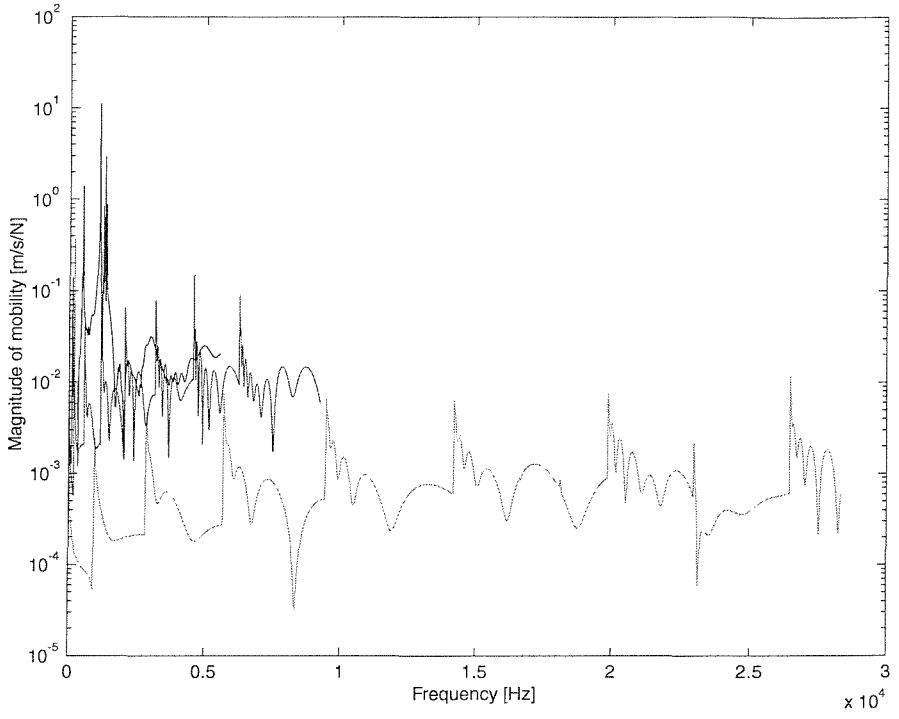

Figure 7.10: Point mobility for case 1(red), 4(green) and 5(blue). $s = 20$, $\theta_o = 0$.

damping of the material).

Just to illustrate how differently the shells really behave in 'real' life, another plot of the mobility is shown in figure 7.10. The only difference between this plot and the previous one is the use of a dimensional frequency scale.

The main conclusion, from this investigation of the influence of the shell material, is that the choice of shell material – at least within the parameters investigated – makes little difference to the dispersion curves and the point radial mobility in the far field, when the results are presented in the dimensionless form used here. The two exceptions are: the cuton frequency of predominantly fluid branches is mainly determined by the Helmholtz number, not the ring frequency of the shell; and the cuton frequencies of the higher order modes are strongly dependent on the fluid loading.

7.2.2 Variation of internal and external fluids

The analytical model review in chapter 5 included the effect of the external fluid loading, but this was later discarded in the formulation of the nondimensional prediction model in chapter 6. The justification given was that the external fluid in the industrial application was only air, and with a heavy fluid loading inside the shell the influence of the light external fluid loading was negligible. The validity of this argument is assessed in this section.

The previous section used a number of examples to show that the heavy fluid loading has an important influence on the response of the coupled system, but it did not provide the limits of when a fluid loading becomes significant in terms of choice of shell material – apparently a density factor of nearly 8 for the wall material along with a longitudinal wave speed factor of more than 5 did not have any major influence, although some differences related to the fluid loading could be seen. To examine the other extreme, namely light fluid loading, air is included in the investigation. So as not to complicate matters too much, the PVC shell from the experiments of part III is used, although as shown in the previous section the choice of shell material is not a major factor anyway. With this shell, the density ratio ρ_f/ρ_s for the heavy fluid loaded case is 0.74, compared with $8.8 \cdot 10^{-4}$ for the lightly fluid loaded case.

7.2.2.1 Effect of external fluid loading

Evidently even air outside a fluid-filled cylindrical shell can be important in some cases, for example where where the shell mass per unit area ($\rho_s h$) is so small, that the added mass effect due to the movement of air becomes an important factor. These cases are however assumed to be extreme in the light of the industrial application and the frequency range of interest. Air outside the shell is therefore assumed to represent a light external fluid loading of the shell.

This light external fluid loading can be combined with three different internal loading cases: vacuum, light and heavy fluid loading.

From the full fluid loading equation (5.15),

$$f_l = \rho_e \omega^2 \frac{\mathrm{H}_n(k_e^r a)}{k_e^r \mathrm{H}_n'(k_e^r a)} - \rho_i \omega^2 \frac{\mathrm{J}_n(k_i^r a)}{k_i^r \mathrm{J}_n'(k_i^r a)}$$

it can be seen that both the internal and the external fluid loading are proportional (amongst other factors) to the fluid densities. If the internal and external fluid is assumed to be the same, then the relative sizes of the fluid loadings is determined by the ratios of the differentiated Bessel and Hankel functions in equation (5.15). In the case of light internal fluid loading, the total fluid loading (being the sum of the light external and internal fluid loading) is relatively small when included in the equations of motion and thus the influence on the calculated wavenumbers is also small. Singularities of the fluid loading equation (5.15) could give a significant fluid loading contribution, even when the densities involved are small, but this has not been observed in the parameter study, probably because it happens only in an extremely narrow frequency band.

When the internal fluid loading is heavy and the external fluid loading is light, then the error made by leaving out the external influence is relatively small, as the fluid loading calculated using equation (5.15) in most cases is completely dominated by the internal fluid loading. The sole exception is when the term related to the internal fluid loading is small, then the relative effect of the external fluid loading term might be of the same magnitude, but the total fluid loading will be the sum of two small terms, and thus insignificant.

The conclusion is, if the external fluid loading is light, the coupled system will be largely unaffected, no matter what the internal fluid loading. The error made by leaving out light external fluid loading, and assuming an external vacuum, is therefore very small.

7.2.2.2 Variation of internal fluid

To compare the effect of the internal fluid loading, the PVC shell with vacuum on the outside is examined using three different internal load cases: vacuum (no fluid loading), air (light fluid loading) and water (heavy fluid loading). This corresponds to cases 3, 2 and 1 in table 7.1.

Figure 7.11 shows the dispersion curves for $n = 0$. The red curve corresponds to the PVC shell used in the experiments in part III filled with water (i.e. heavy fluid loaded), the green curve corresponds to the same shell filled with air (i.e. light fluid loaded) while the blue curve is the same shell in vacuo (i.e. no fluid loading).

It is obvious that some of the dispersion curves of the light fluid loaded shell are very close to those of the in vacuo shell, as they collapse almost perfectly. These curves represent the mainly shell modes that are almost unaffected by the presence of the light fluid loading. There is a small discrepancy at $\Omega \approx 0.9$ where coincidence occurs between a mainly shell branch and a mainly fluid branch. The 'lonely' green curves correspond closely to the hard-walled duct modes.

At low frequencies, the dispersion curves for the light and heavy fluid loading collapse exactly. Apparently, the influence of the fluid loading is small up to $\Omega \approx 0.05$ where the curves start to become separated. The larger wavenumbers of the heavy fluid loaded case correspond to lower phase velocity, so the effect of the contained fluid is to slow down wave propagation in the shell. This is probably also the case in the light fluid loaded case, but the effect is too small to be noticed on the scale of the plots.

The vibrational near field related to the complex branches in the dispersion plot is apparently very much affected by the heavy fluid load. In section 6.2, it was noted the complex wavenumbers were related to local shell deformations near points of discontinuity. In the case of heavy fluid loading the added mass effect of the fluid is relatively larger, thus making the local shell deformations happen over a wider frequency range.

The figures for $n = 1$ and $n = 2$, figure 7.12 and figure 7.13, show the same phenomena. The nondimensional cuton frequency of the lowest fluid wave in figure 7.12 is different for the light and heavy fluid loaded case. As discussed in section 7.2.2, this is because the cuton of mainly fluid waves is more related to the Helmholtz number than to the ring frequency of the shell.

The point mobility of the shell wall is plotted in figure 7.14. On comparing the three curves, the conclusion from the dispersion curves is confirmed: there are virtually no differences between the mobility of the in vacuo shell and the light fluid loaded shell at low to intermediate frequencies. Small discrepancies are noticeable above $\Omega \approx 0.9$. There are some differences between the light and the heavy fluid loaded cases: the peaks

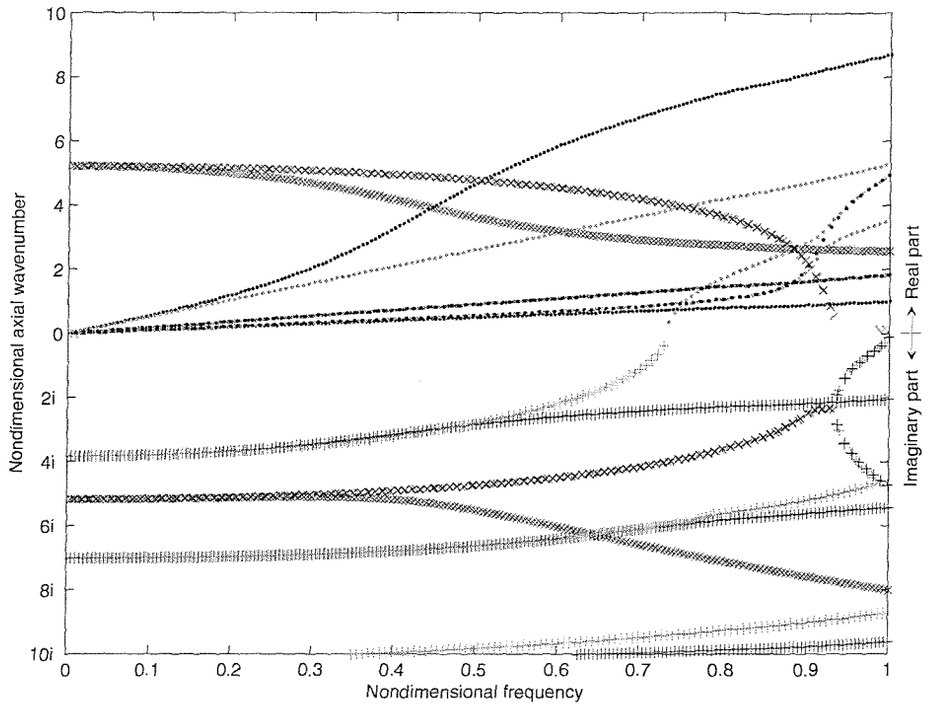

Figure 7.11: Dispersion curves for case 1(red), 2(green) and 3(blue). $n = 0$.

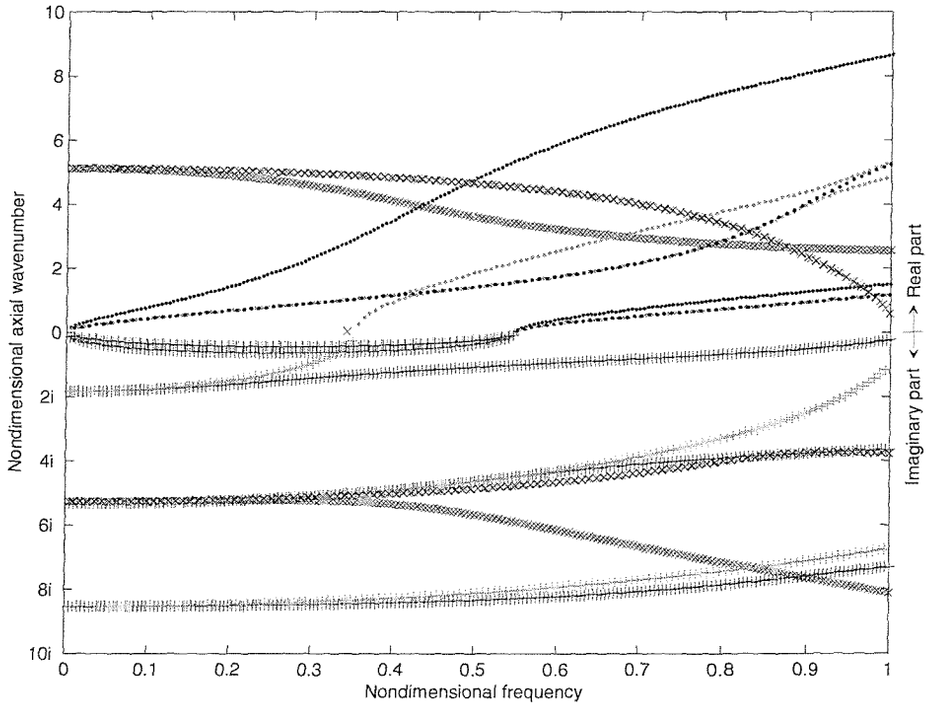

Figure 7.12: Dispersion curves for case 1(red), 2(green) and 3(blue). $n = 1$.

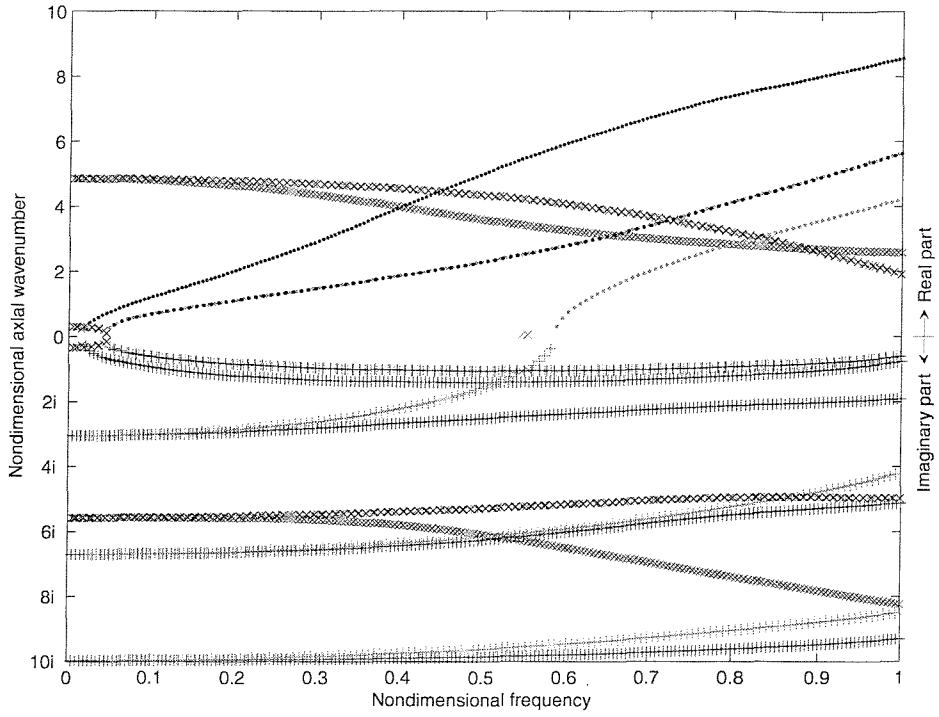

Figure 7.13: Dispersion curves for case 1(red), 2(green) and 3(blue). $n = 2$.

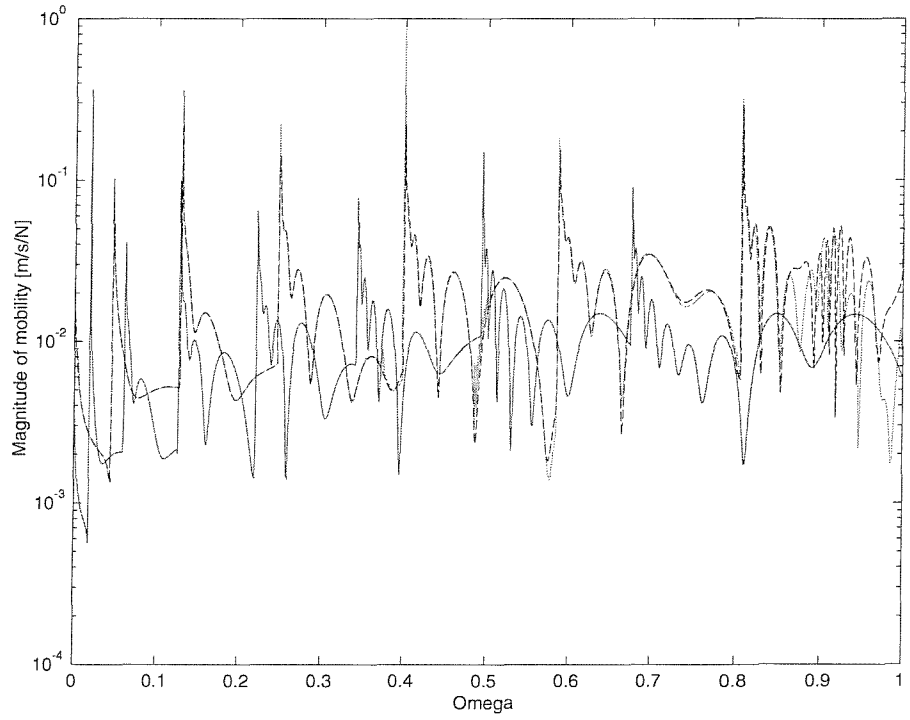

Figure 7.14: Point mobility for case 1(red), 2(green) and 3(blue). $s = 20$, $\theta_o = 0$.

related to cuton of higher order modes appears at lower frequencies for the heavy fluid loaded shell; and the general level of mobility is lower for the heavy fluid loaded shell. The lower level of mobility was expected, as the added mass effect from the heavy fluid loaded case reduces the dynamic response of the shell wall.

7.2.3 Variation of shell geometry

This part of the parameter study investigates the effect of variations of the shell geometry. In the nondimensional formulation, the geometry of the shell is dependent on one parameter, namely the thickness ratio h/a. The thickness ratio can be changed two different ways – by altering h and by altering a. For the in vacuo case, this has the same effect, but in the case of fluid loading the effect is different, as the cuton frequency of the predominantly fluid waves is mainly related to the Helmholtz number. To avoid confusion from the cuton of fluid waves, a is kept constant in this investigation, and the thickness ratio is changed through the thickness of the shell h.

In the present investigation, the shell material is chosen to be PVC, the contained fluid is water, and the mean radius a is the same as for the experiments in part III. Three different cases are investigated: namely, $h/a = 0.059$; $h/a = 0.1$; and h/a=0.25. This correspond to cases 1, 6 and 7 in table 7.1.

The main shell theory used in the present thesis (the Flügge shell theory) is a thin shell theory, i.e. the influence of thickness variations of the shell wall, due to vibrations, is not modelled directly. The Flügge theory and two other thin shell theories are investigated in section 7.3, but as they are all thin shell theories they assume that the thickness ratio is small. The thin shell theories include the effect of finite thickness shells through correction terms related to h/a, in the form of $\beta = \sqrt{h^2/12a^2}$. All thin shell theories perform better the smaller the β. The upper limit on h/a for the shell theory to remain valid is parameter dependent. From the discussions in Leissa (1973), it is assumed that the thickest case in this investigation is close to the maximum allowable thickness, with $h/a = 0.25$.

The dispersion curves for $n = 0$ are shown in figure 7.15. At first glance the three cases seem relatively different, but there are significant similarities. The differences between the cases are related to the complex branches and to the propagating predominantly fluid waves.

For the real wavenumbers the dispersion curves for the predominantly extensional and torsional shell branches collapse completely. The wave speeds of these branches are unaffected by changes of the wall thickness.

For the imaginary wavenumbers, the curves tend to collapse owing to the large relative stiffness of the shell at low frequencies already discussed in section 7.2.2. The apparent stiffness of the shell as seen from the fluid is very high at low frequencies even for the thinnest shell, and the added stiffness from the thicker has no significant influence. As the frequency is increased, the relative stiffness decreases most rapidly for the thinnest shell, slower for the thicker shell, and slowest of all for the thickest shell. The large

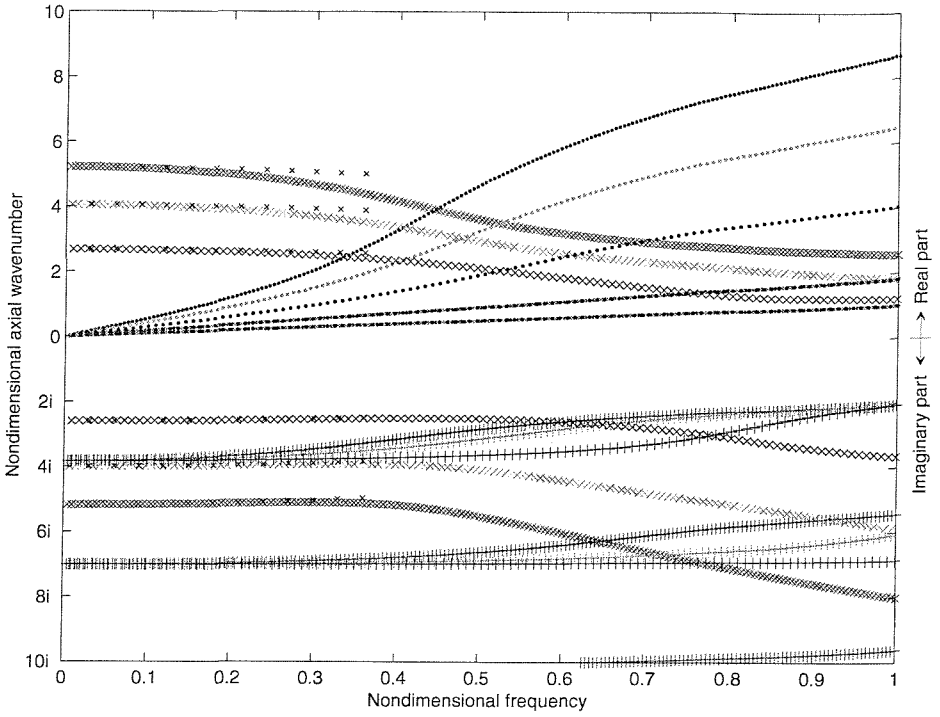

Figure 7.15: Dispersion curves for case 1(red), 6(green) and 7(blue). $n = 0$.

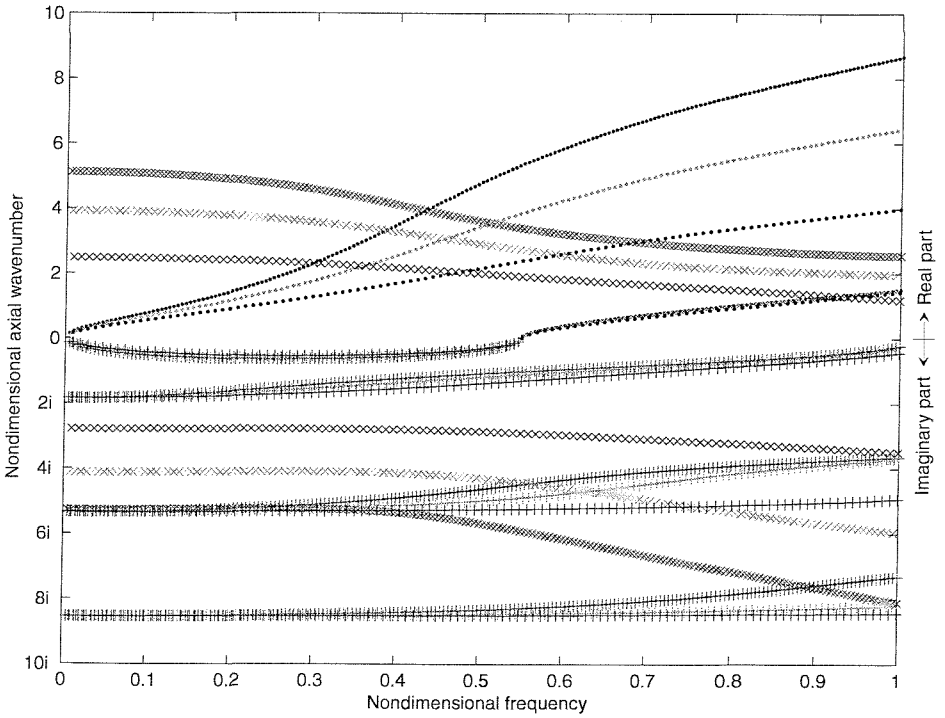

Figure 7.16: Dispersion curves for case 1(red), 6(green) and 7(blue). $n = 1$.

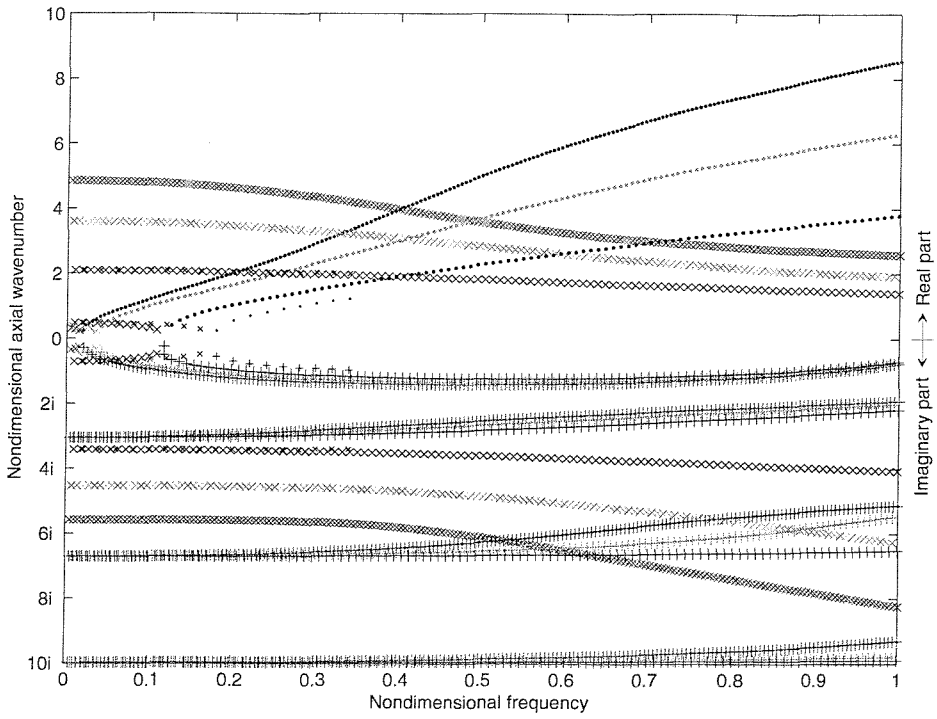

Figure 7.17: Dispersion curves for case 1(red), 6(green) and 7(blue). $n = 2$.

relative stiffness is also the reason for the propagating predominantly fluid wave ($b = 1$). At very low frequencies, the curves for the three cases overlap, but as the frequency is increased the same effect happens as for the imaginary wavenumbers. From the slope of the dispersion curves, it can be concluded that the group speed of the predominantly fluid wave is increased when the thickness of the pipe wall is increased.

At low frequencies, the complex branches behave largely as in vacuo. The small black crosses on figure 7.15 represent the in vacuo dispersion relation for low frequencies. At higher frequencies the trends are very similar for the three cases, and no differences can be seen.

Figures 7.16 and 7.17 show the dispersion curves for the $n = 1$ and $n = 2$ modes. The dispersion curves for the bending mode show the same picture as the curves for the axisymmetric mode. Figure 7.17 shows something interesting, as the cuton of the $n = 2$ mode is happening at a significantly higher nondimensional frequency for case 7 than for case 1 and 6. The small black symbols represent a part of the in vacuo dispersion curves for case 7. Comparing these with the blue curves show that the cuton frequency for the fluid loaded case is significantly lower. In section 7.2.1.1 it was hinted that the cuton frequency of the $n = 2$ could be used to classify the fluid loading of the shell. If this is correct, the fluid loading is still heavy even with the large h/a for case 7.

The point mobilities are plotted in figure 7.18. The larger the h/a ratio, the lower the mobility. This is probably a mass effect, as discussed for the heavy fluid loading. It can be seen that the number of modes cutting on below the ring frequency is reduced

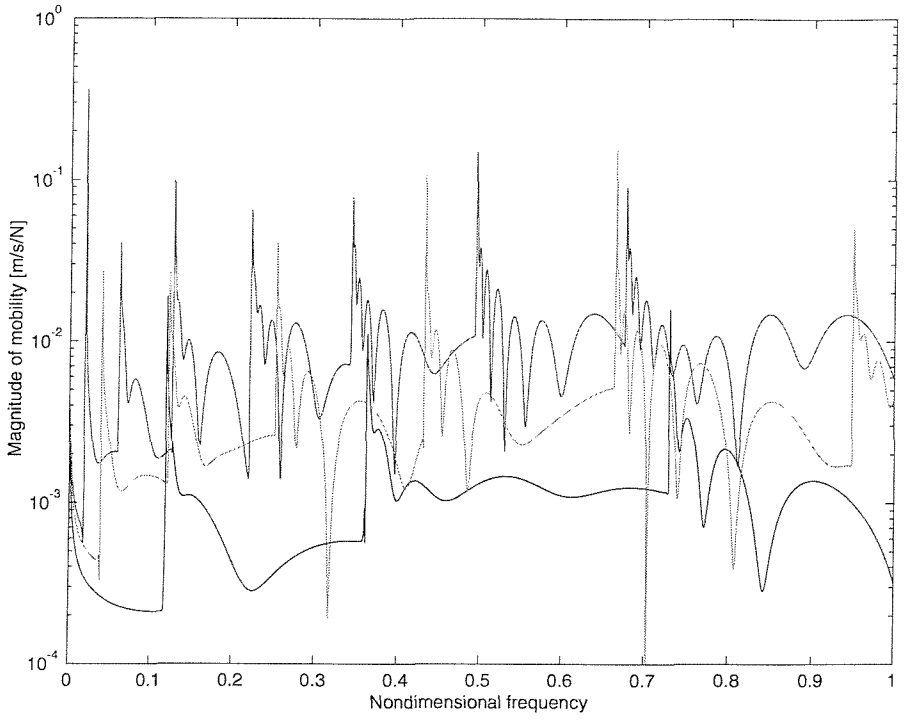

Figure 7.18: Point mobility for case 1(red), 6(green) and 7(blue). $s = 20$, $\theta_o = 0$.

when h/a is increased. This behaviour is predicted for the in vacuo shell by Cremer et al. (1988), but more modes are cutting on for the heavy fluid loaded shell than are predicted for the in vacuo case. This is not surprising, as the cuton frequency for higher order modes is reduced significantly with a heavy fluid load, and more modes will cut on below a specified frequency.

The main conclusion, from this part of the parameter study, is that the thickness ratio of the shell has some effect; but for the parameters investigated, the fluid loading remains heavy even for very large thickness ratios (up to $h/a = 0.25$). However, this conclusion may be wrong, as it is based on results from a shell theory that is taken to the limit.

7.2.4 Conclusion

The main conclusion to be drawn from this parameter study is that in the parameter space of industrial interest, the internal fluid loading is the most important factor causing departures from a collapse on the parameters chosen.

The cuton frequencies of the higher order coupled branches are largely affected by the fluid loading. In the case of light fluid loading case the cuton of the mainly shell waves is close to the cuton frequency of the in vacuo shell, while the cuton of the mainly fluid waves is close to the hard-walled duct. In the case of a heavy fluid loading, the cuton frequencies are significantly reduced for all waves. While the real reason for

this is hidden in the equations, it seems intuitively correct that a heavy fluid loading reduces the effective stiffness of the shell wall. A lower stiffness of the shell would reduce the effective ring frequency $f_{\text{ring,eff}}$, resulting in lower absolute frequencies for the same dimensionless frequency Ω. In a plot with a nondimensional frequency axis based on the ring frequency defined by the wall material alone (the 'normal' f_{ring}), the nondimensional cuton frequency of a fluid loaded wave would thus appear at a lower nondimensional frequency.

7.3 Comparison of different shell theories

An important part of the numerical modelling of shell vibrations is the choice of shell theory. A large number of shell theories exist, see e.g. Leissa (1973), each claiming to have some unique features. Different theories are used for different papers, often without any discussion of the choice of shell theory. No source so far has shown any of the theories to be clearly superior to the others. While it is not possible to promote one theory as superior to the others, it is possible to show the shortcomings of some of the theories. In this section the theories of Donnell-Mushtari, Flügge and Goldenveizer-Novozhilov are compared through their dispersion curves and predicted mobility for an in vacuo shell, corresponding to case 3 in table 7.1.

The three shell theories investigated in this chapter are all eighth-order thin shell theories. Leissa (1973) discusses the differences between the three shell theories in great detail, but in essence the differences are related to the different simplifying assumptions made to achieve the final equations of motion. For all the thin shell theories, a common assumption is the neglect of through-thickness displacement variations. A main difference between the thin shell theories is how they implement correction terms to compensate for the finite thickness of the shell wall.

7.3.1 Donnell-Mushtari theory

The Donnell-Mushtari shell theory is probably the simplest of the thin shell theories presented by Leissa (1973). The shortcomings of the Donnell-Mushtari shell theory are well known, see e.g. Hoff (1955), but nonetheless it is still widely used, probably mainly due to its relative simplicity. Some key papers dealing with the forced response of cylindrical shells use the Donnell-Mushtari shell theory, e.g. Fuller and Fahy (1982), Fuller (1984) and Pavic (1992).

The Donnell-Mushtari theory is used as the basic building block in the reference work by Leissa (1973). Any of the more complicated shell theories in Leissa's work can be described as the sum of two matrices, i.e.

$$L = L_{\text{D-M}} + \beta^2 L_{\text{Mod}} \tag{7.3}$$

where $L_{\text{D-M}}$ is the L-matrix according to the Donnell-Mushtari theory; L_{Mod} is the 'modifying' matrix; and β is the nondimensional thickness parameter defined by in

the comments to equation (5.1). Thus each of the more complicated shell theories differs from the Donnell-Mushtari theory by a matrix-operator which is multiplied by a constant that tends to zero in the lower limit of the h/a ratio.

The Donnell-Mushtari theory presented here is limited to constant thickness, thin-walled shells and it excludes the effects of initial stress, anisotropy, nonhomogeneity, shear deformation, rotary inertia, large deflections and surrounding media. Under these assumptions the Donnell-Mushtari operator is

$$L_{\text{D-M}} = \begin{bmatrix} L_{11} & L_{12} & L_{13} \\ L_{21} & L_{22} & L_{23} \\ L_{31} & L_{32} & L_{33} \end{bmatrix} \tag{7.4}$$

where the elements are

$$L_{11} = -\Omega^2 + \kappa^2 + \frac{1}{2}(1-\nu)n^2 \quad L_{12} = \frac{1}{2}(1+\nu)n\kappa \quad L_{13} = \nu\kappa$$

$$L_{21} = L_{12} \qquad L_{22} = -\Omega^2 + \frac{1}{2}(1-\nu)\kappa^2 + n^2 \qquad L_{23} = n$$

$$L_{31} = -L_{13} \qquad L_{32} = -L_{23} \qquad L_{33} = -\Omega^2 + 1 + \beta^2\left(\kappa^2 + n^2\right)^2 - \mathcal{F}$$

7.3.2 Goldenveizer-Novozhilov theory

The main differences on going from the Donnell-Mushtari theory to the Goldenveizer-Novozhilov theory can be summarised according to Leissa (1973) as

- The stress-displacement relation of the Goldenveizer-Novozhilov theory includes the influence of shell curvature in a fully consistent manner, whereas the Donnell-Mushtari theory neglects terms involving the tangential displacements.
- Terms in the force and moment resultants are examined in the Goldenveizer-Novozhilov theory and a careful analysis is made not to reject any significant terms, no matter their order (see e.g. Niordson (1985)), while the Donnell-Mushtari theory rejects all terms related to curvature of the shell, except for the L_{33} term where a second order term in β is retained. This way the Goldenveizer-Novozhilov theory avoids inconsistencies in the force and moment resultants that are present in the other two shell theories presented here.

The L-matrix of the Goldenveizer-Novozhilov shell theory can be written as

$$L_{\text{GN}} = \begin{bmatrix} L_{11} + L_{11}^{\text{GN}} & L_{12} + L_{11}^{\text{GN}} & L_{13} + L_{11}^{\text{GN}} \\ L_{21} + L_{11}^{\text{GN}} & L_{22} + L_{11}^{\text{GN}} & L_{23} + L_{11}^{\text{GN}} \\ L_{31} + L_{11}^{\text{GN}} & L_{32} + L_{11}^{\text{GN}} & L_{33} + L_{11}^{\text{GN}} \end{bmatrix} \tag{7.5}$$

where the elements without superscripts are the ones from the Donnell-Mushtari formulation, while the superscripted elements are

$$L_{11}^{\mathrm{GN}} = 0 \quad L_{12}^{\mathrm{GN}} = 0 \quad L_{13}^{\mathrm{GN}} = 0 \quad L_{21}^{\mathrm{GN}} = 0$$
$$L_{22}^{\mathrm{GN}} = -\frac{3}{2}(1-\nu)\beta^2\kappa^2 \quad L_{23}^{\mathrm{GN}} = -\frac{3-\nu^2}{\beta}\kappa^2 \quad L_{31}^{\mathrm{GN}} = 0 \quad L_{32}^{\mathrm{GN}} = -L_{23} \quad L_{33}^{\mathrm{GN}} = 0$$

7.3.3 Flügge theory

The differences between the Flügge theory and the other two theories relate to both the stress-displacement relation and the force and moment resultants. The stress-displacement relation used in the Flügge theory is similar to that in the Goldenveizer-Novozhilov theory, but the force and moment resultants are different from both the previous theories. Leissa (1973) remarks that integration of the unsimplified force and moment resultants over the thickness of the shell is extremely cumbersome, and this integration is simplified in the Flügge theory, but in a slightly inconsistent manner cleverly avoided in the Goldenveizer-Novozhilov shell theory.

The full L-matrix for the Flügge theory is shown in equation (6.6), but using the same form as for equation (7.5), the correction terms are

$$L_{11}^{\mathrm{F}} = \frac{1}{2}(1-\nu)\beta^2 \quad L_{12}^{\mathrm{F}} = 0$$
$$L_{13}^{\mathrm{F}} = -\frac{1}{2}(1-\nu)\beta^2 n^2\kappa + \beta^2\kappa^3 \qquad L_{21}^{\mathrm{F}} = 0$$
$$L_{22}^{\mathrm{F}} = -\frac{3}{2}(1-\nu)\beta^2\kappa^2 \qquad L_{23}^{\mathrm{F}} = -\frac{1}{2}(3-\nu)n\beta^2\kappa^2$$
$$L_{31}^{\mathrm{F}} = -L_{13} \qquad L_{32}^{\mathrm{F}} = -L_{23} \qquad L_{33}^{\mathrm{F}} = \beta^2\left(1-2n^2\right)$$

7.3.4 Comparison of computed dispersion relations and mobility

Figure 7.19 shows the $n = 0$ dispersion curves for an in vacuo PVC shell (corresponding to case 3 in table 7.1) calculated using the three different shell theories. The differences are clearly very small indeed, as the curves are indistinguishable from each other.

Figure 7.20 shows the dispersion curves for $n = 1$. In this figure there is an interesting difference at very low frequencies, as a few red crosses can be seen at very low frequency where there only are green and blue dots (difficult to see in figure 7.20 at the scale plotted, but a zoom is shown in figure 7.21). This means that the Donnell-Mushtari shell theory predicts a complex wave where the other two theories predict a propagating wave. At very low frequency there is no red propagating wave, as the first propagating wave cuts on at $\Omega \approx 0.01$. This is clearly an unphysical behaviour, as beam bending can happen at all frequencies. The cuton of the bending mode persists when fluid loading is included (not shown here).

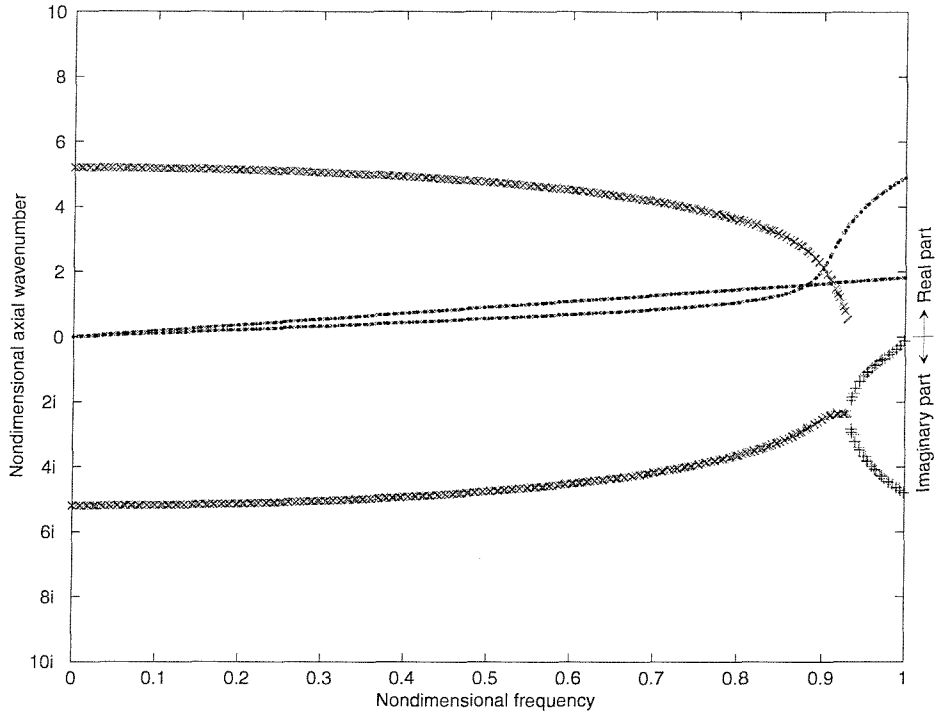

Figure 7.19: Dispersion curves for case 3, $n = 0$. The shell theories of the curves are Donnell(red), Flügge(green) and Goldenveizer(blue).

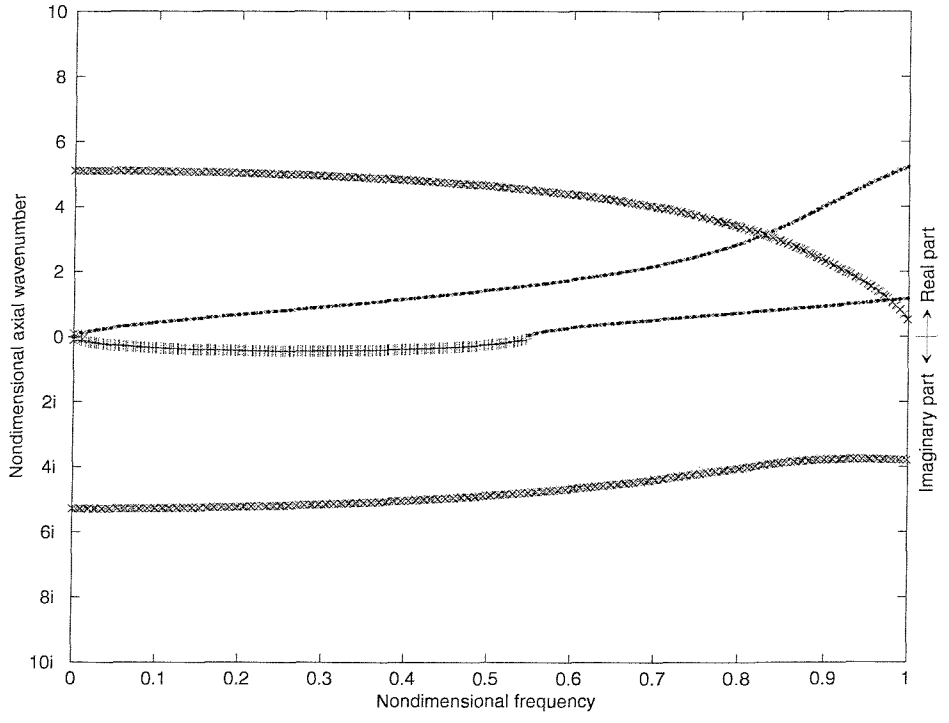

Figure 7.20: Dispersion curves for case 3, $n = 1$. The shell theories of the curves are Donnell(red), Flügge(green) and Goldenveizer(blue).

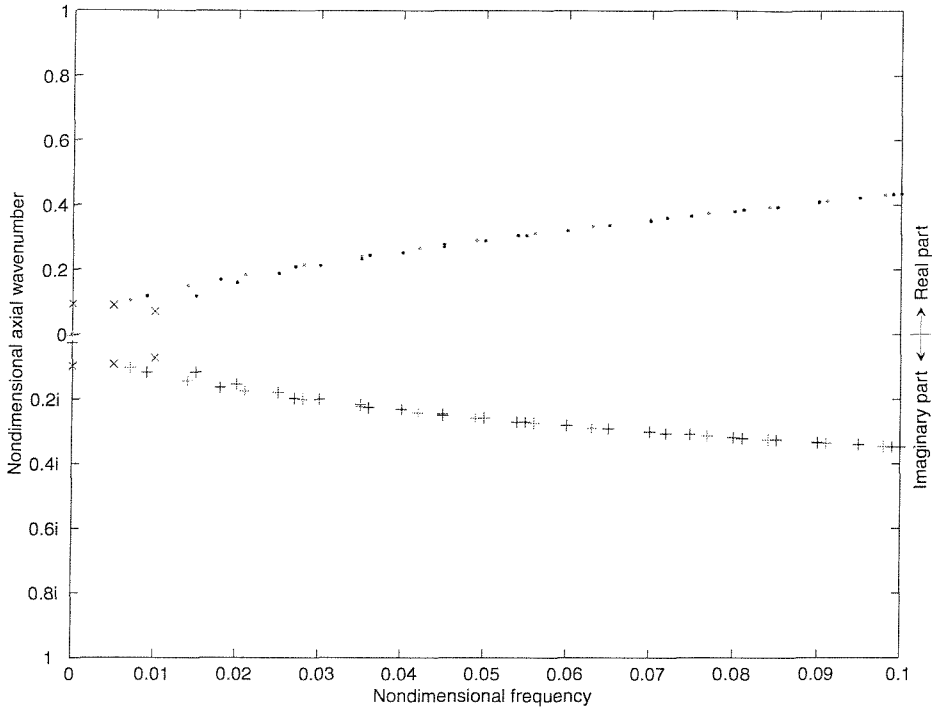

Figure 7.21: Detail of figure 7.20.

The reason for the cuton of the $n = 1$ mode is the exclusion of correction terms in the Donnell-Mushtari theory for all but the (3,3)-term in equation (7.4). The correction terms involving β are very small, but in beam bending for long shells at low frequencies, the main terms largely cancel, leaving the correction terms to dominate. The problem with the Donnell-Mushtari theory arises because the correction terms are inconsistently implemented, since they are included only in the $L_{3,3}$ term, and left out from the rest of the matrix. The two shell theories that include more correction terms have dispersion curves that are very close indeed. Even for small h/a-ratios, the effects of the correction terms are significant at low frequencies where the free wavenumbers are inherently small, or near cuton of higher order modes where the cutting on wavenumber is close to zero. Where the wavenumbers are large, the terms of $L_{\text{D-M}}$ tend to dominate.

The dispersion curves for $n = 2$ are seen in figure 7.22. The predicted cuton frequency of the $n = 2$ mode is significantly higher for the Donnell-Mushtari shell theory than for the other two. Apart from this, the dispersion curves are very close indeed.

In figure 7.23 the point mobility is plotted. In this figure, the Donnell-Mushtari results are again different from the other two shell theories. The cuton of the bending mode is represented in the red curve as a peak at very low frequency. The other two theories produce virtually identical mobility up to $\Omega \approx 0.6$ and significant differences occur only near the ring frequency. Noting that the peaks at high frequencies are due to cuton of higher order modes, this observation agrees with the paper of Hoff (1955), that discusses the precision of the Donnell-Mushtari equations; he predicts errors up to 11 percent in comparison with the Donnell and Flügge equations. Hoff (1955) states that

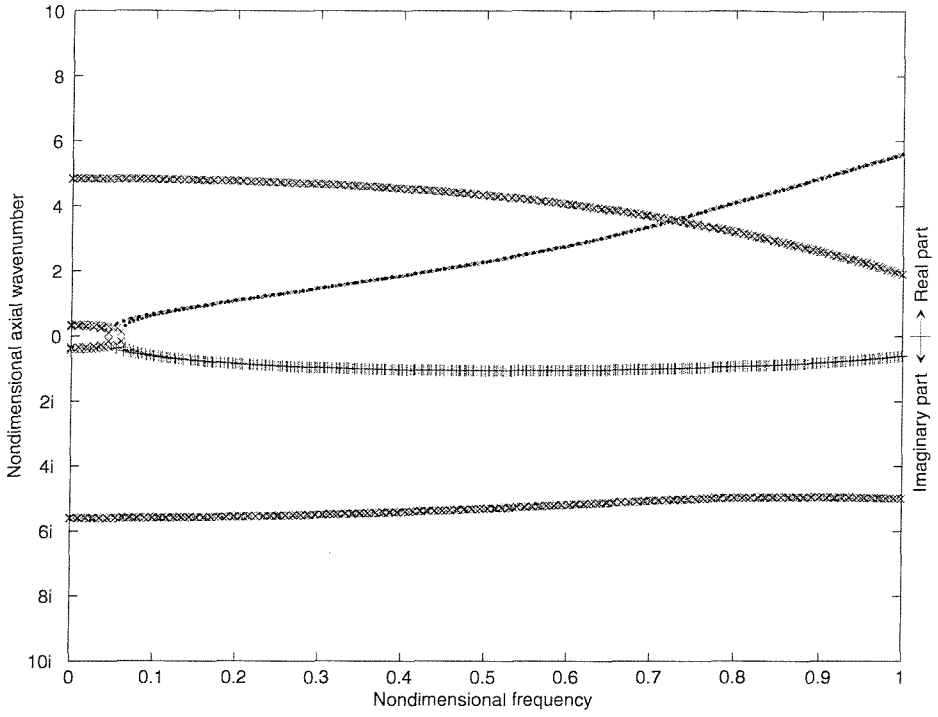

Figure 7.22: Dispersion curves for case 3, $n = 2$. The shell theories of the curves are Donnell(red), Flügge(green) and Goldenveizer(blue).

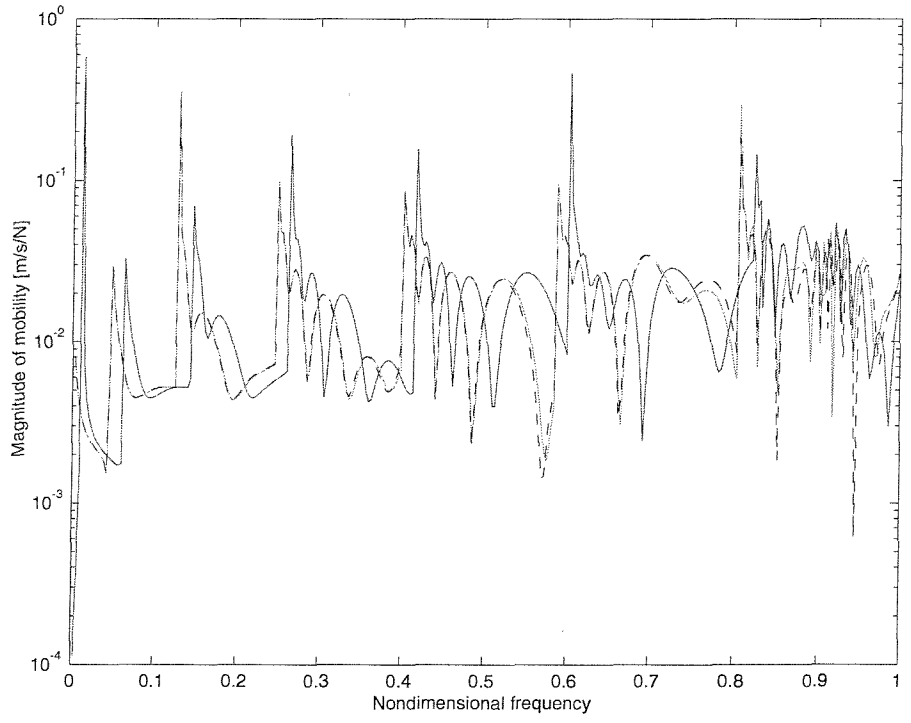

Figure 7.23: Point mobility for case 3. $s = 20$, $\phi = 0$. The shell theories of the curves are Donnell(red), Flügge(green) and Goldenveizer(blue).

the errors in the Donnell-Mushtari shell theory tend to become smaller as the frequency and circumferential mode order becomes larger. This statement cannot be confirmed by the present investigation because of its limited frequency range ($0 < \Omega < 1$).

7.3.5 Conclusion

Three different thin shell theories are compared: Donnell-Mushtari, Goldenveizer-Novozhilov and Flügge. The Donnell-Mushtari theory is the simplest; it leaves out some correction terms to allow for finite thickness of the shell. In the limit of vanishing shell thickness these correction terms are of no importance, except for the bending mode ($n = 1$) at low frequencies, where the correction terms related to finite shell thickness dominate, leaving the Donnell-Mushtari teory with an unphysical cuton of the bending mode.

The other two shell theories produce very similar results, except for a few differences near the ring frequency of the shell. As the frequency range of interest for the present thesis is rather low, extending only up to $\Omega = 0.15$, either of the two theories may be used. It cannot be concluded that the Flügge theory is the best of the three, but it can be concluded that the Donnell-Mushtari theory is not well suited for the industrial application, with its low frequencies and low circumferential mode orders. Either of the two other theories could have been used and the Flügge theory was chosen.

7.4 Summary

A parameter study of shell materials, internal and external fluids and shell geometry has been conducted in this chapter. To limit the complexity of the study the parameters of main industrial interest were investigated through dispersion curves and point mobilities. It was concluded that the internal fluid loading is the most important factor causing departures from a collapse on the shell parameters chosen. Significant changes in both the dispersion curves and mobilities are also related to the fluid loading of the shell. The principal effects of fluid loading observed in the parameter study can by and large be related to the properties of the fluid loading term defined in equation (6.7). This equation predicts that increased shell thickness, decreased shell radius or decreased density ratio, ρ_f/ρ_s, will all decrease the effect of the contained fluid and thus decrease the coupling of the shell and fluid behaviour. All the conclusions presented in this chapter largely confirm this simple interpretation, although the effect may be small.

As the shell theory is a key part of the prediction model in chapter 6, a study was made to compare three different shell theories. The conclusion of this study was that the simplest of them is not well suited for the frequency range of interest to the present thesis, while the other two (including the one used in the parameter study) produce very similar results, that also seem plausible from a physical point of view.

Part III

Experimental measurements of power flow

Chapter 8

Power flow measurements: pipe with light fluid loading

The experiments presented in this chapter are all obtained from measurements on a PVC pipe with air inside and outside. As the external diameter of the pipe is 63 mm and the wall thickness 1.8 mm, the resulting fluid loading is light. The excitation in the measurements is provided by a radial force, and the pipe response is measured using an accelerometer that is moved around the circumference to provide modal measurements of accelerance.

As discussed in the parameter study in chapter 7, light fluid loading has only a marginal influence on the vibration of a pipe. The power flow predictions presented later in this chapter show that the structure-borne power flow in the pipe wall is approximately 2 orders of magnitude times greater than the fluid-borne power flow, when the pipe is excited by a radial point force. All the results regarding the shell vibrational response of the pipe wall in this chapter therefore also apply to the in vacuo shell.

The first section introduces the experimental setup used, while the second presents comparisons between the predicted and measured accelerance. The third section presents two power flow measurement principles to quantify the power flow, and shows a comparison between predicted and measured power flow for a light fluid loaded pipe. The fourth section assesses the measurement principle, and the final section summarises the main conclusions.

8.1 Experimental setup

The light fluid loaded experiments are conducted on a suspended 5 m PVC pipe with air both inside and outside, running through anechoic terminations at either end, as seen in figure 8.1. The excitation of the pipe is provided by an externally applied radial point force at the axial midpoint of the pipe. The test pipe has an outer diameter of 63 mm and a wall thickness of 1.8 mm (corresponding to case 3 in table 7.1), so the

Figure 8.1: Picture of experimental setup.

length of pipe on either side of the excitation point corresponds to approximately 82 radii. All axial distances and circumferential angles were measured from the point of excitation.

A key feature of the test rig is the anechoic terminations at either end of the pipe. The choice of instrumentation and the subsequent postprocessing of the measurements in the experiments relies on the assumption that all vibroacoustic power flow is away from the point of excitation. To accomplish this on a finite pipe, anechoic terminations are used. These anechoic terminations attenuate any reflected waves from the end of the pipe, resulting in a heavily attenuated standing wave pattern between the two anechoic terminations. The anechoic termination is discussed in more detail in section 8.4.1.

The pipe is suspended horizontally by rubber strings having a very low natural frequency (approximately 1 Hz pendulum mode and approximately 10 Hz in stretching). The actual excitation of the pipe is at significantly higher frequencies (reliable measurements are expected above approximately 100 Hz). The vibration of the pipe is thus largely unaffected by the presence of the strings, as the forced excitation is in the mass controlled region of resonance in the rubber strings. Removing some of the strings confirmed that all the results obtained were independent of the suspension.

The excitation is provided by a random signal from the analyser through a power amplifier to a miniature shaker connected to the pipe through a thin (0.8 mm) sting. At the relatively low frequencies of interest, the corresponding structural and fluid wavelengths are relatively long compared to the size of the sting connection, and the excitation therefore behaves to a large extent like a radial point force. The excitation

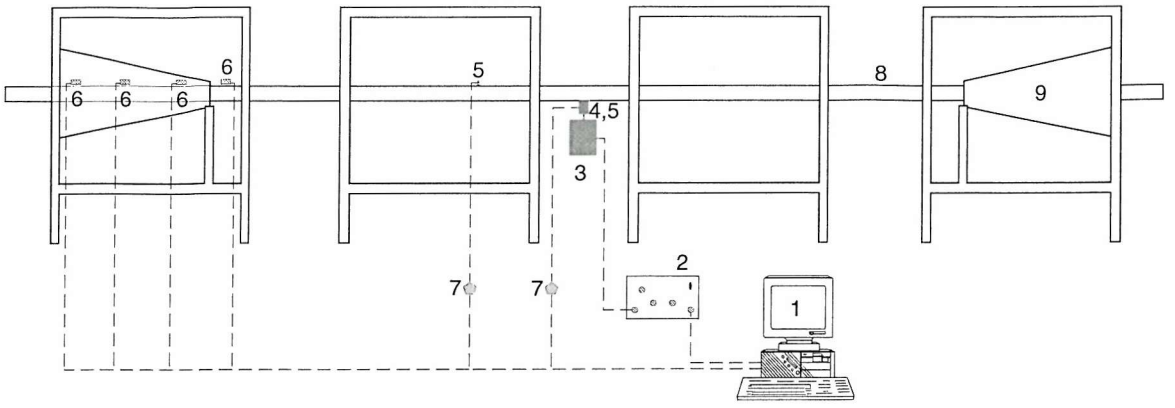

Figure 8.2: Sketch of the experimental setup used for the experiments on a pipe with light fluid loading.

1. B&K Type 3560, PULSE Multi-analyzer and signal generator
2. B&K Type 2706, Power amplifier
3. B&K Type 4810, Mini-shaker
4. B&K Type 8203, Force transducer (3.6 pC/N, 1.1 g)
5. B&K Type 4374, Miniature accelerometer (0.141 pC/m s^{-2}, 0.65 g)
6. B&K Type 4507, Deltatron accelerometer (10 mV/m s^{-2}, 4.8 g)
7. B&K Type 2646, Deltatron charge amplifier (1mV/pC)
8. PVC pipe (L=5 m, D_o=63 mm, h=1.8 mm)
9. Anechoic termination

Table 8.1: Instrumentation used in the experiments with light fluid loading.

is discussed in more detail in section 8.4.3. The radial input force from the shaker is measured using a lightweight force transducer (mass approx. 1.1 g). The acceleration of the point of excitation is measured by a lightweight accelerometer (mass 0.65 g). The power input from the radial force can be deduced from these two measurements, as discussed in section 8.3.1.1. The point response of the pipe wall at different axial and circumferential positions is measured by a lightweight accelerometer (mass 0.65 g). The modal response of the pipe is deduced from accelerometer measurements, using the decomposition technique discussed in section 8.4.4.

The experimental setup is sketched in figure 8.2 and the instrumentation used is listed in table 8.1.

8.2 Accelerance for pipe excited by radial point force

Figures 8.3-8.6 show the measured and predicted modal accelerances for the light fluid loaded case for $n = 0$ to 3. All the figures are made the same way: Measurements are in red colour and predictions are in green. The measurements are at positions 9, 450 and 750 mm from the point of excitation, corresponding to nondimensional positions $s = 0.29$, 14.7 and 25.1. The position closest to the point of excitation is in the vibroacoustic near field, while the other two are in the far field. The near field position is presented with a solid line, the mid position with a dashed line and the farthest with a dash-dot line.

To make the comparison between measured and predicted values as meaningful as possible, some fitting of the material properties has been done. A textbook value of the Young's modulus for PVC is 3,000-4,000 MPa (Vink 1995) with a general Poisson's ratio for hard plastic around 0.4. While the Poisson's ratio is retained, the Young's modulus used in the prediction model has been fitted to the experiments, so the predicted and experimental cuton frequency of the $n = 2$ circumferential mode is the same. The Young's modulus used in the predictions is $E = 3,800$ MPa.

The figures in this section all show the radial accelerance, which is the radial acceleration response of the pipe when excited by unit radial input force. When measuring the accelerance on the B&K analyser, the H_1 estimator is used, with the radial excitation force as the input signal and the acceleration from the accelerometer as the output signal. While the choice of H operator is arguable, see e.g. Fahy and Walker (1998) chapter 6, there is very little difference when using H_2 or H_3. The measured modal accelerance is decomposed from 12 measurement points around the circumference. There is no visual difference when using 24 points for the decomposition.

General comments. A common feature of all measurements is that the agreement between the measurement and prediction improves as the measurement position is moved towards the point of excitation. There are probably three reasons for this: a

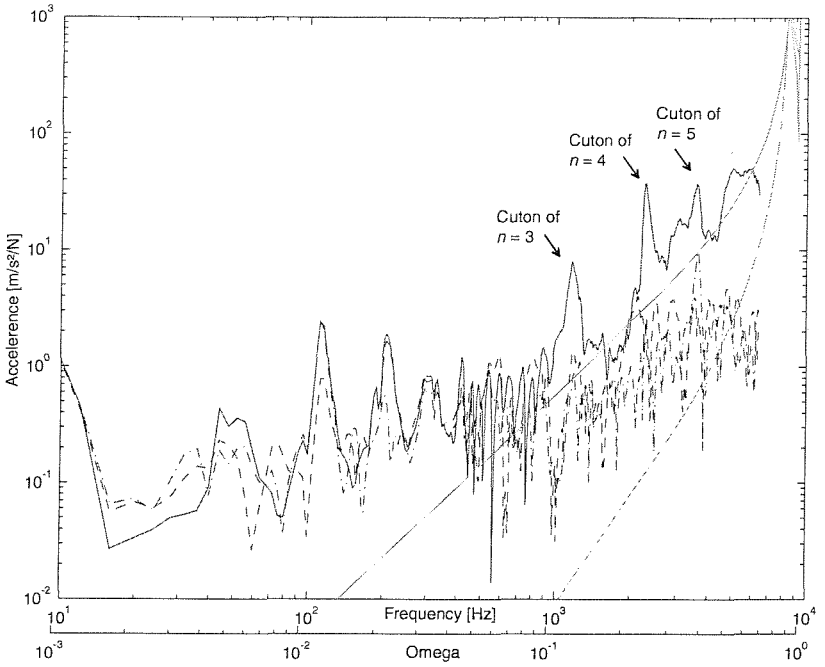

Figure 8.3: Modal accelerance for a pipe with light fluid loading excited by a radial point force, $n = 0$. The predicted response is green and the measured red; the solid line corresponds to $s = 0.29$, the dashed line to $s = 14.7$ and the dash-dot line to $s = 25.1$.

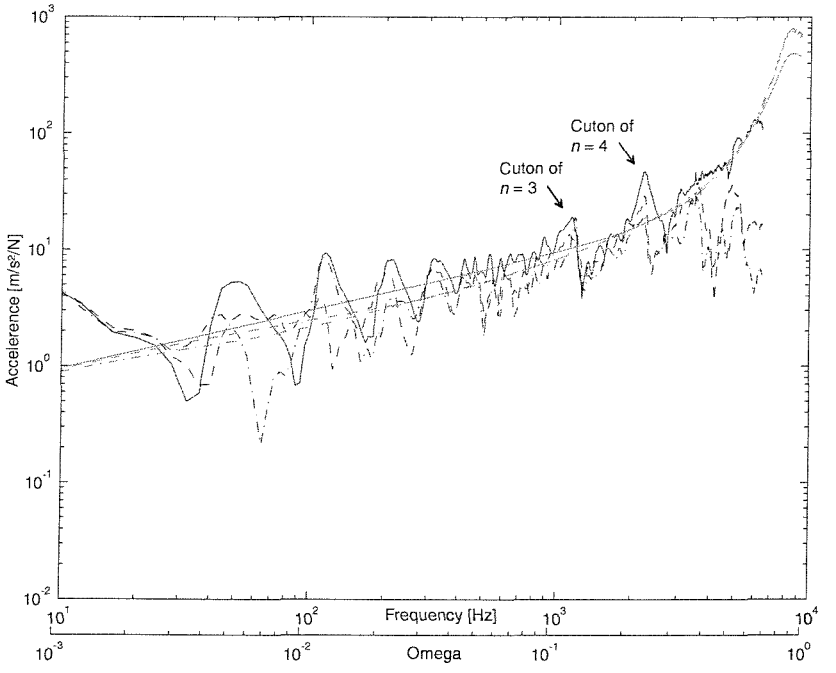

Figure 8.4: Modal accelerance for a pipe with light fluid loading excited by a radial point force, $n = 1$. The predicted response is green and the measured red; the solid line corresponds to $s = 0.29$, the dashed line to $s = 14.7$ and the dash-dot line to $s = 25.1$.

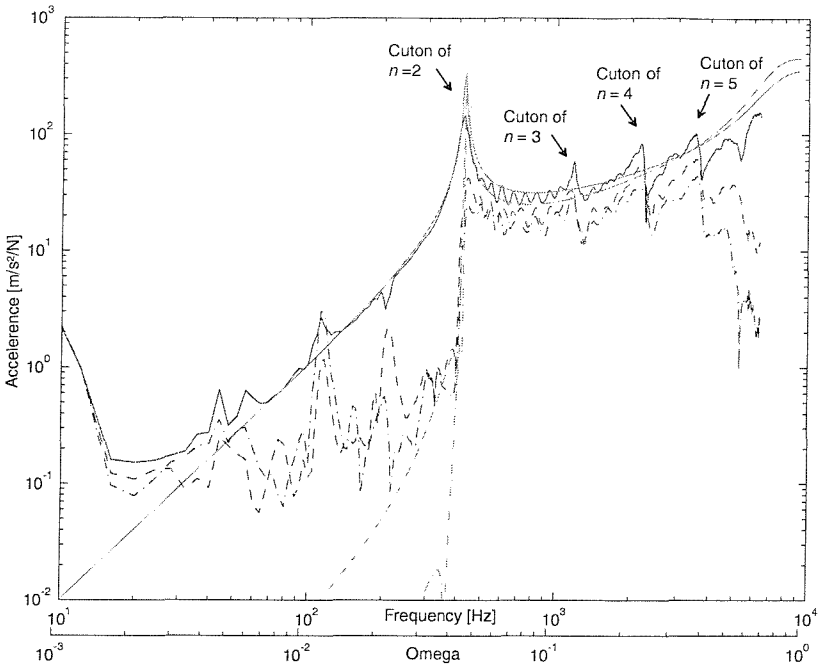

Figure 8.5: Modal accelerance for a pipe with light fluid loading excited by a radial point force, $n = 2$. The predicted response is green and the measured red; the solid line corresponds to $s = 0.29$, the dashed line to $s = 14.7$ and the dash-dot line to $s = 25.1$.

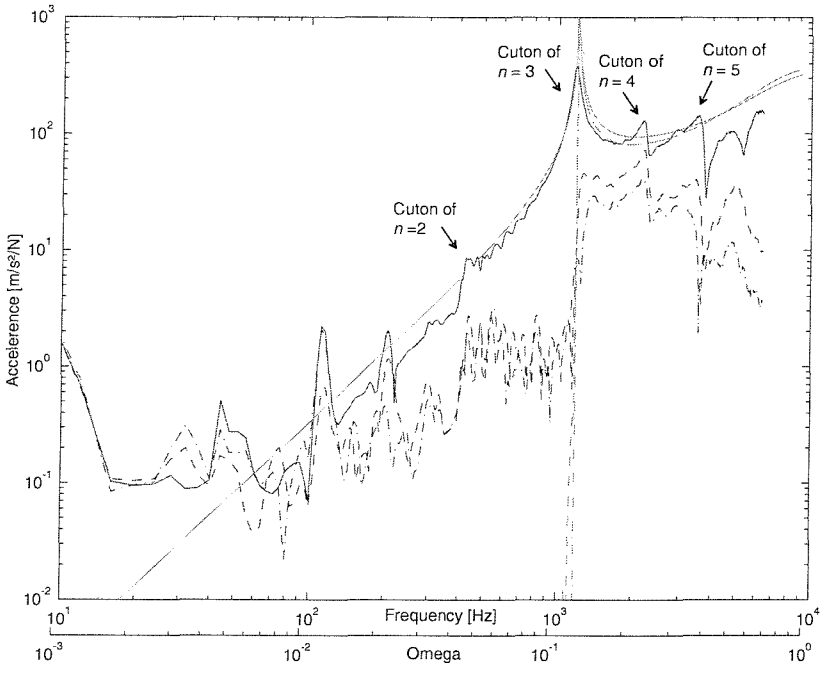

Figure 8.6: Modal accelerance for a pipe with light fluid loading excited by a radial point force, $n = 3$. The predicted response is green and the measured red; the solid line corresponds to $s = 0.29$, the dashed line to $s = 14.7$ and the dash-dot line to $s = 25.1$.

near field effect; a distance effect related to the scattering of the structural vibration by imperfections in the pipe; and a distance effect related to the internal damping of the pipe material.

The near field response of the pipe includes effects from the evanescent and complex branches. These branches tends to broaden the peaks related to cuton of higher order modes, providing a relatively large accelerance response over a wide frequency range.

The PVC pipe used in the experiments is industrial grade and imperfections are visible to the naked eye, as some weld lines are faintly visible on the surface of the pipe, probably due to the production process. This suggests the pipe wall is not homogeneous. Measurements of the pipe wall thickness h and mean radius a show variations up to 10 % around the circumference of the pipe. Neither of these imperfections are modelled in the prediction model and their effects are therefore not incorporated in the predicted response. The longer a wave travels in the pipe, the larger is the accumulated effect of the scattering of vibrational energy by the imperfections, and the larger is the difference between the predicted and the measured response. The effect of the scattering is expected to be larger at higher frequencies, as the relative sizes of the imperfections become larger compared to the wavelength of the vibrational waves in the pipe.

The loss factor of PVC was measured to be approximately 3 %, using the half power bandwidth method, see e.g. Norton (1989). A given distance away from the point of excitation represents fewer wavelengths in the material for low frequency vibrations than for high frequency vibrations. As the loss factor is related to the proportion of vibrational energy lost per cycle, the high frequency response at a given measurement position is attenuated more than the low frequency response. This is consistent with figures 8.3-8.6 where the measured high frequency accelerance at $s = 25.1$ is smaller than at $s = 14.9$.

All the modes with small accelerance at low frequencies (i.e. all modes but the $n = 1$ mode) seem to have a noise floor of approximately $1 \cdot 10^{-1}$ m/s^2/N. This noise floor is not related to the dynamic capabilities of the accelerometer or the force transducer, but to the measurement method technique itself, as the modal decomposition with accelerometers cannot discriminate modes perfectly. When placing the accelerometer around the circumference during the measurement, small errors of placement result in large relative errors in the modal response of the weakly-excited modes, although the absolute magnitude of the errors is very small indeed. This phenomena is dubbed modal leakage, as accelerance apparently 'leaks' from one mode to another. Modal leakage may also be caused by departures from axisymmetric geometry (e.g. the geometry variations mentioned above).

Comments regarding the axisymmetric mode. While the agreement between the measured and predicted accelerance for $n = 0$ is better at high frequencies, it seems quite bad at low frequencies. The predicted response is very small at low frequencies (less than 10^{-5} m/s^2/N at 100 Hz) and the aforementioned noise floor dominates. The reason for this is simply that a radial point force is very inefficient in exciting the axisymmetric mode below the ring frequency.

In the near field of the point of excitation, there are some local shell deformations related to the complex roots of the dispersion relation, as discussed in section 6.2, but they are not propagated to the far field. In figure 8.3 this can be seen as a significantly larger response at $s = 0.29$ than for the two far field points. Close to the ring frequency of the pipe, this difference between the predictions of near and far field tends to disappear when the pipe resonates as a ring. The radial point force is apparently able to excite the ring frequency resonance efficiently, although this is not important for the industrial application.

The peaks at low frequencies are probably a result of modal leakage from the standing bending waves, and from the cuton of the higher order modes (e.g. the $n = 2$ mode at 420 Hz).

Comments regarding the bending mode. The comments for $n = 0$ regarding modal leakage also apply here, where the cuton of the $n = 2$ mode results in a peak at approximately 400 Hz, and likewise for the cuton of the $n = 3$ mode at approximately 1 kHz. The modal leakage to the bending mode mode seems smaller than to the $n = 0$ mode, but this is mainly due to the significant response of the bending mode itself, thus making the relative impact smaller.

A radial point force is very efficient in exciting the bending mode ($n = 1$) of the pipe, and this mode therefore dominates the response of the pipe at low frequencies. From figure 8.4 it can be seen that the predicted accelerance for the bending mode at 100 Hz is approximately 3 $\mathrm{m/s^2/N}$ for $s = 0.29$, while the predicted accelerance for the breathing mode is approximately $7 \cdot 10^{-3}$ $\mathrm{m/s^2/N}$. The predicted response of the bending mode is thus a factor of approximately 430 larger than the breathing mode at 100 Hz. When comparing the measured response of the bending and breathing, the factor is only 30. This is probably an artifact from the accelerometer decomposition method, but this has only has a marginal influence on the total power flow prediction, as shown later.

The peaks below the cuton frequency of the $n = 2$ mode are not related to cuton of other modes, as $n = 2$ is the mode with the lowest cuton frequency. Instead, these peaks probably indicate standing waves in the axial direction, with the characteristic peak-and-trough appearance of a resonance. The anechoic termination is supposed to remove any reflections from the end of the pipe, but apparently it is not very efficient at low frequencies. This is hardly surprising as the anechoic termination is only 0.8 m long while the bending wavelength at 100 Hz is close to 10 m. If better low frequency performance of the measurement of the bending mode were required, it would be necessary to use a longer pipe combined with a larger anechoic termination.

Comments regarding the higher order modes. The $n = 2$ mode is the first mode not cut on from zero frequency. At low frequencies, the modal accelerance is quite small and the measurement noise floor dominates the response, but near the cuton frequency the accelerance rises sharply. There is very good agreement between the theoretical prediction and the measurement, especially in the near field. Peaks are evident at

the cuton frequencies of the higher order modes, probably due to modal leakage. It should be noted that the measured curves at high frequencies show a progressive decay with the distance from the source, while the predicted curves almost overlap. This is interpreted as a damping effect where the damping of the shell material dissipates energy from the propagating branches, thus reducing the response the farther away from the source. The reason for this being more pronounced at high frequencies is probably that the number of vibration cycles needed to propagate to a given distance is larger at high frequencies, while the proportion of energy dissipated per cycle is constant (related to the loss factor of the material). This effect could be investigated in more detail by introducing a complex Young's modulus in the prediction model, but the small discrepancy at high frequencies has been accepted for this study.

The appearance of figure 8.6 is similar to 8.5 apart from the cuton frequency. The modal leakage into $n = 3$ from the cuton of the $n = 2$ mode is not very pronounced in the near field, but for the far field points the accelerance level raises approximately one order of magnitude, probably due to the aforementioned measurement noise floor.

8.2.1 Synthetic point accelerance

A point response can be interpreted as a sum over all circumferential modes, as shown in equations (6.8) and (6.9). In figures 8.7, 8.8 and 8.9 the contributions from the different circumferential modes are summed up for a near field point ($s = 0.29$) and for two far field points ($s = 14.9$ and $s = 25.1$). This summed response, normalised by the point input force, can be interpreted as a synthetic point accelerance, not directly measured but synthesised from all 12 measurement points around the circumference.

Even with the small errors shown in the modal decomposition shown in the last section, the smoothness of the curve in figure 8.7 is striking. The standing waves at low frequencies disturb the otherwise excellent agreement at low to mid frequencies. The measured peaks are slightly lower than the predicted peaks, but this is probably due to the damping of the shell material, tending to reduce the amplitude of the cuton resonance. At high frequencies, the predicted response is slightly higher than the measured. As this is very close to the point of excitation ($s = 0.29$), it is probably not related to damping, but more likely due to the mass loading effects from either the point of excitation or the accelerometer. The local loading effects are discussed in more detail in section 8.4.3.

The measured accelerance curves in figures 8.8 and 8.9 are not as smooth as in figure 8.7, but the overall agreement is good except at high frequencies where the measured response tends to roll off. The detail of the troughs and peaks are smeared out, probably due to the scattering discussed in the last section. The comments from figure 8.7 regarding standing waves and mass loading also apply in the far field. However the roll off at high frequencies is much more evident in the far field than in the near field. This suggests that a significant part of the high frequency energy is dissipated by damping through the almost 15 and 25 radii from the point of excitation.

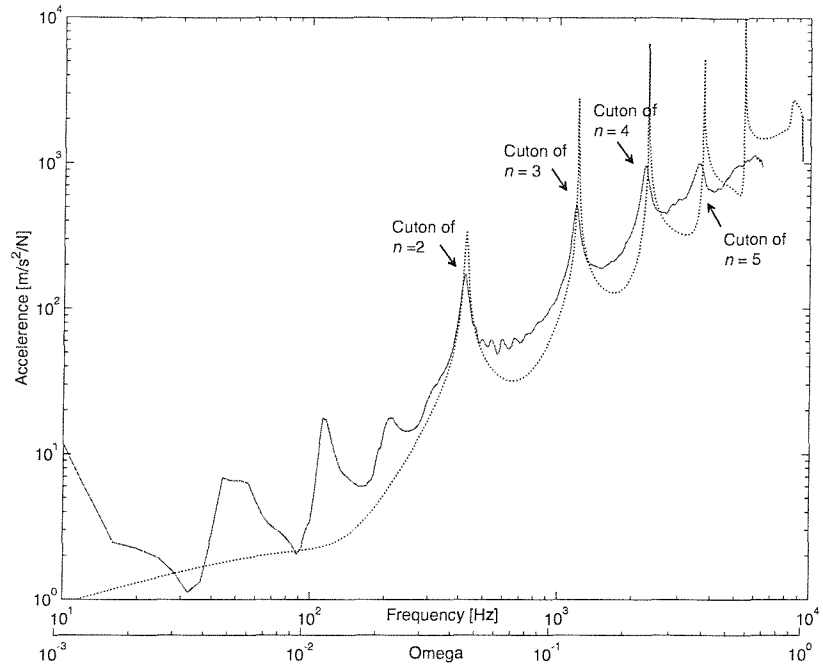

Figure 8.7: Synthetic point accelerance for a pipe with light fluid loading excited by a radial point force, $s = 0.29$. The line for the predicted response is dotted and the measured is solid.

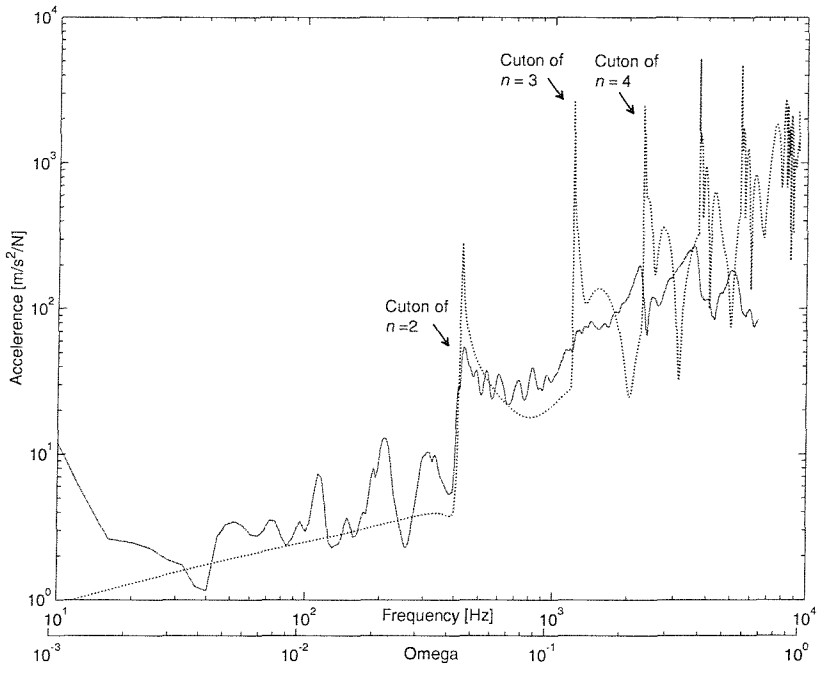

Figure 8.8: Synthetic point accelerance for a pipe with light fluid loading excited by a radial point force, $s = 14.9$. The line for the predicted response is dotted and the measured is solid.

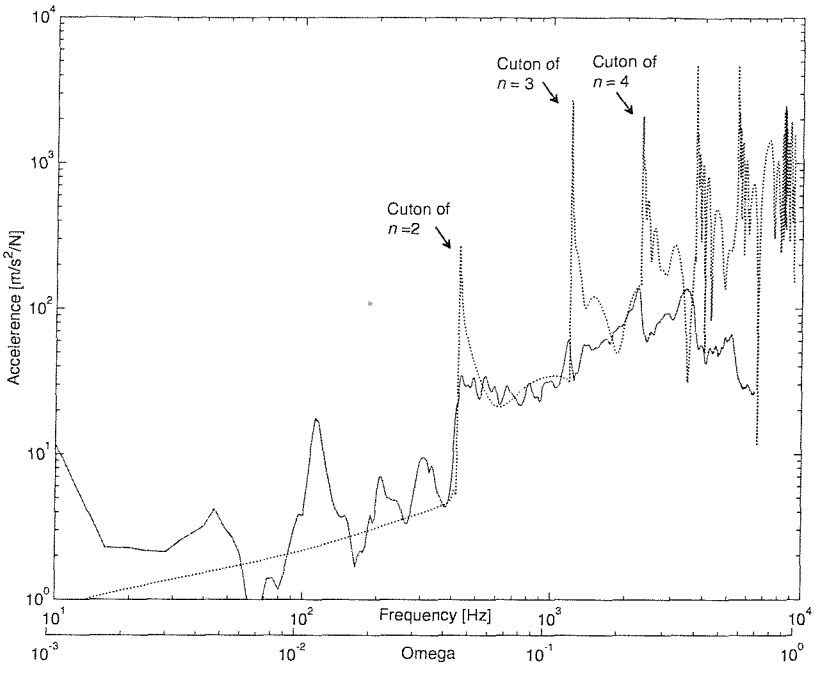

Figure 8.9: Synthetic point accelerance for a pipe with light fluid loading excited by a radial point force, $s = 25.1$. The line for the predicted response is dotted and the measured is solid.

8.3 Comparison of measured and predicted power flow

8.3.1 Measurement of power flow

Two different power flows are relevant for these experiments, namely the input power flow and the transmitted power flow. Unfortunately, only the input power flow can be quantified directly through measurements, while the transmitted power cannot be measured directly. In this section an indirect method of power flow estimation is presented. For a lossless system the two power flows should be identical: this gives a way of validating the indirect power flow method, as the two measurements can be compared.

The input power flow to the pipe can be quantified using the measurement of force input and acceleration of the pipe, as presented in the following section. The transmitted power flow is quantified from modal measurements of the displacement as presented in section 8.3.1.2.

8.3.1.1 Input power to a structure

The time averaged input power flow to the pipe can be calculated using simultaneous measurements of input force from the shaker and the pipe's velocity response. The input force is measured directly using a force transducer, while the velocity is inferred by integration of the measured acceleration response of the point of excitation at the pipe wall.

The time averaged power flow for complex, single frequency harmonic excitation is

$$\langle P_{in} \rangle = \frac{1}{T}\int_0^T F_i V_i dt = \frac{1}{T}\int_0^T \mathrm{Re}(F\mathrm{e}^{-i\omega t})\mathrm{Re}(V\mathrm{e}^{-i\omega t})dt = \frac{1}{2}\mathrm{Re}(FV^*) \tag{8.1}$$

where $F_i = \mathrm{Re}(F\mathrm{e}^{-i\omega t})$ and is the instantaneous force; $V_i = \mathrm{Re}(V\mathrm{e}^{-i\omega t})$ the instantaneous velocity; and $T = 2\pi/\omega$ is the period of vibration. The velocity and force can be related via mobility or impedance by

$$M = \frac{1}{Z} = \frac{V}{F} \tag{8.2}$$

where M and Z are the point mobility and impedance, respectively. Using this relation, equation (8.1) can be rewritten in the forms

$$\langle P_{in} \rangle = \frac{1}{2}|F|^2\mathrm{Re}(M) \tag{8.3}$$

$$\langle P_{in} \rangle = \frac{1}{2}|V|^2\mathrm{Re}(Z) \tag{8.4}$$

The mobility and force magnitude (or the impedance and velocity magnitude) can be extracted from the measurement using the PULSE Multi-analyser.

8.3.1.2 Modal power flow

As shown in section 6.1.4, it is possible to predict the power flow both in the near field and in the far field. In the near field, the power flow computation is complicated, as all branches of a given circumferential mode participate in the redistribution of power flow between the branches. The cross-terms where the force induced by one branch interacts with the displacement produced by another branch play a significant role in this redistribution. However, it is well known that all power flow in the far field is carried by the propagating branches.

In the light fluid loaded case, it is assumed that the power flow in the fluid is negligible in comparison with the power flow in the structure. This assumption is partly justified by the conclusions of chapter 7 where it was shown that the vibrational response was unaffected by the presence of the fluid. Figure 8.10 shows the $n = 0$ predicted far field power flows (structural-borne and fluid-borne) for a pipe with light fluid loading exited by a radial point force. From the figure it is evident that the structural-borne power flow contributes less than 1 % of the total power. Two branches contribute to the

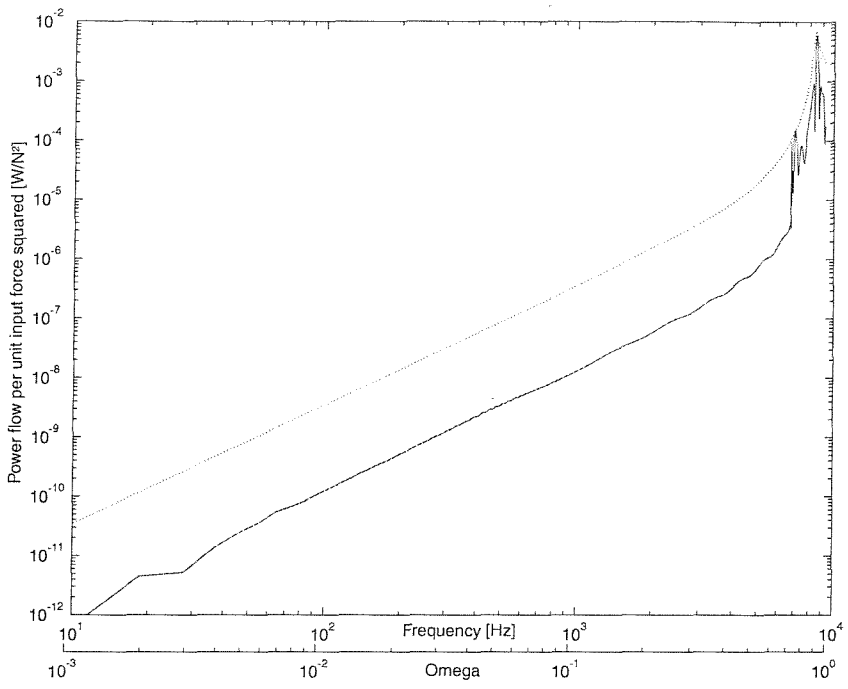

Figure 8.10: Predicted power flow for a pipe with light fluid loading excited by a radial point force, $s = 15$, $n = 0$. The line for the fluid-borne power flow is solid and the structural-borne power flow is dotted.

power flow in figure 8.10: one mainly fluid wave, and one mainly structural axial wave. A closer investigation of the branch contributions shows that the mainly structural wave mainly drives a structure-borne power flow, and the mainly fluid branch mainly drives a fluid-borne power flow.

The predicted power flow in the shell from equation (6.67) is quantified completely for any given branch by the radial displacement complex amplitude, as the axial and tangential displacement is accounted for through the displacement ratios. Likewise the power flow in the fluid for that branch is also quantified by the radial displacement. Given the following assumptions, the transmitted axial power flow at any far point can be inferred from the measured modal displacement:

- It is assumed that orthogonality allows the axial power flow in the different circumferential modes to be treated independently.
- It is assumed that there is only one branch that propagates significant vibroacoustic power for each n, and that any modal radial vibration measured is related to this branch.
- It is assumed that the anechoic termination of the pipe is perfect, and as a result there is one-directional propagation in the pipe.

The transmitted far field modal power flow can – if the assumptions are correct – be

calculated as

$$P_{n,\text{far}} = |w_{n,\text{meas}}|^2 F_{nb} \tag{8.5}$$

where $P_{n,\text{far}}$ is the far field modal power flow; $w_{n,\text{meas}}$ is the measured modal pipe displacement for mode n; and F_{nb} is the modal power flow factor.

The modal power flow factor relates uniquely the modal wall response of the pipe to the modal power flow for given circumferential branch n and branch number b. The power flow factor is determined by the properties of the pipe and the contained fluid and it is not related to the actual excitation of the pipe. The power flow factor can be calculated from any given source that excites the fluid-filled pipe in accordance with the assumptions noted above. In this case, it is convenient to express the modal power flow factor from the excitation of a radial point force, but the same result could be obtained from e.g. an internal monopole, as the dominating branches are the same in both cases. The modal power flow factor can thus be calculated from

$$F_{nb} = \frac{P_{n,1}}{|w_{n,1}|^2} \tag{8.6}$$

where $w_{n,1}$ is the predicted modal pipe displacement for unit radial force input of a doubly infinite pipe; and $P_{n,1}$ is the predicted modal far field power flow for unit radial force input.

For radial point force excitation, the modal power flow can therefore be calculated from

$$P_{n,\text{far}} = \left(\frac{|w_{n,\text{meas}}|}{|w_{n,1}|} \right)^2 P_{n,1} \tag{8.7}$$

If the input force is doubled, so is the displacement response, but the resulting power flow is quadrupled.

The first of the above assumptions is true, if the circumferential Fourier decomposition holds. As shown in the previous section, this is only approximately true due to modal leakage, but in principle it can be assumed that power flow injected into one mode stays in that mode. Departures from axial symmetry in the pipe wall (either geometrical or material properties) will cause scattering from one mode to another, but the pipe is here assumed perfectly axisymmetric.

At low frequencies, there is at most one branch propagating for $n \geq 1$, as shown in the parameter study in chapter 7. Below cuton of the higher order modes, there is no propagating branch, but there is no power flow either, so this violation of the assumption is of no importance. For $n = 0$, there are two propagating branches at low frequencies; one axial and one torsional (plus the disregarded mainly-fluid branch that does not participate significantly in the total power flow). However, the torsional branch is not excited by the radial point force and thus carries no power flow in this case. Therefore the second assumption holds for frequencies of industrial interest provided the excitation is radial, as here.

The third assumption is probably the most questionable, as it will be shown in section 8.4.2 that the anechoic termination is not perfect.

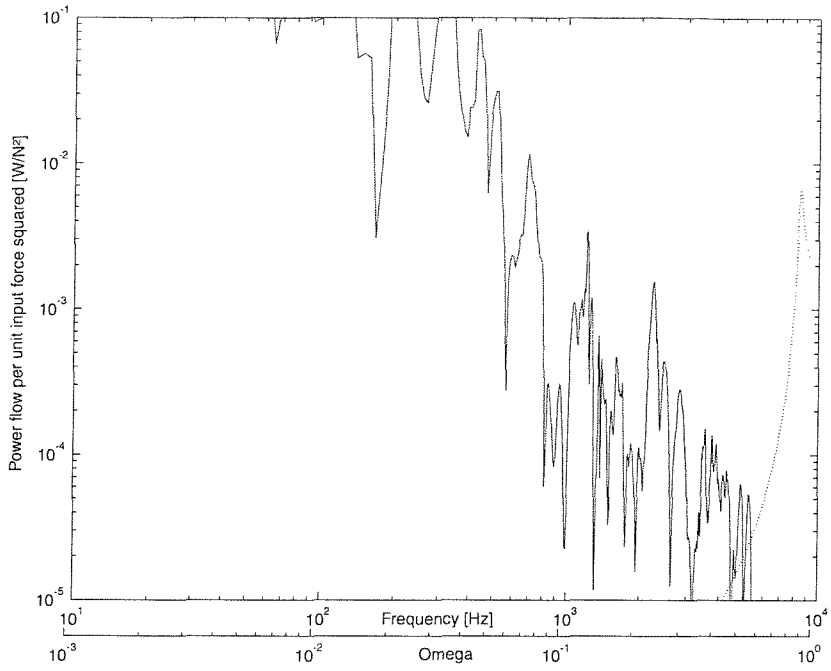

Figure 8.11: Modal power flow for a pipe with light fluid loading excited by a radial point force, $s = 14.7$, $n = 0$. The line for the predicted power flow is dotted and the measured power flow is solid.

8.3.2 Measured and predicted power flow

The modal power flow calculated using equation (8.5) can be seen in figures 8.11 to 8.14 for a single far field position ($s = 14.9$).

The general trends are the same as for the accelerance, but the relative importance of discrepancies between the predicted and measured accelerance is squared according to equation (8.5). For the axisymmetric mode, the measured power flow is way off the predicted power flow, due to the low excitation of this mode at low frequencies by a radial point force. For $n \geq 1$, the measured power flow is smaller than the predicted power flow. This can probably be explained by the damping of the pipe material, as it dissipates energy between the source and the measurement position, as discussed in section 8.2.

Pure standing waves do not propagate any energy. However, when equation (8.5) is used standing waves will contribute to the power flow estimate. This is evident in figures 8.12 and 8.12 where the distinct peaks probably are related to reflected bending waves not removed by the anechoic termination. While the same peaks were seen on the accelerance for the higher order modes, they are missing for the power flow because there is by definition no power flow below the cuton of these modes (under the assumption of one-way propagation on which the power flow calculation is based).

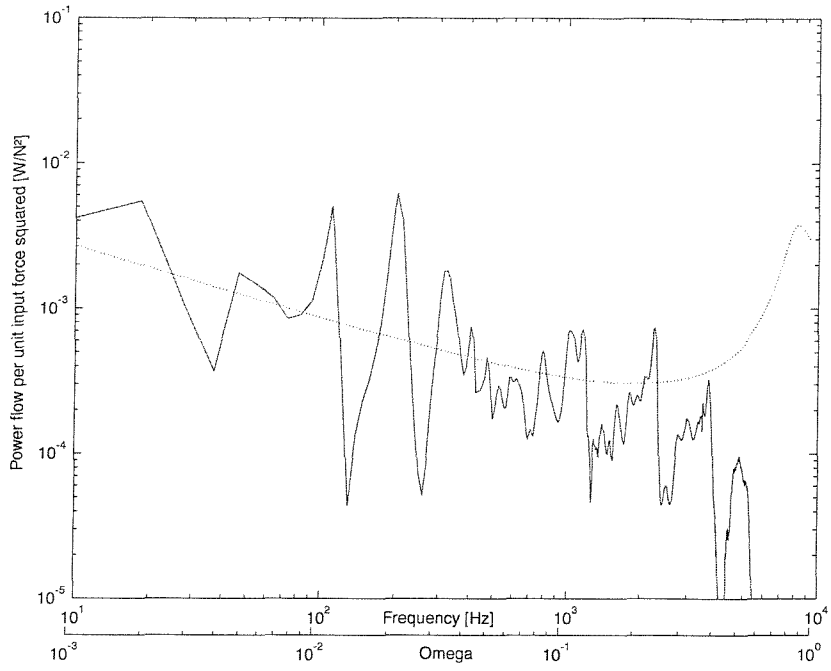

Figure 8.12: Modal power flow for a pipe with light fluid loading excited by a radial point force, $n = 1$. The line for the predicted power flow is dotted and the measured power flow is solid.

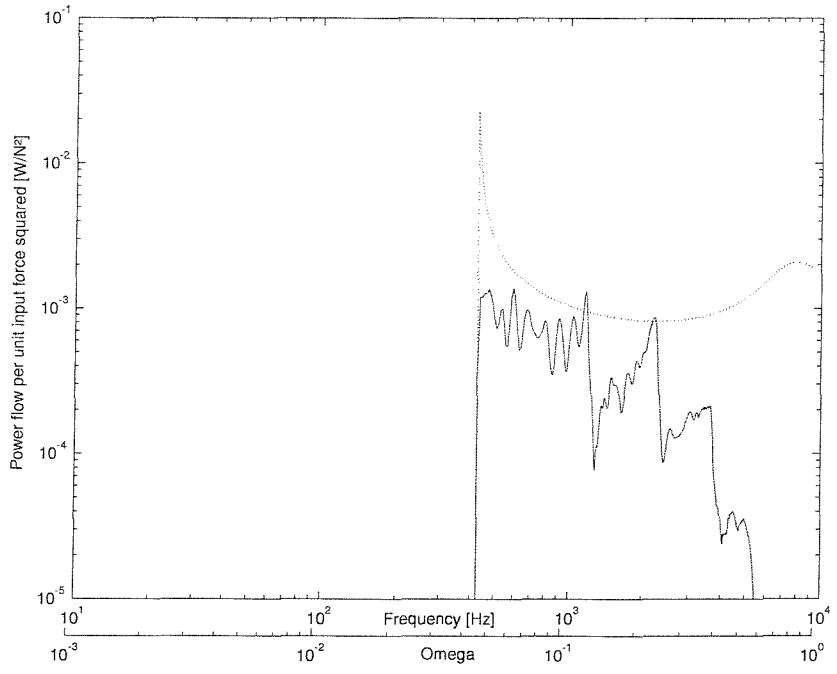

Figure 8.13: Modal power flow for a pipe with light fluid loading excited by a radial point force, $n = 2$. The line for the predicted power flow is dotted and the measured power flow is solid.

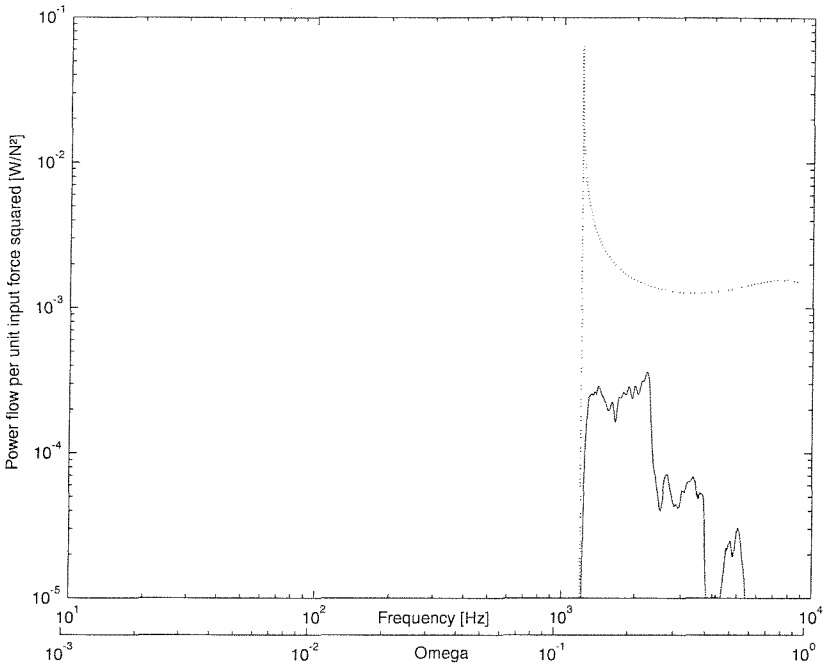

Figure 8.14: Modal power flow for a pipe with light fluid loading excited by a radial point force, $n = 3$. The line for the predicted power flow is dotted and the measured power flow is solid.

8.3.3 Total power flow

The total vibroacoustic power flow carried by the pipe can according to equation (6.69) be found by adding all the modal contributions.

In figure 8.15, the total power flow is plotted for a far field measurement position ($s = 14.9$). The full red line is the sum of all modal contributions $n \leq 6$. It is evident that the measured power flow is a lot larger than the predicted power flow at low frequencies. The broken red line represents the sum of the power flow contributions for modes $1 \leq n \leq 6$, where the agreement between measurements and the prediction is better at low frequencies.

In the same figure, the input power flow measured according to equation (8.3) is plotted with a green curve. Comparison of the input power with the measured power flow shows fair agreement above approximately 100 Hz. Below this frequency the power flow measurement is dominated by unwanted standing waves that violate the assumptions of the power flow measurement method.

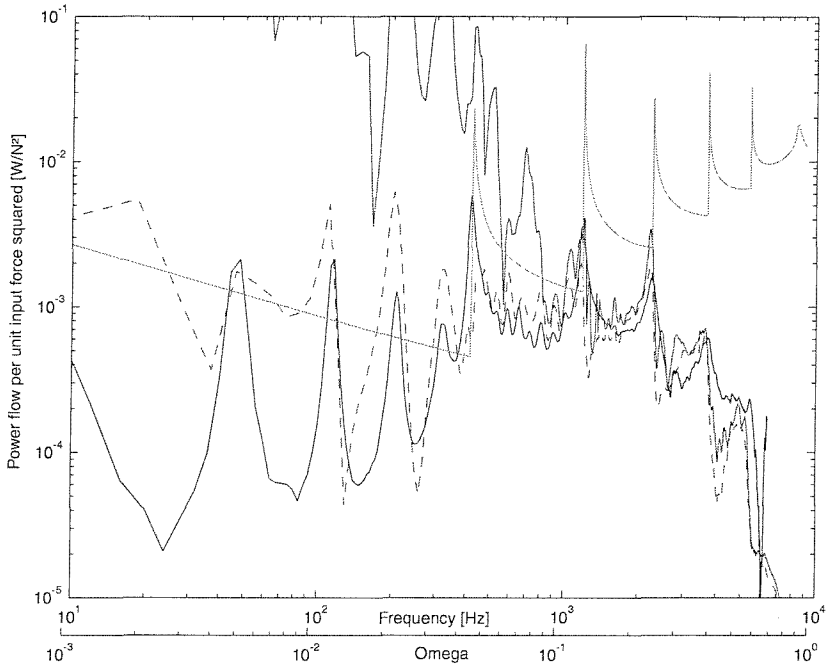

Figure 8.15: Total power flow for a pipe with light fluid loading excited by a radial point force, $s = 14.7$. The predicted power flow is green, the measured power flow is red and the input power flow is blue. The solid red line includes $n = 0$, the dashed red line excludes $n = 0$.

8.4 Detailed comments on the experimental setup

8.4.1 Structural anechoic termination of finite pipe

As discussed in part I, several possible approaches exist when considering power flow measurements in pipes. To justify the assumption from the last section stating that all power flow is directed away from the source in a finite pipe, a significant suppression of the reflections from the ends of the pipe is required. The device to accomplish this is called the anechoic termination.

In the case of the light fluid loaded pipe, the reflections of the internal pressure waves from the open ends of the pipe are simply ignored, as their contribution to both power flow and wall vibration is negligible. The only type of anechoic termination needed in this case is a structural one, to prevent wall vibrations being reflected from the ends of the pipe (for heavy fluid loading, fluid-wave reflections cannot be neglected as noted in section 9.6.2.) To design the structural anechoic termination an understanding of the modes of vibration is crucial. There are essentially three different types of structural vibration: radial, torsional and axial.

Traditionally, many authors eg. Variyart and Brennan (1999) and Feng (1995) have used sandboxes for structural anechoic termination of pipes. The idea of the sandbox is to dissipate the vibrational energy through the relatively high loss factor of sand (5% to 10% according to Norton (1989)). To avoid reflection of vibrational energy when the vibrations enter the sandbox, the sand loading is applied gradually thorough the box. However, there will only be a significant energy transfer to the sand from a given branch if there is significant wall movement, as shear waves in the sand account for most of the energy transfer from the pipe to the sand. More insight than presented here might be obtained using predictions from a model with both internal and external fluid loading, but as the modelling of sand as a fluid with only density and complex speed of sound is probably a significant source of error anyway, no effort in this direction has been made in the present thesis. Instead a common sense design has been used, with a wedge shaped sandbox loading more and more sand along the length.

The mainly axial branches only have a minor radial vibration component due to Poisson coupling. Damping of these modes by sand would therefore require an impractically long sandbox. Brennan et al. (1997) used with some success a beam with a large damped plate connected transversely as an anechoic termination, and the same idea can be applied for a pipe. If the plate impedance is matched properly to the axial impedance of the pipe, the axial components of vibration in the pipe will be converted to bending waves in the plate. The plate bending waves can then be damped using standard vibration control for plates. In the experimental setup used in the present investigation a few 0.8 mm perspex plates were glued to the pipe and damped with patches of absorbing material.

The coupling of the torsional modes is also quite low using only the sandbox, but by applying some fins to the pipe, the coupling to the sand will be significantly better. A few fins were added in the sandbox, but no attempt has been made to model their

effect. Besides, the types of point excitations used in the present thesis would hardly excite any torsional vibration, and the attempt to control the torsional vibration may thus be unnecessary.

The performance of the structural anechoic termination is assessed in the next section. The result of the initial assessment was that the sand loaded the pipe too much and the intended dissipation of energy was not ideal. A better solution, used in the actual experiments reported, was to use a buffer layer of 10 mm foam around the pipe to reduce the resulting external loading of the pipe.

8.4.2 Assessment of the efficiency of the anechoic termination

Using 4 accelerometers (B&K 4507), some optimisation of the sandbox was carried out. Three of the accelerometers were placed equidistantly inside the sandbox (1/4, 2/4 and 3/4 of the length of the sandbox) and one just before the sandbox. Each of the accelerometers measured a radial point accelerance at the position in question. With only sand in the sandbox, the measurements revealed that the main reduction of the radial point accelerance happened in the first quarter of the sandbox. Applying some different materials in addition to the sand revealed that using a foam layer of approximately 10 mm around the pipe in the sandbox yielded the best possible performance of the structural anechoic termination in the light fluid loaded case.

Assuming that only one propagating and one reflected wave exists for each circumferential mode, the radial modal displacement at any point of the pipe can be written as the sum of these two waves:

$$w_n(s) = A_{np}e^{i\kappa_{np}s} + B_{np}e^{-i\kappa_{np}s} \tag{8.8}$$

where index p refers to the propagating branch; A_{np} is the amplitude of the propagating wave; and B_{np} is the amplitude of the reflected wave.

If the modal vibrations are measured at two different axial positions, the amplitude of the incident and reflected waves can be quantified. Let s_c denote the centre position between the two measurement positions 1 and 2. According to equation (8.8), the displacements at these positions are then

$$\begin{aligned} w_n^1(s_c - L) &= A_{np}e^{i\kappa_{np}(s_c-L)} + B_{np}e^{-i\kappa_{np}(s_c-L)} \\ w_n^2(s_c + L) &= A_{np}e^{i\kappa_{np}(s_c+L)} + B_{np}e^{-i\kappa_{np}(s_c+L)} \end{aligned} \tag{8.9}$$

where superscript 1 refers to the measurement position closest to the point of excitation; superscript 2 refers to the other; and $2L$ is the distance between the two measurement positions. Knowing the complex response at each measurement position, equation (8.9) can be solved for the amplitudes using standard methods for two equations with two unknowns (Kreyzig 1998), but it should be noted that the equation tends to be ill-conditioned at frequencies where an integer number of half wavelengths equals $2L$.

The resulting amplitude ratios are plotted in figures 8.16 to 8.19 for $s_c = 19.6$ and $L = 9.8$.

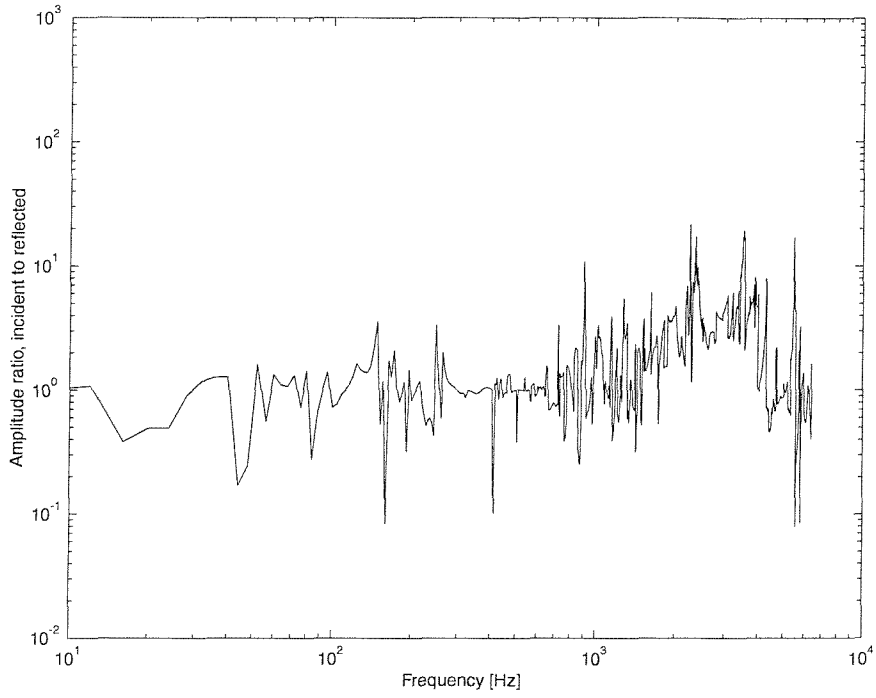

Figure 8.16: Ratio of incident to reflected waves in far field for a pipe excited by a radial point force, $n = 0$.

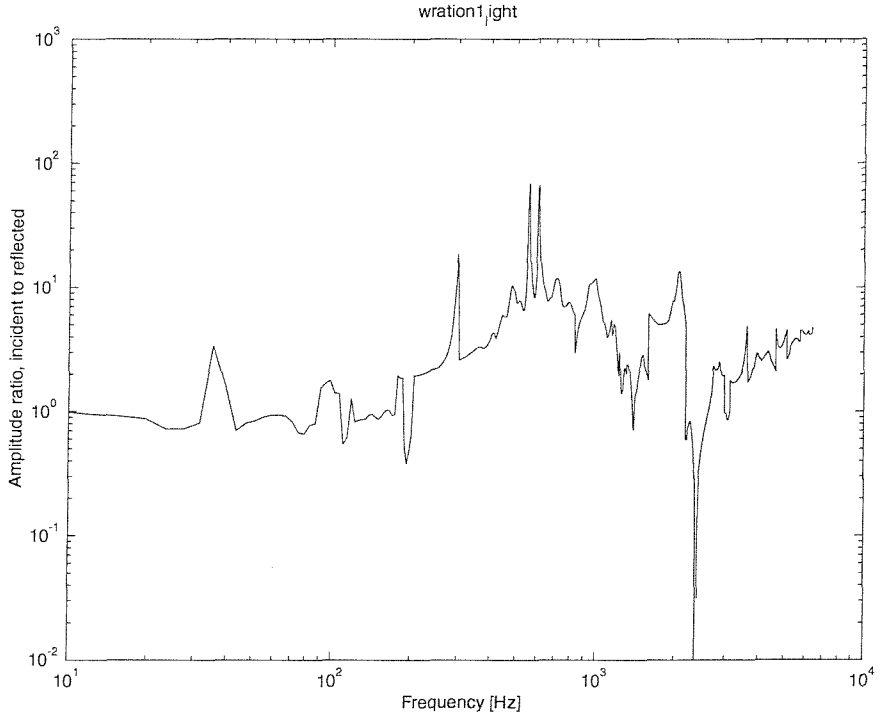

Figure 8.17: Ratio of incident to reflected waves in far field for a pipe excited by a radial point force, $n = 1$.

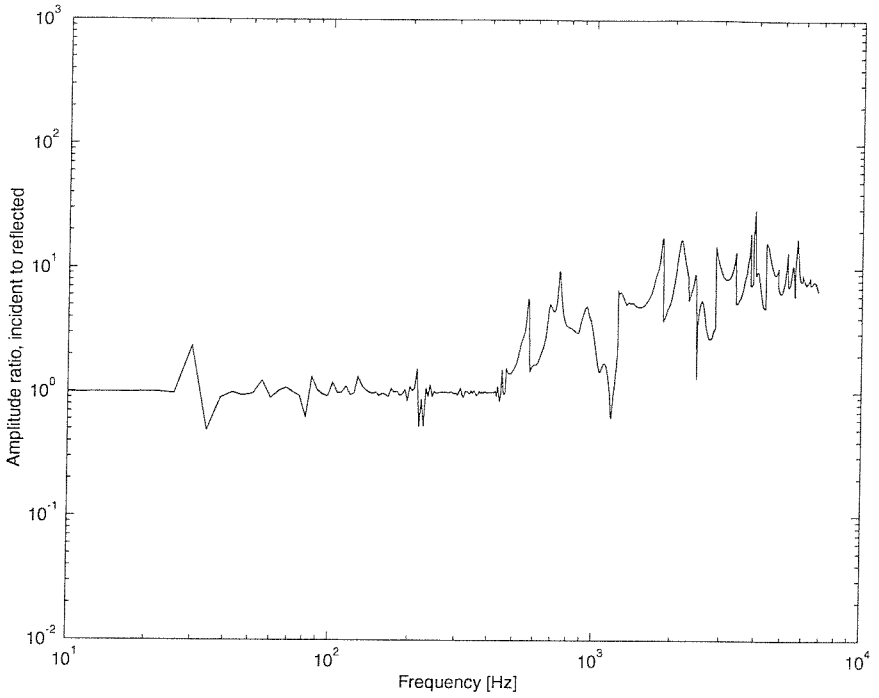

Figure 8.18: Ratio of incident to reflected waves in far field for a pipe excited by a radial point force, $n = 2$.

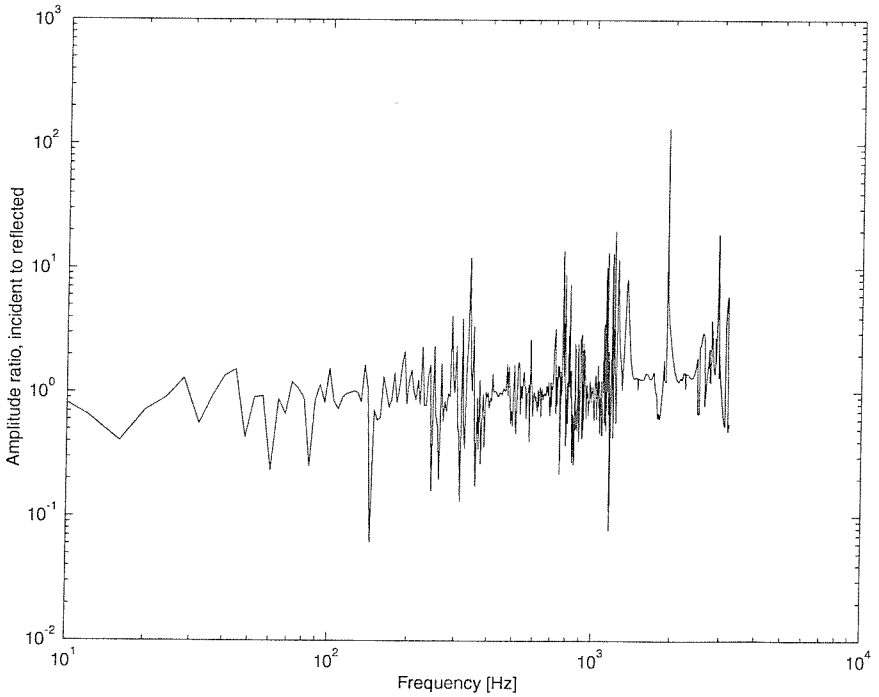

Figure 8.19: Ratio of incident to reflected waves in far field for a pipe excited by a radial point force, $n = 3$.

The general trend is that the efficiency of the anechoic termination is fairly low at low frequencies, reasonable in the mid-frequencies, and fairly low at high frequencies. At low frequencies the wavelengths involved are long compared with the relatively short length of the sandbox, and the effect of the sandbox is expected to be small. At the mid-frequencies, the match of the wavelengths and the length of the sandbox becomes better, while the low efficiency at high frequencies may be related to bad coherence between the two measurement positions, probably related to the relatively high damping of the pipe material.

It should be noted that the distance between the two measurement positions in the figures corresponds to approximately 10 pipe radii. The coherence between the two measurement transducers was fairly low during the experiments, and this probably reduces the confidence in the measured amplitude ratios, as the matrices inverted were badly conditioned. Unfortunately, this problem was identified too late to repeat the measurements with a smaller distance between the two measurement positions. However, it is assumed that the trends in the ratios are correct.

8.4.3 Radial excitation of the shell wall

Two major concerns were addressed during the design of the radial force excitation: the excitation should be as close to a point as possible, to allow direct comparison with the numerical point to point transfer functions from chapter 6; and the pipe should not be penetrated more than necessary to avoid potential leaks in the heavy fluid loaded (water-filled) experiments.

The excitation in the light fluid loaded experiments is provided by a radial force from a mini-shaker connected to the pipe through a short sting. As the sting is flexible (0.8 mm piano wire), most of the moments from misalignment of the axes between the shaker and the pipe are cancelled. The connection from the sting to the pipe is through a small force transducer that is connected rigidly to the geometric midpoint of the pipe.

While direct connection between the force transducer and the pipe with a screw was an easy solution, it was not ideal as it would involve a thread in the pipe wall, thus introducing a potential leak when the pipe is filled with water for the heavy fluid loaded experiments. Instead, a transducer mounting was made by a small cylindrical boss of PVC glued to the pipe wall, as seen on the left hand picture of figure 8.20. To make sure that the M3 thread necessary to connect the force transducer to the pipe was perpendicular to the pipe surface, a cylinder with the same curvature as the outside of the pipe was chosen. The PVC-cylinder alters the dynamic properties of the pipe in two ways, as it adds mass to the vibrational system, and it adds some distributed stiffness, that would affect the point nature of the excitation.

The effect on the point to point response of a fluid-filled pipe from a lumped mass can be estimated as shown by Variyart and Brennan (1999). They present a mobility method that can account for the change in the dynamic behaviour of a high mobility

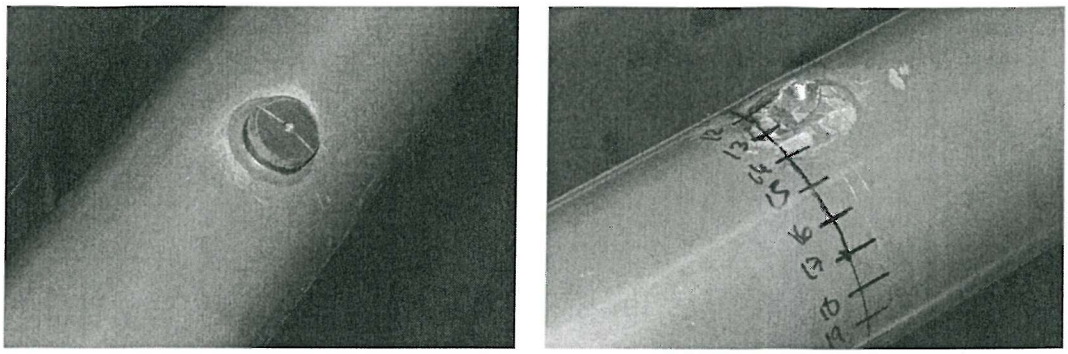

Figure 8.20: Pictures of different connection points of structural excitation.

pipe due to a lumped mass. Dubbing the point of excitation 1 and the lumped mass point 2, the mobility at point 2 can be calculated from

$$\frac{v_2}{F_1} = \frac{M_{12}}{1 + \frac{M_{22}}{M_m}} \tag{8.10}$$

where M_{12} is the transfer mobility from the point of excitation to the point of the mass; M_{22} is the point mobility of the pipe; and $M_m = -1/i\omega m$ is the mobility of the mass.

In this case, the problem is slightly simpler, as the point of excitation and the point of attachment of the point mass are the same. The approximate mass of the PVC-cylinder was 2.3 g and the mass of the force transducer above the piezoelectric element was 1.1 g, making the total added mass at the point of excitation 3.4 g. For the light fluid loaded pipe, the correction at $\Omega = 0.3$ corresponds to less than 1%. The influence of the mass loading of the input arrangement is therefore assumed to be very small.

It is assumed that the distributed stiffness would have a negligible influence on the vibration, as long as the size of the mounting is much smaller than the vibrational wavelength. To verify this, the cylindrical boss was milled smaller as shown on the right hand picture of figure 8.20, thus giving both smaller mass and smaller stiffness. Over the frequency range of interest, no influence could be seen on any of the measurements, and therefore no corrections have been made when comparing the experiments and the predictions.

The shaker setup can amongst other things be seen in figure 9.27.

8.4.4 Modal sensing of pipe vibrations with an accelerometer

Simple point to point transfer functions can simply be measured directly using a point sensor, like an accelerometer. This enables some sort of comparison with a predicted transfer function, but it is difficult to assess the cause of any discrepancies. A modal comparison as in the figures 8.3-8.6 is more enlightening, as e.g. cuton of different modes can be seen directly. In the present thesis, two different techniques of modal

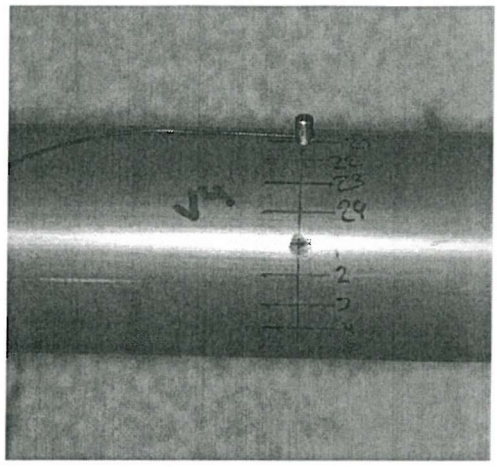

Figure 8.21: Picture of circumferential placement of accelerometer.

measurements are used. The first one uses decomposition of accelerometer measurements and the other one uses modal sensors that are only sensitive to given vibrational modes. In the case of the light fluid loaded experiments, only the accelerometer decomposition method was used.

To avoid any potential problems regarding phase matching of different accelerometers, all measurements are done using the same accelerometer. An obvious consequence is, that the sampling of the different points around the circumference cannot be in real time. The accelerometer measurements are made by placing the accelerometer at a given position and measuring the transfer function to this point. Then the accelerometer is moved to a new position where the new transfer function is measured. The positioning system of the accelerometer is shown in figure 8.21. The modal decomposition technique is presented in the next section.

When measurements are made using an accelerometer, some mass loading of the pipe occurs, as the accelerometer acts like a point mass. This point mass will affect the vibrations locally at the point where the vibrations are sampled, and the acceleration measured by the accelerometer is thus biased by its own mass loading. While the added mass from the accelerometer used is small (the mass of the accelerometer used for the modal decomposition measurements is 0.65 g), it may affect the vibrations at high frequencies, especially for high mobility structures like a thin walled plastic pipe. Using the same mobility method as described in the previous section, the effect of a point mass can be predicted and the measurements can be corrected. In the present thesis, the measurements are not corrected, but instead the mass effect of the accelerometer can be included in the numerical predictions. However, the effect from the small mass loading of the accelerometer is negligible at the scales presented in the figures in this thesis, and the correction is therefore left out. A numerical experiment was conducted with an accelerometer with a mass of 5 g, and here the effect was small, but noticeable.

8.4.4.1 Modal decomposition of accelerometer measurements

A number of different techniques exist for the modal decomposition of accelerometer measurements. Feng (1995) shows a method that utilises the symmetric properties of the vibrations around the circumference to allow the measurements to be conducted only on 180 degrees of the circumference, thus effectively reducing the number of measurement positions by a factor of two. Bourget and Fahy (1993) shows a method that involves moving the measurement positions to align the measurements with the excitation, so that θ_o in the displacement equation equals zero. For the present thesis, a method presented by Variyart and Brennan (1999) is used, as it recovers both the modal amplitude and the angle between the excitation and the measurement reference position (θ_o).

The total radial accelerance, A^r, can be written as the sum of the modal accelerances:

$$A^r = \sum_{n=0}^{\infty} A_n^r = \sum_{n=0}^{\infty} \ddot{B}_n^r = \sum_{n=0}^{\infty}\sum_{b=1}^{\infty} -a\omega^2 W_{nb}^r \cos(n(\theta - \theta_o))e^{i\kappa(s-s_o)} \tag{8.11}$$

Here A_n^r is the modal radial accelerance; B_n^r is the modal radial receptance, found as the displacement per unit force input; and W_{nb} is the modal displacement amplitude. It is convenient to substitute the cos part of the above expression with

$$\cos(n(\theta - \theta_o)) = \phi_c \cos(n\theta) + \phi_s \sin(n\theta) \tag{8.12}$$

this leads to

$$A^r = \sum_{n=0}^{\infty} \varepsilon_n A_n \left[\phi_c \cos(n\theta) + \phi_s \sin(n\theta)\right] \tag{8.13}$$

where $\varepsilon_n = 1$ for $n = 0$ and $\varepsilon_n = 2$ otherwise; $\phi_c = \cos(n\theta_o)$; $\phi_s = \sin(n\theta_o)$; and the constant A_n collects all other terms.

If sampling is made with a point sensor like an accelerometer at N points around the circumference of the pipe, then the sample angle at the j'th measuring position can be written as

$$\theta = \frac{2\pi j}{N} \tag{8.14}$$

and the measured radial accelerance of this point is dubbed H_j^r.

When extracting the circumferential mode m from the N measurements around the circumference, the cosine part of equation (8.13) is evaluated by multiplying both right and left hand side of equation (8.13) with a common factor

$$\frac{1}{N}\cos\left(\frac{2\pi j}{N}m\right) \tag{8.15}$$

Then replacing H^r with the measured accelerance H_j^r and combining the sum of all

measurement points, a new equation forms as

$$\begin{aligned}&\frac{1}{N}\sum_{j=0}^{N-1}H_j^r\cos\left(\frac{2\pi j}{N}m\right)\\&\quad=\frac{1}{N}\sum_{j=0}^{N-1}\sum_{n=0}^{\infty}\varepsilon_n A_n\left[\phi_c\cos(\frac{2\pi j}{N}n)+\phi_s\sin(\frac{2\pi j}{N}n)\right]\cos\left(\frac{2\pi j}{N}m\right)\end{aligned}\tag{8.16}$$

The sine terms will cancel out due to the properties of discrete orthogonality, while the cosine terms will sum up to $\phi_c A_m N$. It should be noted, that aliasing of higher order modes will occur when the number of circumferential modes is more than one half the number of measurement points around the circumference according to the Nyquist sampling theorem. This way, equation (8.16) reduces to

$$\frac{1}{N}\sum_{j=0}^{N-1}H_j^r\cos\left(\frac{2\pi j}{N}m\right)=\phi_c A_m=H_c^r\tag{8.17}$$

The same procedure can be applied for the sine terms and here the result is

$$\frac{1}{N}\sum_{j=0}^{N-1}H_j^r\sin\left(\frac{2\pi j}{N}m\right)=\phi_s A_m=H_s^r\tag{8.18}$$

The total measured accelerance magnitude for mode m is found as

$$A_m=\sqrt{(H_s^r)^2+(H_c^r)^2}\tag{8.19}$$

and the corresponding angle between excitation and vibration is found to be

$$\theta_o=\frac{1}{m}\tan^{-1}\left(\frac{H_s^r}{H_c^r}\right)\tag{8.20}$$

8.5 Conclusion

In this chapter, the response of a fluid-filled pipe with light fluid loading has been assessed through measurements of the modal accelerance. The excitation of the pipe is provided by a radial point force. The measured modal accelerance is compared with the accelerance predicted by the prediction model in chapter 4. A common feature of all the comparisons between the measurement and prediction is that the agreement improves as the measurement position is moved towards the point of excitation; in the near field of the point of excitation the agreement is excellent. The modal measurement shows some modal leakage where accelerance from a strongly excited mode apparently leaks to a weakly excited mode. However, when all the modal contributions are summed to form a so-called synthetic point accelerance, the strongly excited modes dominate the weakly excited modes, effectively removing the effect of the modal leakage.

A measurement method for the vibroacoustic power flow has been presented. Under a quite restrictive set of assumption, the modal power flow is inferred from measurement

of the pipe-wall response (e.g. the accelerance) through a predicted relation between the modal response of the pipe wall and the modal power flow in the far field. Comparison of the measured and predicted modal power flows shows that the agreement at low frequencies is generally good, but at higher frequencies there is a significant roll off. This high frequency roll off can probably be related to the relatively high loss factor of the pipe-wall material. The modal power flows can be summed to form a total power flow. The power input to the fluid-filled pipe from the force excitation can be measured through simultaneous measurements of the input force and acceleration of the point of excitation. Comparison of the predicted input power and the measured power flow shows fair agreement above approximately 100 Hz.

The overall conclusion of this chapter is that the method of power flow measurements presented in chapter 3 has been validated against numerical predictions from the model presented in chapter 6 and vice versa, for a pipe with light fluid loading excited by a radial point force.

Chapter 9

Power flow measurements: pipe with heavy fluid loading

The experiments presented in this chapter are all obtained on a PVC pipe with air outside and water inside, so that the resulting internal fluid loading is heavy. The excitation in the measurements is provided either by an external radial force at the shell wall or by a transmitting hydrophone in the contained fluid. The pipe modal accelerance is measured either by an accelerometer that is moved around the circumference or by modal sensors that measure the modal response directly without post-processing.

The first section introduces the experimental setup used. The second and third sections present measurements of accelerance and power flow when the pipe is excited by a radial force. The fourth and fifth sections present similar measurements, but for the pipe excited by a transmitting hydrophone inside the pipe. The sixth section assesses the measurement principle, and the final section summarises the main conclusions.

9.1 Experimental setup

The experimental setup used in the heavy fluid loaded experiments is identical to the one used in the light fluid loaded experiments, except for a few additions.

The 5 m PVC pipe is filled with water inside, while air is retained on the outside, corresponding to case 1 in table 7.1 on page 74. Due to the relatively low $\rho_s h$ of the pipe, the resulting internal fluid loading is heavy, as discussed in the parameter study in chapter 7.

The structural anechoic termination is kept unchanged from the light fluid loaded experiments, but a fluid anechoic termination is added to suppress reflections in the fluid from the pipe ends. The main feature of the fluid anechoic termination is 30 m of rubber hose. The purpose of the rubber hose is to dissipate the energy in the pressure fluctuations in the water. A special 0.5 m connection pipe matches the fluid impedance gradually from the measurement pipe to the rubber hose. The fluid anechoic

Figure 9.1: Picture of experimental setup.

termination is discussed in more detail in section 9.6.2.

Two types of excitation are used during the experiments, a radial force at the shell wall and a transmitting hydrophone inside the pipe. The setup of the force excitation is exactly the same as for the light fluid loaded experiments in chapter 8. The transmitting hydrophone excites the fluid directly, ideally without any direct excitation of the structure. It is assumed that the hydrophone acts like a point monopole source over the relevant frequency range. The hydrophone excitation is discussed in more detail in section 9.6.1.

The experiments with the radial force excitation are conducted like the light fluid loaded experiments, but in addition to the accelerometer modal decomposition the modal response of the pipe is also measured directly using modal sensors. The modal sensors are made from shaped polyvinylidene fluoride (PVDF) film or from PVDF wire, and due to their shape they are only sensitive to certain circumferential modes. The modal sensors are discussed in more detail in section 9.6.3.

When the transmitting hydrophone is used as a source, the voltage input to the hydrophone is measured. By using the calibration of the hydrophone (the range normalised pressure of the hydrophone was measured in air), the pressure output from the hydrophone can be deduced. There is no simple way of quantifying the acoustic power input from the hydrophone, as the velocity response of the fluid is not measured. The wall response of the fluid-filled pipe is measured using both point and modal measurements.

The experimental setup is sketched in figure 9.2 and the instrumentation used is listed in table 9.1.

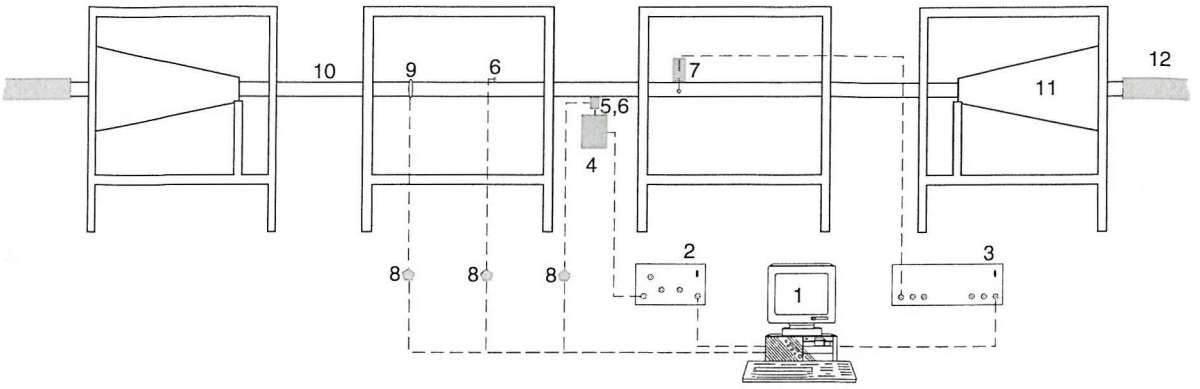

Figure 9.2: Sketch of the experimental setup used for the experiments on a pipe with heavy fluid loading.

1. B&K Type 3560, PULSE Multi-analyzer and signal generator
2. B&K Type 2706, Power amplifier
3. B&K Type 2713, Power amplifier
4. B&K Type 4810, Mini-shaker
5. B&K Type 8203, Force transducer (3.6 pC/N, 1.1 g)
6. B&K Type 4374, Miniature accelerometer (0.141 pC/ms^{-2}, 0.65 g)
7. B&K Type 8103, Hydrophone (0.099 pC/Pa, diameter 9.5 mm)
8. B&K Type 2646, Deltatron charge amplifier (1mV/pC)
9. Modal sensor (PVDF wire or patches of PVDF film)
10. PVC pipe (L=5 m, D_o=63 mm, h=1.8 mm)
11. Anechoic termination
12. Connection pipe and rubber hose (L=30 m, D_o=79.2 mm, h=1.6 mm)

Table 9.1: Instrumentation used for the experiments with heavy fluid loading.

9.2 Accelerance for pipe excited at the pipe wall

Figures 9.3-9.6 show the measured and predicted modal accelerances ($n = 0$ to 3) of a heavy fluid loaded fluid-filled pipe exited by a radial point force. Measurements are plotted in red and predictions in green; the solid line represents a measurement position $s = 0.29$ from the point of excitation; the dashed line corresponds to $s = 14.7$; and the dash-dot line represents $s = 25.1$.

The Young's modulus used for the pipe wall in the prediction model has been fitted, as in the light fluid loaded experiments so the predicted and experimental cuton frequency of the $n = 2$ circumferential mode are the same. The required value of Young's modulus is 5.5 MPa, which is approximately 45 % more than the modulus used in the light fluid loaded case. This may seem contradictory, but the effective increase in the Young's modulus can probably be related to stress stiffening of the shell material. When the pipe is filled with water, the entire system is pressurised. An experiment was made to confirm that the cuton frequency of the $n = 2$ mode varies according to the static pressure of the system: it was found that the higher the static pressure, the higher the cuton frequency, and an approximate relation could be found. While this is an interesting observation, it is not pursued further. All the measurements presented in this chapter are made with $p_s = 100$ kPa, and the predictions are mode with the Young's modulus noted above.

As the experimental setup was prepared for flow through the pipe, the measurements were repeated with a flow of approximately 1,800 kg/h. Apart from a lower coherence during the measurements (probably related to the background noise added from the flow rig), no impact could be seen on the results.

Comparison between light and heavy fluid loading. The two most notable differences between the light and the heavy fluid loading are the generally lower accelerance, and the lower cuton frequencies for the higher order modes for the heavy fluid loaded case.

Knowing that force equals mass times acceleration and the accelerance is acceleration per unit input force, it seems intuitively reasonable that the acceleration response per unit force is reduced when the mass per length of the fluid-filled pipe is increased. For the pipe used in the experiments, the mass is 0.50 kg/m in the air-filled case and 3.44 kg/m in the water-filled case. The ratio of the mass per unit length is close to the approximate factor of 6 observed between the measured accelerances for a pipe with light and heavy fluid loading, respectively.

The observed cuton frequency of the $n = 2$ mode (structural branch) is reduced from approximately 420 Hz when the pipe is air-filled to approximately 180 Hz when the pipe is water-filled. Similarly, the cuton frequency of the $n = 3$ mode is reduced from 1050 Hz to 600 Hz. The reason for this is probably the increased effective mass of the shell wall in the heavy fluid loaded case.

As in the light fluid loaded case, the agreement between measurements and predictions

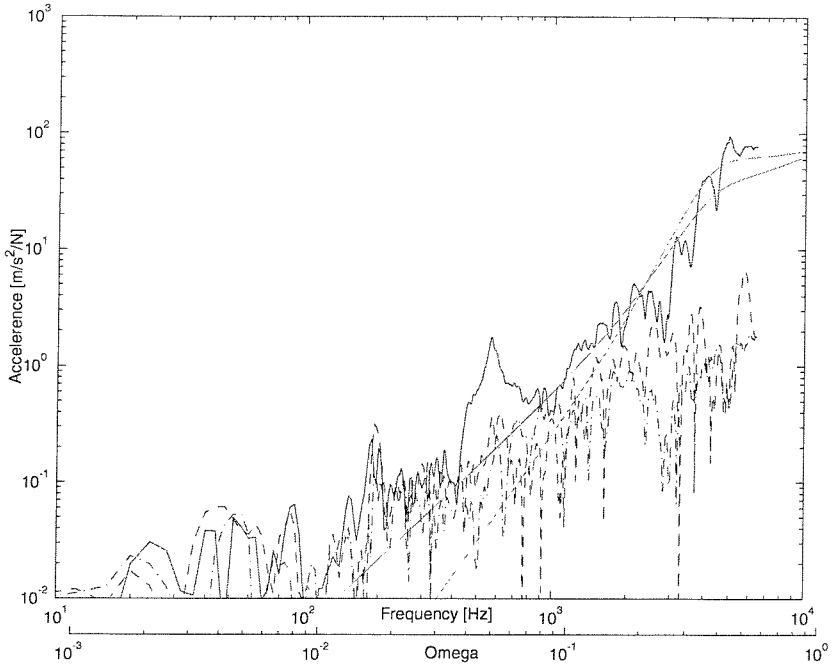

Figure 9.3: Modal accelerance for a pipe with heavy fluid loading excited by a radial point force, $n = 0$. The predicted response is green and the measured red; the solid line corresponds to $s = 0.29$, the dashed line to $s = 14.7$ and the dash-dot line to $s = 25.1$.

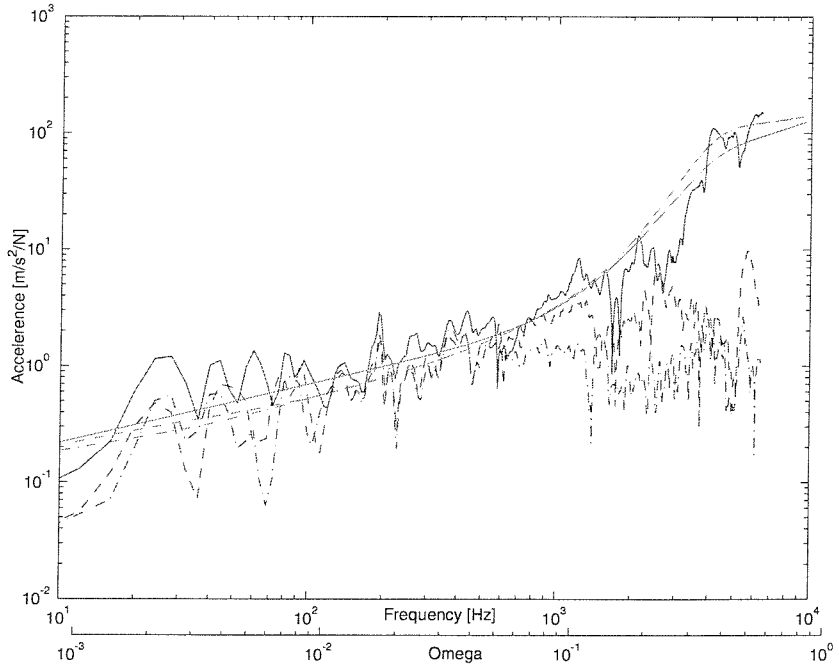

Figure 9.4: Modal accelerance for a pipe with heavy fluid loading excited by a radial point force, $n = 1$. The predicted response is green and the measured red; the solid line corresponds to $s = 0.29$, the dashed line to $s = 14.7$ and the dash-dot line to $s = 25.1$.

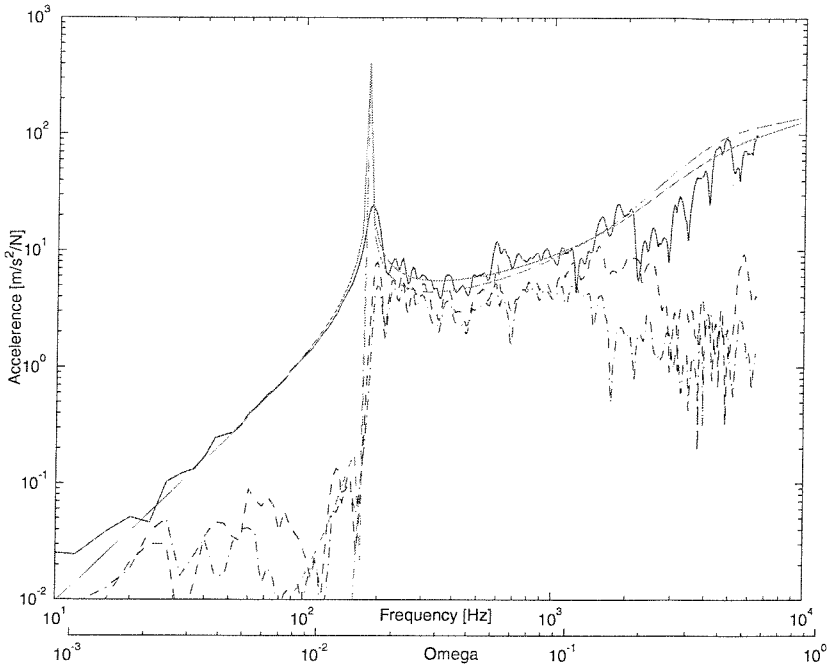

Figure 9.5: Modal accelerance for a pipe with heavy fluid loading excited by a radial point force, $n = 2$. The predicted response is green and the measured red; the solid line corresponds to $s = 0.29$, the dashed line to $s = 14.7$ and the dash-dot line to $s = 25.1$.

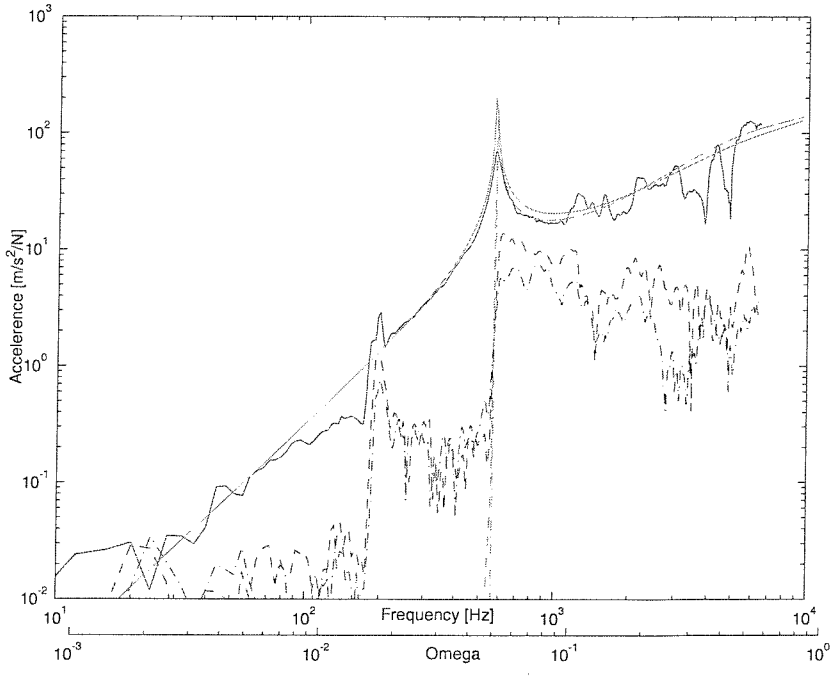

Figure 9.6: Modal accelerance for a pipe with heavy fluid loading excited by a radial point force, $n = 3$. The predicted response is green and the measured red; the solid line corresponds to $s = 0.29$, the dashed line to $s = 14.7$ and the dash-dot line to $s = 25.1$.

improves the smaller the distance between the measurement position and the point of excitation. The discrepancies at the two far field positions at high frequencies seem smaller in the heavy fluid loaded case. A possible explanation for this is that the damping in water is significantly smaller than in PVC, and as the proportion of power flow in the fluid is much larger for the heavy fluid loaded case, the fraction of energy dissipated between the points of excitation and response is smaller.

9.2.1 Comparison of accelerometer and modal sensor measurements

Modal sensors for the modes $n = 0$ to 3 were used to measure the pipe-wall response. The $n = 0$ sensor is a PVDF wire wound an integral number of turns around the pipe. The modal sensors for the rest of the modes are made from thin PVDF film cut into shapes only sensitive to certain modes. Both types of modal sensors are discussed in section 9.6.3. The measurements for each mode are discussed below in turn.

n = 0. Figure 9.7 shows the accelerance in the $n = 0$ mode at $s = 19.7$. The solid line shows measurements obtained by decomposition of accelerometer measurements; the modal sensor measurements are shown with a dashed line; and the predicted accelerance with a dotted line. The agreement between the two measurement techniques is good at intermediate frequencies, but they tend to deviate both at low and high frequencies.

At low frequencies, the modal sensor measurements are much closer to the predicted response than the accelerometer decomposed measurements, as they do not show the noise floor limitations of the accelerometer measurement, discussed in section 8.2. The general sensitivity of the modal sensor (5 turns of PVDF wire) is probably higher than the lightweight accelerometer, but as the noise floor is not thought to be related to limitations in sensitivity, this is probably not the explanation. The noise floor of the decomposed measurements is probably related to errors introduced by the repositioning of the accelerometer around the circumference. The modal sensor measures the response directly, without moving the sensor during the measurement. However, modal leakage may occur due to the overlap of the wire at the ends, as the electrical connection of the wire makes it difficult to know exactly what the sensitive length is. Modal leakage can be seen around 200 Hz in figure 9.7 for both curves, but the level for the modal sensor seems slightly smaller.

The modal sensor measurement tends to roll more off at high frequencies than the decomposed measurements. This may partly be a damping effect and partly a mass effect. The modal sensor is fixed on the pipe by double sided adhesive tape under the sensor, with an additional layer of aluminum coated adhesive tape (to provide electrical shielding) above the sensor. It is well known that adhesive tape introduces substantial damping. The accelerometers used in the decomposed measurements are positioned using beeswax, introducing no damping.

The mass of the sensor will also reduce the response of the fluid-filled pipe as discussed

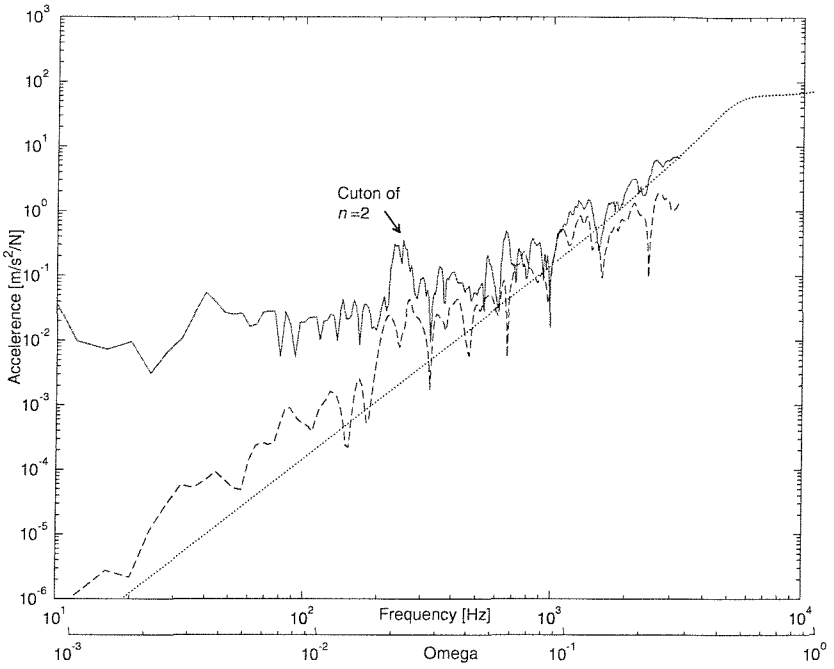

Figure 9.7: Modal accelerance for a pipe with heavy fluid loading excited by a radial point force, $n = 0$, $s = 19.7$. The line for the predicted response is dotted, accelerometer measurements solid, and the modal sensor measurements dashed.

in section 8.4.3, and the effect will be larger the higher the frequency. The PVDF wire (including the adhesive tape) has a total mass of approximately 3.5 g and the accelerometer 0.65 g. Whereas the accelerometer is acting like a point mass, the mass of the modal sensor is distributed around the circumference and the effect is therefore difficult to predict. As shown in 8.4.3, the mass effect of the accelerometer in the frequency range of interest is negligible for the air-filled case; in view of the lower mobility of the pipe in the water-filled case, it can therefore be assumed that the mass effect of the accelerometer is also negligible in this case. The mass loading effect of the modal sensor cannot easily be predicted, but there is no doubt that the lighter the modal sensor, the smaller the impact on the response of the fluid-filled pipe.

The PVDF-film used for the other modal sensors in this thesis could have been shaped to allow measurement of the axisymmetric mode. Due to time constraints, this was not tested during the present investigation, but the reduced mass loading of PVDF-film compared with wire would be an advantage when measuring high mobility pipes.

n = 1. Figure 9.8 shows the measured and predicted accelerance for the bending mode with the same legend as for figure 9.7. The general trends for both measurement methods are the same, but the modal sensor measurement drops more off at high frequencies, probably for the same reasons as discussed for the $n = 0$ modal sensor.

Modal leakage is also evident in figure 9.8. The risk of introducing modal leakage

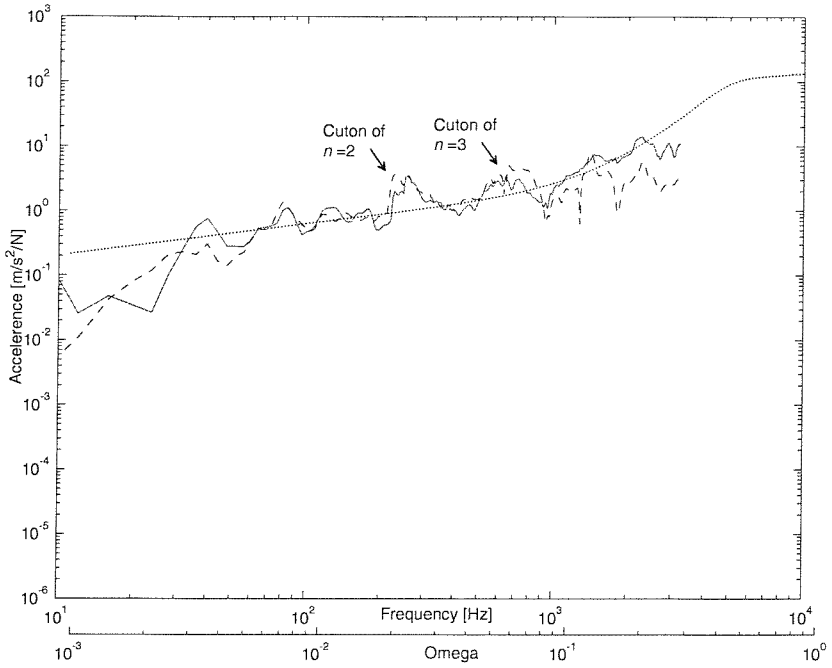

Figure 9.8: Modal accelerance for a pipe with heavy fluid loading excited by a radial point force, $n = 1$, s=9.8. The line for the predicted response is dotted, accelerometer measurements solid, and the modal sensor measurements dashed.

through the measurement method is higher for the modal sensors based on PVDF-film, as the individual patches need to be aligned perfectly to completely cancel other modes, and when shaping and mounting the (prototype) modal sensor it is difficult to get it right for all patches, resulting in small misalignments. Another possible source of modal leakage is bad electrical contact between the patches. During the experiments, the electrical connection between different patches sometimes suddenly disappeared. In most cases this was easy to spot, as the output from the sensor changed completely, but in some cases it might have been left unnoticed.

n $\geq$ 2. Figures 9.9 and 9.10 show the accelerance for the $n = 2$ and $n = 3$ modes, respectively. The trends are the same as for the $n = 0$ and $n = 1$ modes, but as the number of patches is twice the mode number, the relative precision of the modal sensors tends to fall as n rises.

The problems regarding the alignment of the individual patches become significant for the $n = 3$ sensor. As a result the performance of the $n = 3$ modal sensor is poorer than the accelerometer decomposed measurements. The conclusion is that for low n, hand-made modal sensors are a sensible choice; but for higher n, precision is crucial with modal sensors of the design used in this thesis.

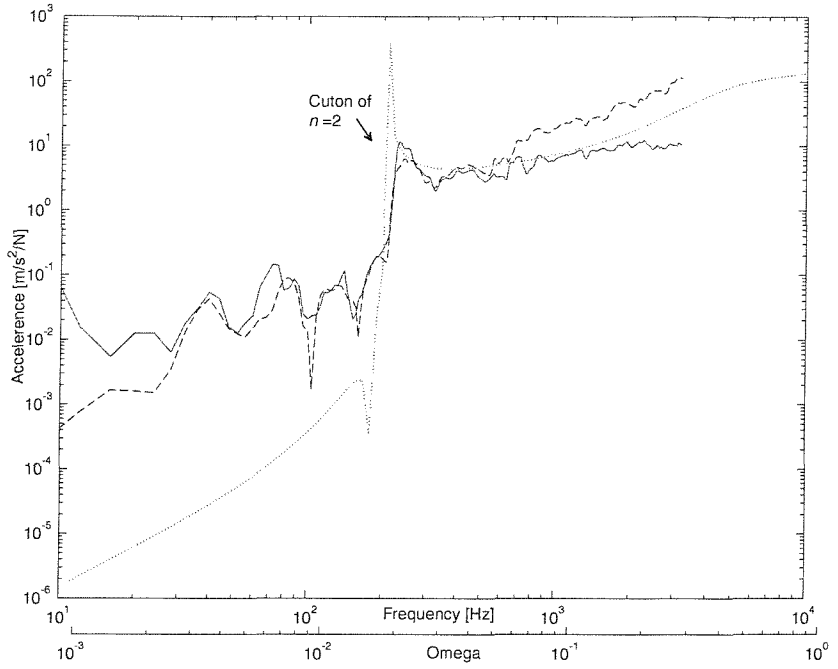

Figure 9.9: Modal accelerance for a pipe with heavy fluid loading excited by a radial point force, $n = 2$, s=24.5. The line for the predicted response is dotted, accelerometer measurements solid, and the modal sensor measurements dashed.

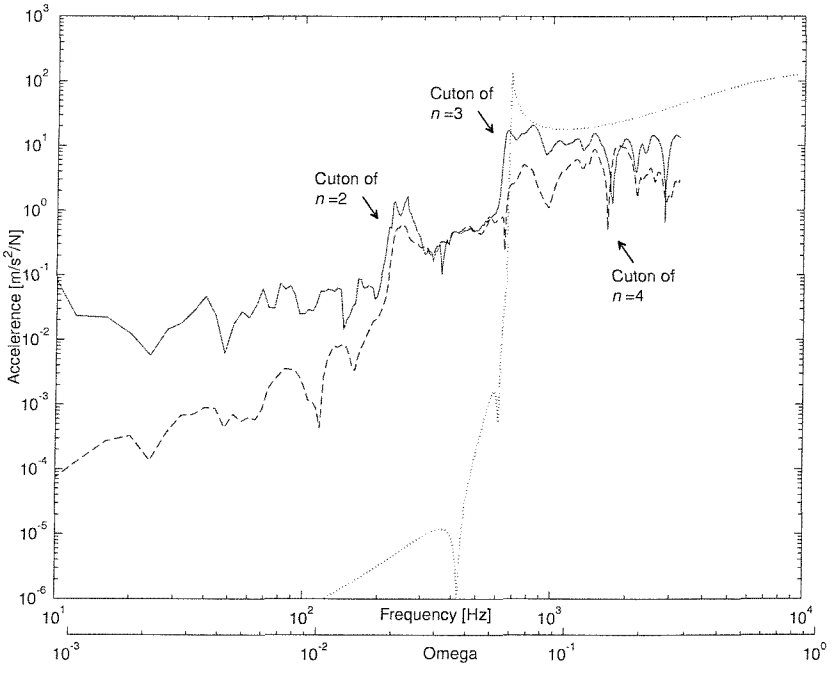

Figure 9.10: Modal accelerance for a pipe with heavy fluid loading excited by a radial point force, $n = 3$, s=14.7. The line for the predicted response is dotted, accelerometer measurements solid, and the modal sensor measurements dashed.

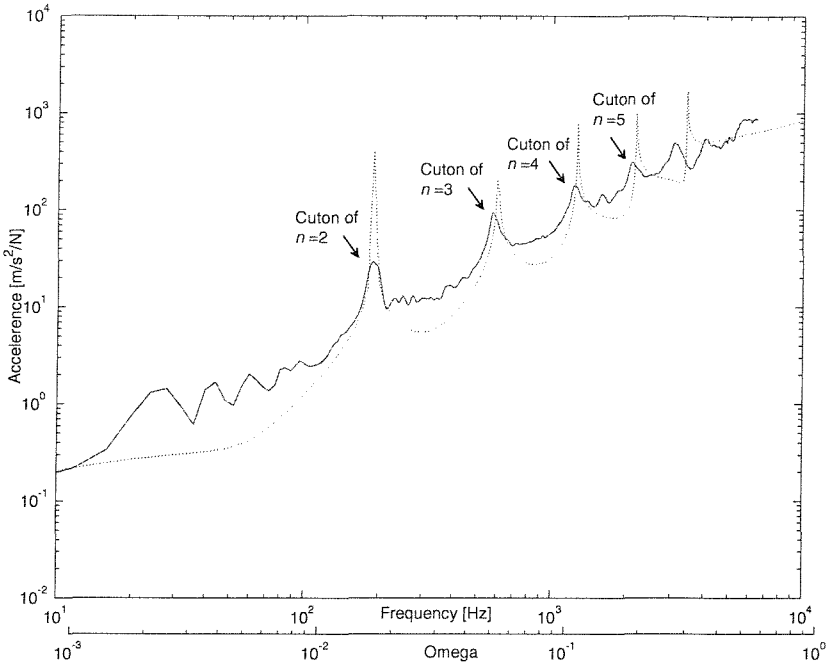

Figure 9.11: Synthetic point accelerance for a pipe with heavy fluid loading excited by a radial point force, $s = 0.29$. The line for the predicted response is dotted and the measured solid.

9.2.2 Synthetic point accelerance

As discussed in section 8.2.1, the synthetic point accelerance is the sum of all measured modal contributions at a given axial position. For this reason, the synthetic point accelerance only makes sense for the accelerometer decomposed measurements, as they are taken at the same axial position, while the modal sensors are at different axial positions. A sum of modal responses as measured by modal sensors would therefore not be related to the point response of the pipe wall, and would hardly have any physical relevance at all.

Figures 9.11-9.13 show the synthetic point accelerances for the axial positions $s = 0.29$, $s = 14.9$, and $s = 25.1$.

The curve in figure 9.11 is not as smooth as the corresponding curve for the light fluid loaded case (figure 8.7), but the overall agreement is still impressive. The low frequency accelerance is still dominated by peaks, which can be related to standing waves of primarily the bending mode. The measured curve does not possess the same dynamic range as the predicted curve: the cuton peaks are lower than predicted and the troughs between the peaks are not as deep as the predicted ones.

The agreement between the measured and predicted accelerance in figures 9.12 and 9.13 is fair, but the measured curves tend to roll off at high frequencies. While the general level of accelerance is lower for the heavy fluid loaded pipe than for the light

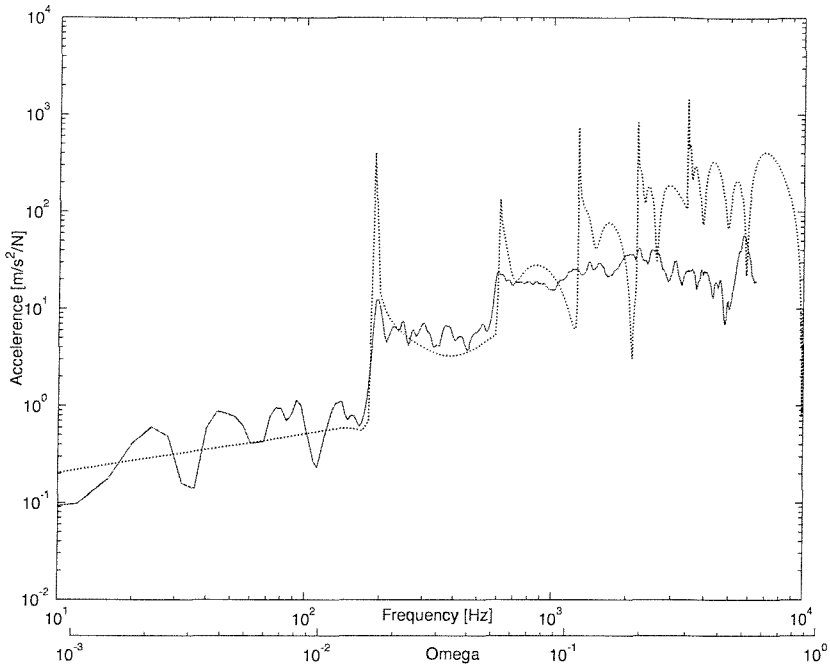

Figure 9.12: Synthetic point accelerance for a pipe with heavy fluid loading excited by a radial point force, $s = 14.9$. The line for the predicted response is dotted and the measured solid.

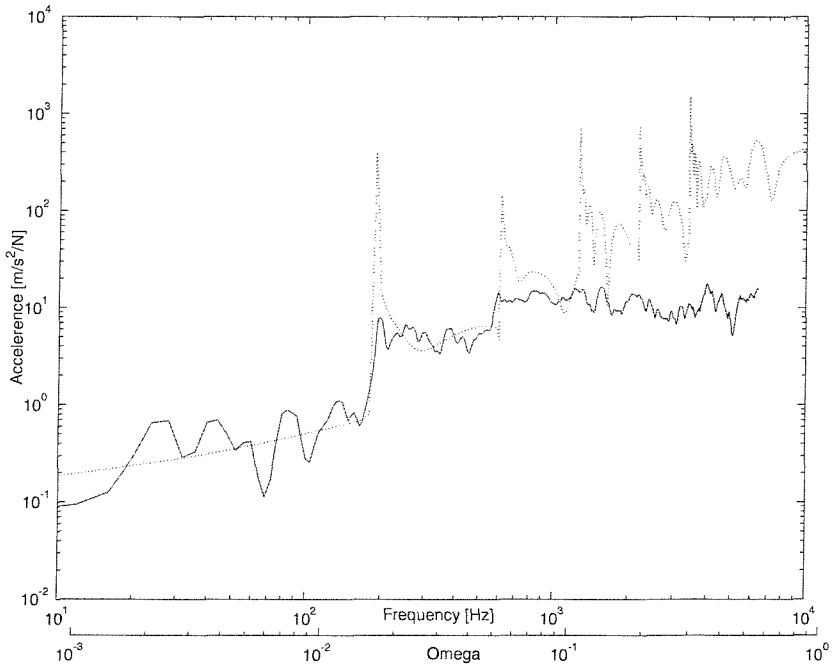

Figure 9.13: Synthetic point accelerance for a pipe with heavy fluid loading excited by a radial point force, $s = 25.1$. The line for the predicted response is dotted and the measured solid.

fluid loaded pipe, the features of the curves are very similar.

The roll off and the smearing of the details of the measured curves are both discussed in section 8.2.1.

9.3 Power flow for pipe excited at the pipe wall

9.3.1 Principle of modal power flow measurement

In section 8.3.1 two different principles for power flow measurement are proposed: one for the input power to a structure, and another for the modal power flow.

The input power measurement method is valid no matter the level of the fluid loading. The input power will of course be dependent on the fluid loading, since both input force and the resulting acceleration of the point of excitation are affected by the properties of the internal fluid. For the heavy fluid loaded case, the input power per unit input force is expected to be smaller than for the light fluid loaded case, as the acceleration response of the pipe wall is smaller due to the added mass of the water-filled pipe.

The three assumptions presented in section 8.3.1 to justify the modal power flow measurement method, were:

- It is assumed that orthogonality allows the axial power flow in the different circumferential modes to be treated independently.
- It is assumed that there is only one branch that propagates significant vibroacoustic power for each n, and that any modal radial vibration measured is related to this branch.
- It is assumed that the anechoic termination of the pipe is perfect, and as a result there is one-directional propagation in the pipe.

For the first and the last of these assumptions, the comments presented in section 8.3.1 also apply here. It is argued below that the second assumption also remains valid for the heavy fluid loaded case.

For light fluid loading, the argument regarding the second assumption was that for $n \geq 1$ at most one mode was propagating and that for $n = 0$, the axial structural branch dominated the other two. In the case of heavy fluid loading, the first statement still applies for $n \geq 1$. However, for $n = 0$ the response of the pipe wall is no longer dominated by the axial structural branch, but by the axial fluid branch. When the fluid loading is heavy, the pipe walls appear relatively soft. For the water-filled PVC pipe used for the experiments presented in this chapter, more than 99 % of the power flow in the $n = 0$ mode is carried by the fluid for $\Omega < 0.3$, as seen in figure 9.14. The torsional branch is not excited by radial excitation, and therefore carries no power flow in this case.

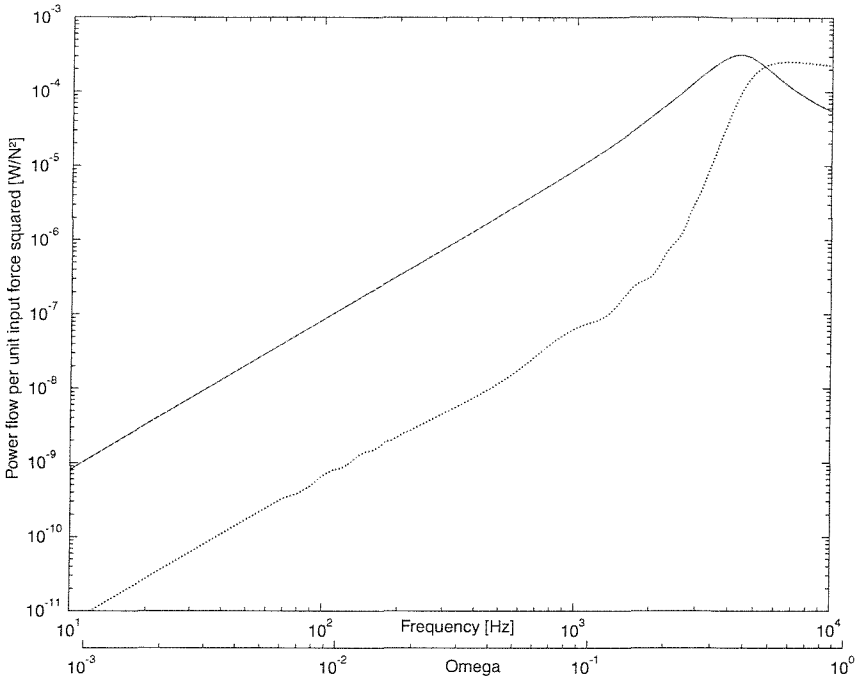

Figure 9.14: Predicted power flow for a pipe with heavy fluid loading excited by a radial point force, $s = 15$, $n = 0$. The line for the fluid-borne power flow is solid and the structural-borne power flow is dotted.

The modal far field power flow can therefore still be calculated from the measured pipe response, using equation (8.5) that is restated here for convenience:

$$P_{n,\text{far}} = \left(\frac{|w_{n,\text{meas}}|}{|w_{n,1}|} \right)^2 P_{n,1}$$

It should be noted that the above comments regarding the power flow only apply strictly for sufficiently heavy fluid loading. For intermediate fluid loadings (e.g. a steel pipe filled with water), the picture is not so clear although the error made by applying the above method turns out to be small. This is discussed in more detail in chapter 11.

9.3.2 Modal power flow results for point force excitation

The modal power flow measured using the method presented in the previous section is plotted for $n = 0$ to 3 in figures 9.15-9.18. The power flow is measured using both the accelerometer decomposition method and the modal sensor method.

For each n, the modal power flow is measured at various axial positions (the positions of the different modal sensors). Some of the measurement positions are relatively far away from the point of excitation (up to 25 radii), but the modal power flow is theoretically the same at all axial positions, as the modes are supposed to be orthogonal (the first

assumption in the previous section) so that power injected into one mode n stays in that mode. The constant-power prediction is, however, only true for lossless media, and as there is a substantial loss in the pipe material (the loss factor of PVC was measured at approximately 3 %), the power injected by the source tends to be underestimated at a far field measurement point. The underestimation becomes larger, the further away from the source.

Figures 9.15-9.18 show that it is generally true for all modes (disregarding individual peaks) that the measured power flow is smaller than the predicted. The sole exception is for $n = 2$ (figure 9.17). Here the power flow measured by the modal sensor is larger than the predicted response from approximately 700 Hz upwards. A possible explanation for this behaviour is modal leakage from the $n = 3$ mode, which cuts on at approximately this frequency.

The modal power flow of the $n = 0$ mode measured with the modal sensor is clearly closer to the predicted response than the accelerometer method at low frequencies. On the other hand the roll off at high frequencies is more pronounced for the modal sensor measurements. This is a general trend (except for $n = 2$ discussed above), and as discussed in the previous section, it can probably be related to the local damping effect from the adhesive tape used to position the modal sensor and the aluminum tape used to shield the modal sensor from external electrical disturbances.

As discussed in the previous section, the bad performance of the $n = 3$ modal sensor is probably caused by small misalignments of the individual patches of the modal sensor.

9.3.3 Total power flow

Figure 9.19 shows the total power flow. In view of the problems discussed with the individual modal power flows, the agreement between the measurements and the predicted response is surprisingly good for the modal sensor measurements. The accelerometer method overestimates the power flow at low frequencies by several decades; this can be related to error in the $n = 0$ mode, as discussed in section 8.3.3 for the light fluid loading case. Neither of the measurement methods is capable of capturing the predicted cuton peaks of the higher order modes, but still the overall agreement is quite good.

9.4 Fluid excited pipe: accelerance measurements

All the previous measurements presented in this thesis have been excited by a radial force applied externally on the pipe wall. The measurements presented in the rest of this chapter, are all excited by a hydrophone transmitting in the contained fluid. The wall response measurements are all done using the modal sensors. It might have been be possible to assume stationarity and then use the accelerometer decomposition method, but measurements with modal sensors are much more practical as they require no repeat testing and no ($n \neq 1$) or little ($n = 1$) postprocessing.

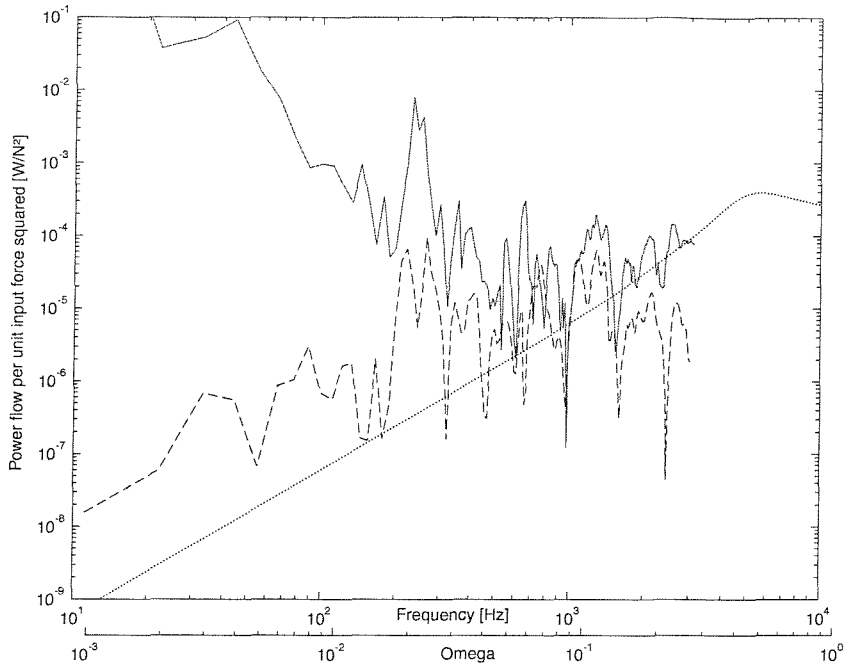

Figure 9.15: Modal power flow for a pipe with heavy fluid loading excited by a radial point force, $n = 0$, $s = 20$. The line for the predicted power flow is dotted, the accelerometer measured solid, and the modal sensor measured dashed.

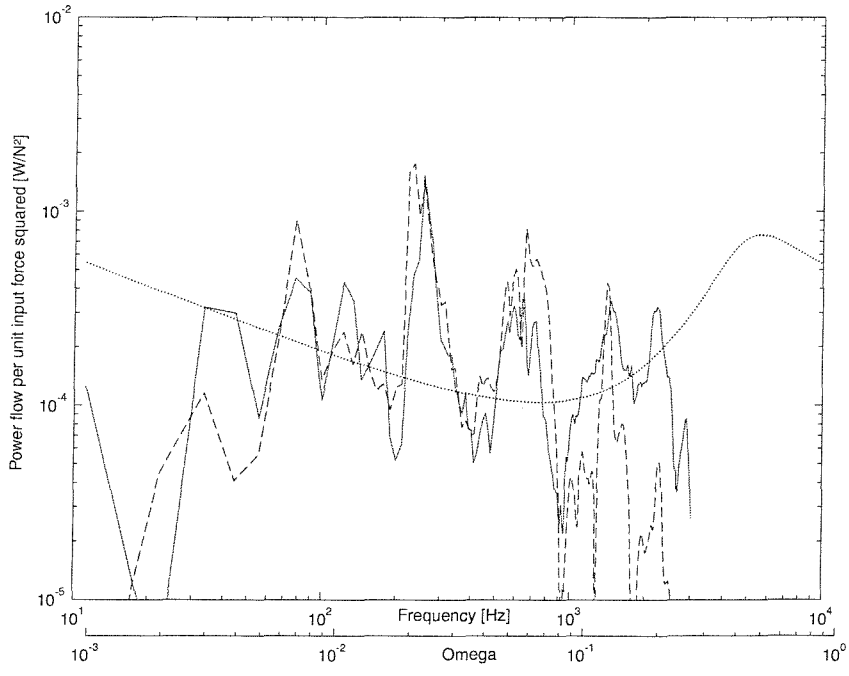

Figure 9.16: Modal power flow for a pipe with heavy fluid loading excited by a radial point force, $n = 1$, $s = 4.9$. The line for the predicted power flow is dotted, the accelerometer measured solid, and the modal sensor measured dashed.

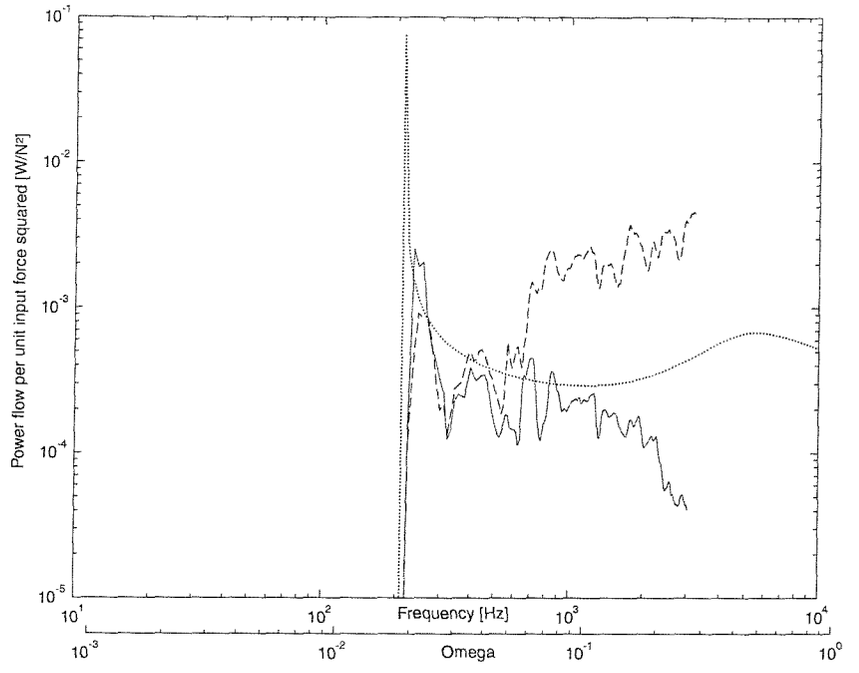

Figure 9.17: Modal power flow for a pipe with heavy fluid loading excited by a radial point force, $n = 2$, $s = 24.5$. The line for the predicted power flow is dotted, the accelerometer measured solid, and the modal sensor measured dashed.

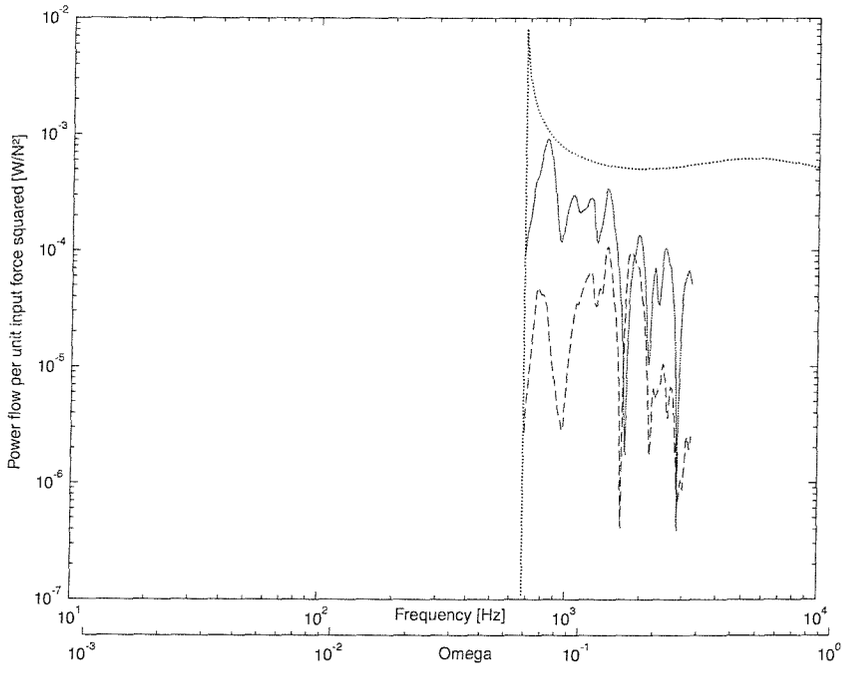

Figure 9.18: Modal power flow for a pipe with heavy fluid loading excited by a radial point force, $n = 3$, $s = 14.7$. The line for the predicted power flow is dotted, the accelerometer measured solid, and the modal sensor measured dashed.

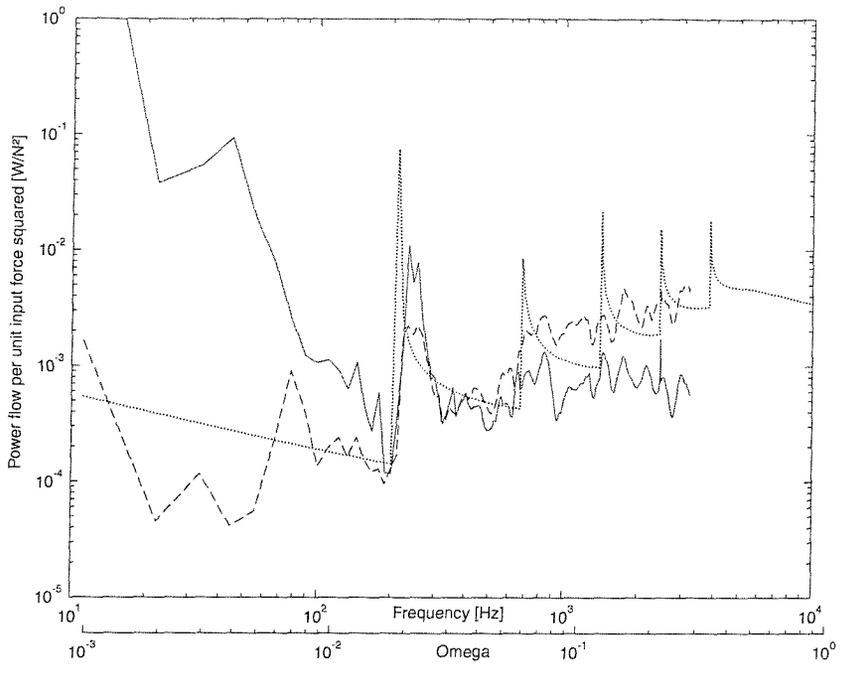

Figure 9.19: Total power flow for a pipe with heavy fluid loading excited by a radial point force. The line for the predicted power flow is dotted, the accelerometer measured solid, and the modal sensor measured dashed.

The measurement setup of the transmitting hydrophone is discussed in section 9.6.1. For reasons discussed in section 9.6.1, no excitation was provided below 100 Hz. When comparing the hydrophone excited measurements with the point force excited measurements, it should be kept in mind that the frequency range between 10 and 100 Hz (where most of the peaks due to standing waves are) is not included in the hydrophone excited measurements.

During the early experiments with the transmitting hydrophone, the hydrophone was placed on the axis of the pipe. If the hydrophone behaved like a point monopole, only the $n = 0$ mode (both fluid and structural) should be excited at low frequencies. However, this was not the case and other modes were excited. Measurements of the far field pressure radiated by a hydrophone, made by B&K (Bruel&Kjaer 1992) in a free field, have shown that a hydrophone to a large extent behaves like a monopole (omnidirectional radiation). Inside the pipe, the hydrophone is not in a free field and it is questionable whether the active element of the hydrophone is sufficiently small, compared with the shortest wavelengths involved, to be regarded as a point source. There is the further issue of the blockage due to the hydrophone body, and another complication is the support of the hydrophone which acts as a rigid connection between the hydrophone and the pipe wall. The point monopole on the axis of the pipe excites only the $n = 0$ mode because the excitation of modes with $n \geq 1$ cancels due to the symmetry of the excitation. All the complications mentioned above disturb the ideal situation of symmetry, and therefore other modes are excited by the hydrophone even

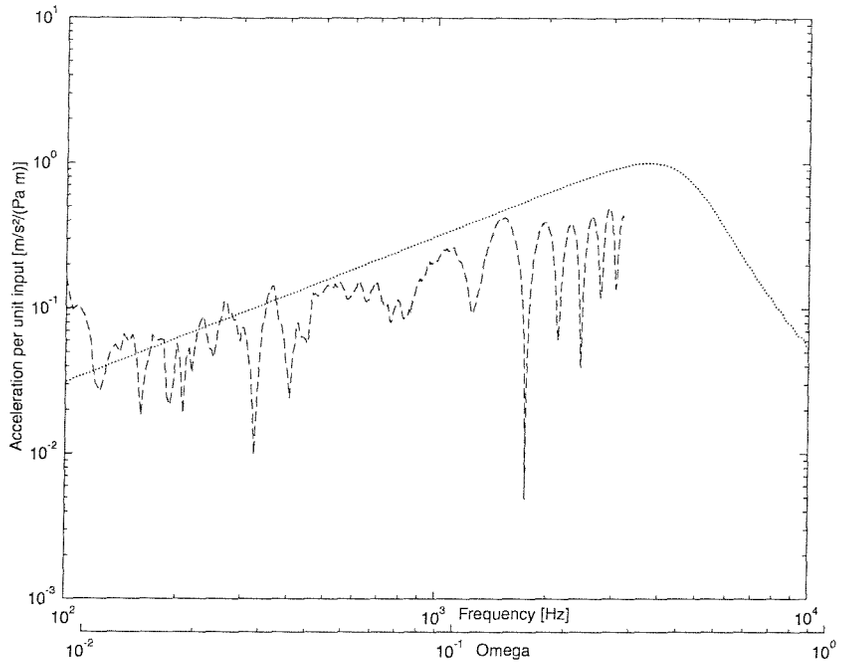

Figure 9.20: Modal accelerance for a pipe with heavy fluid loading excited by a transmitting hydrophone, $n = 0$, $s = 20$. The line for the predicted accelerance is dotted and the modal sensor measured dashed.

when it is placed on the centerline.

To provide an excitation of the fluid that is not relying so much on the symmetric properties, the hydrophone is placed halfway between the centerline and the pipe wall. In the predictions, the excitation is a point monopole placed at $(r_o, \theta_o, s_o) = (0.5, 0, 0)$.

Figures 9.20-9.22 show the modal accelerance for modes $n = 0$ to 2.

For $n = 0$, there is generally good agreement between measurement and prediction of the accelerance. There are some troughs in the measured accelerance, but strangely hardly any peaks. The modal leakage from the cuton of the higher modes is hardly noticeable. There is a slight roll off of the measured accelerance, but the roll off is significantly smaller than for the point force excited measurement. The reason for this is probably that the damping in the pipe wall material has less significance for fluid excitation, as most of the power flow is contained in the fluid.

Comparison of the measured accelerance with the predicted accelerance for the $n = 1$ mode (figure 9.21) shows there are rather large discrepancies at both high and low frequencies. The high frequency roll off is probably related to the damping in the shell wall discussed above. As noted in section 9.6.1, the local reinforcement inserted in the pipe wall to accommodate the hydrophone support affected the local properties of the pipe wall. The discontinuity of the pipe wall affects the cuton of the $n = 2$ mode, which could result in significant modal leakage. The level of accelerance at approximately 200 Hz is approximately the same for the $n = 1$ and $n = 2$ modes, but

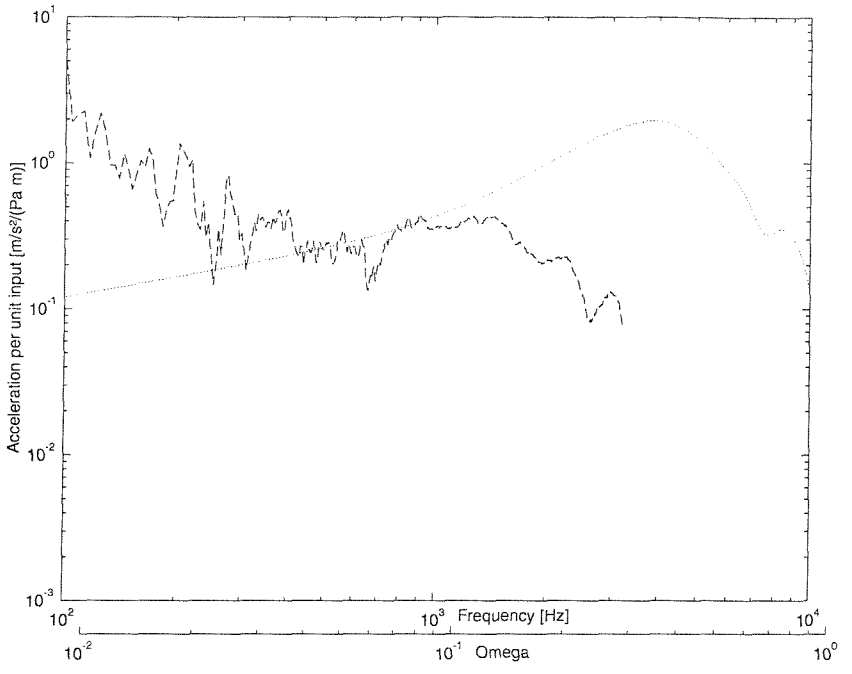

Figure 9.21: Modal accelerance for a pipe with heavy fluid loading excited by a transmitting hydrophone, $n = 1$, $s = 4.9$. The line for the predicted accelerance is dotted and the modal sensor measured dashed.

this may be a coincidence.

The measured accelerance for the $n = 2$ mode (figure 9.22) has a significant accelerance response below cuton of the first structural branch. This was also the case for the experiments excited by a radial point force, so it may be related to modal leakage from other modes. The cuton of the first structural branch is clearly visible, but the peak is not resolved during the measurements. At the cuton frequency of the $n = 3$ mode there is a clear trough in the measured accelerance for $n = 2$. This is probably related to some sort of modal interference through misalignment of the patches that make up the modal sensor, as a closer examination of the complex response obtained from the PULSE Multi-analyzer shows a change of sign at this frequency. If there are misalignments then the response from the different patches might be slightly out of phase, producing a complicated interference that cannot easily be interpreted. Above the cuton frequency the general agreement between the measured and predicted accelerance is good, although the measurements show a slight overestimation of the accelerances.

The modal accelerance for the $n = 3$ mode is not plotted as all the comments made for figure 9.22 also apply for $n = 3$, except that the accelerance is smaller than predicted.

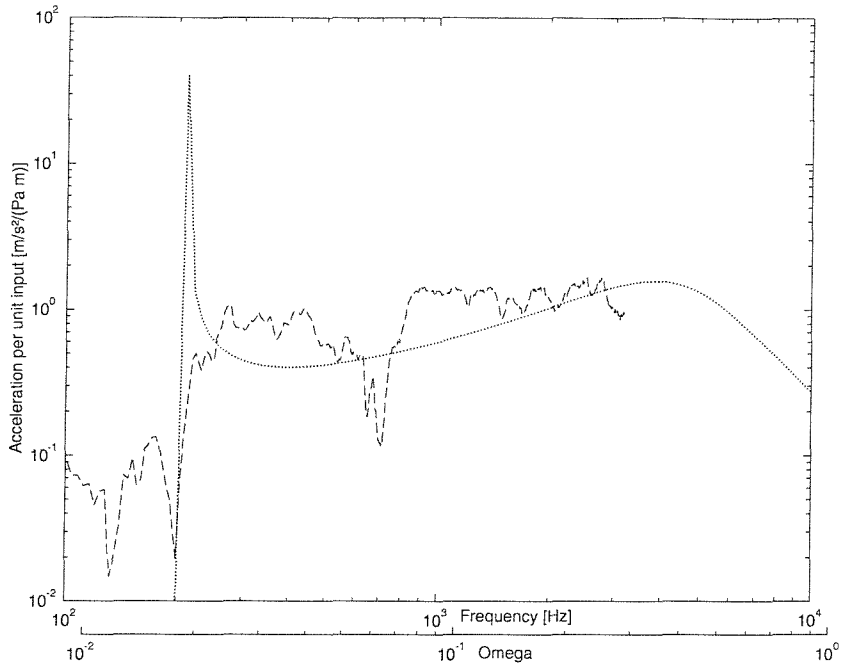

Figure 9.22: Modal accelerance for a pipe with heavy fluid loading excited by a transmitting hydrophone, $n = 2$, $s = 24.5$. The line for the predicted accelerance is dotted and the modal sensor measured dashed.

9.5 Fluid excited pipe: power flow measurements

The power flow measurement method for heavy fluid loading presented in section 9.3.1 also applies when the fluid filled pipe is excited by a monopole in the internal fluid, as the modal power flow is dominated by the same branches. However, this is not generally the case and other types of excitation may lead to different dominating branches. While other types of excitation are not addressed in the present thesis, the power flow measurement method can be adapted, provided the conditions discussed in section 9.3.1 are met and a suitable modal power flow factor is defined.

As noted in section 8.3.1.2 it would be possible to express the modal power flow factor using predicted results from an internal monopole, but as the resulting power flow is the same when the assumptions in question are met there is no point in doing so.

9.5.1 Modal power flow

The modal power flows presented in this section are calculated using equation (8.5) along with the wall accelerance measurements from the previous section. The modal power flows inferred from this was are plotted in figures 9.23-9.25 (modes $n = 0$ to $n = 2$), with the predicted power flows also plotted for for comparison.

Figure 9.23 shows broad agreement for the $n = 0$ mode in respect of overall trends, but

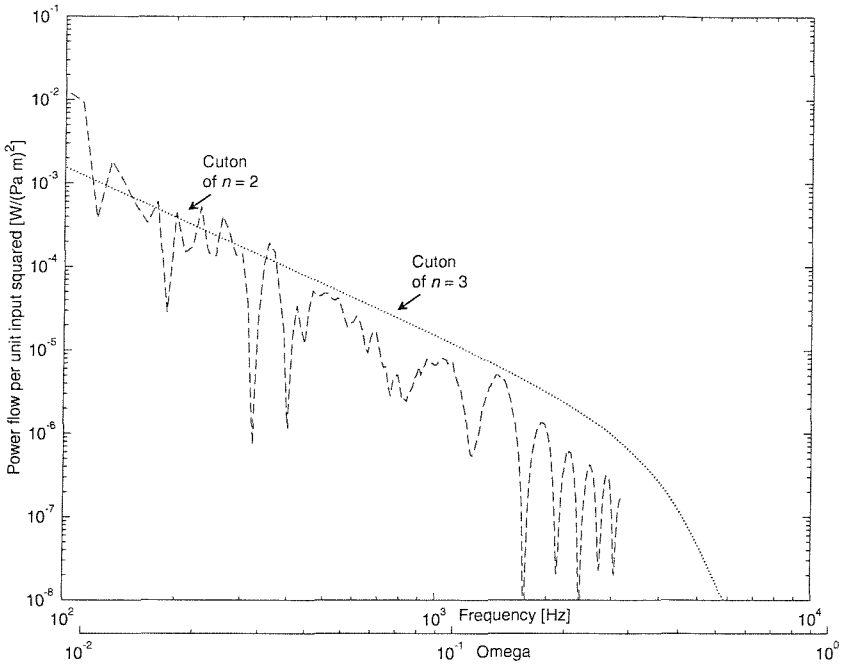

Figure 9.23: Modal power flow for a pipe with heavy fluid loading excited by a transmitting hydrophone, $n = 0$, $s = 20$. The predicted power flow is dotted, and the modal sensor measured dashed.

the measured power flow is impaired by the large number of troughs dipping several orders of magnitude below the predicted power flow. The dips are apparently not related to the cuton frequencies of higher order modes.

At low frequencies the measured power flow for the $n = 1$ mode (figure 9.24) is 2 decades larger than the predicted power flow. At mid-frequencies there is a good agreement between the measured and predicted power flows, but at high frequencies the measured power flow is several decades smaller than the predicted power flow. Taking a broad view on figure 9.24 the overall trend in the measured power flow is different from the trend in the predicted power flow. A slight dip can be seen in the measured accelerance approximately at the cuton frequency of the $n = 3$ mode.

The same dip at the $n = 3$ cuton frequency can be seen in figure 9.25 ($n = 2$). The dip is not predicted theoretically, and a possible reason is the modal interference discussed in the previous section. Away from these frequencies, the power flow inferred from the measurement of the $n = 2$ mode tends to be higher than the theoretical prediction based on modelling the hydrophone as a monopole source.

9.5.2 Total power flow

The modal contributions of the power flow from $n = 0$ to $n = 3$ have been summed in figure 9.26.

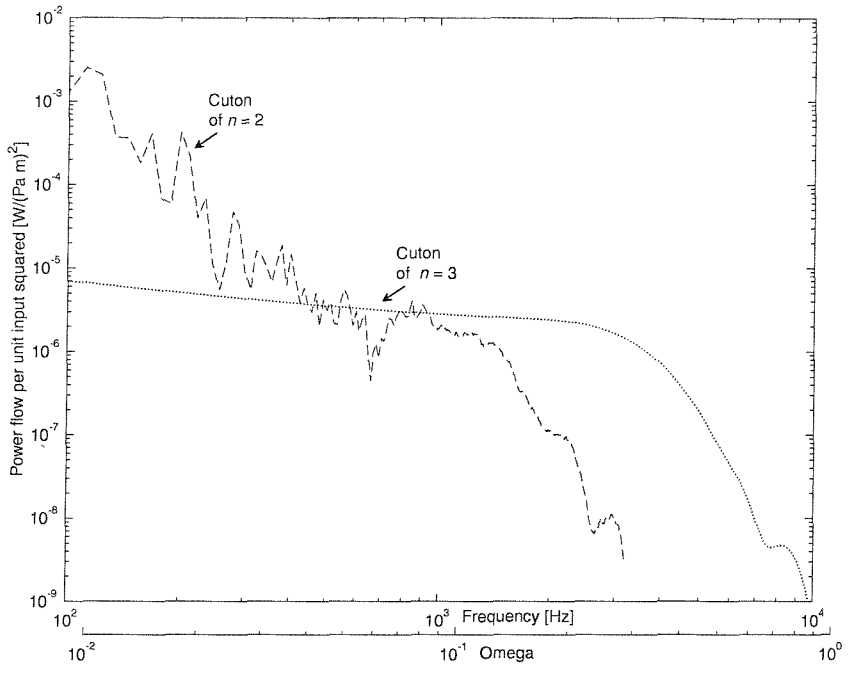

Figure 9.24: Modal power flow for a pipe with heavy fluid loading excited by a transmitting hydrophone, $n = 1$, $s = 4.9$. The predicted power flow is dotted, and the modal sensor measured dashed.

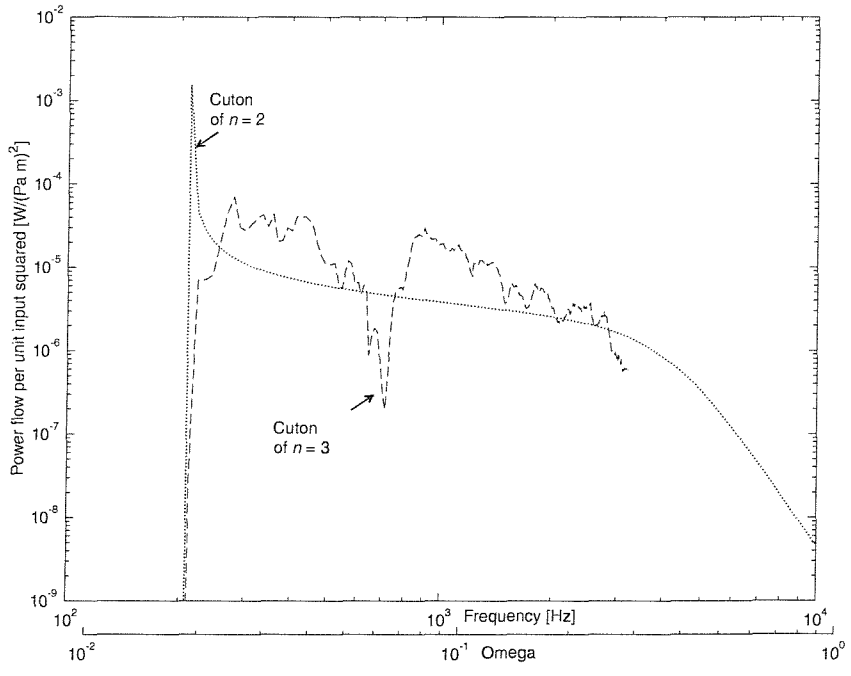

Figure 9.25: Modal power flow for a pipe with heavy fluid loading excited by a transmitting hydrophone, $n = 2$, $s = 24.5$. The predicted power flow is dotted, and the modal sensor measured dashed.

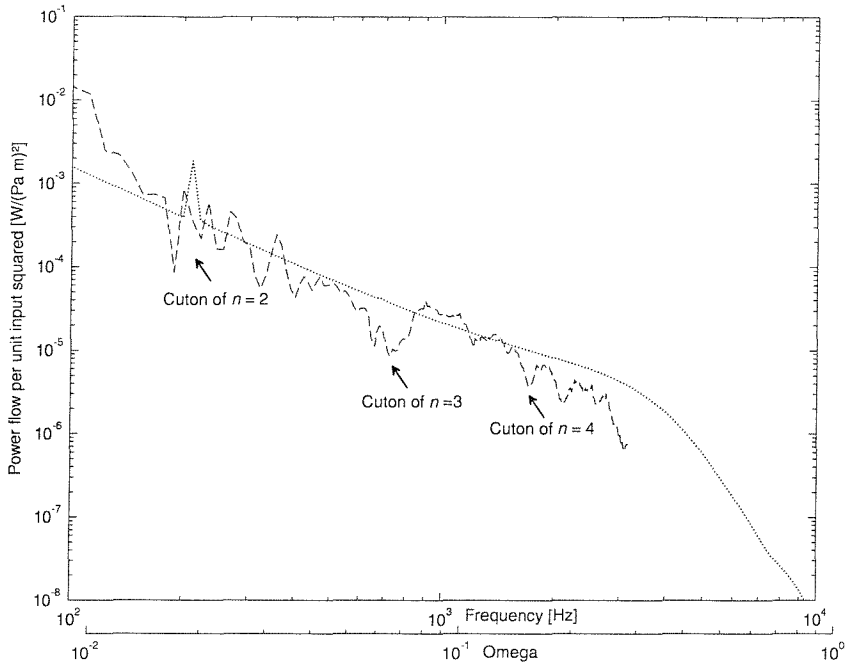

Figure 9.26: Total power flow (modes n=0,1,2,3) for a pipe with heavy fluid loading excited by a transmitting hydrophone. The predicted power flow is dotted and the and the modal sensor measurements dashed.

As for the force excited measurements, the agreement between the measured and the predicted power flow using the modal sensors is striking. To obtain such good agreement from the somewhat erratic behaviour of some of the modal power flows, requires that none of the large dips seen in each of the modal power flows happens at the same frequencies for different modes. It may be that some of the dips are caused by insufficient anechoic termination; but as the different modal measurements are made at different axial positions, the frequencies of the standing wave troughs will be different.

The relatively poor measurements of the modal power flow for $n = 1$ and $n = 3$ make hardly any contribution to the total power flow, as the total power flow is largely dominated by $n = 0$ at low frequencies and $n = 2$ at high frequencies.

9.6 Detailed comments on the experimental setup

9.6.1 Hydrophone excitation of the fluid

While a transmitting hydrophone in theory could be used as a source of excitation for both light and heavy fluid loaded experiments, the hydrophone proved a relatively inefficient sound source in air, and the signal to noise ratio was too small to make reliable measurements.

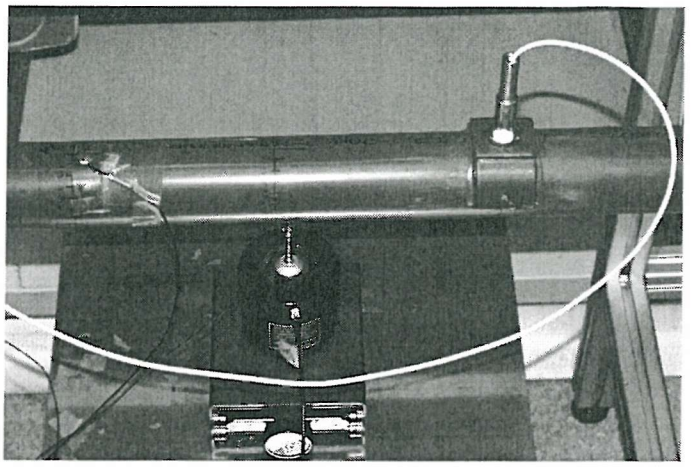

Figure 9.27: Hydrophone mount.

In the water-filled pipe, the hydrophone provided a reasonable signal to noise ratio in the single frequency and sweeping modes, but not in the broadband mode. All experiments were therefore made in sweeping mode with peak hold on the PULSE Multi-analyser. If any sudden extraneous noise disturbed the measurement, it was simply repeated. During the experiments this happened quite often for frequencies below 100 Hz, so the excitation was sweeping only from 100 Hz upwards and results below this frequency was discarded.

To position the hydrophone inside the pipe a hydrophone mount was used, as seen in figure 9.27. The hydrophone mount allowed the hydrophone to be traversed along a diameter of the pipe, but the position of the hydrophone was fixed in the axial and circumferential direction. As the water-filled pipe was pressure tested to at least 400 kPa the hydrophone mount had to be rather large to provide enough adhesion area to be glued to the pipe. The mount covered almost π radians of the circumference and undoubtedly added significant added mass and stiffness to the pipe, but it is difficult to quantify the resulting error on the measurements.

The smallest available hydrophone was a B&K 8103 hydrophone with a diameter of 9.5 mm and a length of approximately 25 mm. This is by no means a point source in a pipe with a diameter of approximately 60 mm, but again it is difficult to quantify the resulting error on the measurements.

The mount of the hydrophone was less than ideal during the measurements, partly due to the mass and stiffness effects already discussed, but also due to the radial orientation of the hydrophone. Given the rather large hydrophone, the preferred orientation would have been axial not radial. With a coaxial placement of the pipe and the hydrophone, axisymmetric excitation would have been possible, thus not exciting any modes other than $n = 0$. Unfortunately the practical problems with a coaxial placement were too many, and the radial placement was chosen as it was reasonably easy to install.

The hydrophone was calibrated in air to find a source calibration factor, expressed as the distance normalised pressure in a free field. By assuming a very high source

impedance of the hydrophone in comparison with the heavy fluid loaded pipe, the calibration factor for the hydrophone could be used along with the density of the internal fluid to find the corresponding monopole source strength:

$$S = iC_H\omega^2\rho_f V \tag{9.1}$$

where S is the monopole source strength (distance-normalised pressure) as it appears in equation (5.17); $C_H = 9.92 \cdot 10^{-15}$ m^3/V is the hydrophone calibration factor for the hydrophone used during the experiments; and V is the voltage supplied by the B&K 2713 power amplifier.

9.6.2 Fluid anechoic termination of finite pipe

The basic concept of the fluid anechoic termination used in the present thesis is to continue the measurement pipe into a long flexible rubber hose, that will dissipate the energy of any acoustic pressure fluctuations. The main difficulty with this approach is to avoid reflection of fluid-borne sound at the impedance jump between the measurement pipe and the connected rubber hose; and to ensure that all fluid-borne sound is dissipated in the rubber hose.

The minimise the impedance jump problem, an impedance matching segment was added between the measurement pipe and the rubber hose. The idea of this segment is to gradually match the pipe-wall impedance from the measurement pipe to the rubber hose. To make the impedance match, the end of the measurement pipe (approximately the last 0.5 m) is perforated with an increasing density of holes in the axial direction and the long rubber hose is then clamped to the measurement pipe just before the first perforation. The distribution of the holes at the ends of the measurement pipe was designed so the impedance was gradually lowered from the wall impedance of the measurement pipe to the impedance of the rubber hose.

Even though the impedance matching segment reduced the reflection of fluid-borne sound, a greater length of rubber hose could possibly have reduced the reflections further, but 30 m was the practical limit and no further attempts were made.

9.6.3 Modal sensing of pipe wall vibration using modal sensors

Two different types of modal sensors were used during the experiments: a PVDF-wire wound around the pipe for the axisymmetric $n = 0$ mode, and patches of PVDF film for $n = 1$ to $n = 3$.

9.6.3.1 PVDF wire method for measuring the axisymmetric mode

The PhD-thesis by Briscoe (1994), and the subsequent papers by Pinnington and Briscoe (1994) and Briscoe and Pinnington (1996), describe a method of measuring

the radial component of axisymmetric vibrations of a pipe, using a piezoelectric PVDF wire wound around the circumference of the pipe. Briscoe (1994) showed that a PVDF wire (Vibetek 20, Ormal Ltd.) has a constant charge sensitivity over a wide frequency range and is well suited as an axisymmetric modal sensor.

If a wire is wound N times around a pipe, then the extension of the wire ΔL can be related to the radial component symmetric displacement w by $\Delta L = 2\pi N w$, provided no offset error is introduced by the finite thickness of the pipe wall and the wire. The charge produced by an extension of the wire is $C = S\Delta L$, where S is the charge sensitivity of the wire (approx. $2.4 \cdot 10^8$ pC/m for Vibetek 20). The radial component of vibration can thus be deduced from

$$w = \frac{C}{2\pi N S} \tag{9.2}$$

This relation assumes that the charge generated in the PVDF wire from axial and torsional stresses in the pipe is negligible. This assumption was assessed in Briscoe (1994) and he concluded that it was completely justified. Also the measurement error related to overlap in the winding of the wire around the pipe was assessed and his conclusion was, that if good care was taken in cutting the wire to match an integral number of turns around the pipe, the contributions from higher order modes to the measured result would be negligible too.

9.6.3.2 Shaped PVDF film sensors for higher order modes

The shaped sensors used in the present thesis are based on the work by Variyart and Brennan (1999). They applied the shaped sensor principle for a modal sensor for $n = 2$, but not for $n = 1$ and $n = 3$. Theoretically, the shaped sensor principle can also be applied for the axisymmetric mode, but this has not been done for the present thesis.

The shaped sensor consists of patches of piezoelectric (PVDF) film bonded to the outside of the pipe. The patches are then connected electrically in a special way to amplify certain circumferential modes and cancel the rest. A picture of a prototype modal sensor can be seen in figure 9.28.

It is assumed that the bonding is complete, so the strain on the outside of the pipe is replicated in the piezoelectric material. Furthermore the added mass, added stiffness, and added damping are assumed to be negligible, so the vibration of the pipe is unaffected by the presence of the piezoelectric material. As shown during the experiments in the present thesis with the modal sensors, this might not always be the case.

Some of the background detail for the shaped modal sensors is presented in appendix A, but for a more complete reference see Variyart and Brennan (1999).

The PVDF-film modal sensors are displacement sensors, so the charge generated is proportional to the radial displacement of the pipe wall. The total displacement can

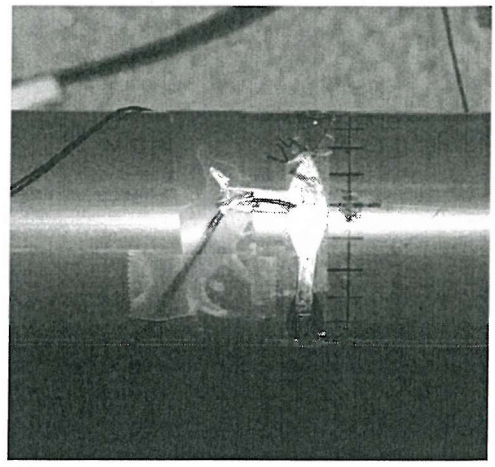

Figure 9.28: Prototype $n = 3$ modal sensor mounted on pipe wall.

be written as the sum of the modal displacements:

$$w = \sum_{n=0}^{\infty} w_n = \sum_{n=0}^{\infty} \sum_{b=1}^{\infty} aW_{nb}^r \cos(n(\theta - \theta_o)) e^{i\kappa(s-s_o)} \tag{9.3}$$

Here W_{nb} is the modal displacement amplitude to be recovered through the measurements. In the application of the equation it is convenient to substitute the cos part of the above expression, as the angle between excitation and vibration, θ_o, is not known, with

$$\cos(n(\theta - \theta_o)) = \phi_c \cos(n\theta) + \phi_s \sin(n\theta) \tag{9.4}$$

where $\phi_c = \cos(n\theta_o)$ and $\phi_s = \sin(n\theta_o)$.

A modal sensor for $n = 1$. For the $n = 1$ mode, the cross section of the pipe is unaltered and thus the main strain at low frequencies is related to the axial stretching of the pipe that accompanies bending (the pipe acts like a beam). When the dominant strain is in the axial direction, the charge is generated by the $n = 1$ modal sensor in accordance with equations (A.11) and (A.12) in appendix A.

At low frequencies, there will be only one propagating branch ($b = 1$) for the bending mode and it is therefore not necessary to sum up the contributions for different branches.

The simplified charge equations for the cosine and sine $n = 1$ modal sensors are then:

$$\begin{aligned} q_{c,n=1} &= 4\pi\phi_c e_{32} y_o a \kappa_{11} W_{11} e^{i\kappa_{11} s_c} \mathrm{J}_1(\kappa_{11} b_s) \\ q_{s,n=1} &= 4\pi\phi_s e_{32} y_o a \kappa_{11} W_{11} e^{i\kappa_{11} s_c} \mathrm{J}_1(\kappa_{11} b_s) \end{aligned} \tag{9.5}$$

where e_{32} is a piezoelectric stress constant; y_o is the offset of the sensor from the midplane of the pipe wall; s_c is the center position of the sensor; and $b_s = b/a$, where b is half the width of the sensor.

From equation (9.5) a cosine and a sine part of the modal displacement amplitude can be recovered. By combining the sine and cosine parts, the modal displacement amplitude for for $n = 1$ can be obtained as

$$W_{11} = \sqrt{(\phi_c W_{11})^2 + (\phi_s W_{11})^2} \tag{9.6}$$

If needed θ_o can be found as

$$\theta_o = \frac{1}{n} \tan^{-1} \left(\frac{q_{s,n=1}}{q_{c,n=1}} \right) \tag{9.7}$$

Unfortunately, the axial wavenumber appears in the equation (9.5) and this is a bit disturbing, as post-processing is needed to calculate the response. Equation (9.5) is only valid below the cuton frequency of the second propagating branch for $n = 1$, because the summation over the branches is left out.

A modal sensor for $n = 2$. The $n = 2$ mode is also dubbed the ovalling mode, for the simple reason it bounces back and forth in the distinct shape of two ovals. This generates large circumferential strains that can be detected using equations (A.15) and (A.16) in appendix A. It is possible to reduce these equations further by using the small argument series expansion of the Bessel function, Morse and Ingard (1968),

$$\mathrm{J}_n(z) = \frac{(\frac{z}{2})^n}{n!} - \frac{(\frac{z}{2})^{n+2}}{1!(n+1)!} + \frac{(\frac{z}{2})^{n+4}}{1!(n+2)!} - \ldots \tag{9.8}$$

Using this, the charge equations can be reduced to

$$\begin{aligned} q_{c,n=2} &= 2\pi\phi_c e_{31} b_s y_o a \sum_{b=1}^{\infty} \frac{3}{(1+\frac{y_o}{a})} W_{2b} e^{i\kappa_{2b} s_c} \\ q_{s,n=2} &= 2\pi\phi_s e_{31} b_s y_o a \sum_{b=1}^{\infty} \frac{3}{(1+\frac{y_o}{a})} W_{2b} e^{i\kappa_{2b} s_c} \end{aligned} \tag{9.9}$$

where e_{31} is a piezoelectric stress constant. For frequencies below the cuton of the second propagating branch for $n = 2$, the summation can be left out and the displacement amplitude can be recovered as for the $n = 1$ modal sensor. The axial wavenumber is not appearing in equation (9.9) and therefore no subsequent postprocessing is necessary, as the relation between the charge and the displacement amplitude can be formulated as a charge sensitivity that can be stored in the PULSE Multi-analyzer.

A modal sensor for $n = 3$ The main characteristic of the $n = 3$ or teddy bear mode is the same as for the $n = 2$ mode with large circumferential strains. The reduced charge equations for the $n = 3$ mode are

$$q_{c,n=3} = 2\pi\phi_c e_{31} b_s y_o a \sum_{b=1}^{\infty} \frac{8}{(1+\frac{y_o}{a})} W_{3b} e^{i\kappa_{3b} s_c} \tag{9.10}$$

$$q_{s,n=3} = 2\pi\phi_s e_{31} b_s y_o a \sum_{b=1}^{\infty} \frac{8}{(1+\frac{y_o}{a})} W_{3b} e^{i\kappa_{3b} s_c} \tag{9.11}$$

For frequencies below the cuton of the second propagating branch for $n = 3$, the summation can be left out and the displacement amplitude can be recovered as for the $n = 2$ modal sensor.

Modal sensors for $n \geq 4$ By using equations (A.15) and (A.16) in appendix A modal sensors can be created for arbitrary high n. However, as shown in section 9.2.1 the precision regarding the shaping and the mounting of the sensors become even more crucial the higher the mode n.

9.7 Conclusion

The measurement principles presented in part I of the present thesis have been applied to a pipe with heavy fluid loading with good results. The excitation of the pipe is provided both by a radial point force at the shell wall and a transmitting hydrophone in the interior fluid, and the conclusions for each type of excitation are presented separately in what follows.

9.7.1 Experiments with structural excitation

The response of the pipe wall has been measured by modal decomposition of accelerometer measurements and by modal sensors. Both types of measurements are compared with predictions from the prediction model in chapter 6.

If one compares the pipe with light fluid loading and the pipe with heavy fluid loading, the two most notable differences are the generally lower levels of accelerance and the lower cuton frequencies for the heavy fluid loaded pipe. The reduced level of accelerance is related to the increased mass of the fluid-filled pipe in the case of heavy fluid loading, while the lower cuton frequencies of the higher order modes can be explained by the lower relative stiffness of the shell wall for the pipe with heavy fluid loading. Apart from these differences, the conclusions from chapter 8 drawn from the experiments on a light fluid loaded pipe also apply for a heavy fluid loaded pipe.

The measured accelerance obtained by using the PVDF wire as a modal sensor for the $n = 0$ mode compares significantly better with the predicted accelerance at low frequencies than the accelerance obtained through decomposition of accelerometer measurements. The modal sensor for $n = 1$ and the decomposed measurements produce similar accelerances that compare well with the predicted accelerances. However, at low frequencies both the modal sensors for $n = 2$ and $n = 3$ and the modal decomposition method measure accelerances higher than predicted.

For the higher order modes, the sharp increase in accelerance at the cuton of the first

structural branch of the higher order modes is resolved nicely in all measurements, but the $n = 2$ modal sensor measures a larger accelerance than predicted at higher frequencies, while for $n = 3$ both the modal sensor and the accelerometer decomposition measure smaller accelerances than predicted.

The modal sensors are easy to use and they produce generally smaller modal leakage than the modal decomposition of accelerometer measurements, but especially for the higher order modes the patches of the modal sensor need to be shaped and mounted with high precision to obtain quality measurements.

The conclusion regarding the modal measurement technique is that both measurement principles are workable, but the measurements with the modal sensors are a lot faster. If the modal sensor principles used in the present investigation could be taken beyond the early prototype state to allow for higher precision and reliability, then their performance would undoubtly be even better than shown during these experiments.

9.7.2 Experiments with fluid excitation

The response of the pipe wall is measured solely by modal sensors during the experiments with fluid excitation. The fluid excitation is provided by a transmitting hydrophone inside the pipe. Otherwise the experimental setup is similar to the experiments excited by a structural force.

Generally the tendencies regarding the measured modal accelerances are the same as for the structural force measurements: in particular the accelerance measured by the $n = 0$ modal sensor compares well with the predicted accelerance. For $n = 1$ the measured accelerance is larger than predicted at low frequencies, but lower than predicted at higher frequencies. Below cuton of the structural branch of both the $n = 2$ and $n = 3$ modes the measured accelerance is higher than the predicted accelerance, while the measured accelerances at higher frequencies are higher than predicted for $n = 2$ and lower than predicted for $n = 3$.

The total power flow measured by the modal sensors compares surprisingly well with the predicted total power flow. The relatively poor measurements of the modal power flows for $n = 2$ and $n = 3$ at low frequencies make hardly any contribution to the total power flow, while the $n = 2$ mode dominates at higher frequencies where the measurements of the modal power flow for $n = 0$, $n = 1$ and $n = 3$ are relatively poor.

The main conclusion from the experiments with fluid excitation is that the measurements and the predictions for each mode generally agree quite closely, where the mode makes a significant contribution to the power flow.

Part IV

Conclusion, discussion and industrial implications

Chapter 10

Conclusion and discussion

As stated in chapter 2 the main objective of the research programme is to find ways of quantifying hydroacoustic noise sources coupled to a fluid-filled pipe system. There is an industrial interest in both experimental and numerical approaches to this problem. In the present thesis an experimental and a numerical simulation method have both been investigated.

The main conclusions are listed below. In the following two sections the conclusions from the two methods are presented separately. The chapter ends with an appraisal of the entire research programme.

10.1 List of conclusions

- The concept of numerical calculation of the vibroacoustic power flow excited by the turbulent flow past a flow obstruction inside fluid-filled pipes have been devised. The concept involves three steps: numerical calculation of the fluid flow, construction of a vibroacoustic analogy, and calculation of the vibroacoustic power flow from the equivalent mechanical and acoustical sources. Numerical calculation of the fluid flow is not part of the present thesis, the vibroacoustic analogy is presented in chapter 4, and chapter 6 presents the calculation of the vibroacoustic power flow.

- The relative Mach number scaling for monopole, dipole and quadrupole type sources that applies in a free field also applies inside pipes with light and heavy fluid loading. The relative scaling of multipole source is investigated in chapter 4.

- For fluid-filled pipes the vibroacoustic response and the vibroacoustic power flow can be predicted for two fundamentally different types of excitation: mechanical (via the structure) and acoustical (via the fluid). The structural excitation is in the form of a point force, while the acoustical excitation is in the forms of a point monopole, a point dipole, and a point quadrupole in the interior fluid. Chapter

6 contains the prediction model for point force and point monopole excitation, while the derivation of point dipoles and the point quadrupoles from the point monopole Green function is presented in chapter 4.

- The vibroacoustic power flow in anechoically terminated fluid-filled pipes with light and heavy fluid loading can be measured for frequencies below 0.2 times the ring frequency of the pipe using either an accelerometer array or shaped PVDF modal sensors. Chapter 3 presents the power flow measurement concept, while the experiments are presented in chapters 8 and 9.

10.2 Experimental quantification of vibroacoustic power flow

The concept of the experimental method has been presented in chapter 3. The validation tests of chapter 8 and 9 were carefully designed to create a common scenario that allows both numerical prediction and experimental realisation. This is accomplished through doubly infinite pipes in the numerical prediction, and anechoic termination of the finite pipe used in the experiments. When the scenario is established, comparison of the measured and predicted response of the pipe wall allows the vibroacoustic power flow in the experimental realisation to be inferred from the predicted vibroacoustic power flow subject to certain conclusions being met. These are: the power flow in different circumferential modes can be treated independently; only one propagating branch for each circumferential mode; and there are only outgoing waves from the noise source. These assumptions are quite restrictive, but they allow the experimental quantification of the vibroacoustic power flow using only one set of measurements of the modal response of the pipe wall. If more sets of measurements were available, some of the assumptions could be relaxed; this is discussed in more detail in chapter 11.

The experimental quantification principle has been validated by comparison between controlled experiments and numerical predictions in two cases where the above assumptions are met: pipe with light internal fluid loading, and pipe with heavy internal fluid loading. In both cases external fluid loading is present as there is air on the outside of the pipe. However, a part of the parameter study in chapter 7 assesses the effect of light external fluid loading of the pipe. The conclusion was that regardless of the internal fluid loading, the light external fluid loading has a negligible effect on both the dispersion curves and the calculated mobility of the experimental setup used in the verification experiments. As a result, the external fluid loading is disregarded in the present thesis (i.e. replaced by vacuum in the prediction model, from chapter 6, used to validate the experiments). Therefore any reference to e.g. 'light fluid loading' implies that no external fluid load is present and the internal fluid loading is light.

In chapter 8, the measurement principles suggested in chapter 3 have been applied to a pipe with light fluid loading. The excitation of the pipe is provided by a radial point force. The measured modal accelerance is compared with the accelerance predicted by the prediction model in chapter 6. A common feature of all the comparisons between

the measurement and prediction is that the agreement improves as the measurement position is moved towards the point of excitation; in the near field of the point of excitation, the agreement is excellent. The modal measurement shows some modal leakage where accelerance from a strongly excited mode apparently leaks to a weakly excited mode. However, when all the modal contributions are summed to form a so-called synthetic point accelerance, the strongly excited mode dominates the weakly excited modes, thus effectively removing the effect of the modal leakage.

The agreement at low frequencies between the measured and predicted modal power flows is generally good, but at higher frequencies there is a significant roll off. This high frequency roll off can probably be related to the relatively high damping of the pipe-wall material.

The modal power flows can be summed to form a total power flow. The power input to the fluid-filled pipe from the force excitation can be measured through simultaneous measurements of the input force and acceleration of the point of excitation. Comparison of the input power with the measured power flow shows fair agreement above approximately 100 Hz.

Chapter 9 presents experiments on a pipe with heavy fluid loading. The excitation of the heavy fiuid loaded pipe is provided both by a radial point force at the shell wall and a transmitting hydrophone in the interior fluid.

The structural excitation of the pipe with heavy fluid loading is the same radial point force used as excitation during the experiments on a pipe with light fluid loading. A comparison between the results obtained from a pipe with light fluid loading and a pipe with heavy fluid loading, shows that the two most notable differences are the generally lower levels of accelerance and the lower cuton frequencies for the heavy fluid loaded pipe. The reduced level of accelerance is related to the increased mass of the fluid-filled pipe in the case of heavy fluid loading, while the lower cuton frequencies of the higher order modes can be explained by the lower relative stiffness of the shell wall for the pipe with heavy fluid loading. Apart from these differences, the conclusions from chapter 8 drawn from the experiments on a light fluid loaded pipe also apply for a heavy fluid loaded pipe.

During the experiments excited by a radial point force, the accelerance was measured using two different measurement principles: modal decomposition of accelerometer measurements and directly with modal sensors. The measured accelerance obtained by using the modal sensor for $n = 0$ (a PVDF wire wound around the circumference of the pipe) compares significantly better with the predicted accelerance at low frequencies than the accelerance obtained through modal decomposition of accelerometer measurements. The modal sensor for $n = 1$ (a number of shaped PVDF patches connected electrically to amplify the wanted mode and cancel the rest) and the modal decomposition measurements produce similar accelerances that compare well with the predicted accelerances. The sharp increase in accelerance at the cuton of the first structural branch of the higher order modes are resolved nicely in all measurements, but the modal sensor for $n = 2$ measures larger accelerance than predicted at higher frequencies, while both the $n = 3$ modal sensor and the accelerometer decomposition

method measure smaller accelerances than predicted.

The conclusion regarding the modal measurement technique is that both measurement principles are workable, but the measurements with the modal sensors are a lot faster. If the modal sensor principles used in the present investigation could be taken beyond the early prototype state to allow for higher precision and reliability, then their performance would undoubtly be even better than shown during these experiments.

The modal response of the pipe wall was solely measured by modal sensors during the experiments with the transmitting hydrophone. Generally the tendencies regarding the measured modal accelerances are the same as for the structural force measurements: in particular the accelerance measured by the $n = 0$ modal sensor compares well with the predicted accelerances.

The total power flow measured by the modal sensors compares surprisingly well with the predicted total power flow. The relatively poor measurements of the modal power flows for $n = 2$ and $n = 3$ at low frequencies make hardly any contribution to the total power flow, while these modes dominates at higher frequencies where the measurements of the modal power flow for $n = 0$ and $n = 1$ are relatively poor.

For all measurements on pipes with light and heavy fluid loading and structural and fluid excitation, the conclusions have been that the agreement between measured and predicted total power flow generally is good. However are power flow measurements obtained with the measurement principle proposed in the present thesis only as good as the measurements of the pipe response, and the greatest possible care should be taken to ensure that the conditions for the response measurements are as close as possible to the ideal situation used in the predictions of the power flow. The largest single source of error in the power flow measurements as presently set up is probably reflections from inefficient anechoic terminations. Other sources which may be important are geometric imperfections in the pipe (pipe bends, thickness variations, etc.), material imperfections in the pipe (e.g. weld lines and cast defects), and bubbles in the contained fluid.

When experiments are conducted in industrial applications using the vibroacoustic measurement principle presented in the present thesis, it is difficult to predict the load impedance of the pipe. For this reason the exact conditions of any power flow measurements should be stated along with detail of the experimental setup.

It was the original intention also to present in this thesis measurements of the vibroacoustic power flow in a heavy fluid loaded pipe excited by the turbulent fluid flow past a flow obstacle. Unfortunately, problems with the experimental setup made it impossible to obtain a full set of modal response measurements, and time did not allow for another set of measurements once the problems with the experimental setup were taken care off. However the preliminary results were very encouraging, and no new problems or shortcomings regarding the experimental method were identified during the fluid flow excited experiments.

10.3 Numerical prediction of vibroacoustic power flow

In chapter 4, the concept of numerical calculation of vibroacoustic power flow from a flow obstruction in a fluid-filled pipe has been presented.

The calculation involves three steps:

i) Solution of the incompressible unsteady flow around a flow obstruction inside the pipe using Computational Fluid Dynamics.

ii) Construction of a vibroacoustic analogy that transforms the vibroacoustic excitation of the flow past the flow obstruction into an equivalent problem, where vibroacoustic excitation by structural and fluid point sources is applied to an unobstructed fluid-filled pipe without flow.

iii) Calculation of the vibroacoustic power flow from the equivalent point sources.

The present thesis concentrates on steps ii) and iii) since a feasibility study showed that it is very complicated to obtain an unsteady time-resolved solution of the fluid flow. Step ii) involves the vibroacoustic analogy discussed in chapter 4, and the prediction model in chapter 6. Step iii) also involves chapter 6, and is the main focus of part II.

A key part of chapter 4 is the investigation of the relative scaling of monopole, dipole and quadrupole type sources inside a fluid-filled pipe. In free fields there is a well established expectation regarding the relative scaling: if the Mach number is sufficiently low the radiated power in the free field for each source type scales as: $1{:}\mathrm{Ma}^2{:}\mathrm{Ma}^4$. The conclusion of the investigation is that the relative scaling remains the same inside a fluid-filled pipe, but the so-called cross-over Mach number is reduced significantly in the case of a pipe with heavy fluid loading. However, it is shown that the cross-over Mach number is still approximately one order of magnitude higher than typical Mach numbers of industrial interest in the present thesis.

The result from the relative scaling investigation for sources inside a fluid-filled pipe simplifies step ii) above. The transformation from the vibroacoustic excitation of the flow past a flow obstruction into the equivalent problem is simplified considerably, as both the fluid monopole and fluid quadrupole excitation can be left out of the calculation.

Another simplification of the vibroacoustic analogy comes from the inclusion of tailored Green functions in the formulation. The tailored Green functions of a fluid-filled pipe are closely linked to the complex point-to-point response functions of the pipe. The prediction model in chapter 6 provides relevant transfer functions for fluid-filled pipes, excited either by point forces at the pipe wall or by point monopoles in the contained fluid. As noted above, the monopole itself is left out of the actual calculation, but from the tailored monopole Green function it is relatively easy to construct the corresponding dipole Green functions (and quadrupole Green functions, but they are left out as well).

As implied above, the prediction model in chapter 6 is capable of calculating the

vibroacoustic response and the vibroacoustic power flow in an doubly infinite fluid-filled pipe for two different types of excitation: mechanical (via the structure) and acoustical (via the fluid). The structural excitation is assumed to be in the form of a point force applied to the shell, while the fluid excitation is in the form of a point monopole in the interior fluid. The prediction model is nondimensionalised to reduce the number of input groups to a minimum. The prediction model is used heavily in part III where experimental results from controlled experiments are compared with the predicted results.

Through a limited parameter study in chapter 7, the influence of some of the input parameters to the numerical model has been investigated through dispersion curves and point mobilities. Here it is concluded that the internal fluid loading is the most important factor causing departures from a collapse on the parameters chosen. Significant changes in both the dispersion curves and mobilities are related to the fluid loading of the shell. An important part of the prediction model is the shell theory used. At the end of chapter 7 three different shell theories are compared. The conclusion of this study is that the Donnell-Mushtari shell theory is not well suited for the relatively low frequency range and low circumferential mode orders of interest to the present thesis. The Goldenveizer-Novozhilov and the Flügge shell theories produce very similar results that seem plausible from a physical point of view. Either of these theories could have been used for the prediction model, and the Flügge theory was chosen for the present thesis.

As noted in section 10.2, the experiments of part III and the predictions using the model from chapter 6 produce similar results. The pragmatic approach to validation used in this thesis is that both the experiments and the prediction model are of such a complicated nature, that if they compare well it cannot be a coincidence. The overall conclusion is thus that the experiments validate the numerical model and vice versa.

10.4 Appraisal

The overall objective of this research programme is to find ways of quantifying hydroacoustic noise sources coupled to fluid-filled pipe systems. Two approaches have been investigated in the present thesis: experimental and numerical simulation.

Both approaches have been successful in their own rights: controlled experiments have shown that the vibroacoustic power flow from vibroacoustic sources in a fluid-filled pipe can indeed be measured using the proposed principles of measurement. The investigation of the vibroacoustic analogy have shown that the calculation of the vibroacoustic power flow in a fluid-filled pipe excited by the fluid flow past a flow obstruction is feasible, if an unsteady time-resolved solution of the fluid flow is provided. Confidence in each of the approaches has been gained by comparing them as much as possible.

However, the original intention regarding the calculation of the vibroacoustic power flow from a flow obstruction in a fluid-filled pipe was to conduct controlled experiments of a common scenario, and then compare the calculated power flow with an experimentally

obtained power flow. As the research programme progressed it became more and more evident that the 3 years time span of a Danish Industrial PhD did not allow for such an ambitious goal. In the view of the author this would be the final test for the concepts presented in the present thesis.

Chapter 11

Implications regarding the industrial application

As noted in chapter 10, the objectives of the formal research programme have been met. However the present thesis is the product of an industrial PhD under the terms of the Danish Academy of Technical Sciences. In the Danish Industrial PhD Fellowship programme one of the main tasks of the PhD student is to apply the present knowledge (including sources from literature and the existing knowledge of the university) to the benefit of the industrial sponsor. The purpose of this chapter is to put the results from the present thesis into the industrial context presented in chapter 1.

It was discussed in chapter 4 that it is not possible to obtain an unsteady time-resolved solution of the fluid flow using the industrial CFD-code Star-CD. This reduces the practical industrial use of the proposed concept of applying numerical calculation methods to vibroacoustic power flow excited by fluid flow in a pipe. Nonetheless the concept will become workable when future industrial CFD-codes are capable of solving the unsteady fluid flow.

The prediction model from chapter 6 can be used directly to answer simple questions of the type: does a force in the fluid drive the fluid-filled shell more efficiently than the same force applied to the shell wall; or how far away from a point of excitation does the power flow redistribute between evanescent and propagating waves in a given application? However, the answers obtained by the prediction model may be of limited industrial interest, as strictly speaking they only apply for infinite pipes. The prediction model would be more useful from an industrial point of view if it included some of the common complications present in heating systems, for example pipe bends, radiators or reservoir tanks. This is presented as a suggestion for further work in chapter 12.

On the basis of the experiments presented in part III, it was concluded that the experimental method proposed in chapter 3 for power flow measurements is workable for fluid-filled pipes with both light and heavy internal fluid loading. A key part of the arguments leading to the positive conclusion concerns the modal power flows: if the power flow in each of the circumferential modes can be measured independently, then

the total power flow is the sum of the modal power flows. The proposed method in its present form only allows one branch for each mode to contribute significantly to the modal power flow. For the parameter range of industrial interest this is always the case for $n \geq 1$, as there is at most one structural wave propagating in the frequency range of industrial interest. For $n = 0$ there are three branches that potentially can contribute to the power flow at low frequencies: one mainly fluid wave, one mainly torsional structural wave, and one mainly axial structural wave. In part III it was argued that the torsional wave only contributes to the power flow if it is excited, and by assuming it is not excited, it can be disregarded. This leaves the mainly fluid wave and the mainly axial structural wave. For light fluid loading, it was argued that the power flow contribution from the fluid wave was negligible, leaving only the structural branch to contribute significantly to the modal power flow for $n = 0$. Exactly the opposite argument was used for the heavy fluid loading: only the fluid wave contributes significantly to the modal power flow for $n = 0$.

The obvious question of industrial interest is then: in the industrial applications presented in chapter 1, can the fluid loading of the water-filled pipes be labelled as either light or heavy? Table 7.3 on page 74 shows the geometric properties of some pipes of industrial interest. Most of the pipes will be undoubtly be heavy fluid loaded if they are water filled, but the standard 1" steel pipe steel pipe has a relatively large h/a ratio combined with the relatively high density of steel. In the following it is investigated whether the fluid loading for this shell is heavy.

Throughout the thesis two different methods have been used to characterise the fluid loading of the shell: the cuton frequencies of the higher order modes, and the proportion of the power flow in the shell and in the fluid, respectively. For a light fluid loaded shell the cuton frequencies of the higher order modes are very close to the in vacuo cuton frequencies, and when the pipe wall is excited by a radial point force the power flow for the $n = 0$ mode is mainly carried by the pipe wall.

Figure 11.1 shows a detail of the $n = 2$ dispersion curves for the water-filled 1" steel pipe, along with the corresponding in vacuo dispersion curves. The conclusion drawn from the figure is that the fluid loading is not light, as there is a some difference between the cuton frequencies of the first $n = 2$ structural wave in the in vacuo and water-filled case. Figure 11.2 shows the predicted power flows for the water-filled 1" steel pipe when the pipe wall is excited by a radial point force. The power flow is plotted for three different axial positions: the solid lines correspond to $s = 15$, the dashed lines to $s = 25$, and the dotted lines to $s = 20$. As can be seen, the green curves for the different axial positions do not coincide. This behaviour is predicted by Fuller (1984), and is related to the axial dependance of the power flow equations. The result is that the total axial vibroacoustic power flow is independent of the axial position, but the distribution between fluid and structure varies with the axial position. It should be noted that this effect is not related to the redistribution of power near the point of excitation, and it is not a near field effect at all.

The red curves in figure 11.2 almost coincide on the scale plotted, indicating that the fluid-borne power flow is responsible for the main part of the total power flow. In figure

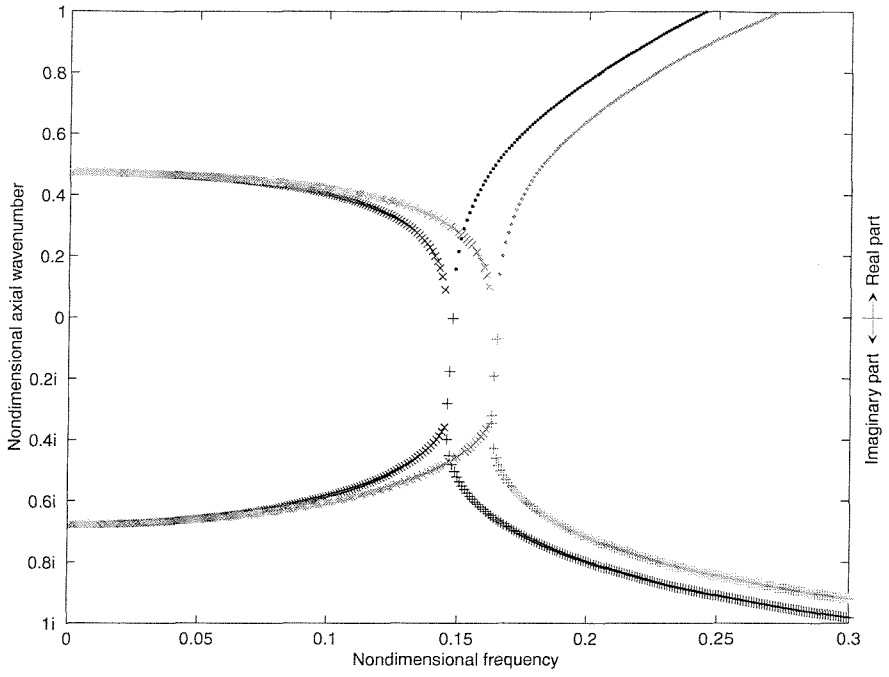

Figure 11.1: Cuton of the first $n = 2$ structural wave for a 1" steel pipe. The green curves represent the pipe in vacuo and the blue curves the water-filled pipe.

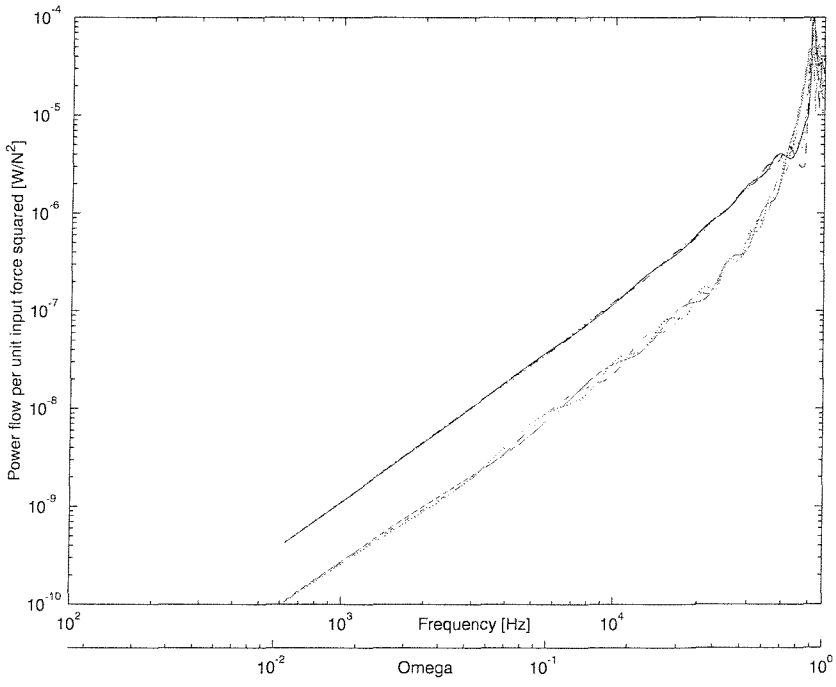

Figure 11.2: Predicted power flow for a water-filled 1" steel pipe excited by a radial point force, $n = 0$, $s = 15, 20, 25$. The water-borne power flow is red and the structural-borne power flow is green.

9.14 showing the predicted power flow distribution for a pipe with heavy fluid loading, the difference between the fluid-borne and the structure-borne power flow for $n = 0$ is approximately a factor of 100. The corresponding figure 8.10 for the pipe with light fluid shows a factor of approximately 0.01 (in this case the structure-borne power flow is larger than the fluid-borne power flow). In figure 11.2 the difference is reduced to approximately a factor of 5. The conclusion drawn from this is that the fluid loading of the water-filled 1" steel pipe is definitely not light but not truly heavy either.

This kind of fluid loading is dubbed intermediate. For the method of power flow measurements proposed in the present thesis, the intermediate fluid loading may pose a problem. As noted above, the power flow measurement method relies on the assumption that one branch dominates the power flow for $n = 0$ at the frequencies of industrial interest. If both the mainly fluid wave and the mainly axial structural wave contribute significantly to the power flow, it may not be possible to relate the modal power flow in the $n = 0$ mode to the pipe wall modal response as in equation (3.1). Equation (3.1) predicts the power flow through a relation between the power flow and the pipe wall response. If two different branches contribute to the power flow, the same two branches also contribute to the pipe wall response.

By measuring the pipe wall response at one axial position only, it is not possible to deduce which proportion of the pipe wall response is related to the fluid wave, and which proportion of the pipe wall response is related to the structural wave. It is highly plausible that the relation between the pipe wall response for the mainly fluid wave and the fluid-borne power flow is significantly different from the relation between the pipe wall response for the mainly structural axial wave and the structure-borne power flow. To remove this possible source of error, another suggestion for further work is an expansion of the proposed method of power flow measurements to allow for two or more contributing branches for each circumferential mode.

As shown in figure 11.2 the structure-borne power flow for a water-filled 1" steel pipe with structural excitation in the form of a point radial force is approximately a factor of 5 smaller than the fluid-borne power flow. The error made by assuming that the entire pipe wall response is related to the mainly fluid wave is therefore relatively small. In the industrial application of the present thesis the error caused by this simplification is probably acceptable. A more important source of error in the industrial application is the lack of anechoic termination of finite pipes. One of the suggestions for further work presented in chapter 12 is an investigation of different anechoic terminations.

Chapter 12

Suggestions for further work

During the course of the present research project, a number of suggestions for further work have emerged.

The experimental method proposed to quantify the vibroacoustic power flow in a fluid-filled pipe relies on some restrictive assumptions. Some of these assumptions can be relaxed if the underlying prediction model is improved as discussed below, so that the predictions involved are made for the special measurement situation in question. Another way of improving the proposed experimental method is through multiple sensors. With more sensors it would be possible to decompose multiple waves for a given circumferential mode. By measuring the pipe wall response at two axial positions, it is possible to deduce which proportion of the radial pipe wall response is related to the fluid wave, and which proportion of the pipe wall response is related to the structural wave. Another possibility is to include sensors measuring the torsion of the pipe. From measurements of the pipe torsion, the power flow carried by torsion of the pipe can be quantified by a relation similar to equation (3.1). However, the power flow carried by the cross terms of the different branches would have to be considered for the multiple wave method.

In the case of a single branch for each mode, multiple sensors would allow the decomposition of forward and backward propagating waves along the pipe. This would effectively remove the need for anechoic terminations of the finite pipe, as the part of pipe wall response related to the outgoing wave could be retrieved and put into equation (3.1). The power flow inferred from the equation would then be for the outgoing wave alone.

Using the proposed power flow measurement method as is, the results can be improved through improvements to the anechoic termination. The measured estimate of the real power flow in a fluid-filled pipe is as good as the measurement of the modal response. If the measurement of the modal response is improved through better anechoic terminations, so is the power flow measurement. Under controlled conditions in the laboratory, different designs of anechoic terminations can be investigated and improved.

The prediction model from part II can be improved significantly by including different

complicating effects. It would be simple to include the effect of damping in the model through a complex Young's modulus. Inclusion of damping in the prediction model would allow a closer investigation of the high frequency roll off of the accelerance measurements presented in part II.

In the present form no form of discontinuities are allowed in the prediction model. In the industrial application of the present thesis very complicated discontinuities of the pipes are encountered, e.g. heat radiators. It is probably not realistic to expand the present model to such complications, but more simple discontinuities could be used as building blocks for more complicated ones. The ability to predict the vibroacoustic response of a pipe with a bend would be very useful. At the pipe bend there will be branch conversion and reflection, as e.g. axial waves incident on the bend from one side may be partly reflected as axial waves and partly leave the bend on the other side as bending waves. Fuller (1981) shows a method to predict the effects of wall discontinuities on the propagation of flexural waves in in vacuo pipes. It would probably not be very difficult to combine the present prediction model with the method of Fuller (1981) to allow for prediction of the vibroacoustic response in fluid-filled pipes with wall discontinuities. Other useful expansions of the prediction model include local reinforcements of the pipe (e.g. flanges or tread connections of different parts) or local impedance changes (e.g. where two pipes of different dimensions are connected).

Although industrial CFD-codes are not capable of producing an unsteady time-resolved solution of the fluid flow, further investigation of the proposed method of numerical calculation of vibroacoustic power flow from a flow obstruction in a fluid-filled pipe is possible using a purpose built CFD-code, e.g. an unsteady RANS code as presently used in university research. The experimental setup used in chapter 9 can easily be expanded to provide modal measurements of the pipe wall response when the fluid-filled pipe is excited by the fluid flow past a flow obstruction. In fact a feasibility study of such an experimental setup was made during the course of the present research project, and the results were promising.

Appendices

Appendix A

Charge equations for shaped PVDF film sensors

The shaped modal polyvinylidene fluoride (PVDF) sensors used in the present thesis, are using the piezoelectric film material in 'stretching-mode', converting mechanical strain to an electric charge, through the direct piezoelectric effect. The relation between strain and charge can be found from

$$D_3 = \varepsilon_{33} E_3 + e_{31} S_\theta + e_{32} S_z \tag{A.1}$$

where D_3 is the electric displacement; ε_{33} is the permittivity at constant stress; E_3 is the electric field ; S_θ is the circumferential strain; S_z is the axial strain; and e_{31} and e_{32} are the piezoelectric stress constants, determined from

$$\begin{bmatrix} e_{31} \\ e_{32} \end{bmatrix} = \begin{bmatrix} E_P/(1-\nu_P^2) & \nu_P E_P/(1-\nu_P^2) \\ \nu_P E_P/(1-\nu_P^2) & E_P/(1-\nu_P^2) \end{bmatrix} \begin{bmatrix} d_{31} \\ d_{32} \end{bmatrix} \tag{A.2}$$

where E_P is the PVDF Young's modulus; ν_P is the PVDF Poisson's ratio; and d_{31} and d_{32} are the piezoelectric strain constants.

Using the shell theory of Flügge (1962), the axial and circumferential strains at a distance y_o from the mid-surface can be expressed as

$$\begin{aligned} S_z &= S_{ez} + S_{iz} \\ S_\theta &= \frac{1}{1+\frac{y_o}{a}} (S_{e\theta} + S_{i\theta}) \end{aligned} \tag{A.3}$$

where $S_{ez} = \partial u/\partial z$ is the axial stretching strain in the axial direction; $S_{iz} = -y_o\, \partial^2 w/\partial z^2$ is the bending strain in the axial direction; $S_{e\theta} = 1/a\ (\partial v/\partial\theta + w)$ is the stretching strain in the circumferential direction; and $S_{i\theta} = -y_o/a\ (\partial^2 w/\partial\theta^2 - \partial w/\partial\theta)$ is the bending strain in the circumferential direction.

Flügge (1962) states, that for the $n = 0$ mode, the extensional deformation in stretching dominates at frequencies well below the ring frequency, while the higher order modes $n \geq 1$ are dominated by the in-extensional deformation of bending well below the ring

frequency. Variyart and Brennan (1999) quotes a book by Timoshenko and Woinowsky-Krieger for stating, that one of the conditions condition for in-extensional deformation is $\partial v/\partial\theta = -w$.

Considering only $n \geq 1$ at frequencies well below the ring frequency, the axial and circumferential strains reduce to

$$\begin{aligned} S_z &= -y_o \frac{\partial^2 w}{\partial z^2} = -\frac{y_o}{a^2}\frac{\partial^2 w}{\partial s^2} \\ S_\theta &= \frac{y_o}{(1+\frac{y_o}{a})a^2}\left(\frac{\partial^2 w}{\partial\theta^2} + w\right) \end{aligned} \tag{A.4}$$

If the two surface electrodes of the PVDF sensor is connected through a charge amplifier, the resulting electrical connection cancels the electric field between the two surface electrodes so that E_3 is zero. Using this along with the reduced stresses the electric displacement of equation (A.1) becomes

$$D_3 = -e_{31}\frac{y_o}{(1+\frac{y_o}{a})a^2}\left(\frac{\partial^2 w}{\partial\theta^2} + w\right) - e_{32}\frac{y_o}{a^2}\frac{\partial^2 w}{\partial s^2} \tag{A.5}$$

Using the arrangement with the charge amplifier, the generated charge is approximately the average of the electric displacement integrated over the effective area of both sides of the surface electrodes. With a sinusoidal shape of the modal sensor, this equation can be expanded to

$$q = \int_{s_c - b_s F(p\theta)}^{s_c + b_s F(p\theta)} \int_0^{2\pi} \left(e_{31}S_\theta + e_{32}S_x\right) a^2 \mathrm{d}\theta \mathrm{d}s \tag{A.6}$$

where q is the generated charge; s_c is the center position of the sensor; $b_s = b/a$, where b is half the width of the sensor; $F(p\theta)$ is the shape function of the sensor; and p is the main circumferential mode of sensitivity of the sensor. It is assumed, that the width of the sensor is small compared to the wavelengths involved, so that the variation of the strain across the sensor is negligible. As the alignment of the sensor to the vibrations involved is not known a priori, the shape function can be both sine and cosine. In the following derivations, the cosine shape is chosen, but the equations could also be cast in a form using the sine shape.

The radial displacement is assumed to have the general form

$$w = \sum_{n=0}^{\infty}\sum_{b=1}^{\infty} aW_{nb}(\phi_c\cos(n\theta) + \phi_s\sin(n\theta))e^{i(\kappa_{nb}s - \omega t)} \tag{A.7}$$

Integrating the cosine part of the axial contribution of equation (A.6), yields

$$\begin{aligned} q_{c,z} = \int_{s+}^{s_c + b_s\cos(p\theta)} \int_0^{2\pi} \Bigg(&-\frac{y_o}{a^2}\sum_{n=0}^{\infty}\sum_{b=1}^{\infty}(i\kappa_{nb})^2 aW_{nb} \\ &(\phi_c\cos(n\theta) + \phi_s\sin(n\theta))e^{i(\kappa_{nb}s - \omega t)}\Bigg)\mathrm{d}\theta\mathrm{d}s \end{aligned} \tag{A.8}$$

where the integral in the axial direction can be separated and evaluated, thus

$$\begin{aligned}\int_{s_c-b_s\cos(p\theta)}^{s_c+b_s\cos(p\theta)} e^{i\kappa_{nb}s}\mathrm{d}s &= \frac{-i}{\kappa_{nb}}e^{i\kappa_{nb}(s_c+b_s\cos(p\theta))} + \frac{i}{\kappa_{nb}}e^{i\kappa_{nb}(s_c-b_s\cos(p\theta))} \\ &= \frac{2e^{i\kappa_{nb}s_c}}{\kappa_{nb}}\sin(\kappa_{nb}b_s\cos(p\theta))\end{aligned} \tag{A.9}$$

with the use of the Euler sine formula. The sine can be expressed using Bessel functions as

$$\sin(\kappa_{nb}b_s\cos(p\theta)) = 2\sum_{m=1}^{\infty}(-1)^{m-1}\mathrm{J}_{2m-1}(\kappa_{nb}b_s)\cos\left((2m-1)p\theta\right) \tag{A.10}$$

If equation (A.9) and (A.10) are substituted into equation (A.8), the integral in θ can with the use of orthogonality be evaluated as

$$q_{c,z} = 4\pi\phi_c e_{32}y_o a\sum_{n=0}^{\infty}\sum_{b=1}^{\infty}\kappa_{nb}W_{nb}e^{i\kappa_{nb}s_c}\sum_{m=1}^{\infty}(-1)^{m-1}\mathrm{J}_{2m-1}(\kappa_{nb}b_s)\delta_{nm} \tag{A.11}$$

where $\delta_{nm} = 1$ if $n = (2m-1)p$ and $\delta_{nm} = 0$ otherwise.

In case of the sine shape function, the result is almost the same:

$$q_{s,z} = 4\pi\phi_s e_{32}y_o a\sum_{n=0}^{\infty}\sum_{b=1}^{\infty}\kappa_{nb}W_{nb}e^{i\kappa_{nb}s_c}\sum_{m=1}^{\infty}\mathrm{J}_{2m-1}(\kappa_{nb}b_s)\delta_{nm} \tag{A.12}$$

By combining the sine and cosine parts, the total charge generated by axial strains for arbitrary orientation can be obtained from:

$$q_{t,z} = \sqrt{q_{c,z}^2 + q_{s,z}^2} \tag{A.13}$$

and the orientation angle can be found as

$$\theta_o = \frac{1}{n}\tan^{-1}\left(\frac{q_{s,z}}{q_{c,z}}\right) \tag{A.14}$$

The circumferential part of equation (A.6) can likewise be evaluated and the corresponding results are:

$$q_{c,\theta} = 4\pi\phi_c e_{31}y_o a\sum_{n=0}^{\infty}\sum_{b=1}^{\infty}\frac{(n^2-1)}{(1+\frac{y_o}{a})\kappa_{nb}}W_{nb}e^{i\kappa_{nb}s_c}\sum_{m=1}^{\infty}(-1)^{m-1}\mathrm{J}_{2m-1}(\kappa_{nb}b_s)\delta_{nm} \tag{A.15}$$

$$q_{s,\theta} = 4\pi\phi_s e_{31}y_o a\sum_{n=0}^{\infty}\sum_{b=1}^{\infty}\frac{(n^2-1)}{(1+\frac{y_o}{a})\kappa_{nb}}W_{nb}e^{i\kappa_{nb}s_c}\sum_{m=1}^{\infty}\mathrm{J}_{2m-1}(\kappa_{nb}b_s)\delta_{nm} \tag{A.16}$$

From the Bessel function sum, it can be seen that the a sensor intended for $n = 1$ also will pick up vibrations for $n = 3$, $n = 5$ etc. due to the cross sensitivity. This cross sensitivity has been investigated for the $n = 2$ modal sensor by Variyart and Brennan (1999), and the conclusion of this investigation was that the influence of other modes is small provided the width of the sensor is kept reasonably small. At low frequencies the influence from other modes is not really a problem in the far field, where the higher order modes are well below their cuton frequency.

Bibliography

Amini, A. and I. Owen (1995). A practical solution to the problem of noise and vibration in a pressure-reducing valve. *Experimental Thermal and Fluid Science 10*, 136–141.

Beranek, L. E. and I. L. Vér (1993). *Noise and Vibration Control Engineering.* Wiley.

Bourget, S. and F. J. Fahy (1993). Vibrational power flow measurement along a thin cylindrical pipe. *4Th International Congress on Intensity Techniques: Structural Intensity and Vibrational Energy Flow*, 153–157.

Brennan, M. J. et al. (1997). The dynamic coupling between piezoceramic actuators and a beam. *Journal of the Acoustic Society of America 102(4)*, 1931–1942.

Brentner, K. S. (1996). An efficient and robust method for predicting helicopter rotor high-speed impulsive noise. *Journal of Sound and Vibration 203(1)*, 87–100.

Briscoe, A. R. (1994). *Axisymmetric power flow transmision in fluid filled pipes.* Ph.d. thesis, University of Southampton, ISVR.

Briscoe, A. R. and R. J. Pinnington (1996). Axisymmetric vibrational power measurement in empty and fluid filled pipes. *Journal of Sound and Vibration 192*(4), 771–791.

Bruel&Kjaer (1992). Intruduction to underwater acoustics. *B&K Application notes.*

Cremer, L., M. Heckl and E. E. Ungar (1988). *Structure-borne Sound* (2nd ed.). Springer-Verlag.

Crighton, D. G. and F. G. Leppington (1971). On the scattering of aerodynamic noise. *Journal of Fluid Mechanics 46*, 577–597.

Curle, N. (1955). The influence of solid boundaries upon aerodynamic sound. *Proceeedings of the Royal Society, Series A 231*, 505–514.

Davies, H. G. and J. E. Ffowcs Williams (1968). Aerodynamic sound generation in a pipe. *Journal of Fluid Mechanics 32(4)*, 765–778.

Donnell, L. H. (1933). Stability of thin-walled tubes under torsion. *NACA Technical Report no. 479.*

Durant, C. et al. (1999). Vibroacoustic response of a thin cylindrical shell excited by a turbulent internal flow: comparison between numerical prediction and experimentation. *Journal of Sound and Vibration 229(5)*, 1115–1155.

Fahy, F. and J. Walker (1998). *Fundamentals of Noise and Vibration.* E & FN Spon.

Fahy, F. J. (1985). *Sound and structural vibration* (1st ed.). Academic Press.

Feng, L. (1994). Acoustic properties of fluid filled elastic pipes. *Journal of Sound and Vibration 176*, 399–413.

Feng, L. (1995). Experimental studies of the acoustic properties of a finite elastic pipe filled with water/air. *Journal of Sound and Vibration 189*(4), 511–524.

Ffowcs Williams, J. E. and L. H. Hall (1970). Aerodynamic sound generation by turbulent flow in the vicinity of a scattering halfplane. *Journal of Fluid Mechanics 40*, 657–670.

Ffowcs Williams, J. E. and D. L. Hawkings (1969). Sound generation by turbulence and surfaces in arbitrary motion. *Proceeedings of the Royal Society, Series A 264*, 321–342.

Finnveden, S. (1997a). Formulas for modal density and for input power from mechanical and fluid point sources in fluid filled pipes. *Journal of Sound and Vibration 208*(5), 705–728.

Finnveden, S. (1997b). Simplified equations of motion for the radial-axial vibrations of fluid filled pipes. *Journal of Sound and Vibration 208*(5), 685–703.

Finnveden, S. (1997c). Spectral finite element analysis of the vibration of straight fluid-filled pipes with flanges. *Journal of Sound and Vibration 199*(1), 125–154.

Flügge, W. (1962). *Stresses in Shells* (2nd ed.). Springer-Verlag.

Fox, R. W. and A. T. McDonald (1985). *Introduction to fluid mechanics* (3rd ed.). John Wiley & Sons, Inc.

Fuchs, H. V. (1993). Generation and control of noise in water supply installations. part 2: Sound source mechnisms. *Applied Acoustics 28*, 59–85.

Fuller, C. R. (1980). The effects of wall discontinuities on the propagation of flexural waves in cylindrical shells. ISVR technical report 106, Institute of Sound and Vibration Research, University of Southampton.

Fuller, C. R. (1981). The effects of wall discontinuities on the propagation of flexural waves in cylindrical shells. *Journal of Sound and Vibration 75*(2), 207–228.

Fuller, C. R. (1983). The input mobility of an infinite circular cylindrical elastic shell filled with fluid. *Journal of Sound and Vibration 87*(3), 409–427.

Fuller, C. R. (1984). Monopole excitation of vibrations in an infinite cylidrical elastic shell filled with fluid. *Journal of Sound and Vibration 96*(1), 101–110.

Fuller, C. R. (1986). Radiation from an interior monopole through an elastic pipe. *Journal of Sound and Vibration 109(2)*, 259–275.

Fuller, C. R. and F. J. Fahy (1982). Characteristics of wave propagation and energy distributions in cylindrical elastic shells filled with fluid. *Journal of Sound and Vibration 81*(4), 501–518.

Hoff, N. J. (1955). The accuracy of Donnell's equations. *ASME Journal of applied mechanics 54*, 329–334.

Howe, M. S. (1997). *Acoustics of fluid-structure interactions.* Cambridge University Press.

Kelley, C. T. (1994). *Iterative Methods for Linear and Nonlinear Equations.* SIAM Frontiers no16. SIAM.

Kiil, H. E. (1982). *Ventilgeometrier, EF 83.* Ph. D. thesis, Technical University of Denmark.

Kreyzig (1998). *Advanced Engineering Math* (8th ed.). John Wiley & Sons.

Lee, S. (1997). Unsteady aerodynamic force prediction on a square cylinder using $k - \epsilon$ turbulence models. *67&68*, 79–90.

Leissa, A. W. (1973). *Vibration of shells* (First ed.). National Technical Information Service.

Lighthill, M. J. (1952). On sound generated aerodynamically, I. General theory. *Proceeedings of the Royal Society, Series A 211*, 564–587.

Lowson, M. V. (1982). Assessment and prediction of wind turbine noise. *Flow solutions report 92/19, ETSU W/13/00284/REP*, 1–59.

Lyn, D. A. (1992). Ensemble-averaged measurements in the turbulent near wake of a square cylinder. *Interrimreport, Purdue University, West Lafayette, Indiana, USA.*

Morse, P. M. and K. U. Ingard (1968). *Theoretical Acoustics* (1st ed.). Priceton University press.

Murakami, S. and A. Mochida (1995). On turbulent vortex sheding flow past a 2d square cylinder predicted by cfd. *54/55*, 191–211.

Nakano, M. et al. (1988). Noise and vibration related to the pattern of supersonic annular flow in a pressure reducing gas valve. *Journal of Fluid Engineering, Transactions of the ASME 110*, 55–61.

Niordson, F. I. (1985). *Shell theory.* Elsevier Science Publishers B.V.

Norton, M. P. (1989). *Fundamentals of noise and vibration analysis for engineers.* Cambridge University Press.

Pavic, G. (1976). Measurement of structure-borne wave intensity, part i: formulations of the methods. *Journal of Sound and Vibration 49*, 221–230.

Pavic, G. (1990). Vibrational energy flow in elastic circular cylindrical shells. *Journal of Sound and Vibration 142*(2), 293–310.

Pavic, G. (1992). Vibroacoustical energy flow through straight pipes. *Journal of Sound and Vibration 154*(3), 411–429.

Pinnington, R. J. and A. R. Briscoe (1994). Externally applied sensor for axisymmetric waves in a fluid filled pipe. *Journal of Sound and Vibration 173*(4), 503–516.

Rodi, W. et al. (1997, June). Status of large eddy simulation: Results of a workshop. *Transactions of the ASME, Journal of Fluid Engineering 119*, 248–262.

Simmons, C. (1997). Radiator valves: Determination of the sound power level in the laboratory. *Nordtest project 1222-95.*

Skelton and James (1997). *Theoretical acoustic of underwater structures* (1st ed.). Imperial College Press.

Variyart, W. and M. J. Brennan (1999). Measurements of flexural propagating waves in pipes using shaped PVDF modal sensors. *ISVR Technical Memorandum No. 847*, 1–62.

Vickery, B. J. (1966). Fluctuating lift and drag on a long cylinder of square cross-section in a smooth and in a turbulent stram. *Journal of Fluid Mechanics 25*, 481–494.

Vink (1995). *Plastguiden* (4th ed.). Vink AS.

Wilcox, D. C. (1998). *Turbulence modelling for CFD* (2nd ed.). DCW Industries.

Xu, M. B. and X. M. Zhang (1998). Vibration power flow in a fluid-filled cylindrical shell. *Journal of Sound and Vibration 218(4)*, 587–598.